ABSTRACT

Title of Dissertation: EXPERIMENTS AND SEMI-EMPIRICAL MODELING OF BUOYANCY-DRIVEN, TURBULENT FLAME SPREAD OVER COMBUSTIBLE SOLIDS IN A CORNER CONFIGURATION

Dushyant Madhav Chaudhari,
Doctor of Philosophy,
2021

Dissertation directed by: Professor Stanislav I. Stoliarov,
Department of Fire Protection Engineering

The increased use of engineered complex polymeric materials in the construction industry has highlighted their fire hazard. Screening of these materials, especially during the developmental stage, before safe commercial application requires standardized testing, which can be expensive. This research investigates the possibility of utilization of computational capability to predict fire hazard for facilitating screening of wall-lining materials in an important standardized configuration – a corner geometry without a ceiling. It also aims to fundamentally understand the dynamics of interactions between condensed-phase pyrolysis, gas-phase combustion, and flame heat feedback during concurrent, buoyancy-driven flame spread. Consequently, hierarchical experiments and modeling from

small-scale to large-scale scenarios were performed using samples having mass in orders of magnitude between a milligram to a kilogram. Small-scale experimental data were inversely analyzed to develop comprehensive pyrolysis models using a hill-climbing optimization technique in a comprehensive pyrolysis solver, ThermaKin. Large-scale experiments performed over a non-charring, non-swelling material with well-characterized condensed-phase pyrolysis – Poly (methyl methacrylate) (PMMA) – provided valuable data for fast-response (13 s response) calorimetry, well-resolved flame heat feedback (maximum ± 6 kW m^{-2} error) at 28 locations, and radiation intensities at spectrally-resolved narrowband wavelength (900 ± 10 nm) corresponding to soot emissions during the flame spread. An empirical flame heat feedback model obtained from large-scale experiments conducted over PMMA was then coupled with the pyrolysis model to develop a low-cost semi-empirical model for simulating fire dynamics during flame spread. The hierarchical experiments and modeling framework was further applied to two important wall-lining materials, Polyisocyanurate foam and Oriented Strand Board, to scrutinize the robustness of the developed modeling framework. The study has presented a systematic methodology that predicted the fire dynamics in the large-scale tests over the three studied materials and can be judiciously extended to other materials. To further improve the large-scale modeling predictions, it is necessary a) to reduce the pyrolysis parameter and the flame heat feedback uncertainty below the minimum ±10% observed uncertainty, b) to quantify the convection-radiation contribution to the flame heat feedback, and c) to investigate the ability to generalize the empirical flame heat feedback model to other materials.

EXPERIMENTS AND SEMI-EMPIRICAL MODELING OF BUOYANCY-DRIVEN, TURBULENT FLAME SPREAD OVER COMBUSTIBLE SOLIDS IN A CORNER CONFIGURATION

by

Dushyant Madhav Chaudhari

Dissertation submitted to the Faculty of the Graduate School of the
University of Maryland, College Park, in partial fulfillment
of the requirements for the degree of
Doctorate of Philosophy
2021

Advisory Committee:

Professor Stanislav I. Stoliarov, Chair
Professor Christopher Cadou, Dean's Representative
Professor Arnaud Trouvé
Professor Johan Larsson
Dr. Isaac Leventon

Acknowledgements

Beginnings are always difficult, be it writing acknowledgements or starting a Ph.D. I remember when I started in June 2017, there were moments when innocent stupidity got the best of me, and I created problems never seen before by my advisor, Dr. Stanislav Stoliarov (Stas). For example, my then fidgety hands dropped a thin 5 mm diameter lid inside a long inaccessible tube of the small-scale experimental setup. The lid needed to be rescued by a pair of tweezers operated by precise steady hands of a colleague or giving away over $5000 to a licensed technician. That was the first time I realized how much more I still need to get better with these experiments and myself. Over years, Stas was involved in all matters – be it data processing or experimental troubleshooting, encouragement to continue working, or feedback ranging from critically discouraging to encouraging on writing, research ideas. I am deeply grateful for the depth of his technical knowledge, for his compassionate and fun ways of addressing problems, for his uninterrupted availability, for his forgiving (most of the times) and encouraging nature. Thank you, Dr. Stas!!

I had stumbled upon Stas when I was trying to find the advisor for my PhD while reading the acknowledgement section of Dr. Isaac Leventon's thesis. Isaac has intermittently been a part of this journey – by providing a map of college park for things to do before I arrived, questioning and suggesting better ways to perform my experiments, inviting for being a part of experiments at NIST and his favorite Christmas tree burning competition, exchanging the heat flux gauges, and most importantly, being a part of my committee and providing excellent helpful comments on my dissertation. I am extremely grateful for having you as a committee member. I also immensely thank my committee members providing valuable feedback during the proposal meeting which has encouraged me to make this dissertation better. Thank you, Dr. Christopher Cadou for being the Dean's representative and suggesting improved ways to analyze the data/model, Dr. Arnaud Trouve for feedback on experiments from the modeling perspective, Dr. Johan Larsson for encouraging to emphasize valuable results. I also would like to thank Dr. Peter Sunderland for being part of the proposal committee.

All this research would have been impossible to be performed in relative peace without support in the form of funding from Federal Aviation Administration (FAA Grant no. 16-G-017) and DuPont De Nemours Inc. Personally, I would like to thank Dr. Richard Lyon from FAA for the valuable literature. I am extremely grateful for Dr. Mark Beach and Dr. Kali Suryadevara from Dupont De Nemours Inc. for their routine trips for project updates, providing samples for conducting experiments, and helpful technical discussions.

This brings me to my research colleagues and/or guides, and faculty/staff who have been instrumental during this time. Having negligible prior experience in experiments before the PhD, I remember initially creating complicated (yet creative) and sometimes unrealistic designs for my setup. Olga, the previous lab manager sat with me and taught me the basics of different types of fittings, connections, lab machinery, for which I am grateful for. I will be grateful for Fernando, the current lab manager and a previous post-doc, who made being in the lab much more efficient, clean and also invested time and patience to teach me experimental nuances (especially MFC, MCC, and calibrations (his

nemesis)). I personally would like to thank Josh Swann and Yan Ding for their patience to teach and pass down their legacy of TGA-DSC, CAPA experiments and modeling. A fraction of my PhD, I will now say fortunately, coincided with Greg Fiola's masters, whose research was a part of my research. Greg's innovative ways of simplifying experiments/sample preparation, technical discussions and exchanging ideas for data processing and experiments, his help (especially the knife) with the experiments, and sometimes philosophical discussions were immensely valuable to this experience. Thanks, Greg Folia (Mr. Nothing + ∞, misspelled on purpose). Other Stas' research group colleagues, Ahmed Said, Chris Lee, Conor McCoy, Hongen Zhou, Jacques De Beer, Jessica Tilles, Joe Alsacio, Lucas Sommerfield, Ryan Chaffer, Will Saar, made working in the furnace (internal name of the group) bearable, fun, supportive, and extremely motivating. Apart from these, FPE research colleagues – Evan, Lana, Priya, Xingyu, Sriram, Andres, Hadi, Dennis, Deepanshu, Mohammed, Parham – were also amazing for having conversations and maintain sanity in the FPE department. I also am grateful to Brian Sullivan for all the uninterrupted business and order requests, Christine O'Brian, Darius Craig, Kerri Poppler James for supportive administrative formalities, Nicole Hollywood for administrative help and her daughter's Girl Scout cookies, and Dr. James Milke for supporting all the department activities and talks in the graduate room area.

Outside the University, I can't thank enough the friends at the memorable 201 and at the Adelphi house. Being an international student, they are like a family. The circle of social importance kept on changing for me as people moved to different cities, states, countries, and found their own life in this span of time. During the times when PhD took away some of the social life and work became a priority, it was humbling to know the constant support from all these people. Naming all of them is impossible, but I thank Angela, Arafat, Arjun, Dipesh, Ellen, Jair, Katy, Linda, Mayuresh, Neeraj, Palak, Rohit and Tanika, to name a few, for their continuous support and retrospective/philosophical conversations (whether intentionally or not) when needed. And Taís, we met half way through this journey but I can't thank enough for balancing me out and keeping me motivated when times were rough – Muito Obrigado!!

Finally, I thank my mother, my father, and my brother back in India, who continually backed me during the PhD. When I fell into the trap of feeling like an intruder in this academic world, my mom's compassionate presence, my dad's courage and reminder of humble beginnings, and my brother's lively and amusing company, gave me sufficient hope and optimism to get through this.

Now, here I am, and it seems that all of this was worth it, but only time will tell if I have become dumb, or dumber. Thank you all!!

Table of Contents

Table of Figures

Table of Tables

List of Abbreviations

ASTM	American Society of Testing and Materials
CAPA II	Controlled Atmosphere Pyrolysis Apparatus II
CEN	European Committee for Standardization
CFD	Computational Fluid Dynamics
CHF	Critical Heat Flux
DAQ	Data Acquisition System
DSC	Differential Scanning Calorimeter
DSLR	Digital Single-Lens Reflex
EPS	Expanded Poly (styrene)
FAA	Federal Aviation Administration
FDS	Fire Dynamic Simulator
FPA	Fire Propagation Apparatus
FPI	Fire Propagation Index
FTIR	Fourier Transform Infrared Spectroscopy
GA	Genetic Algorithm
HRR	Heat Release Rate
ISO	International Standards Organization
MDF	Medium Density Fiberboard
MLR	Mass loss rate
MS	Mass Spectrometry
NIST	National Institute of Standards and Technology
OSB	Oriented Strand Board
PA	Polyamide
PEEK	Poly (ether-ether-ketone)
PET	Poly (ethylene terephthalate)
PIR	Polyisocyanurate
PLA	Poly (lactic Acid)
PMMA	Poly (methyl methacrylate)
POM	Poly (oxy-methylene)
PP	Polypropylene
PVC	Poly (vinyl-chloride)
SBI	Single Burning Item
SCE	Shuffled Complex Evolution
SNB	Statistical Narrow Band
STA	Simultaneous Thermal Analysis
TGA	Thermogravimetric Analysis
TRP	Thermal Response Parameter
WSGG	Weighted Sum of Grey-Gas Model
XPS	Extruded Poly (styrene)

List of Symbols

Variable	Unit	Description
y_p	cm	Pyrolysis zone length
$\dot{m}''_F$	kg m^{-2} s^{-1}	Mass flux from the pyrolysis region
y_e	cm	Length of extension region
y_f	cm	Length of the flame
$\dot{q}''$	kW m^{-2}	Flame heat flux
$\dot{q}''_{k,p}$	kW m^{-2}	Conductive heat flux to the extension region from pyrolysis region in the direction of the flame spread
T_{flame}	K	Maximum flame temperature
T_∞	K	Ambient temperature
T_{surf}	K	Surface temperature of the solid
A_p	m^{-2}	Area of pyrolysis region
ΔH_c	kJ g^{-1}	Heat of combustion
E	MJ per kg of O_2 consumed	Energy released from combustion of organic solids per kg of oxygen consumed
m_a	kg s^{-1}	Mass flow rate of inlet air before combustion
m_e	kg s^{-1}	Mass flow rate of gases after combustion
$Y^a_{O_2}$	$(-)$	Oxygen mole fraction in inlet air before combustion
$Y^e_{O_2}$	$(-)$	Oxygen mole fraction in gases after combustion
Q'	kW m^{-1}	Heat release rate per unit width
$\dot{Q}'''$	kW m^{-3}	Heat release rate per unit volume of the flame
Q''_{BB}	kW m^{-2}	Black body emissive power of the flame per unit area
k_a	$kW^{-1/3}$	Corresponds to extinction coefficient
λ	$m^2 s^{-1}$	Thermal diffusivity of a solid
t	s	Time
E_r	J $mol^{-1}K^{-1}$	Activation energy
A_r	s^{-1} if first order reaction	Pre-exponential factor
λ	W $m^{-1}K^{-1}$	Thermal conductivity of the solid
ρ	kg m^{-3}	Density of the solid
C_p	J $kg^{-1}K^{-1}$	Specific heat capacity
ΔH_r	J kg^{-1}	Heat of reaction
v	$(-)$	Mass-based stoichiometry coefficient of the reaction
ε	$(-)$	Emissivity
β	K s^{-1}	Heating rate
R	J $mol^{-1}K^{-1}$	Universal gas constant
κ	$(-)$	Degree of conversion in TGA

$\boldsymbol{T}$	K	Temperature
$\boldsymbol{m_0}$	(g)	Initial mass of the reactant
$\boldsymbol{r_i}$	s^{-1} if first order reaction	Mass-fraction based reaction rate of i^{th} component
$\boldsymbol{\alpha}$	m^{-1}	Absorption coefficient
$\boldsymbol{C_f^e}$	$(-)$	Theoretical flow coefficient of averaging pitot tube
$\boldsymbol{\gamma}$	$(-)$	Molar ratio of CO_2 and H_2O produced per O_2 consumed for a complete combustion of a fuel in air
$\boldsymbol{X_{O_2}^t}$	$(-)$	Oxygen mole fraction in the exhaust flow at time, *t*
$\boldsymbol{X_{O_2}^m}$	$(-)$	Oxygen mole fraction measured by the oxygen sensor
$\boldsymbol{r_{H_2O}^0}$	$(-)$	Molar ratio of H_2O and O_2 in the inlet air (ambient air)
$\boldsymbol{X_{H_2O}^0}$	$(-)$	Ambient water vapor mole fraction
$\boldsymbol{P_{H_2O}^v}$	Pa	Saturation pressure of water vapor
$\boldsymbol{RH^0}$	%	Relative humidity of inlet air (ambient air)
$\boldsymbol{P_a}$	Pa	Ambient environmental pressure
$\boldsymbol{T_e}$	K	Temperature of exhaust gas flow
$\boldsymbol{M_{O_2}}$	kg mol^{-1}	Molecular weight of oxygen species
$\boldsymbol{M_e}$	kg mol^{-1}	Molecular weight of exhaust gas flow
$\boldsymbol{I_{900\,nm}^{cam}}$	$(-)$	Value of intensity measured by the camera
$\boldsymbol{I_{900\,nm}^{b}}$	$(-)$	Black body intensity at local temperature, *T*
$\boldsymbol{k_{900\,nm}^{soot}(s)}$	m^{-1}	Soot extinction coefficient, which includes absorption and scattering, along path line, *s*
$\boldsymbol{HRR_{error}}$	(%)	Average HRR error for simulations
FIGRA	kW s^{-1}	Fire Growth Rate Index

Chapter 1: Dynamics of Flame Spread and Pathway to Prediction

1.1. Introduction

Assessment and understanding of the fire hazard posed by increasing use of polymers around the world is vital for ensuring their safe application. Synthetic polymers and composites based on both natural and synthetic polymers have replaced traditional materials and are increasingly used due their versatility and economic reasons. As of 2015, the production of polymers has increased exponentially to more than 350 million tons since 1960 [1]. About 16% of these produced polymers are used in building and construction industry [1,2]. Their adaptability, low cost and low weight paved the way to substitute traditional alternatives such as glass and metal. However, being mostly hydrocarbon in nature, their introduction in the structural environment also showcased the fire hazards associated with these polymers. In 2018, incidents involving fires in structures accounted for about 40% of total 1.3 million fire incident reported in the United States of America (USA) [3]. In the same study, a home fire was estimated to occur once every 87 seconds, with one death around every 3 hours accounting for about 70% of total deaths due to fire.

Improving the life and environment safety entails gaining knowledge of phenomena such as pyrolysis, combustion, toxic gas and soot production and their interdependence that causes the fire to spread. Prescriptive standards require materials to be tested in apparatuses carefully designed to emulate scenario-specific thermal conditions that the material may be exposed in its final application. These tests are classified into reaction-to-fire tests that examine the response, such as ignition, thermal decomposition, flammability, flame spread and gaseous emissions, of a material to fire, and resistance-to-fire tests that examine the

ability of the material to contain a fully-developed fire. Reaction-to-fire hazard parameters that quantify phenomenon such as the heat release rate (HRR), ignition, flame heat feedback, dripping, smoke obscuration, extinction, and flame spread, are important indicators of a material's propensity to support early-growth of fire. The materials are then classified based on their fire hazard parameters on a relative ranking scale. The relative scaling forms a basis for screening the materials for their final application. Standardized tests have been developed and maintained by organizations such as American Society of Testing and Materials (ASTM) [4], Federal Aviation Administration (FAA) [5], International Standards Organization (ISO) [6], and European Committee for Standardization (CEN) [7].

As the construction industry moves towards increasing use of complex synthetic polymers such as insulations, composite materials, engineered woods, the standardized testing and classification of new materials is becoming increasingly complex [8]. The scientific community, understanding this challenge, is progressively favoring the development of tools that can predict the fire behavior of a material in a test standard [9–11]. Such prediction capability, if applied during the development phase of a material, can potentially help screen new materials and drastically reduce the monetary cost of standardized testing of new materials. Consequentially, the fire incidents and its impact on life and environmental safety can be controlled.

Standardized tests that expose the materials to flames ranging from Bunsen burner flames to 15 m high enclosure fire scenarios result in quantifying the reaction-to-fire parameters and classification of product based on comparative analysis that is specific to the test configuration and condition. Karlsson et. al [12] and Bill and Croce [13] argued

that the data available from such tests are non-fundamental in nature and thus cannot be reliably used to predict results of another fire scenario, especially for complex materials. Bill and Croce [13] also suggested ultimate transition to computer based predictive models can be achieved by promoting application of small-scale property measurements to first-principle models of larger-scale experiments. A step forward is to fundamentally understand the dynamics of the flame spread problem and to apply available scientific methods to improve the prediction capabilities.

1.2. Flame Spread Problem

The fundamentals of the flame spread phenomenon have been studied theoretically and experimentally for more than 50 years [14–17] and attempts have been made to assess material performance using semi-empirical models and comprehensive computational fluid dynamic models for about 30 years [10,11,18–20]. Williams [15] provided a comprehensive theoretical overview of mechanism of flame spread in 1977 wherein the "fundamental equation of flame spread" [14] was elaborated to clarify the modes of communication between the burning fuel and non-burning fuel that drive fire spread. The equation of flame spread [15] relates the net energy per unit area incident on the unburnt fuel to the product of fuel density, the velocity of flame spread, and the enthalpy per unit mass of unburnt fuel to raise its temperature to an 'ignition temperature'. The dominant heat transfer mechanisms, limitations imposed by diffusion, chemical kinetics, and thermal thickness of fuel bed during the fire spread were discussed for well-ventilated and under-ventilated, concurrent and countercurrent flame spread on continuous and discrete surfaces.

Generally, when a combustible, solid material is heated, it undergoes a thermal decomposition process, influenced by aerobic or anaerobic environment, resulting in release of pyrolyzates (combustible or non-combustible gases). This thermal decomposition along with associated mass and heat transfer through the degrading material is referred as pyrolysis. For a vertical wall, Figure 1-1 illustrates release of pyrolyzates from the pyrolyzing region of length, y_p, at a flux of $\dot{m}''_F$. These gases can auto-ignite or ignite due to an external source in the gas phase resulting in a continuous flame, of length y_f, extending over the unburnt, virgin fuel in the flame extension region, y_e. The extension region is also referred as preheating region [16] or combusting plume region [21].

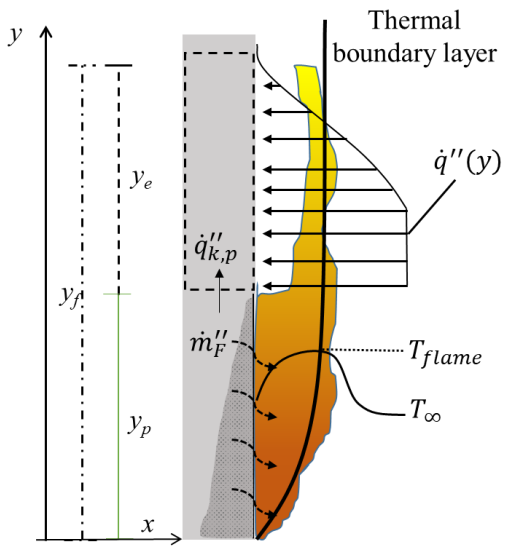

Figure 1-1. Schematic of thermal and fluid flow during a flame spread

The surface temperature of the non-charring pyrolyzing region is maintained at the 'ignition temperature' as the net heat flux from the flame, including re-radiation, in this region promotes decomposition. The communication between burnt and unburnt fuel is possible in the extension region by heat transfer from the flame, given by flame heat flux,

$\dot{q}''$, or conductive heat transfer, given by conductive heat flux, $\dot{q}''_{k,p}$, through the sample in the direction of the spread. Heat transfer to the unburnt fuel further initiates thermal decomposition, pyrolyzate production, and a spreading flame as a result of non-linear increase of flame height and extension region in concurrent flame spread scenarios.

Flame spread is thus governed by cyclic feedback [15,22] between three interdependent phenomena – 1. Gas-phase combustion of pyrolyzates, 2. Heat transfer to the unburnt region, and 3. Condensed-phase pyrolysis. Controlling mechanisms for flame spread over continuous surfaces for concurrent than countercurrent spread [15] are 1) flame to surface heat flux (dominant for concurrent than countercurrent spread) and 2) chemistry that controls the pyrolyzate production rate. Therefore, for a specific flame spread scenario, understanding these controlling mechanisms is important and have been studied individually over decades. Various methods of quantification and quantification challenges of these phenomena are discussed in following three sub-sections.

1.2.1. Gas-Phase Combustion

Gas-phase combustion of pyrolyzates promotes development of a continuous flame supported by the pyrolysis region. Complete mechanisms of combustion process through elementary reactions of underlying species are understood for relatively simple hydrocarbon species, such as methane [23]. However, simplified elementary mechanisms that may accurately predict associated heat release are computationally expensive. Gas-phase reaction chemistry is usually faster than flame spread-rate controlling pyrolyzate production kinetics. Therefore, a relatively simpler approach to estimate heat release rate is desired for screening materials based on their fire hazard. The energy released by gas-

phase pyrolyzate combustion process was found to be the single-most crucial parameter that characterizes the fire hazard of a material [24]. This is because it directly impacts the flame feedback and mass loss rate of pyrolyzates. The energy released can be impacted slightly by incomplete combustion product emissions resulting from the use of fire retardants. Quantification of the energy released during combustion assist in defining key parametric values that can be used in empirical models to predict flame spread in standardized fire scenarios and also classify materials based on their thermal hazard [25,26].

The heat release rate, HRR (kW), is quantified using several established calorimetry procedures, which can primarily be classified into three principles based on the measurement of,

1. Mass loss rate,
2. Specific species' concentration change, and
3. Convective losses [27].

1.2.1.1. Calorimetry based on mass loss rate measurements

The mass loss rate measurement expressed in terms of a mass loss rate, $\dot{m}_F$ (kg s^{-1}) can be used to calculate the heat release rate (kW) if the complete heat of combustion, ΔH_c (kJ g^{-1}), of the pyrolyzate gas is known,

$$\text{HRR} = \dot{m}_F \cdot \Delta H_c \cdot 10^3 \qquad (1\text{-}1)$$

Accuracy of HRR from this approach is promising for combustion process that produce primarily complete combustion products, carbon dioxide and water vapor.

However, this expression may overestimate the HRR in case of incomplete combustion, if the inefficiency of the combustion process is not incorporated by accounting for the ratio of carbon monoxide to carbon-dioxide, whose information may require experimental measurements. Also, the HRR is sensitive to the value of ΔH_c. Pyrolyzate gases released from organic condensed-phase materials consist of mostly Carbon, Hydrogen, Oxygen, Sulphur and Nitrogen atoms. A stoichiometric combustion reaction for a typical hydrocarbon pyrolyzate gas can be generally written as,

$$C_x H_y O_z + \left(x + \frac{y}{4} - \frac{z}{2}\right)(O_2 + 3.76\, N_2) \rightarrow xCO_2 + \frac{y}{2} H_2O + 3.76\left(x + \frac{y}{4} - \frac{z}{2}\right) N_2 \quad (1\text{-}2)$$

Standard, complete heat of combustion, defined as the energy released per unit mole or gram of the reactant at 298 K and 1 atm, can be either calculated from the known heats of formation of reactants and products of the combustion reaction or measured experimentally in an oxygen bomb calorimeter [23,28,29]. The former method may require computational software for compounds with complex chemical formula, while the latter approach, which utilizes an apparatus at higher pressure and elevated oxygen concentration, can yield complete heat of combustion that incorporate heat released by oxidation of solid carbonaceous residue which may not be flammable in normal atmospheric conditions [29]. A correspondence between heat of combustion and carbon atoms, functional contribution from chemical groups in the monomer or the repeat unit of a polymer was tabulated by Cardozo [30] and the list was expanded by Van Krevelen [31]. However, calculating heat of combustion by functional group contribution requires knowledge of exact chemical composition of gaseous products of pyrolysis, which is

almost never available, and also imposes computational demands and necessitates tabular data for reference.

From the various approaches possible to obtain a ΔH_c value of the pyrolyzates, lower or net heat of combustion where water in products is considered to be in gas phase, as observed in a real fire scenario, is commonly used in fire science than gross heat of combustion which considers water in combustion products as liquid phase and the enthalpy of process of liquefaction of water vapor is accounted for. Net heat of combustion of several organic compounds are found to be between 20 to 50 kJ g^{-1} [28]. The net heat of combustion of a complex polymer can be dependent on the environmental conditions and many other material variables such as different molecular structure of different pyrolyzate gases released during pyrolysis of the same material, material dripping, and fire retardancy (halogenated polymers) which affects the char yield [32]. For such cases, relying on the knowledge of net heat of combustion for calculating HRR is not always possible. While this approach is helpful in quantifying the effective heat of combustion of polymers, direct measurement of HRR is usually done by the principle of oxygen consumption calorimetry, which is based on measurement of oxygen depletion.

1.2.1.2. Calorimetry based on specific species' concentration change

In 1917, heat of combustion of various organic liquid and gaseous fuels was analyzed by Thornton [33] and found to be nearly the same per unit mass of oxygen consumed. Decades later in 1980, Hugget [34] quantified this value for several solid combustibles as, E = 13.1 ± 0.68 MJ per kg of oxygen consumed and a revised value of E = 12.9 ± 0.9 was later suggested by Tewarson, by conducting experiments on a larger set

of materials [35]. For many organics compounds, it was also found that the energy released per kg of CO_2 and CO produced was 13.3 ± 1.5 MJ, and 11.1 ± 2 MJ respectively [35].

This valuable information have been then used extensively, using a general expression Eq. (1-3), to calculate HRR [36] by monitoring the change in oxygen, CO_2, and/or CO species' concentration in the inlet air of mass flow rate, m_a (kg s^{-1}), having oxygen mole fraction as $Y_{O_2}^a$ and the exhaust flow rate, m_e (kg s^{-1}) having oxygen mole fraction $Y_{O_2}^e$ after combustion.

$$\text{HRR} = E\left(m_a Y_{O_2}^a - m_e Y_{O_2}^e\right) \qquad (1\text{-}3)$$

Use of this expression further requires computation and corrections for oxygen concentration depending on measurement of CO_2 or H_2O in the sampling gas stream, which are formulated in one approach by Janssens [37]. Another approach has been standardized in ASTM 1354 [4], where oxygen depletion factor, volumetric expansion factor are considered for correcting removal of specific chemical species from the sampling gas. More detailed formulae employing oxygen consumption model have been developed for cases where inlet and outlet streams are measured for soot, CO_2, H_2O species [38], or for cases where the inlet oxidizer stream is diluted [39].

The advantage of oxygen consumption calorimetry is that it can be applied to experimental setups ranging from small-scale [5], bench-scale [4,40] to large-scale [6,7] test setups. However, the uncertainty in HRR calculation using oxygen consumption method is affected by the uncertainty in oxygen measurement (3-6 % contribution) [41], extent of oxygen depletion in the combustion process [37], consideration of moisture content (1-3% contribution) [42], the consideration of sootiness and incomplete

combustion (CO formation) of the flame (3-14 % contribution) [42], the accuracy of measuring mass-flow rate of the exhaust-flow (1-5 % contribution) [43], and the locations at which exhaust gas temperature is measured (less than 2 % contribution) [44]. Janssens [45] quantified the variability in heat release rate measurement procedure for various test standards and encouraged systematic calculation of transport times, response times, noise and drift of instrumentation, multiple testing with calibration burners for uncertainty calculation, and validation with standard reference materials to improve the accuracy of HRR measurements.

1.2.1.3. Calorimetry based on convective loss measurements

The portion of the heat release rate which interacts with the air stream and releases energy convectively, can be determined by using an approach developed by Smith [46], where the convective portion of the HRR is calculated by monitoring enthalpy change of the walls which interact with the exhaust flow. A series of temperature measurements is required and this approach provides HRR similar to if obtained from using oxygen consumption method for fuels with low radiation-convection ratio, such as methane. However, lack of knowledge of radiative fraction of the combustion process makes this impractical for calculating total HRR in large, radiative dominant, turbulent fires.

1.2.2. Heat Transfer to the Unburnt Region

Heat feedback to the unburnt region of the fuel can result either from the interaction between the hot combustion products and the solid surface, or from conduction through the solid surface parallel to the direction of spread. Heat feedback was quantified for range of sample orientations from $\theta = -90°$ (downward flame spread) to $\theta = +90°$ (upward flame

spread) by analyzing heat flow vector patterns for flame spread over Poly (methyl methacrylate) [47]. From these tests, heat transfer rate from gas-phase onto the unburnt fuel was found to be 99% of total heat transfer input to the sample for vertical sample orientations ($\theta = +90°$), and decreases to 56% for $\theta = -90°$. The conductive heat transfer rate in the direction of the spread is thus much smaller than the rate of heat feedback from the flame for upward flame spread. Concurrent (upward spread) is thus, faster than countercurrent flame spread for which the heat transfer is dominated in the direction of flame spread by parallel thermal conductivity through the condensed-phase and gas-phase conduction from the extending flame [47–49]. Heat feedback from the flame, because of buoyancy-induced convective transport of hot combustion products, in concurrent, upward flame spread can be either radiative or convective in nature [16,50]. Due to diffusion and convective gas transport in the same direction that fastens the spread rate, understanding concurrent flame spread has great practical importance with the perspective of improving life and environmental safety of materials in a built environment.

Laminar upward flame spread has been studied fundamentally to gain insight into the dynamics of early growth phase of a fire [50–53]. Flame spread studies were performed earlier on relatively large scale physical dimensions to induce turbulent conditions without a quantitative basis to classify turbulent characteristics of fires [54]. The transition to turbulence for upward, buoyancy driven flame spread resulting from boundary layer non-uniformities induced by several physical and flow-field parameters, is estimated using heat transfer analysis to occur above Grashof number of $Gr = 5 \times 10^7$ [55]. The transition to turbulence was investigated by Honda and Ronney [56] by performing flame spread experiments on fuel beds of varying width, pressure, thickness, and oxygen concentration.

They validated a theoretical model, developed through non-dimensional analysis of the boundary layer, to interpret transition to turbulence. Radiation was identified to be primary mode of heat transfer in turbulent flame spreads, with the turbulence dependent on the width of the sample. Laminar flame spread, whose dominant heart transfer mode is convection, is also found to be sensitive to the width of the sample [17,57]. Pizzo et. al [57] also observed that the transition from laminar to turbulent flow occurs at a critical width-normalized heat release rate, *Q'*, which decreases with increase in the sample width for narrow samples of width less than 0.05 m.

Total flame heat fluxes for flame spread scenario have been measured on either single wall fire or fires supported by obstructed geometries that effect the air entrainment and thereby flame dynamics. Schematic of these surfaces is shown in Figure 1-2 and heat fluxes measured on these surfaces and their importance is discussed in the following two sub-sections.

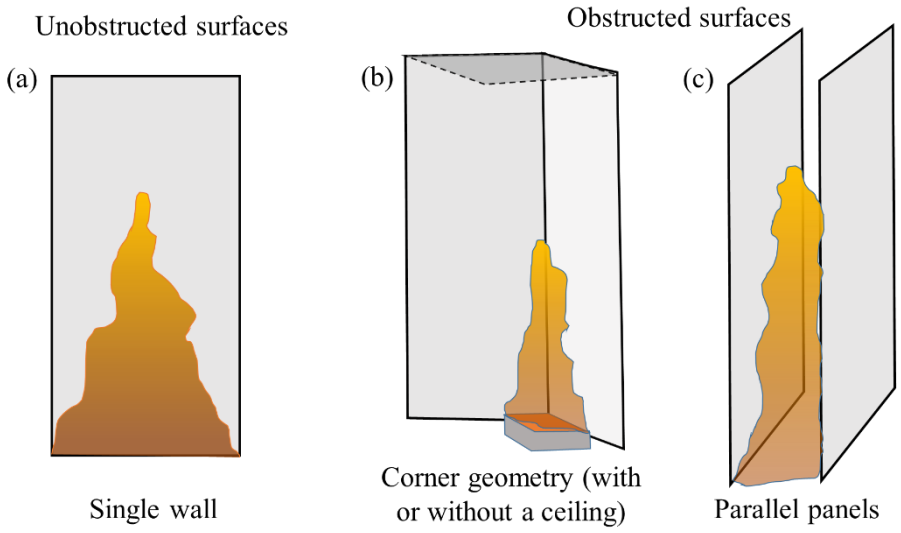

Figure 1-2. Schematic of wall geometries supporting flame spread used for flame heat feedback measurement in the literature

1.2.2.1. Heat Flux on Unobstructed Surfaces

Flame heat flux, $\dot{q}''$, measured as the incident energy per unit area, in the extension region, as discussed earlier, is a dominant and most crucial parameter for a concurrent spread [22]. The behavior of flame heat flux in the pyrolysis region (y_p), extension region ($y_e = y_f - y_p$) and beyond was explored experimentally and theoretically by various researchers for concurrent flame spread over a single wall geometry, as illustrated in Figure 1-2 (a) [16,54,58–60]. Integral equations for the flame spread phenomenon reduced by non-dimensional analysis provided insights into the dependency of flame heat flux on the flame height [58,60]. The flame heat flux, pyrolysis height, flame height, heat release rate or non-dimensional version of either of these quantities are usually correlated together to develop empirical relationships that may be used for the purpose of empirical modeling. These correlations are often in form of power law expressions. Flame heat flux was generally observed to increase from the lower region of the pyrolysis zone to a constant value near the onset of extension region, and then decreases either linearly [61] or decay with a power law [18] in the extension or continuous flame region and fitted to decay with a power law beyond the flame tip. Lattimer [62] reported a simplified flame heat flux dependence with height normalized by flame height. The relation distributed the total heat flux data along the height in two sections,

$$\dot{q}'' = 30\ kW\ m^{-2} \qquad ; y/y_f < 0.7 \qquad (1\text{-}4a)$$

$$\dot{q}'' = 12.3\left(y/y_f\right)^{-2.5} \qquad ; y/y_f > 0.7 \qquad (1\text{-}4b)$$

This relation fit reasonably well for the experimental data on flames over vertical surfaces for a range of fuels. Experimental data [58,60] which were used for this fit

suggested flame heat flux to be nearly independent of the fuel, as also reviewed by Tsai et. al [16]. This was advantageous as the integral models that attempted to predict upward turbulent flame spread over combustible materials utilized a constant flame heat flux in the range of 20-35 kW m^{-2} for the pyrolyzing region [18,63–65]. However, closer observation of experimental data indicated that the experimental peak flame heat flux ranged from 20-60 kW m^{-2}; about 20-30 kW m^{-2} for Masonite board, cardboard and white pine board, and a value higher than 30 kW m^{-2} for Poly (methyl methacrylate) (PMMA) and Polyurethane foam [62].

Early upward flame spread experimental studies also developed empirical correlations that relate pyrolysis region, y_p, and the flame length, y_f, with a power law dependence, $y_f = a \cdot y_p^n$, where a and n are empirically derived constants. The exponent, n was empirically derived by different researches to be n = 0.78 [66]; n = 0.71 [67]; n = 2/3 [54]. Experiments performed by Tsai and Drysdale incorporated the width-dependence of the heat release rate by using width-normalized HRR, Q', and developed a similar power law correlation which related the flame height to Q' , $y_f = b \cdot (Q')^k$, where, the exponent was determined to be k = 1 in laminar spread region, for Q' < 20 kW m^{-1} and k = 2/3 in turbulent spread region, for Q' >20 kW m^{-1} [68].

A comprehensive experimental analysis of heat fluxes on non-combustible walls from fires of size 53 kW to 523 kW fueled by propane gas burners was performed by Back et al. [61]. The peak flame heat flux at the centerline in a radiative dominant flame, a characteristic of a turbulent diffusion flame, was correlated with HRR. Peak heat flux was modeled by considering mean beam length of an emitting flame volume, represented as a grey gas. The mean beam length was empirically related to the 1/3 power of heat release

rate per unit volume of the flame ($\dot{Q}'''$) and the correlation was expressed in the form of Eq. (1-5),

$$\dot{q}'' = Q_{BB}^{i''} \cdot \left[1 - \exp\left(-k_a (\dot{Q}''')^{1/3}\right)\right] \quad (1\text{-}5)$$

In Eq. (1-5), $Q_{BB}^{i''}$ is the area-normalized blackbody emissive power of the flame, and k_a corresponds to extinction coefficient. For radiant wall-fires, the flame heat flux is also found to be a function of soot formation, a gas-phase phenomenon, [69], with differences in peak heat fluxes observed to be a maximum of 15 kW m^{-2} between less sooty methane and ethane flames compared to sootier ethylene and propylene flames.

1.2.2.2. Heat Flux onto Obstructed Surfaces

Flame heat flux on surfaces with obstructed air entrainment, usually due to the presence of a physical obstruction as illustrated in Figure 1-2 (b, c), is another practical scenario observed in real fire incidents. The effect of walls placed in a corner geometry, or parallel to each other on flame heat flux is a subject of importance. Confinement of the flame inhibits air flow into the combustion region and impact the flame height and thereby, the flame heat flux distribution [70–72]. Higher flame heat flux is observed, due to confinement and surface re-radiation, in scenarios where combustible surfaces are in a corner and a parallel geometry [71–73]. Experiments performed to quantify flame heat fluxes on walls with inhibited entrainment flows are performed at larger scale, which represent realistic fire-incident scenario. However, unlike the parallel panel fires, corner fires almost never become under-ventilated, making fires supported by combustible surfaces in a corner arguably better for studying flame-solid interaction [62]. The larger scale of the experiments makes the fires turbulent, buoyancy-driven which augments the

experimental and personnel cost challenges for quantifying aspects of flame dynamics. Flame dynamics of interests include HRR, convection-radiation split for the flame feedback, flame geometry, flame sootiness, pyrolysis zone and developing strong correlations between these parameters. Therefore, fire supported by walls placed in a corner geometry is a subject of importance for this study and detailed literature review for fires supported by corner geometry will be discussed in Section 1.3.

1.2.3. Condensed-Phase Pyrolysis

As discussed briefly earlier, the condensed-phase pyrolysis is the rate limiting process defining the HRR. Thus, primary parameter of importance that needs to be predicted is the rate of pyrolyzate production (also called as burning rate). The pyrolyzate generation rate impacts the time to ignition, combustion and thus, fire size which eventually affects the flame heat feedback to the unburnt surface. The process of pyrolyzate production involves radiative and convective heat transfer between the gas phase within the fluid and thermal boundary layer of the pyrolysis region, and thermal transport inside the condensed-phase that induce mass transfer of pyrolyzates out of the condensed-surface. The decomposition process is initially controlled by chemical kinetics for non-charring thermoplastic and char-forming polymers at low heating rates, then transitions to internal heat transfer control as the reaction zone decreases and ablative surface mass loss regime is established at severe external heating, and becomes controlled by both external and internal heat transfer after significant char formation [74].

Ablative regime, observed in a spreading flame, characterized mathematically as Stefan's problem, models the pyrolysis by assuming an infinitely rapid decomposition

reaction once the material reaches a critical ignition temperature [75]. Many such models assume that the decomposition of solid will be primarily from the surface and that the surface temperature is independent of heat losses. The conduction time scale in this regime controls pyrolyzate generation and thus the time to ignition [76]. Conductive thermal penetration depth, δ_t, within a material is related to material thermal diffusivity, λ ($m^2\ s^{-1}$), by $(\lambda t)^{0.5}$ where t is the time. Analytical thermal theories of ignition [76,77] are derived for simplified semi-infinite materials considering the characteristic ignition temperature for thermally-thin materials, where the thermal penetration depth is greater than or equal to the material thickness, and thermally-thick materials, where the thermal penetration depth is significantly smaller than the physical thickness and temperature gradients inside the material. This theory is the foundation for standardized fire hazard parameters that indicate pyrolyzate production propensity. These parameters such as Critical Heat Flux (CHF, defined as net external heat flux at or below which sustained piloted ignition does not occur), Thermal Response Parameter (TRP, an indicator which relates time to ignition to net heat flux), Fire Propagation Index (FPI, related to fire propagation rate), Heat Release Parameter (HRP, a material specific property defined as the ratio of heat released to heat of gasification) provide a good first level approximation for classifying materials into four groups of non-propagating, decelerating propagation, accelerating propagation, nonaccelerating propagation [26,35,49,78].

However, such characterization lacks inclusion of the fundamental nature of pyrolyzate production, which is impacted by finite rate chemical kinetics, complexity in the charring nature of polymers, non-flaming mass loss at lower heat fluxes, and radiation in porous media [79]. Analytical thermal theory of ignition was shown to be sensitive to

finite-thickness effects and heat dispersion in longitudinal direction [80,81]. Importance of understanding chemical kinetic mechanism for a polymer decomposition was emphasized by Kashiwagi in [82], where lack of consideration and impact of kinetic parameters of decomposition, bubbling process, melt-flow in simplified analytical models were discussed. Characterization of decomposition mechanism has been performed using experimental data [83,84] obtained from Thermo-gravimetric Analysis (TGA) coupled with Mass Spectrometry (MS) and Fourier Transform Infrared Spectroscopy (FTIR), and sometimes molecular-level interactions are explored by using reactive molecular dynamic theory [85,86]. However, application of reaction rate theories to design condensed-phase decomposition mechanism is limited due to complexity involved in measurement of decomposition kinetic and other parameters [87,88].

For the application in fire scenarios, a more general approach which characterizes a decomposition reaction mechanism using small-scale experiments has become more popular [89–91]. In one approach, thermal decomposition is studied by analyzing experimental mass loss curves obtained from TGA. Kinetic parameters of an apparent single-step or multi-step reaction in series or parallel following an Arrhenius equation are determined to describe the thermal decomposition curve. Kinetic parameters, namely activation energy, E_r, and pre-exponential factor, A_r, are determined by iso-conversional methods [90,92] or inverse analysis assisted by numerical modeling [89,93–96]. Cone calorimeter experimental data are also used to derive kinetic parameters with systematic methods that utilize multi-parameter optimization algorithms [97].

The thermal decomposition mechanism however describes only a portion of the pyrolysis process and parameters required for comprehensive description of the pyrolysis

process are also important. Other parameters characterize associated thermodynamics of the decomposition, thermo-physical aspects such conduction and swelling/intumescence, in-depth radiative absorption. In the remainder of the dissertation, a set of properties which quantify the kinetics of decomposition, associated thermodynamics, thermo-physical behavior (mass and heat transfer, dripping etc.), optical properties (absorption and emission) will be referred to as comprehensive pyrolysis models. The process of parameterizing comprehensive pyrolysis models relevant to this study is discussed in Section 1.4.

1.3. Experiments and Modeling of Fires Supported by Corner Geometry

Narrowing down from the various aspects of flame spread problem described in previous section, fires supported by vertical flammable corner walls are more hazardous than fires on single walls because of radiative heat feedback between burning surfaces and larger flame heights associated with inhibited air entrainment [71,72]. Additionally, unlike parallel wall fires, corner wall fires are almost never ventilation controlled [62]. Thus, it can be argued that flame spread in a flammable vertical corner represents a perfect scenario for the analysis of interactions between a buoyancy-driven flame and pyrolyzing solid fuel. Accurate modeling of such interactions is critical for prediction of fire growth [88,98]. Computational fluid dynamics (CFD) fire models are increasingly used for this purpose [99–101] but their ability to accurately model flame spread is currently limited. The reasons for this limitation are thought to include absence of accurate property data for relevant solid fuels and insufficient accuracy of thermal transport and combustion sub-models implemented in CFD fire simulators [88,102].

1.3.1. Experimental studies

Previous experimental investigations of fires in vertical combustible and non-combustible corners, unconfined or confined by a ceiling, can be roughly divided into two groups: those involving measurement of the heat release rate (HRR) accompanied by pyrolysis zone monitoring [103–107] and those involving measurement of flame geometry, solid fuel temperature and total incident heat flux onto the fuel surface [10,107–112].

Corner fire experiments with a ceiling have been usually performed in a setup standardized in the ISO-9705 Room Corner scenario, which is a reaction-to-fire test for wall and ceiling lining materials [6]. In this test, wall and ceiling lining materials are exposed to a square propane burner fueled to produce a 100 kW fire for ten minutes followed by a 300 kW exposure for the next ten minutes or either until the room reaches flashover or the HRR exceeds 1000 kW. Flame heat flux distribution were mapped by Lattimer [109] on non-combustible walls, placed in a ISO-9705 Room Corner setup, exposed to propane fueled line and square burners with fires of intensity 100 kW and 300 kW. Kokkala [112], earlier in 1993, performed one of the early experiments that quantified and correlated heat fluxes on similar 2.4 m high walls placed in an open, non-combustible corner without a ceiling. Flame heat fluxes in both the studies increased with heat release rate, with maximum value of about 100 kW m^{-2}, and decreased horizontally (laterally) away from the corner following a half-Gaussian distribution [109]. However, the flame heat fluxes were impacted by presence of the ceiling, where the hot smoke layer build-up complicates the solid-flame interaction due to re-radiation from walls and hot-smoke layer [109,111–113]. Flame heat flux to a cold wall (water-cooled heat flux gauge) was similar until the height of 1.2 m for both cases and was found to be higher for corner environment

with the ceiling above this height, with a maximum difference of 20 kW m^{-2} [111]. This difference correlate well with black-body radiation from observed maximum gas temperature of around 900 K near the corner closer to the ceiling [113]. The condensed-phase and flame interaction is complicated by the hot-smoke layer in a corner scenario with the ceiling and thus, is not ideal for the study the dynamics of flame spread on materials.

Flame heat fluxes in fires supported by corner walls which are dependent on the HRR are also sensitive to physical aspects of the burner such as its relative stand-off distance from the corner walls, and geometry [103,105,114]. A stand-off distance of the burner, such as the 5 cm recommended by Williamson [103], provides sufficient pre-heating time and an ability to study the material's potential for ignition and propagation. At this distance, the heat fluxes (30 to 40 kW m^{-2} for 150 kW burner HRR) near the burner flame makes assessment of flame spread possible compared to a stand-off distance of 0 cm (50 to 60 kW m^{-2}) and 10 cm (20-30 kW m^{-2}) where respective too severe or not so severe heat fluxes cause either fast propagation and burnout of fuel or does not challenge the wall material, respectively. Peak flame heat flux along the height of the wall were found to increase with burner diameter in an exponential relation [103,114], and flame heat fluxes were steady until a critical height, $y/y_f < 0.4$, after which the heat flux decrease linearly and exponentially, [114], an extension to Eq. (1-4a). Similarly, flame heights, pyrolysis fronts and gas temperatures were also found to be dependent on HRR and burner geometry in these studies.

Among vertical corner fire experiments without a ceiling, a scenario realized in EN-13823 Single Burning Item (SBI) test [7] is used most widely for both research [101,106,107,115–119] and classification of wall lining materials [120]. In this test, a

propane burner placed about 4 cm away from the walls, emulating a waste paper basket fire, is utilized as an ignition source. The total incident heat flux from this source to 1.5 m tall non-combustible wall panels was measured in two relatively recent studies [115,117]. The burner HRR was varied between 15 and 55 kW to study its impact on the flame heat flux and flame height. Zhang et. al [117] used symmetric 1 m wide panels while Zeinali et. al [115] used EN-13823 recommended long and short panels of 1 m and 0.5 m width, respectively. The heat flux to the walls in the vicinity of the burner was found to be about 40 kW m^{-2} (as measured by a water-cooled heat flux gauge) for a 30 kW HRR in both the studies and the relative increase in the heat flux with HRR was lower for an HRR change beyond 30 kW. The panel surface temperatures indicated that the thermal load was higher on the shorter panels due to a non-uniform flow field. Zeinali et. al. [107] also performed perhaps the most comprehensive measurements of flame spread on a flammable lining, medium density board, in the SBI scenario. They collected spatially resolved solid fuel temperature together with the HRR and flame heat flux to the walls. However, the flame heat flux, which is arguably the most important and direct measure of interactions between the flame and the solid fuel, was measured only in three physical locations (two gauges at 8 cm from the corner but at different heights and another gauge further away from the corner) and thus was not resolved spatially. For corner fire experiments without the ceiling, the solid fuel and flame interaction data are limited at present. A spatially resolved distribution of these interactions is identified to be crucial for improving the prediction capability of flame spread.

1.3.2. Modeling Efforts

Predicting flame spread of a material in standardized corner tests such as ISO-9705 Room Corner test [6], and the SBI [7] is of interest to aid assessment and screening of new materials before commercialized production. Models used for the prediction of fire hazard can be either empirical/semi-empirical in nature or based on first-principle computational fluid dynamic solvers.

1.3.2.1. Empirical/Semi-empirical Models

These type of models solve ordinary differential equations in simplified numerical form or integral form to predict HRR for material in a room corner test setup [121,122] or SBI setup [123]. BRANZFIRE [122] is a popular computer model for predicting the outcome of Room Corner test, while ConeTools [123,124] is popular to compute the outcome of the SBI as well as Room Corner test. These models calculate time to ignition based on:

1. Constant flame heat flux in the extension region;
2. Correlations of flame height and upper layer temperature with HRR;
3. Pyrolysis area growth-rate estimated as a function of time to ignition, the dimensions of the wall, and the pyrolysis region.

Data used in these semi-empirical models are derived from HRR and other measurements from cone calorimeter experiments. These models require minimal computational resources and provides nearly instantaneous predictions. However, due to a large number of assumptions that simplify the fire growth parameter and fire dynamics, the accuracy of these predictions is limited.

Another approach in semi-empirical modeling is scaling-up approach, where different phenomena as described in Section 1.2, are modeled from small-scale to large-scale [88]. The complexity of the model is increased hierarchically by introducing boundary conditions describing small-scale pyrolysis to large-scale fire scenarios. Leventon et. al. [125] formulated a flame heat feedback model based on mass loss rate measurements and coupled this with comprehensive pyrolysis model for PMMA in a comprehensive pyrolysis solver, ThermaKin. They produced reasonable predictions of HRR and mass loss rate for a laminar flame spread over PMMA [125]. The flame heat feedback model was generalized later [53] for non-charring, charring polymers which manifest wide range of soot production, dripping behavior and sample burnout. Similar functional form for flame heat flux dependence on mass loss rate was used later by Lannon et. al. [110], coupled with comprehensive pyrolysis model, to develop a model to predict flame spread dynamics over several types of medium density fiberboard (MDF) materials in a ISO-9705 Room Corner scenario. This model which utilized pyrolysis model developed using inverse analysis of TGA and Cone Calorimeter experimental data resulted in limited accuracy for predicting HRR results for few samples. However, it showcased the potential of fast yet promising predictions obtained by coupling comprehensive pyrolysis models and flame-feedback model without accurate gas-phase combustion modeling.

1.3.2.2. Computational Fluid Dynamic (CFD) models

Comprehensive computer techniques, namely CFD, which also simulate gas-phase combustion in corner scenarios manage to provide better but still mixed results than empirical/semi-empirical models [10,101,116,117,119,126–128]. Although promising efforts are devoted to improve CFD modeling, this numerical approach is intricate due to

the complexity of modeling sub-process such as heat transfer, pyrolysis, turbulence, combustion, and soot production. For example, a simplified weighted-sum-of-grey-gases (WSGG) model for radiation, compared to the Statistical Narrow Band (SNB) model which accounts for the spectral dependence of radiation, almost always underestimated heat release rate and pyrolysis front region for flame spread scenarios over PMMA [117,128]. The radiative and convective portions of the heat flux predictions for different radiation models were compared and found to be sensitive to soot yield specified in the model and subsequent gas temperature predictions of the combusting plume. The sensitivity of outputs to radiation model selection emphasize the need for spatially resolved experimental data for validation purposes.

Complexity in modeling the pyrolysis process of the material has also impacted CFD predictions. Yan et. al. [10] estimated pyrolyzate gas production rate either by assuming HRR equivalent to Cone Calorimeter HRR data or by solving simplified conduction equation numerically with a one-step pyrolysis based on the critical "pyrolysis temperature". Such simplified treatment of pyrolysis of the material provided reasonable HRR estimations for particle board in an ISO 9705 Room Corner setup. However, radiation heat fluxes were under-predicted compared with experimental data. They also highlighted the need for accurate quantification of thermo-physical properties such as thermal conductivity, specific heat capacity to accurately predict the flame spread phenomenon.

Over the following years, aided by new experimental and computational techniques, modeling of the pyrolysis process shifted towards increasingly accurate treatment of thermal decomposition reactions [101,119]. Although the flame spread model developed by Hjolman et al. in Fire Dynamic Simulator (FDS) classified two complex

textile materials reasonable well according to EN-13823 specifications, large discrepancy was observed in predicted and experimental HRR for flame spread over these two textiles and a particle board in an SBI scenario [119]. The relative errors in HRR predictions were attributed to difficulties in accurate pyrolysis parameter estimations. Zeinali et. al [101] utilized FireFOAM 2.2x platform for modeling flame spread over medium density fiberboard (MDF) in an SBI setup. Pyrolysis of MDF was modeled as a single-step, first-order, Arrhenius-type thermal decomposition reaction. Predictions of HRR based on non-uniform density parameter provided rise, peak HRR value, and time at peak HRR within the experimental error. Predictions based on uniform density parameter underestimated the peak HRR value and time at peak HRR significantly. However, HRR was predicted to decay faster for predictions based on non-uniform density parameter and under-predicted experimental HRR at later times. Predicting flame heat fluxes and flame spread propagation was challenging for both the parameter cases, due to inaccurate fire prediction downstream of the propane burner.

The observed discrepancies in CFD model predictions and experiments were thus attributed to unresolved length scales near the flame front [10,126], inaccurate sub-models defining soot production and radiation [117,128] and, in the case of modeling of the SBI test on medium density board [101], to uncertainties associated with spatial non-uniformity of the solid fuel density.

1.4. Comprehensive Pyrolysis Models

It is evident by now that the pyrolysis model of a material affects the flame spread dynamics. The pyrolysis modeling is, as discussed in Section 1.2.3, either based on

analytical methods that assume mass loss from surface at constant ignition temperature [49,78], or based on comprehensive techniques that take into account apparent chemical kinetics and other relevant pyrolysis properties [10,89,129–135]. The former approach simplifies the physics and limits its applicability for predicting flame spread, while the latter requires parameter estimations which can demand extensive measurements whose uncertainty can affect the predictions, as discussed in Section 1.3.2.2. Emphasis will be given here on the discussion of the comprehensive pyrolysis model development and the intended scope of its utilization will be discussed in Section 1.7.

Comprehensive pyrolysis modeling, unlike analytical techniques, require dedicated pyrolysis solvers, such as Gpyro [135,136] and ThermaKin [129,137], or solvers in-built CFD software such as FDS wherein the flexibility for altering the reaction mechanism is limited compared to dedicated pyrolysis solvers [138]. Gpyro and ThermaKin solve unsteady mass and energy equations including thermal and mass transfer for a thermally degrading sample. They offer greater flexibility in pyrolysis modeling with the capability to simulate global decomposition reactions in one or two-dimensions for a discretized solid exposed to specified external heating conditions. Gpyro, which can be coupled with FDS, offers optimization techniques for extracting the parameters while ThermaKin requires user interference that, apart from being slightly user-time intensive, helps keep parameters such as the order of reaction within physically meaningful values. ThermaKin accounts for in-depth radiation and re-radiation[137], unlike surface re-radiation in Gpyro [136], and thereby allowing simulation of wide range of pyrolysis and fire scenarios. ThermaKin also provides easy compatibility to simulate multi-step reactions in series or parallel and has been successfully used in characterization of chemical kinetics and thermodynamics for

thermal decomposition of several non-charring polymers [91] such as polypropylene (PP), poly(oxy-methylene) (POM), poly(lactic acid) (PLA), poly(methyl methacrylate) (PMMA), polyamide 6,6 (PA 66), and charring polymers [91,132] such as poly(vinyl-chloride) (PVC), poly(ethylene terephthalate) (PET), poly (ether-ether-ketone) (PEEK). ThermaKin, in two-dimensional module Thermakin2Ds, also allows prescription of heat flux boundary conditions emulating flame heat flux dependence with flame height or mass loss rate by using an empirical correlation, as employed in previous studies [53,110,125].

Thermal decomposition is modeled by apparent mechanisms constituting Arrhenius-type reactions. Kinetic parameters (Activation energy, E_r, and pre-exponential factor, A_r) that can describe a thermal decomposition reaction are extracted by use of data from bench-scale tests such as cone calorimeter [4], Fire Propagation Apparatus (FPA) [139] or milligram-scale tests such as Thermo-Gravimetric Analysis (TGA) [140] at different heating rates. However, the parameters derived from bench-scale tests require experimental data from tests performed at various heat fluxes and poses slight disadvantages [89] due to assumption that the flame heat flux is constant upon ignition and the pyrolysis rate is a function of surface temperature (which has been demonstrated experimentally that this is not the case [141]). The importance of sub-surface region on the rate of mass-loss rate production was emphasized and accounting for in-depth phenomenon during the pyrolysis kinetics parameterization process is crucial to gain accuracy. Therefore, chemical kinetics of the pyrolysis process are parameterized with greater accuracy by using experimental mass loss and mass loss rate (MLR) data from TGA, where a milligram-scale sample, in good thermal contact with a metal or ceramic crucible is heated at a controlled heating rate, β, in an inert nitrogen atmosphere.

Once the mass loss and MLR data is available, the parameterization is either done by iso-conversional methods or inverse-analysis (model-fitting) method of the experimental data. Iso-conversional methods, such as the Kissinger method [92], can model only a single-step thermal decomposition or clearly distinguishable multiple reactions. It relies on the dependence of position of the peak mass loss rate and activation energy. A_r and E_r are determined by considering degree of conversion, κ, and a functional law of rate of variation, $f(\kappa)$, which is chosen based on global reactions. The rate of change of the degree of conversion is written in the form,

$$\frac{d\kappa}{dt} = \beta \frac{d\kappa}{dT} = k(T) f(\kappa) = A_r \cdot \exp\left(-\frac{E_r}{RT}\right) \cdot f(\kappa) \qquad (1\text{-}6)$$

Where β is the heating rate, K s^{-1}, R is universal gas constant, 8.314 J mol^{-1} K^{-1}, T is temperature in K. Degree of conversion, $\kappa = \big(m_0 - m_i(t)\big)/(m_0 - m_\infty)$, is defined based on initial mass, m_0, mass at time t, $m_i(t)$, and the mass at the end of the reaction, m_∞. The type of functional law employed to derive values for A_r and E_r can impact the accuracy of the chemical kinetic model [92]. Limitations imposed by the arbitrary selection of the functional form and single-step reaction makes this approach undesirable for an objective of developing a universal approach.

The necessity of inverse analysis techniques for property analysis was discussed by Marquis et. al. [142] and Batiot et. al. [87], where the sensitivity of the pyrolysis model to the compensation effect of A_r and E_r, reaction order, n, stoichiometric coefficient, υ was studied. The decomposition reaction of a heated solid can be simplified by assuming it reacts to form a pyrolyzate gas and a solid residue with mass-fraction, Y_i, as shown in Eq. (1-7). The mass-based reaction rate, r_i, for i^{th} component, is given by Eq. (1-8).

$$R \rightarrow \upsilon_i \cdot P + (1 - \upsilon_i) \cdot G \qquad (1\text{-}7)$$

$$r_i = \frac{dY_i}{dt} = -A_{r.i} \cdot \exp\left(-\frac{E_{r,i}}{RT}\right) \cdot Y_i^n \qquad (1\text{-}8)$$

Lyon [143] correlated this reaction rate to the mass loss rate (MLR) observed in TGA and simplified a first order Arrhenius-type reaction rate expression to obtain estimates of A_r and E_r based on peak MLR value, $r_{i,p}$, and the temperature at the peak, T_p, observed in the experimental MLR data, as given by Eq. (1-9) and Eq. (1-10). Here, m_0 is the initial mass of the reactant.

$$E_r = \frac{eRT_p^2 r_{i,p}}{(1 - \upsilon)\beta m_0} \qquad (1\text{-}9)$$

$$A_r = \frac{er_{i,p}}{(1 - \upsilon)m_0} \exp\left(\frac{E}{RT_p}\right) \qquad (1\text{-}10)$$

However, using these estimates for A_r and E_r require further optimization to accurately predict the MLR observed in TGA. This optimization can be performed either manually or automated using algorithms such as Genetic Algorithm (GA) [93,144], Shuffled Complex Evolution (SCE) [97,145] using bench-scale experimental data and analyzing the fit with an evaluation function. Recently, a hill-climbing optimization algorithm, was developed by Fiola et. al. [146] using ThermaKin, which provided faster and yet precise chemical kinetic parameters (A_r, E_r, and υ) of thermal decomposition for materials with simple and complex apparent decomposition mechanisms.

As discussed in Section 1.2.3 and shown in Figure 1-3, thermal decomposition mechanism is a part of the comprehensive pyrolysis model and the thermodynamics

associated with decomposition reactions, parameters describing thermo-physical behavior, optical parameters are important for characterizing heat and mass transfer through the degrading solid sample. Once the chemical kinetic parameters are derived, the heats of reactions and specific heat capacities of the intermediates (if multiple reactions similar to Eq. (1-7) are modeled in series or parallel) are estimated from heat flow data obtained from the DSC curve. Direct measurement of heat capacities through other experimental tools, although labor intensive, is also possible. Quantification of heats of reactions and constant or temperature dependent heat capacity of reactants can be performed by inverse analysis by following a methodology developed by Li et. al. [91,130]. This methodology first requires development of baseline heat flow, without considering heats of reactions, followed by calculation of endothermic or exothermic heats of reactions. Complete parameter set that describe chemical kinetics and associated thermodynamics of the decomposition process has been employed further to estimate heats of combustion from microscale combustion calorimeter (MCC) and thermo-physical properties from gasification apparatus such as Controlled Atmosphere Pyrolysis Apparatus II (CAPA II) or Fire Propagation Apparatus (FPA). An overview of comprehensive pyrolysis model development methodology discussed here is shown below in Figure 1-3.

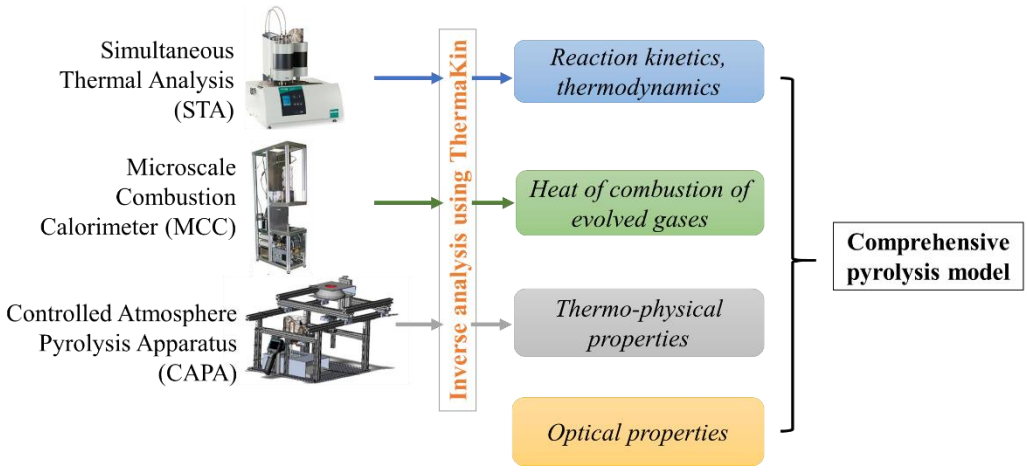

Figure 1-3. Schematic of a methodology for developing comprehensive pyrolysis model

Heat of combustion of different pyrolyzates from a material that has multi-step decomposition may not be the same due to different chemical structure of the gases released during the decomposition process. Heat of combustion has been generally treated as a material specific quantity, as discussed in Section 1.2.1, for the solid material but considering contribution from individual pyrolyzates can provide accurate estimations for complex materials with multi-peak decomposition reaction. The information of heat of combustion is obtained from heat release rate (HRR) data from MCC, where a milligram-scale sample, similar to TGA, is pyrolyzed in inert N_2 atmosphere and the emanating gases are completely combusted in a combustor maintained at 900 ºC and fed with oxygen to maintain air environment for fast and complete combustion of gases during the transport time through the combustor [5]. The HRR is measured downstream using oxygen consumption calorimetry. The MCC experiment can be simulated in ThermaKin and multiplying the predicted MLR with heats of complete combustion for individual pyrolyzate gas species. The heats of combustion values are varied until the experimental and predicted HRR are within required uncertainty [147].

Finally, characterizing thermo-physical properties such as thermal conductivity, *k*, density, ρ, radiative properties such as emissivity, ε, absorption coefficient, α, are essential to understand the heat and mass transfer process during the pyrolysis of the solid. These property values can be individually adopted from previously measured values reported in literature, measured from experiments that can quantity respective quantities (such as guarded hot plate method for thermal conductivity) or estimated from bench-scale gasification tests. CAPA II was specifically developed for these purposes to inversely analyze the information of mass loss, back surface temperature, and visual camera images of intumescence for an axisymmetric coupon-sized sample exposed to known external radiative heat flux in inert N_2 atmosphere [40]. The radiative and convective heat transfer to the top surface is very well resolved and characterized along the axis and radial directions to account for the impact of sample intumescence [40]. ThermaKin, in 2D axisymmetric module ThermaKin2Ds, has been used to inversely analyze experimental data to estimate constant or temperature dependent values for thermal conductivity, density. The change of the thermo-physical parameters for subsequent intermediates in case of a multi-step reaction is determined based on evolution of the experimental data and assumed to change fractionally from first reactant to last reactant, either dependent or independent of the stoichiometric coefficient.

1.5. ThermaKin

All modeling in this work was conducted using ThermaKin [129], a numerical pyrolysis solver that was developed to compute transient rate of gaseous fuel production from fundamental physical and chemical properties of constituents of a pyrolyzing solid. It solves unsteady mass and energy conservation equations for a 1D as well as two-

dimensional (2D) problems [148], including non-uniform swelling axisymmetric intumescent samples [132]. In this work, ThermaKin2Ds version 6, was utilized during pyrolysis model development and flame spread modeling.

In ThermaKin2Ds, materials are represented by elements containing mixtures of one or more components. Each component is categorized as solid, liquid, or gas and have a set of temperature dependent properties associated with it. Physical and chemical changes can take place for a component during a reaction. Materials, defined initially in terms of material thickness, mass fraction of constituting components, and temperature, can undergo subsequent reactions in response to mass or heat boundary conditions prescribed for the top and bottom boundaries. The governing equations solved by ThermaKin are summarized in Eq. (1-11) through (1-17).

$$\frac{\partial \xi_j}{\partial t} = \sum_{i=1}^{N_r} \theta_i^j r_i - \frac{\partial J_j^x}{\partial x} + \frac{\partial}{\partial x}\left(\xi_j \int_0^x \frac{1}{\rho}\frac{\partial \rho}{\partial t} dx\right) \quad (1\text{-}11)$$

$$r_i = A_{r,i} \exp\left(-\frac{E_{r,i}}{RT}\right) \xi_{COMP1} \xi_{COMP2} \quad (1\text{-}12)$$

$$J_g^x = -\rho_g \lambda \frac{\partial\left(\xi_g/\rho_g\right)}{\partial x} \quad (1\text{-}13)$$

$$\sum_{j=1}^{N} \xi_j c_j \frac{\partial T}{\partial t} = \sum_{i=1}^{N_r} \Delta H_{r,i} r_i - \frac{\partial q_x}{\partial x} - \frac{\partial I_{ex}}{\partial x} + \frac{\partial I_{rr}}{\partial x} - \sum_{g=1}^{N_g} c_g \left(J_g^x \frac{\partial T}{\partial x}\right) + c\rho \frac{\partial T}{\partial x} \int_0^x \frac{1}{\rho}\frac{\partial \rho}{\partial t} dx \quad (1\text{-}14)$$

$$q_x = -k \frac{\partial T}{\partial x} \quad (1\text{-}15)$$

$$\frac{\partial I_{ex}}{\partial x} = -I_{ex} \sum_{j=1}^{N} \kappa_j \xi_j \quad (1\text{-}16)$$

$$\frac{\partial I_{rr}}{\partial x} = \frac{\varepsilon \sigma T^4}{I_{ex}^0} \frac{\partial I_{ex}}{\partial x} \qquad (1\text{-}17)$$

Eq. (1-11) represents mass conservation equation for a j-th component, written in terms of mass-based concentration of a component, ξ_j (kg m^{-3}). The first term on the right in the mass conservation equation accounts for the consumption or production of j-th component. θ_i^j is negative if the component is being consumed and positive for a component being produced. The mass flow (accounted only for gaseous components) in and out of the element is considered in term 2. Term 3 considers the mass transfer due to expansion or contraction of the material. Reaction rate of a component is written according to Eq. (1-12). In absence of the second reactant, ξ_{COMP2} is set to 1. Arrhenius parameters, $A_{r,i}$ and $E_{r,i}$, for a reaction are often computed from inverse analysis of milligram scale thermogravimetric experiments. Mass transport of gaseous products within the condensed phase is dependent on its volumetric concentration gradient, as shown in Eq. (1-13). Conservation of energy equation, Eq. (1-14), equates the rate of change of sensible heat of the element to relevant processes on the right hand side, which include: heat associated with chemical reaction (term 1); heat conduction (term 2) defined in terms of Eq. (1-15); in-depth radiation absorption from an external source (term 3) calculated according to Eq. (1-16); re-radiation to the surrounding (term 4) calculated according to Eq. (1-17); convection due to mass flow of gases (term 5); and changes in sensible heat due to expansion or contraction of the material (term 6).

The symbols in Eq. (1-11) through (1-17) are defined as follows: t (s) is time; N_r is the number of reactions occurring within an element; ρ is density (kg m^{-3}); c_p is the heat capacity (J kg^{-1} K^{-1}); N is number of components in an element; ΔH_r is the heat of reaction

(positive if exothermic) (J kg^{-1}); A_r is pre-exponential factor (s^{-1} if first-order and kg^{-1} m^{-3} s^{-1} if second-order reaction); E_r is activation energy (J mol^{-1}); R is universal molar gas constant (J mol^{-1} K^{-1}); λ is the gas transfer coefficient (m^2 s^{-1}); k is thermal conductivity (W m^{-1} K^{-1}); κ is the radiation absorption coefficient normalized by density (m^2 kg^{-1}); ε is emissivity; σ is Stefan-Boltzmann constant (W m^{-2} K^{-4}); I_{ex} is the external radiation (including in-depth) absorbed by the sample (W m^{-2}); and I_{rr} is the re-radiation to the environment (W m^{-2}).

Additional details of governing equation and verification can be found elsewhere [129,132,148]. Flexibility allowed by ThermaKin2Ds for prescribing mass and heat transfer boundary conditions makes it possible to simulate and study wide range of pyrolysis and fire scenarios. This feature of ThermaKin was utilized to develop comprehensive pyrolysis model and subsequently model flame spread over materials.

1.6. Motivation

The hazards of material flammability and flame spread sometimes manifest as impactful incidents such as the one in Grenfell towers in 2017 [149,150] where fire spread over the outer building cladding resulted in 72 fatalities. Such incidents emphasize the importance to better understand the material flammability and flame spread hazards. The scientific community realizes the need for predicting flame-spread hazards posed by flammable materials in a standardized testing environment so that new materials can be screened before commercial application and save high monetary costs required to make standardized testing possible.

Flame spread over combustible materials in a corner geometry challenges the material to a severe hazard and standardized tests commonly use this scenario for screening wall-lining materials. However, coupling of gas-phase combustion, flame-solid interaction, and condensed-phase pyrolysis phenomena which govern the flame spread often are either simplified in semi-empirical models leading to inconsistent scaling of empirical correlations and hazard parameters used in the models to a large scale scenario, or require comprehensive characterization of input parameters for computational fluid dynamic (CFD) models and require well-resolved experimental data for model validation.

This project is motivated by the incidents that highlight the present needs to better understand material flammability and the flame spread problem, by the thorough literature review of available scientific methodologies, and by the presently lacking experimental data for validating modeling approach. The fundamental understanding of controlling mechanisms of phenomena (gas-phase combustion, heat transfer to unburnt region, and pyrolysis) such as solid-flame interaction and thermal decomposition kinetics are necessary to carefully characterize governing phenomenon and better predict material flammability. This can be achieved by creating experimental conditions that isolate the desired phenomenon from another. Therefore, this research is motivated to employ hierarchical experimentation and modeling of different materials in order to create a systematic methodology for predicting flame spread in a large corner fire scenario and to provide a comprehensive dataset for the evaluation of advanced CFD-based approaches.

1.7. Research Objectives

The flame spread problem is a complex interrelation between thermally degrading and possibly physically deforming solid sample, gas-phase combustion accompanied by soot formation, and interaction of unburnt fuel and the flame in the direction of the fire spread. Although each of these sub-phenomena have been individually studied fundamentally for more than half a century, the available experimental data is limited by the measurements which are either material specific or constrained to interpret fire growth parameters for standard reaction-to-fire scenarios. There is a recognized need for predicting the fire spread over a combustible material so that the material can be screened for their flammability and flame spread propensity.

The objectives of the research, motivated by the current state-of-the-art modeling and measurement techniques, are broadly classified in the following three points:

1. Develop and validate comprehensive pyrolysis models for the studied materials by implementing a hierarchical modeling approach. A comprehensive pyrolysis solver, ThermaKin, was utilized to simulate small-scale experiments and inversely analyze the data, as illustrated in Figure 1-3, to estimate relevant chemical kinetic, thermodynamic, and thermo-physical parameters.
2. Build a comprehensive dataset for key parameters which govern the flame spread over three materials in the large-scale corner configuration. The materials were chosen such that the impact of a range of flammability behaviors such as HRR, charring and sooting propensity can be investigated. Primary focus was to achieve fast-response, synchronized calorimetry, spatially resolved flame heat flux, resolved flame radiation

emissions, and flame structure during the flame spread process and investigate the impact of fuel on the flame spread process. To achieve this objective, it was necessary to design and build an experimental setup to study buoyancy-driven, turbulent flame spread in a large-scale corner configuration.

3. Develop a low-cost, semi-empirical model, using large-scale test data and comprehensive pyrolysis model to predict heat release rate of flame spread in the large-scale corner. For this, the validated comprehensive pyrolysis model was coupled with the information from large-scale experiments as a final stage of the hierarchical modeling. The influence of the input parameters such as solid-flame interaction, pyrolysis parameters was investigated to better understand their impact on the flame spread process.

1.8. Material Selection

Three materials, Poly(methyl methacrylate) (PMMA), Polyisocyanurate (PIR) foam, and oriented strand board (OSB), were selected for this study. The motivation here was to begin with a relatively simple material (PMMA) and increase the complexity with other materials (PIR and OSB) to understand the dynamics of the flame spread process.

PMMA is arguably the most studied solid combustible in the field of fire science. The main reason for such popularity is this material's nearly ideal thermal decomposition behavior characterized by the absence of charring or swelling and a remarkably simple pyrolyzate composition dominated by its monomer [151]. PMMA has been a benchmark material to understand a wide range of fire dynamics phenomena including analysis of burning rates [55,94,152], flame heat fluxes [53,152,153], and flame spread dynamics

[50,55,125,154–156]. The kinetics of the thermal decomposition of PMMA was also investigated extensively at both the molecular [83,86,157] and engineering model levels [91,135,145,158]. Thus, investigations on PMMA would potentially help in understanding gas-phase flame heat feedback and in collection of comprehensive flame spread data on a material with well-resolved condensed-phase behavior, which can be used for development and evaluation of flame spread modeling approaches

PIR foam and OSB were selected because they are materials with practical importance since they are widely used as wall-lining materials in the built environment. Secondly, the motivation was to understand flame spread over materials exhibiting charring and complex thermal decomposition. A wall-lining insulation material, PIR foam, is a material of known practical importance in thermal insulation of residential buildings, where 30% of lost energy contribution comes from space heating and cooling [159]. PIR foam with closed-cell structure is identified to be increasingly favored due to its relatively low cost and lower global warming potential from emanating emissions than Aerogel, expanded (EPS) and extruded (XPS) polystyrene foam insulation [160]. OSB, on the other hand, is an engineered composite wood product used more widely than plywood and particle board, and commanding more than 66% of global structural panel market as of 2016 [161]. OSB, being used in exterior and interior wall construction, was therefore selected due to its increasing practical importance in built environment as a wall-lining material.

1.9. Dissertation Outline

The remainder of this dissertation is structured in the following manner. The information in the next three chapters is distributed such that each chapter discusses the details of experiments and modeling for one material starting with PMMA, then PIR foam, and finally OSB. Each chapter begins with the description of small-scale experiments and pyrolysis model results. This is followed by the discussion of large-scale experiments and flame spread modeling. Chapter 2 provides general description of experimental setups (both small-scale and large-scale test setups) and the modeling (both pyrolysis modeling and flame spread modeling) framework which are utilized and referred to in subsequent chapters. Each chapter ends with respective conclusion. Chapter 5 includes general concluding remarks and proposes future work.

Appendix A provides derivation and validation of calorimetry expressions used for oxygen consumption calorimetry. Appendix B provides miscellaneous plots and information as referred from specific chapters and also provides radiation heat flux data obtained from flame spread experiments performed over PMMA.

Chapter 2: Experiments and Modeling of Pyrolysis and Flame Spread over Black Cast Poly (Methyl Methacrylate)

A large scale experiment was developed to experimentally study dynamics of buoyancy-driven, turbulent flame spread problem over different polymers. This chapter discusses the experiments performed over Poly(methyl methacrylate) (PMMA), whose thermal decomposition is known to be non-charring, non-swelling in nature and has been well-characterized by various studies. PMMA is generally manufactured via either an extrusion or a casting process, which impacts the mechanical and thermal behavior of the synthesized polymer [145,162]. Cast PMMA has higher molecular weight than the extruded PMMA and usually does not exhibit melt flow. This reduces the complexity introduced by melting on a larger scale. Therefore, cast PMMA was selected for this study. Furthermore, a black cast PMMA was selected because of its high absorption coefficient, thus, reducing the impact of in-depth radiation absorption which complicates modeling. The black coloring was also speculated to reduce the reflection from the surface during large-scale experiments thereby aiding processing of images captured by the Digital Single-Lens Reflex (DSLR) camera. Therefore, a cast black PMMA by the tradename ACRYLITE black 9H01 GT, manufactured by Evonik, was purchased as 0.58 ± 0.02 cm thick, 121 cm × 244 cm sheets. Samples for all the experiments were cut and prepared from these sheets.

2.1. Small-Scale Experiments

2.1.1. TGA-DSC Experiments

Thermogravimetric Analysis (TGA) and Differential Scanning Calorimetry (DSC) were conducted on cast black PMMA in Simultaneous Thermal Analyzer (STA) Netzsch 449 F3 Jupiter. The apparatus exposes both a reference crucible and a sample-containing crucible to a temperature scan defined by a specific heating program while continuously measuring mass evolution and heat flow to the sample as a function of time and temperature. The STA was calibrated according to previously established procedures [91] to maintain a quantitative relationship between the measured and the true value of the temperature of the sample holder, ensure accurate heating program, and accurate heat flow measurements. The calibration was performed by using six organic compounds with known melting point temperature having a range of about 313 K to 1000 K and known corresponding enthalpy of melting.

Seven PMMA samples with mass of 4-7 mg were prepared by finely grounding the sample in a powder form and kept in the desiccator for at least 24 h before the experiments. All experiments were conducted using platinum-rhodium crucibles with lids having a small hole which allowed for the escape of gaseous decomposition products. Before each experiment, a baseline test was performed using an empty crucible under identical heating conditions to measure and correct for differences in environment, buoyancy effects, and asymmetry of the furnace and sample crucibles. All experiments were conducted in inert atmosphere maintained by 50 ml min^{-1} N_2 flowrate. PMMA samples were heated, consistent with prior experiments [163], at a rate of 10 K min^{-1} to ensure samples did not

experience significant temperature and concentration gradients, thus isolating thermal decomposition kinetics and energetics from the transience introduced by heat and mass transport lag.

2.1.2. MCC Experiments

Microscale Combustion Calorimetry (MCC) [5] is an apparatus designed to obtain instantaneous heat release rate for complete combustion of the pyrolyzate gases evolving during a controlled atmosphere pyrolysis of a sample. In this apparatus, a milligram-scale sample was placed in a ceramic crucible and pyrolyzed in an inert pyrolyzer section maintained by 80 ml min^{-1} N_2 flowrate. The evolving pyrolyzate gases pass through a combustor section which was maintained at 1173 K and replenished with oxygen at 20 ml min^{-1} to ensure complete combustion of gaseous pyrolyzates in an aerobic and excess oxygen atmosphere. The HRR was estimated via oxygen consumption calorimetry following Method A [5] by monitoring flow rate and oxygen concentration downstream of the combustor section. Before each experiment, the oxygen sensor was calibrated against two reference concentration, one for 0 vol. % O_2 using Nitrogen and another for 20.95 vol. % O_2 using compressed dry air. The air flowmeter at the outlet of the test section was calibrated against calibration-independent volumetric flow calibrator which calculated flow rate based on the rise time of a piston in a cylindrical annulus of known volume. The MCC heat release rate calculation was validated every test day by running the MCC for a Polystyrene sample having a mass of around 2.5 mg to 3 mg. The heats of combustion derived from the validation tests were always around 39.7 ± 0.5 kJ g^{-1}, which is in agreement with the standard reference value of 39.7 kJ g^{-1} [5].

Four tests were performed on black cast PMMA samples weighing between 4 and 5 mg. The samples were pyrolyzed in anaerobic conditions at a nominal heating rate of 1 K s^{-1}. The residue yield was determined after each test to check how it relates with the TGA results.

2.1.3. Broadband Radiation Absorption Experiments

Radiation absorption coefficient, α, was measured by using a technique developed by Linteris et. al [164] and later adopted in other studies [165–167]. In this experimental setup, shown in Figure 2-1, a thin cast black PMMA sample, 0.1 cm thick, was irradiated with a collimated heat flux and measured as incident on a water-cooled Schmidt-Boelter heat flux gauge. The irradiation with and without the sample in place is compared for broadband absorption coefficient estimation.

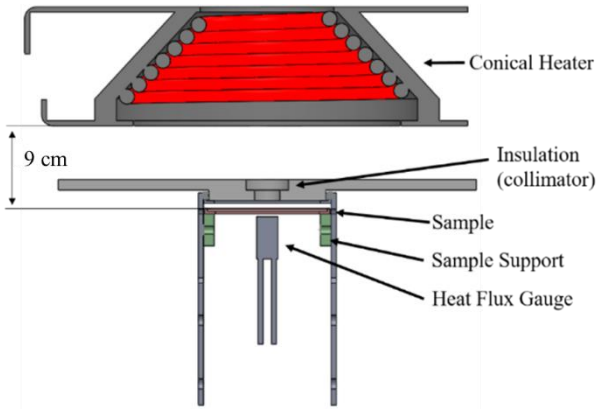

Figure 2-1. Schematic of the apparatus for the measurement of the radiation absorption coefficient

An incident heat flux of approximately 5 kW m^{-2} without the sample in place was compared with the heat flux transmitted through the thin sample. The data of transmitted radiant heat flux was measured for short intervals of 3 s to ensure that the sample does not

decompose and the gauge does not read heat flux data affected by conduction. Upon the collection of sufficient data, the radiative heat through the sample was treated as one-dimensional (1D), parallel to axis of collimated flux. The absorption coefficient was measured using a generalized version of beer-Lambert law [164], $\alpha = \left(2\ln(\varepsilon) - \ln(I_T/I_0)\right)/\rho\delta$, where δ is the thickness (0.1 cm), I_T is transmitted radiation through the thin sample, I_0 is the heat flux without the polymer sample in place. Data were obtained for 6 tests on black cast PMMA.

2.1.4. Controlled Atmosphere Pyrolysis Apparatus II (CAPA II) Experiments

Controlled Atmosphere Pyrolysis Apparatus II (CAPA II), depicted in Figure 2-2, is an instrument designed to facilitate analysis of thermo-physical changes a solid undergoes during pyrolysis or gasification process [40]. This gasification apparatus (utilizing water-cooled chamber walls) provides well-defined boundary conditions and simultaneous measurement of back surface temperature, mass loss, and shape profile evolution for an axisymmetric, 7 cm diameter disk samples exposed to radiant heat. The atmosphere is maintained at oxygen concentration below 1 vol. % to ensure measurements are free from oxidation effects, which emulates a solid burning under a continuous diffusion flame [154]. The radiation from conical heater was carefully characterized to account for changes in sample surface position and angular orientation. Convective losses on the front and back of the sample surfaces have also been carefully characterized and validated with experimental data, details of which can be found elsewhere [40].

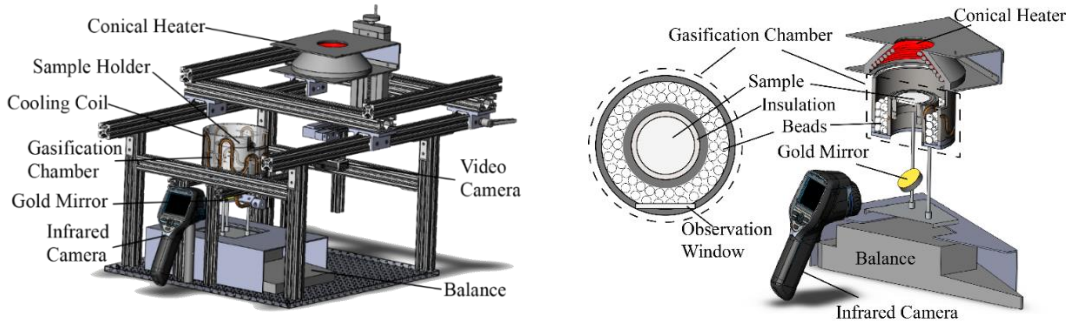

Figure 2-2. Schematic of Controlled Atmosphere Pyrolysis Apparatus II (CAPA II)

CAPA II experiments were performed on 0.58 cm thick, 7 cm diameter disk samples of cast black PMMA at an external radiant heat flux of 25 and 60 kW m^{-2}. Test at each heat flux was repeated twice. The data for the back surface temperature using the IR camera, mass-loss using the mass balance data acquisition, and profile expansion using the video camera were simultaneously obtained in these experiments. Kaowool PM insulation rings were cut to encircle the sample to create nearly adiabatic radial boundary condition. Samples were epoxied to the copper foil to maintain good thermal contact for measuring back surface temperature and reduce effect of swelling, morphing, and flowing. Back surface of the copper foil was painted with high emissivity ($\varepsilon = 0.95$) to facilitate back surface temperature measurement using an IR camera. The emissivity corrections necessary to process the back surface temperature was validated by exposing a copper plate to a set radiant heat flux. The copper plate was installed with three surface thermocouples on the back side for validation purposes. Back surface temperature measurements were made at 12 points representing 4 radial locations (r = 0, 1, 2 and 3 cm from the center).

2.2. Small-Scale Experiment Results

Results from milligram-scale experiments (STA and MCC) performed on PMMA are summarized in Figure 2-3 as a function of sample temperature, *T*. All uncertainties reported were calculated using repeated experiments as two standard deviations of the mean. A major decomposition of PMMA begins at around 550 K, which is close to earlier reported values for PMMA [47,76,152], with a peak mass loss rate observed around 640 K. A small loss of mass around 460 K was observed before the major decomposition which is attributed to vaporization of residual solvent retained in the polymer matrix. The residue left behind after complete pyrolysis in STA was negligible (less than 0.5%) and similar yield was obtained from MCC experiments. An endothermic heat flow is observed in DSC corresponding to the temperature range of the major decomposition observed in the MLR curve. The HRR observed in MCC also show peak HRR at temperature corresponding to peak MLR observed in TGA. The heat of combustion of cast black PMMA, obtained from analysis of MCC data, was estimated to be 24.1 ± 0.5 kJ per g of lost mass.

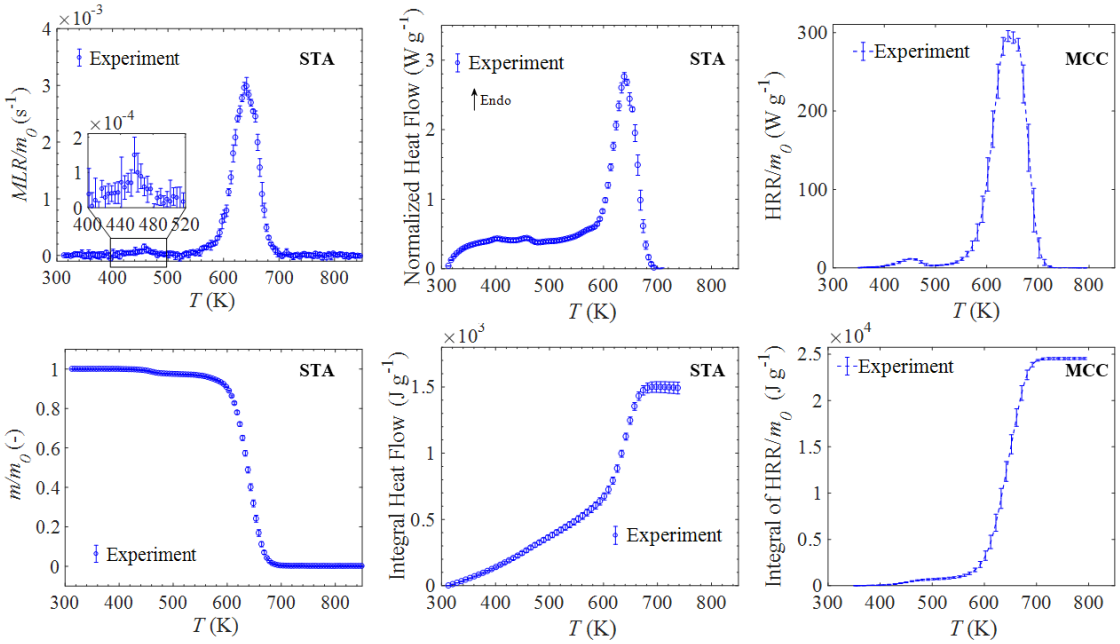

Figure 2-3. STA (TGA-DSC) and MCC experimental results for cast black PMMA

Back surface temperature and area-normalized mass loss rate data for CAPA II experiments performed on black PMMA are shown in Figure 2-4 as a function of time, *t*. Here t = 0 s represents the time when the sample was exposed to the set radiant heat flux. The error bars in these plots represent two standard deviation of the mean. The mass loss rate begins at around 110 s for the 25 kW m^{-2} test and at around 20 s for the 60 kW m^{-2} test. Higher peak for mass loss rate is observed for higher heat flux of 60 kW m^{-2} than 25 kW m^{-2}. The back surface temperature, T_{back}, rises slower for 25 kW m^{-2} than 60 kW m^{-2}. The T_{back} was obtained by averaging temperature data at 12 points, where three points at four radial distance from the center of the PMMA disk (0, 1, 2, and 3 cm) were analyzed from the IR images. The small-scale experiment data were then used to develop and validate a comprehensive pyrolysis model for PMMA.

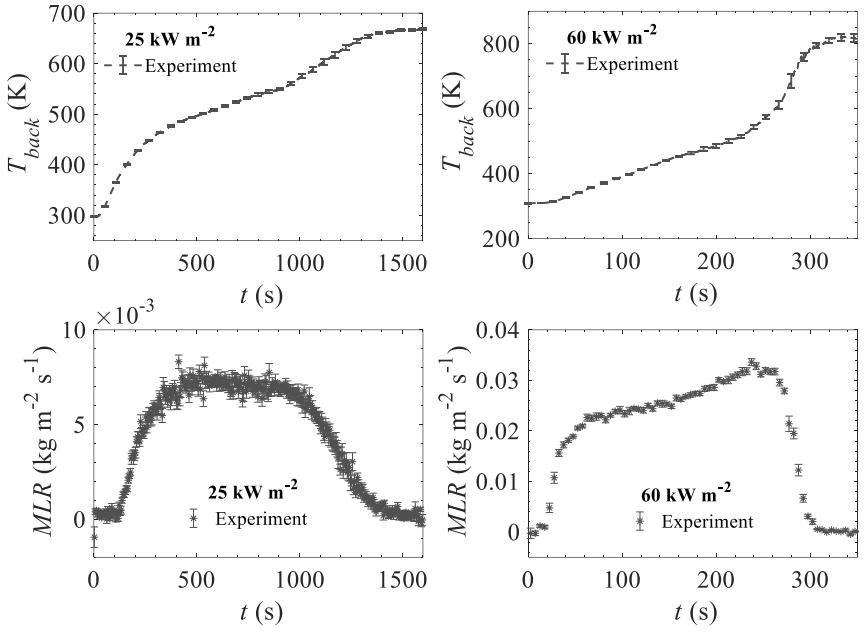

Figure 2-4. CAPA II experimental data for cast black PMMA

2.3. Comprehensive Pyrolysis Modeling Framework

2.3.1. Reaction Kinetics

First the chemical reaction kinetics were characterized by modeling TGA experiments conducted at 10 K min^{-1}. TGA was simulated for a thermally thin PMMA sample prescribed as one spatial element. The element temperature was forced to follow experimental temperature profile by prescribing a high convection coefficient of 1×10^5 W m^{-2} K^{-1}, at the boundary. The temperature profile was prescribed as an instantaneous heating rate, $\beta(t)$, of the Simultaneous Thermal Analysis (STA) which can be simulated with an exponentially decaying profile, given by Eq. (2-1). In this equation, K (K s^{-1}), L (s^{-1}), M (s^{-1}), and N (-) are adjustable parameters determined by fitting experimental instantaneous heating rate data with this equation. The mass flow boundary conditions were defined such that gaseous pyrolyzate instantaneously escaped from the element.

$$\beta(t) = \frac{dT}{dt}(t) = K(1 - (\exp(-Lt))(\cos(Mt) + \mathrm{N}\sin(Mt)) \quad (2\text{-}1)$$

Initial global decomposition reaction scheme constituting of single or multiple reactions in series or parallel was decided based on the peaks observed in the MLR curve of TGA experiments. The reaction parameters including pre-exponential factor, A_r, activation energy, E_r, and mass-based stoichiometry, υ, were the parameter variables for the hill-climbing optimization algorithm, which was developed in another study [146,168], thereby simplifying the manual optimization process adopted in previous studies [91,130,147,169]. A goodness of fit criterion, $\mathrm{GoF_M}$, given by Eq. (2-2) was introduced to serve as a target for the optimization process.

$$\mathrm{GoF_M} = \frac{0.6}{\mathrm{Exp\ MLR_{max}}}\sqrt{\frac{\sum_i^{\mathrm{N}}(\mathrm{Exp\ MLR_i - Model\ MLR_i})^2}{\mathrm{N}}} + \frac{0.4}{\mathrm{Exp\ m_{max}}}\sqrt{\frac{\sum_i^{\mathrm{N}}(\mathrm{Exp\ m_i - Model\ m_i})^2}{\mathrm{N}}} \quad (2\text{-}2)$$

In Eq. (2-2), m is sample mass and summations are over all (N) experimental data points. This $\mathrm{GoF_M}$ criteria was a combination of 60 % of MLR fit and 40 % mass fraction fit, determined as a best compromise between capturing MLR and mass fraction for PMMA and PIR foam. The initial guesses for A_r and E_r were calculated using approximate solution for first-order reaction kinetics obtained by Lyon [143], as shown in Eq. (1-9) and Eq. (1-10). The initial values of υ for each global reaction were obtained directly from the TGA mass fraction data.

The ThermaKin2Ds solution obtained with the kinetic parameters was used to compute $\mathrm{GoF_M}$. Subsequently, multiple sets of new A_r, E_r and υ were generated for every reaction by modifying the $\mathrm{MLR_{peak}}$ and $\mathrm{T_{peak}}$ inputs in small negative and positive

increments. A given set of $\mathrm{MLR_{peak}}$, $\mathrm{T_{peak}}$, and υ that produced the lowest $\mathrm{GoF_M}$ value was retained. The hill climbing process was repeated until no reduction to the $\mathrm{GoF_M}$ could be achieved.

The key feature of the presented algorithm was that the iterations were performed in the $\mathrm{MLR_{peak}}$ and $\mathrm{T_{peak}}$ parameter space (the corresponding A_r and E_r pair was computed with Eq. (1-9) and Eq. (1-10)). Operating in this space provided clearer relationship between the values of the incremental changes and the impact of these changes on the simulated TGA profiles. The reaction mechanism (number of reactions, order, and/or series-parallel reaction scheme) was altered and optimized to best fit the experimental TGA MLR curve. The algorithm was implemented as a MATLAB script that called ThermaKin2Ds (C++ code compiled into an executable file) as a subroutine.

Black cast PMMA samples were modeled as thermally thin using a single spatial element with 1×10^{-5} m size and time step of 0.01 s in ThermaKin2Ds. Changing these integration parameters by a factor of two did not alter the simulation results, indicating convergence.

2.3.2. Thermal Decomposition Thermodynamics

After characterizing the kinetics of the thermal decomposition using the TGA data, the DSC data was inversely analyzed to capture the associated thermodynamics during thermal decomposition. Primary information deduced from this inverse analysis were the heat capacity of solid intermediates described in the reaction mechanism, quantity and the rates (with respect to temperature) of heat absorbed (or released) during each decomposition reaction and/or phase transition. To quantify these, the experimental heat

flow data were first divided by instantaneous heating rate to determine the heat capacity of the initial, unreacted component pre and post-glass-transition temperature. Heat capacity of intermediate components was assumed to be the same for all components as the heat capacity determined for post-glass transition state. A baseline heat flow that represented sensible heat flow as a function of temperature throughout the decomposition was constructed using the kinetic mechanism and the heat capacity values. Heats of reactions were estimated as the difference of the integral of DSC heat flow and the constructed DSC baseline.

2.3.3. Heat of Combustion

Once the reaction kinetics and thermodynamics of the thermal decomposition were modeled, the complete heat of combustion for individual gaseous components were estimated using the MCC experimental data. Effective total heat of combustion was obtained via integration of the HRR curve and normalization of the integral by the total mass lost. Similar to STA experiments, MCC was then simulated in ThermaKin2Ds as a thermally thin pyrolyzing single element following a prescribed instantaneous heating rate profile. Then, the heat of combustion of individual gaseous component (initially assigned as the effective total heat of combustion) were multiplied by the corresponding pyrolyzate mass flow rate predicted by Thermakin2Ds. The resulting HRR was then normalized by the initial mass and compared with the MCC experimental data. The heat of combustion values for individual gaseous components were then adjusted until the average error between experimental and predicted HRR was less than 5%.

2.3.4. Thermo-Physical Properties

The data from CAPA II were then used to parameterize the thermo-physical properties (thermal conductivity and density) of intermediate components that, along with optical properties, which dictate the heat transfer through the sample during pyrolysis. CAPA II was simulated in one-dimensional (1D) version of the ThermaKin2Ds solver. The convective and radiative boundary conditions of the CAPA II were fully implemented in the model. Gaseous mass transport through the condensed phase was defined such that gaseous products experienced no resistance to outflow. Mass flow was not permitted through the back boundary, which was defined as a single-element of copper representing the copper foil used in experiments. The properties of the copper foil used during the simulation of CAPA II were obtained from Ref. [170].

The mean back surface temperature profile obtained in the CAPA II experiments performed at a specific external heat flux were used to parameterize thermal conductivities, *k*, of condensed-phase components through inverse modeling. The thermal conductivity parameters were optimized to fit experimental back surface temperature T_{back} data. A single goodness of fit criterion, GoF_T, given by Eq. (2-3) was introduced to serve as a target of the optimization process.

$$GoF_T = \sqrt{\frac{\sum_i^N \left(\frac{\text{Exp } T_{back,i} - \text{Model } T_{back,i}}{\text{Exp } T_{back,i}} \right)^2}{N}} \qquad (2\text{-}3)$$

Thermal conductivities of the intermediate components were either considered constant or represented as a polynomial function (degree 1, 2 or 3) with temperature. Temperature independent thermal conductivity of 0.1 W m^{-1} K^{-1} was assigned as the initial

starting point for the hill-climbing search algorithm. The optimization was repeated with a range of physically meaningful initial guesses to ensure that the resulting parameter values correspond to the global minimum of GoF_T. Thermal conductivity of air at 600 K, 0.04 W m^{-1} K^{-1} [171] was used as the lower limit for the optimization process to obtain physically meaningful conductivity values for the solid intermediate components.

The sample profile expansion during CAPA II tests was quantified to obtain critical profile expansions during the gasification process. Any intumescence (swelling) observed in the experiments was captured in ThermaKin2Ds simulations by densities of intermediate components decreasing with reaction steps. Decreasing component densities had an impact on the sample thickness. The densities of intermediate components were optimized using a goodness of fit criteria for density (GoF_D), similar to Eq. (2-3). The GoF_D ensured that the densities of intermediate solid components are optimized to accurately capture the mean experimental profile expansion data, assuming that the sample undergoes axisymmetric, radially uniform 1D profile expansion.

Final optimized thermo-physical property value along with optimized reaction kinetic and associated thermodynamics were then validated against experimental MLR data of CAPA II tests, and the back surface temperature of the CAPA II test data which was not used for thermo-physical properties' optimization.

Black PMMA CAPA II simulations were conducted at time step of 0.01 s and spatial discretization of 5×10^{-5} m. Changing these integration parameters by a factor of 2 did not alter the simulation results, indicating convergence.

2.4. PMMA Pyrolysis Model

The PMMA decomposition was represented in the model by two consecutive first-order reactions (Rxn) whose stoichiometry, Arrhenius parameters, A_r and E_r, and heats of reactions, ΔH_r, are summarized in Table 2-1. The first reactant shown here is $PMMA_{melt}$ representing the PMMA component after glass transition at 395 K. A glass transition temperature of 395 K was implemented into the model to capture the protuberance in the heat flow and has no associated mass loss. Two linear temperature dependent heat capacity functions were obtained by DSC data analysis for temperature before and after the glass transition temperature. These values are reported later in Table 2-2. The gaseous pyrolyzate ($PMMA_{gas}$) was assigned a heat capacity of 2000 J kg^{-1} K^{-1}, which corresponds to the average ideal gas heat capacity of the MMA monomer between 400 and 500 K [146].

Table 2-1. Decomposition reaction mass-based stoichiometry, kinetic parameters, and heat of reaction (positive heat values correspond to endothermic reactions) for cast black PMMA.

Rxn #	Reaction Equation	*Ar* (s^{-1})	*Er* ($J \cdot mol^{-1}$)	ΔH_r ($J \cdot kg^{-1}$)
1	$PMMA_{melt} \rightarrow 0.98\,PMMA_{int} + 0.02\,PMMA_{gas}$	4.95×10^{16}	1.64×10^{5}	5×10^{3}
2	$PMMA_{int} \rightarrow 0.002\,PMMA_{char} + 0.998\,PMMA_{gas}$	1.35×10^{11}	1.64×10^{5}	817×10^{3}

Comparison of experimental TGA mass loss rate and DSC heat flow with the model fits are shown in Figure 2-5. The onset temperature of the main thermal decomposition estimated to be about 550 K is accurately predicted by the model.

The heat of combustion of for cast PMMA was determined to be 24.1 ± 0.5 kJ per g of lost mass using the MCC data. Due to negligible mass loss and heat production contribution of Reaction 1, the same heat of combustion was assigned for the gaseous products of both reactions.

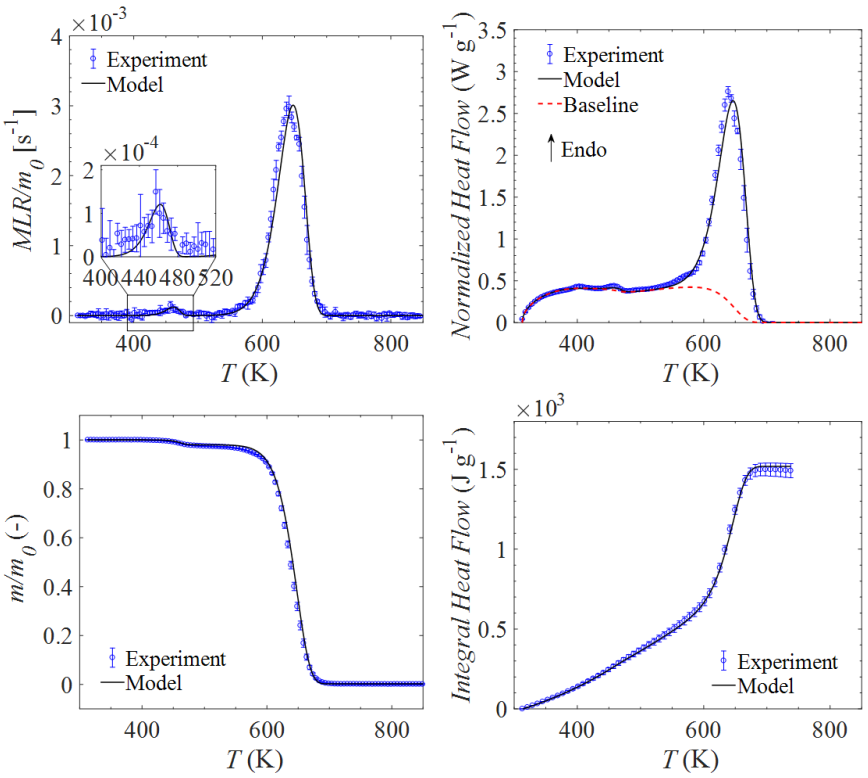

Figure 2-5. PMMA model fit compared with experimental data obtained from STA tests performed at 10 K min^{-1}

Back surface temperature data from CAPA II tests performed at 25 kW m^{-2} were used to estimate the thermal conductivity of intermediate components. The thermo-physical properties of condensed-phase components ($PMMA_{melt}$, $PMMA_{int}$, and $PMMA_{char}$) defined in the model were set to be equal to each other and are listed in Table 2-2. The comparison of model fit and experimental data at 25 kW m^{-2} is shown in Figure 2-6. Absorption coefficient was calculated using the methodology described in Section

2.1.3. Emissivity value was obtained from measurements performed previously by Linteris et. al [164]. Absorption coefficient, obtained from experiments discussed in Section 2.1.3, and emissivity values for all the components were assumed to be the same as that of cast black PMMA. Due to almost non-existent profile expansion observed during CAPA II tests, the densities of the intermediate components were also assumed to be the same as measured for the cast black PMMA.

Table 2-2: Thermo-physical and optical properties of cast black PMMA.

Property	**Units**	**PMMA**
Density	kg m^{-3}	1210 ± 30
Thermal conductivity	W m^{-1} K^{-1}	0.16, T < 395 K 0.34 - 4.2×10^{-4}×T, T > 395 K
Heat capacity	J kg^{-1} K^{-1}	-1390 + 8.33×T, T < 395 K 851 + 3.07×T, T > 395 K
Emissivity	-	0.96
Radiation absorption coefficient	m^2 kg^{-1} (m^{-1})	2.38 ± 0.23 (2870 ± 280)

The full pyrolysis property set was validated against CAPA II mass loss rate profiles and mean back surface temperature profile for 60 kW m^{-2} tests. Figure 2-6 shows the comparison of experimental data for CAPA II and model fit and predictions for the back surface temperature and MLR for both the heat fluxes.

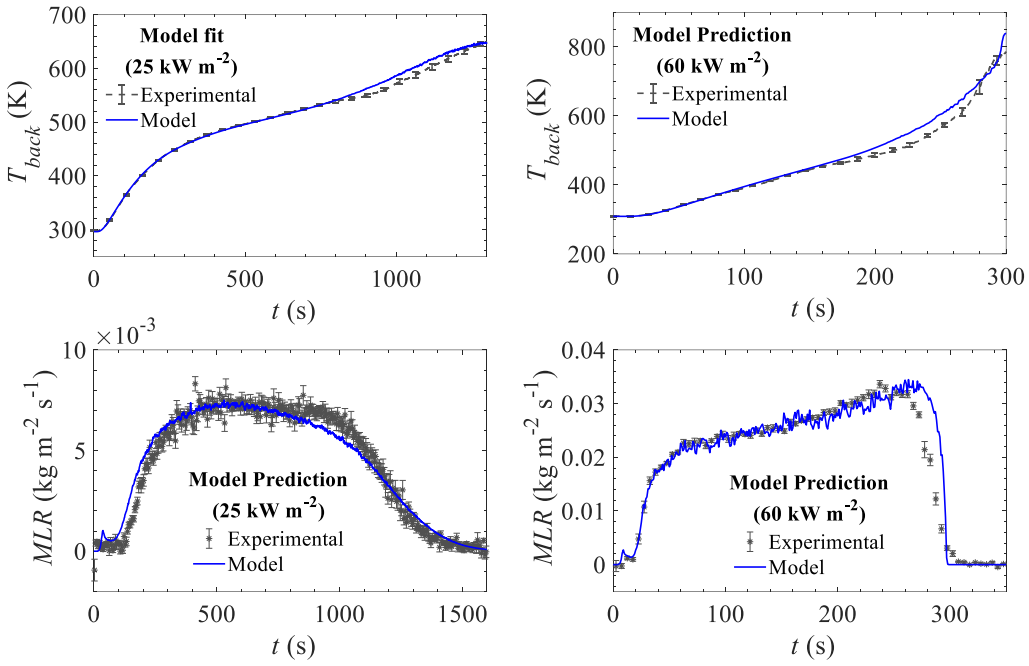

Figure 2-6. Comparison of back surface temperature and mass loss rate experimental data with model fit and predictions for CAPA II

The pyrolysis model predicts the mass loss rate and back surface temperature reasonably well during majority of the decomposition process in the gram-scale CAPA II experiments. This comprehensive pyrolysis model was then utilized later for flame spread modeling.

2.5. Large-scale Experiment Setup and Instrumentation

A large-scale experimental setup was built to study dynamics of buoyancy driven turbulent flame spread. This setup was maintained the same for experiments on all types of materials tested. This section details the experimental setup and the exhaust gas diagnostics necessary for the calorimetry which were consistent for tests over all materials.

The experimental setup, shown in Figure 2-7, consisted of two identical panels of desired test material rigidly mounted onto a 1.27 cm thick Marinite I calcium silicate board in a symmetrical corner geometry. Marinate-I which held the panels rigidly in vertical position is a refractory fire-resistant, structural insulation manufactured by BNZ materials Inc. This board was chosen by considering the screw holding strength to mechanically hold the material with screws and bolts, without rupture. The insulation board had nearly uniform properties across the temperature range of 290 to 550 K. The properties are density, ρ = 737 kg m^{-3}, specific heat capacity, C_p = 1260 J kg^{-1} K^{-1} and thermal conductivity, k = 0.13 W m^{-1} K^{-1} across the temperature range of 290 K to 550 K.

The vertical distance from the top of the burner sidewalls was the y coordinate used in the current analysis; y = 142.5 cm corresponded to the top of the panels. Experiments were performed under an exhaust duct system equipped with baffles for adjusting the exhaust flow and outlet for gases outside the building for safe evacuation. The exhaust duct was a 28 cm inner diameter pipe with circular cross section.

The corner-wall assembly was placed under a 200×200 cm exhaust collection hood, whose bottom edge was 220 cm above the floor. A flame resistant curtain extended 160 cm from bottom of the hood towards the floor and was used to constrain the volume of the enclosure. A fabric mesh covered the remaining 60 cm to help homogenize the incoming air flow. The room was equipped with inlet louvers for replenishing fresh air being consumed by the fire.

The panel material mounted in the corner geometry was ignited by a propane sandbox burner, build in accordance with EN 13823 [7]. The burner was placed 4 cm from both the panels and was fueled with a constant flow of propane at 21.23 SLPM ($6.47 \times 10^{-}$

^{4} kg s^{-1}) corresponding to the HRR of 30 kW. The burner was on for the entire duration of the experiment. A K-type Stainless Steel (SS) sheathed thermocouples with 0.02 cm wire diameter was installed to monitor time of propane burner ignition such that the sensing element was about 1 cm above the burner surface. This time of ignition was used to synchronize all the data collected during the experiment.

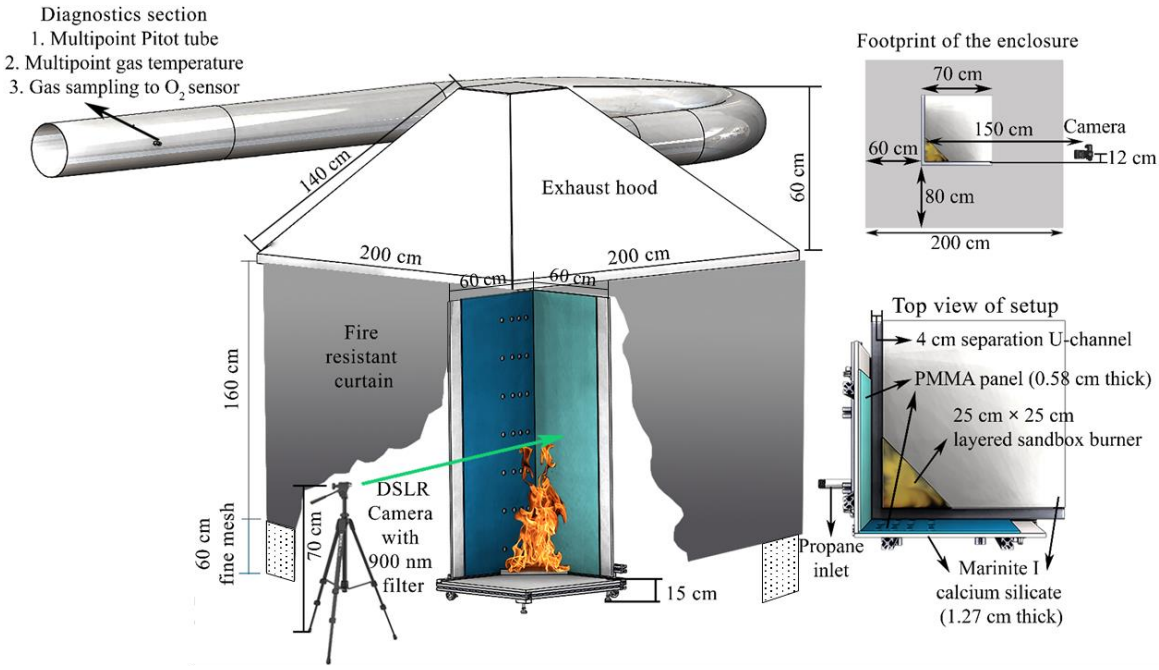

Figure 2-7. Schematic of large-scale experimental setup

2.5.1. Exhaust Gas Diagnostics

Diagnostics on the exhaust gases were done in an instrumentation section, 120 cm in length and about 500 cm downstream of the connection to the collector hood. The cross section of this section with schematic of instrumentation in it is shown in Figure 2-8. This section was about 20 duct-diameters downstream of the collector hood and thus sufficient for assuming fully-developed and well-mixed flow. All the instruments in the instrumentation section were located as close as possible to each other in direction of the

flow (approximately 15 cm) but separated sufficiently across the circumference of the duct to provide diagnostics as locally close as possible but avoid errors in downstream measurements due to flow disturbances produced by the upstream instruments.

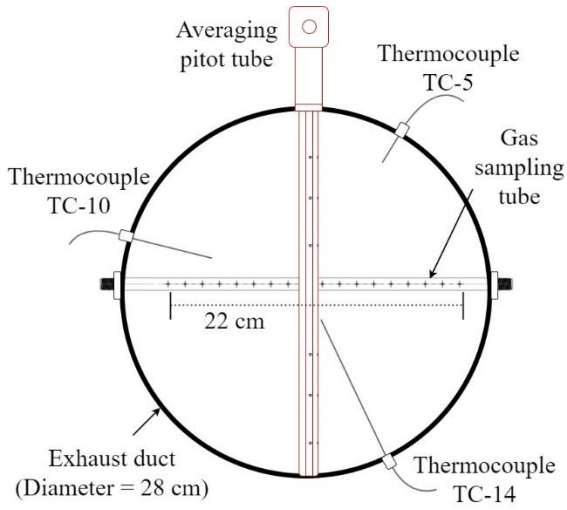

Figure 2-8 : Cross section of instrumentation section (not to scale)

2.5.1.1. Exhaust Temperature

Spatially distributed, multiple measurements of the exhaust gas temperatures are recommended to minimize the error propagation in mass flow rate and HRR estimations [44]. Temperature of the exhaust gases flowing through the duct were measured in this setup using three K-type Stainless Steel (SS) sheathed thermocouples with 0.02 cm sheathed probe diameter, located 5 cm, 10 cm and 14 cm from the duct wall, separated at 120^{o} angle from each, across the circumference of the duct. They are labeled as TC-5, TC-10 and TC-14 in Figure 2-8. The time constants of these thermocouples, to reach 63.2% of a step change is less than 1 second, as reported by the manufacturer. These thermocouples were cleaned regularly to remove any soot deposition during large-scale experiments. The

average temperature from these thermocouples, T_e, was used as temperature of the exhaust gases for all calorimetry calculations.

2.5.1.2. Exhaust Flow Rate

Veris Verabar averaging Pitot tube V100 connected to Setra 264 pressure transducer was used to measure differential pressure in the exhaust. The Verabar had a ±1% full-scale (FS) accuracy for 0 to 249 Pa differential pressure and a theoretical flow coefficient, C_f^e, of 0.753 as provided by the manufacturer. The high and low pressure outlets of the Verabar were connected to a Setra model 264 differential pressure transducer having a range of 5 to 249.088 Pa and ±1% FS accuracy to read the pressure differential. Combustion effluent was extracted through the hood was calculated using Eq. (2-4) which is derived from Bernoulli's equation.

$$V_e = \frac{C_f^e A_{duct}}{\rho_e} \sqrt{\frac{2\Delta P}{T_e}\left(\frac{P_a M_e}{R}\right)} \qquad (2\text{-}4)$$

In this equation, C_f^e is the calibration coefficient of the pitot tube, 0.753, which was provided by the manufacturer; A_{duct} is the area of cross section of the exhaust duct in m^2; ρ_e is the density of the exhaust gases in kg m^{-3}, ΔP is the pressure differential measured by the pitot tube in Pa; P_a is the environmental pressure in Pa; T_e is the mean temperature of the diagnostics section thermocouples in K; and R is the universal gas constant, 8.314 J mol^{-1} K^{-1} . M_{O_2} and M_e are the molecular masses of oxygen and exhaust flow gas mixture in kg mol^{-1}, respectively. M_e was approximated by the molecular mass of incoming air, considering its moisture content. Additional details of how different variables were estimated are given in Appendix A: Calorimetry.

The flowrate was varied and preliminary calorimetry was performed for propane burner set for 30 to 60 kW equivalent HRR and PMMA pool fire discussed in Appendix A.3. The exhaust flowrate of 0.56 m^3 s^{-1} provided the best compromise between well-ventilated environment and well-resolved oxygen concentration reduction associated with the studied combustion processes. Therefore, during the experiments, the exhaust flow rate was set as $V_e = 0.56\ m^3\ s^{-1}$.

2.5.1.3. Gas Sampling System

A gas sampling system was designed to ensure fast gas transport and a minimal delay in the gas concentration measurements. Schematic of the designed system is shown in Figure 2-9. Exhaust gases were sampled through a custom designed sampling system at the volumetric flowrate of 1×10^{-4} m^3 s^{-1}. A sampling probe was made of 0.953 cm inside diameter stainless steel tube. Sampling holes 0.2 cm in diameter and center-to-center separation of 1.27 cm were drilled along the length of the tube. This spacing and diameter of the holes were decided by calculating the ratio of pressure drop and velocity across the hole to the respective pressure drop and velocity across the entire sampling tube for the theoretical desired uniform flow velocity of sampling. The resulting ratio of pressure drops and velocities was greater than 10 and 1 respectively and the uniform sampling was verified during the setup of the system. Since most of the fully-developed flow was expected to be closer to the center, these holes covered 80 % of the central length of the tube, as shown in Figure 2-8.

A 3K series Boxer diaphragm pump with brushed motor was used to sample gases. The particulates in the exhaust gases were first removed using a Silica inorganic resin filter,

supplied by United Filtration capable of removing 99.5% of particles larger than 1×10^{-6} m. This particulate filter was replaced after about a set of three experiments which corresponded to the manufacturer recommended change in weight due to particulate matter accumulation. A 100 cm long copper tube section with 0.953 cm inner diameter used between the sampling tube and the pump ensured that the ambient atmosphere cools the sampling gas by natural convection to maintain suitable temperatures for downstream equipment.

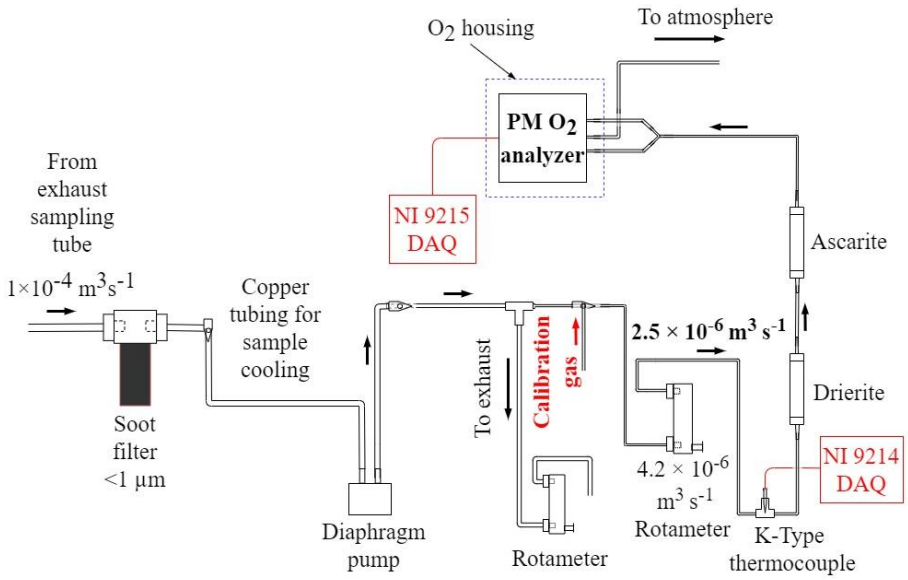

Figure 2-9 : Process flow diagram of exhaust gas sampling and analysis system

Out of the sampled gas, only 2.5×10^{-6} m^3 s^{-1}, controlled by the Aalborg rotameter equipped with a needle valve, was routed to the gas scrubbers. This fractional flowrate maintained sampling rate requirements of the oxygen sensor, ensured fast response to dynamic changes in the duct, and did not result in deactivation of Drierite and Ascarite during the studied combustion processes. A 10-20 mesh indicating Drierite (calcium sulphate impregnated with cobalt chloride) was used to scrub water vapor from the sample

gas. A 30 mesh Ascarite (Sodium Hydroxide coated Silica) was used to scrub carbon-dioxide. A K-Type thermocouple was used to monitor the temperature of the sampling gas entering the oxygen sensor for safety.

Oxygen measurement was done by using a paramagnetic (PM) sensor, PM1111E, supplied by Hummingbird Sensing Technology. The sensor was set-up in a fast response configuration and was highly repeatable with intrinsic error < 0.1 % O_2. The analog sensor response from 0 – 100 Vol. % O_2 corresponds to linear 0 – 1 V output when the outlet was vented to atmosphere. The response time of the sensor, corresponding to 10 – 90 % of a step change in oxygen concentration was reported by the manufacturer to be less than 300 ms. Calibration of the oxygen sensor was performed before each test using nitrogen (0% O_2) and dry air (20.95% O_2) cylinders as calibration gases. A three way valve in the sampling system, as shown in Figure 2-9, was installed to allow switching between exhaust gas sampling and calibration of the sensor using the calibration gases. Corrections were done for the delay of 10 s associated with the transport of gases through the sampling system. The response time of the gas sampling system, defined as time required by the sensor to reach 63% of the total step change, was determined to be 3 s.

2.5.2. Ambient Condition Measurements

Ambient pressure, temperature, relative humidity, and dew point were monitored using iBTHX-W sensor (manufactured by Omega Inc.). This sensor was connected locally using the Ethernet connection to obtain data, independent of the data acquisition system. The sensor, referred as PTH sensor hereafter, has the manufacturer reported accuracy to measure ambient pressure within ± 200 Pa for 1×10^3 to 1.1×10^5 Pa, ambient relative

humidity (RH) within ± 2 % for 10 to 90 % RH, and temperature within ± 0.5 K for 278 to 318 K. Ambient measurements were made at 2 second interval throughout the duration of a test.

2.5.3. Data Acquisition System (DAQ)

LabVIEW 2017, operated on Dell Inspiron 15-5000, was used to acquire all the analog signals from a CompactDAQ USB chassis, c-DAQ-9174. The chassis was plugged with NI 9215, a ± 10 V, 16 bit resolution input module for reading the differential pressure and oxygen sensor analog response. All thermocouples were connected to a 16 channel, 24 bit resolution NI 9214 temperature module with ± 0.1 K accuracy, setup to measure K-type thermocouple output. All heat flux gauges were connected to two 24 bit, 4 channel NI 9211 module having the capability to measure ± 80 mV. All the signals were obtained at 10 Hz frequency. All the data obtained is synchronized based on time to ignition of the propane burner flame, as described in detail along with the calorimetry derivation and validation experiments in Appendix A: Calorimetry.

2.6. Large-Scale Experimental Measurements

A 0.58 ± 0.02 cm thick cast black PMMA was rigidly mounted onto Marinite I calcium silicate board using twelve 0.32 cm diameter steel fasteners. The exposed surface area of each PMMA panel was 50×146 cm^2. All the measurements for the calorimetry were performed using the setup and diagnostics mentioned in Section 2.5. Additionally, focus of these experiments was to quantify flame-solid interaction, flame radiation emissions and flame structure during the flame spread process. Along with these, additional measurements were conducted for radiation heat flux from the PMMA spreading flame to

locations outside of the flame, the detailed results and experimental schematic are provided in Appendix B: Miscellaneous Plots.

2.6.1. Heat Flux Gauge Measurements

Eight water-cooled Schmidt-Boelter heat flux gauges with 9.53-mm-diameter gauge manufactured by Medtherm were installed flush with the exposed PMMA panel surface to measure the heat feedback from the flame. The cooling water temperature was maintained at 291 ± 7 K. The sensors were cleaned, repainted and recalibrated against a standard gauge traceable to NIST reference before every experiment. The calibration heat flux ranged from 15 kW m^{-2} to 55 kW m^{-2} and thus covered the spectrum of potential heat fluxes to be observed in the experiments.

The gauge locations were defined by the distance from the corner (x) and the distance from the top edge of the burner (y), as shown in Figure 2-10. These locations were selected based on the observations of the evolution of flame in preliminary experiments.

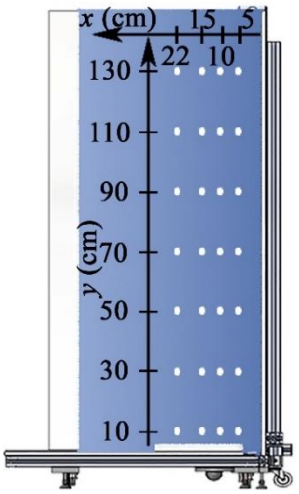

Figure 2-10. Complete set of 28 locations of heat flux gauges (white circles) used in flame spread experiments with PMMA panel

The gauges were moved to different locations in different experiments so that at least two temporal heat flux profiles were obtained for each of the 28 selected locations. Some gauges were positioned at the same location on the opposite panels in preliminary tests to verify that the heat feedback was symmetric.

2.6.2. Flame Spread Imaging

A Nikon D800 DSLR camera was placed 150 cm away and focused on one of the PMMA panels, as shown in Figure 2-7, to record a video of the spreading flame at 30 frames per second (fps). The sensor of the camera was modified to extend the spectral sensitivity to the near-infrared by removing the antialiasing and IR cut-off filters. The camera was then mounted with a 900 nm (±10 nm) band pass filter during the experiments. This particular wavelength was selected because it provided imaging of the radiation from a single but highly important flame species: soot; the emissions from other flame species and hot PMMA surface were negligible at this wavelength [172]. Using monochromatic imaging also helped ensure that the presented results don't depend on a particular sensor technology or camera settings. As long as the sensor's response is linear, as it was in the current study the same relative intensities would be measured regardless of the equipment used [173]. The camera was set at ISO 320, F-9 aperture and exposure time of 5 ms to provide well-resolved images, while avoiding saturation. The camera was spatially calibrated using a lined grid attached onto the PMMA surface before each experiment.

2.7. Large-Scale Experimental Results

All corner spread experiments began with propane ignition followed by the ignition of PMMA, which was accompanied by a crackling noise. Visual observation and the

audible sound of PMMA ignition assisted in verifying the time to ignition derived from a quantitative criterion using HRR profile. PMMA was noted to ignite around 45 ± 3 s after the propane burner ignition. The images captured by the DSLR tracked the flame progression over the entire test duration. Snapshots of raw unprocessed images are shown every 20 s in Figure 2-11 from 10 s to 190 s. The reference of length-scale shown in the figure shows the extents of the panel height and width that were used for post-processing of the images. Here, t = 0 s corresponds to the burner ignition.

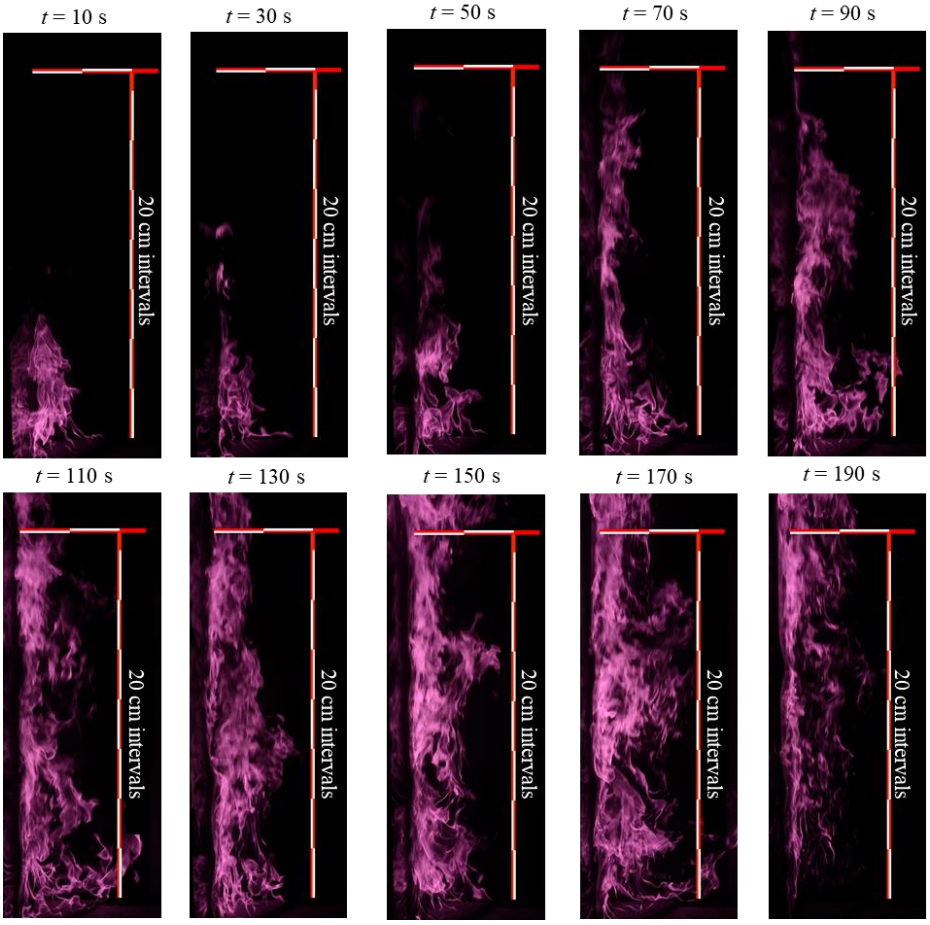

Figure 2-11. Raw unprocessed images showing flame spread captured by the modified DSLR camera with 900 nm IR filter

2.7.1. Heat Release Rate

The calculation of heat release rate was based on oxygen consumption calorimetry, similar to the approach used in the cone calorimetry standard [4]. However, additional care was taken to correct for changes in the oxygen concentration associated with the removal of water and CO_2 from the oxygen sensor flow. Both environmental moisture, and H_2O and CO_2 generated in combustion were taken into account. These corrections for the calorimetry were theoretically derived for a control volume of the hood by assuming mass flow rate of the inlet air, which constitutes only nitrogen, oxygen and water vapor, is unaffected by the combustion process. Detailed derivation of the equations and validation of the calorimetry expressions are provided in Appendix A: Calorimetry.

The total amount of combustion products, γ, represented as the molar ratio of CO_2 and H_2O produced per O_2 consumed, was calculated for a gaseous pyrolyzate with known molecular formula, assuming complete combustion. In the case of the current experiments where the main fuel was PMMA which is known to degrade into its monomer ($C_5H_8O_2$); therefore, $\gamma = 1.5$ was used. Oxygen mole fraction in the exhaust flow at a time *t*, $X_{O_2}^t$, was calculated from the mole fraction measured by the sensor, $X_{O_2}^m$, using Eq. (2-5)

$$X_{O_2}^t = \frac{X_{O_2}^m}{1 + \gamma\left(\frac{X_{O_2}^{m,0}}{\left(1 - X_{O_2}^{m,0}\right) + X_{O_2}^m} - X_{O_2}^m\right) + r_{H_2O}^0 X_{O_2}^m} \qquad (2\text{-}5)$$

where $X_{O_2}^{m,0}$ is the measured oxygen mole fraction baseline and $r_{H_2O}^0$ **is** the baseline for the moisture content of the inlet air flow expressed as the molar ratio of H_2O and O_2. Data collected before and after each experiment were used for determining a linear baseline to

account for drifts in the ambient conditions and the calibrated sensors. Ambient water vapor mole fraction, $X_{H_2O}^0$, and $r_{H_2O}^0$ were computed by Eq. (2-6) and (2-7) to correct for the drift in ambient conditions.

$$X_{H_2O}^0 = \frac{(RH^0)/100 \times P_{H_2O}^v}{P_a} \quad (2\text{-}6)$$

$$r_{H_2O}^0 = \left(\frac{1}{X_{H_2O}^0} - 1\right)^{-1} \frac{1}{X_{O_2}^{m,0}} \quad (2\text{-}7)$$

where, P_a is the ambient pressure, and RH^0 is the relative humidity. The saturation pressure of water vapor, $P_{H_2O}^v$, is calculated using Tetens equation which estimates the vapor pressure within 1% of values reported in NIST Webbook [174].

The heat release rate, HRR was computed using Eq. (2-8) by incorporating Eq. (2-5) through (2-7).

$$\text{HRR} = EC_f^e A_{duct} \left(\frac{2\Delta P}{T_e}\left(\frac{P_a M_e}{R}\right)\right)^{0.5} \frac{M_{O_2}}{M_e}\left(X_{O_2}^0 - X_{O_2}^t\right) \quad (2\text{-}8)$$

where E is the empirical constant, 13.1 × 10^3 kJ per kg of oxygen consumed [34]. M_{O_2} and M_e are the molecular masses of oxygen and exhaust flow gas mixture in kg mol^{-1}, respectively. M_e was approximated by the molecular mass of incoming air, considering its moisture content. Rest of the variables are the same as used in Eq. (2-4).

Aside from the manufacturer-supplied calibration of the Pitot tube, the HRR calculation did not include any adjustable parameters and was validated by measuring the heat release of a pool fire fueled by a 50×50 cm^2 plate of PMMA. The heat of combustion of PMMA determined by integrating the HRR and dividing the integral by the combusted

mass was determined to be 24.1 kJ g^{-1}, which is within uncertainties of typical literature values [175]. The response time of the calorimeter was subsequently evaluated by introducing step changes in the propane burner flow and monitoring the calculated HRR signal. The response time, defined as time taken for the signal to reach 63% of total step change corresponding to the propane burner flow, was found to be 13 ± 2 s. The response time included primarily 10 s mixing and gas transport delay inside the enclosure.

The results of the HRR measurements obtained for the corner-wall flame spread experiments, which include propane burner contribution, are summarized in Figure 2-12. Here, t = 0 s corresponds to the burner ignition and the data is shown for the experiment duration, t_e = 185 s. The HRR is shown until the burner was turned off. The HRR data were post-processed by taking a 1 s moving average and further averaging them between six experiments. The error bars represent uncertainties calculated from the scatter of the data as two standard deviations of the mean of seven tests (T1 through T7). The average uncertainty in the HRR was about 10%.

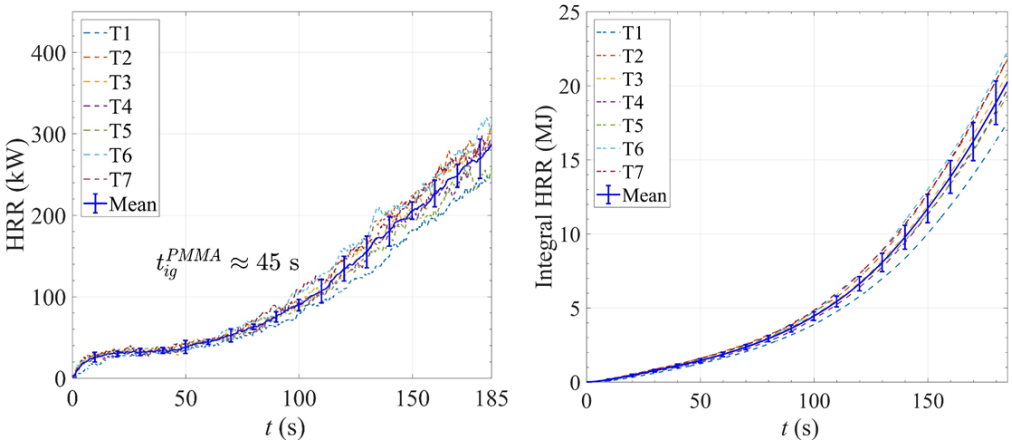

Figure 2-12. Instantaneous and integral HRR for all tests (T1 through T7 and mean) measured in the corner-wall flame spread experiments performed on PMMA

The HRR profile shows an asymptotic rise immediately after the burner ignition which corresponds to the development of the burner flame. The burner flame heat release reaches a steady state, 31 ± 3 kW, approximately 15 s after its ignition. The PMMA panels ignite 45 ± 3 s after the burner ignition. This ignition time $\left(t_{ig}^{PMMA}\right)$ was identified from the inflection of the HRR curve, defined as the time when the total HRR increases 20% above the steady propane burner contribution. This time was further confirmed through visual observations of flame growth and time corresponding to the onset of crackling noise heard when PMMA begins to decompose during the experiments. The inflection point is followed by an exponential rise in the HRR corresponding to flame spreading on the PMMA panels. Once the flames reach the top of the panels, the HRR tends to increase somewhat linearly to the maximum of about 280 kW at t = 185 s. It is important to point out that all current experiments were terminated before any portion of the PMMA panels was completely consumed or detached from the backing material.

2.7.2. Flame Heat Flux

Two datasets of flame heat flux available at each location were first averaged and synchronized from the time of propane ignition. The heat flux data were then post-processed by binning them in 10 s intervals. This interval of temporal bins was selected to simplify data analysis. Average error was calculated for each of the 10 s bins as two standard deviations of the mean plus 3% systematic error of the calibration. The average uncertainty was determined to be about 10%.

The results of flame heat flux, $\dot{q}''$, measurements are summarized in Figure 2-13 in the form of contour plots provided for ten points in time selected to illustrate the

progression of the corner-wall flame spread process. The heat flux data from 28 locations were linearly interpolated to a uniform 0.5 cm grid for the locations encompassing the extents of gauge locations on the wall. This flame heat flux includes the radiation contribution from the other burning PMMA surface. Surface radiative losses that reach the adjacent panel were estimated as black body radiation from a burning PMMA surface at 640 K (peak MLR temperature observed in TGA tests, see Section 2.2) and assuming 50% of the radiation reaches the cold gauge surface on the adjacent panel. The surface radiative losses were estimated to be less than 10% of the maximum observed $\dot{q}''$. A more detailed estimation of surface radiative losses is provided in Chapter 3:.

Contour plot at t = 15 s represents the heat flux distribution shortly after the propane burner ignition; t = 45 s contour plot represents the time of ignition of PMMA. At subsequent times, the data reflect upward and much slower lateral (away from the corner) flame spread on the PMMA surface. The maximum heat flux observed is about 65 kW m^{-2} after about t = 120 s at x = 10 cm, y = 70 cm. The values of the heat fluxes measured at t = 15 s at the following (x, y) locations (specified in cm): (8, 16), (8, 75) and (20, 30) are compared in Table 2-3 with available literature data for the burner set at the 30 kW HRR in an SBI setup. The values obtained in the current work are essentially within the range of flame heat fluxes reported in the most recent publication [115].

Table 2-3. Comparison of heat flux data (in kW m^{-2}) for steady propane burner from this study and literature data.

Sensor location (x, y)	Interpolated value from this study	Zeinali et al. [115]	Zhang et al. [176]	EGOLF [177]
(8, 16)	40 ± 4	44-55	25-30	55
(8, 75)	20 ± 3	16-23	20-25	21
(20, 30)	11 ± 2	14-18	10-15	14

The data also show a persistent reduction in the value of the heat flux at about 50 cm above the burner. This height approximately corresponds to the length of the burner flame and this reduction is speculated to be associated with air entrainment promoted by the burner flame that narrows the flame in this region and cools the solid surface.

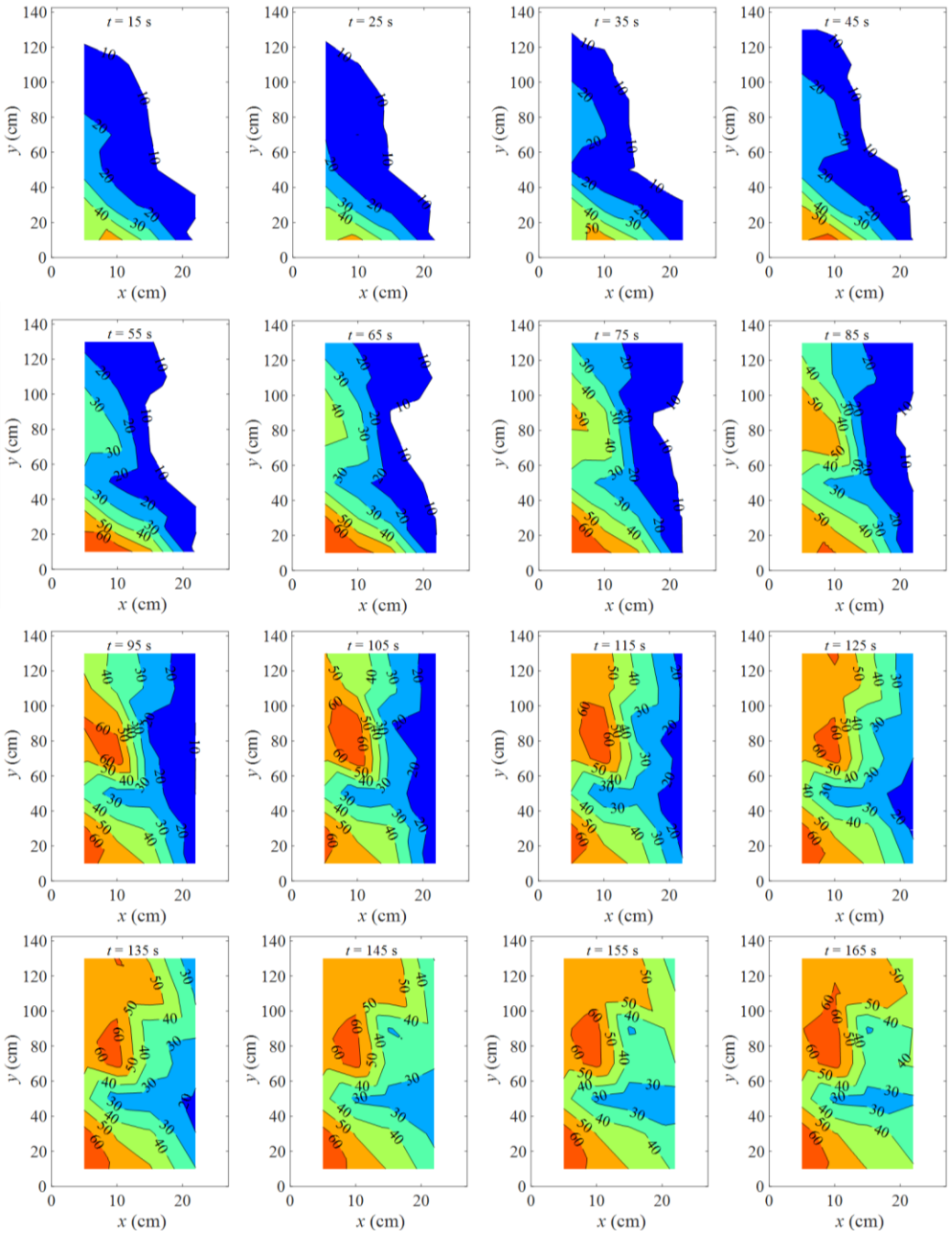

Figure 2-13. Interpolated mean heat flux to water-cooled heat flux gauges positioned flush with a PMMA panel surface during key phases of flame spread on the corner wall

For buoyancy-driven flames, the wall flame heat flux profiles have been observed to be a function of heat release rate [62]. For the current experiments, the relationships

between $\dot{q}''$ at different locations and HRR are summarized in Figure 2-14. To generate these relationships, the HRR data were binned in 10 s intervals similar to heat flux data. At most locations, the relationship is a nearly linear rise with increasing HRR followed by a plateau, which is indicative of the flame reaching a given position on the surface. A notable exception is the measurements collected at the greatest distance from the corner (x = 22 cm), where the plateau is never reached because the flame does not fully spread this far in the lateral direction.

Figure 2-14 also shows empirical fits of the experimental data. The following expression, Eq. (2-9),

$$\dot{q}'' = \frac{e \; - \; a \cdot \exp(-b \cdot \mathrm{HRR}) \; - \; c \cdot \exp(-d \cdot \mathrm{HRR})}{f \; + \; a \cdot \exp(-b \cdot \mathrm{HRR}) \; + \; c \cdot \exp(-d \cdot \mathrm{HRR})} \qquad (2\text{-}9)$$

was found to produce fits that captured the experimental data with sufficient accuracy (the coefficient of determination greater than 0.97). The expression parameters, *a*, *b*, *c*, *d*, *e* and *f*, are given in Figure 2-14. Parameters *b* and *d* are in kW^{-1}; the rest are in kW m^{-2}.

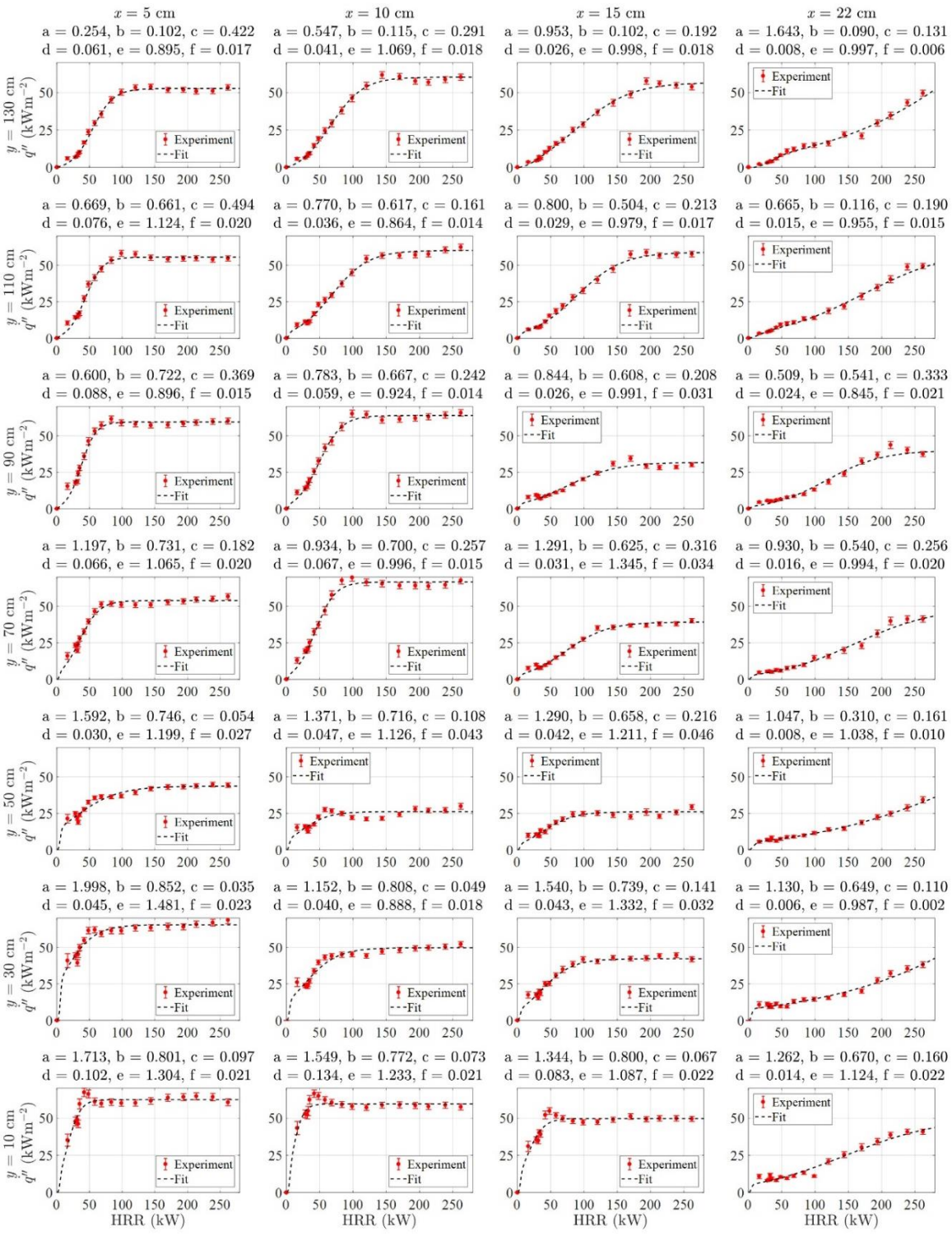

Figure 2-14. Mean heat fluxes to water-cooled heat flux gauges presented as a function of the total measured heat release rate (including propane flame contribution)

2.7.3. Image Analysis

The analysis of the video recorded through a 900 nm narrow band filter was carried out as follows. First, the RGB images representing individual frames were converted to grayscale using an unweighted mean of the three channels. This grayscale signal was determined to be proportional to the incident radiation intensity in earlier experiments involving imaging of a black body furnace [173]. Second, the grayscale images were binned in 10 s intervals (300 frames per bin) and averaged (the same manner as the HRR and $\dot{q}''$ data). Third, the pixel positions were converted to physical positions using the same coordinate system as was used for the heat flux gauge measurements (shown in Figure 2-13). This conversion required interpolation between the pixel data, which physical positions differed slightly due to slight differences in the camera location from experiment to experiment. The spatial calibration factor (pixels/cm) varied between 9.2 to 12 pixels cm^{-1} from experiment to experiment. The interpolation was accomplished by mapping all data onto a uniform 0.5 cm grid through averaging together individual intensities of pixels located within 0.25 cm radius of each grid point. Thus, the final dataset from each experiment had a spatial resolution of 0.5 cm. Finally, the data from individual experiments were averaged together.

The mean intensities normalized by the absolute maximum value of intensity found across all binned time intervals and experiments are presented in Figure 2-15. As in the case of the flame heat flux, these data are provided in the form of contour plots at fifteen key points in time, which illustrate the progression of the corner-wall flame spread process. The uncertainties in the intensity data were calculated from the scatter of individual data points as two standard deviations of the mean and were found to be less than 1% of the

maximum intensity. These intensities can be calculated, using Eq. (2-10), from the results of CFD simulations by integrating monochromatic radiative intensity, $I_{900\,nm}$, along the line, s, connecting a given point (x, y) on the PMMA panel surface to the center of the camera lens [172]:

$$I^{\mathrm{cam}}_{900\,nm}(x,y) \propto \int_s \left(k^{\mathrm{soot}}_{900\,nm}(s) I^{\mathrm{b}}_{900\,nm}(T) - k^{\mathrm{soot}}_{900\,nm} I_{900\,nm}(s) \right) ds \qquad (2\text{-}10)$$

In Eq. (2-10), $I^{\mathrm{cam}}_{900\,nm}$ represents the value of intensity measured by the camera; $I^{\mathrm{b}}_{900\,nm}$ is the black body intensity at the local temperature, T; and $k^{\mathrm{soot}}_{900\,nm}$ is the extinction coefficient that includes effects of absorption and scattering by soot and is related to the soot volume fraction. The line s is defined in the Cartesian coordinates as follows,

$$(x_s, y_s, z_s) = (x, y, 0) + \frac{s}{\sqrt{(12-x)^2 + (70-y)^2 + 150^2}} \times (12 - x, 70 - y, 150) \qquad (2\text{-}11)$$

where z_s corresponds to the coordinate that is perpendicular to the surface of the PMMA panel with the panel surface located at z_s=0. Eq. (2-11) is expressed in the units of cm and is obtained using a known position of the center of the camera lens, $(12,70,150)$.

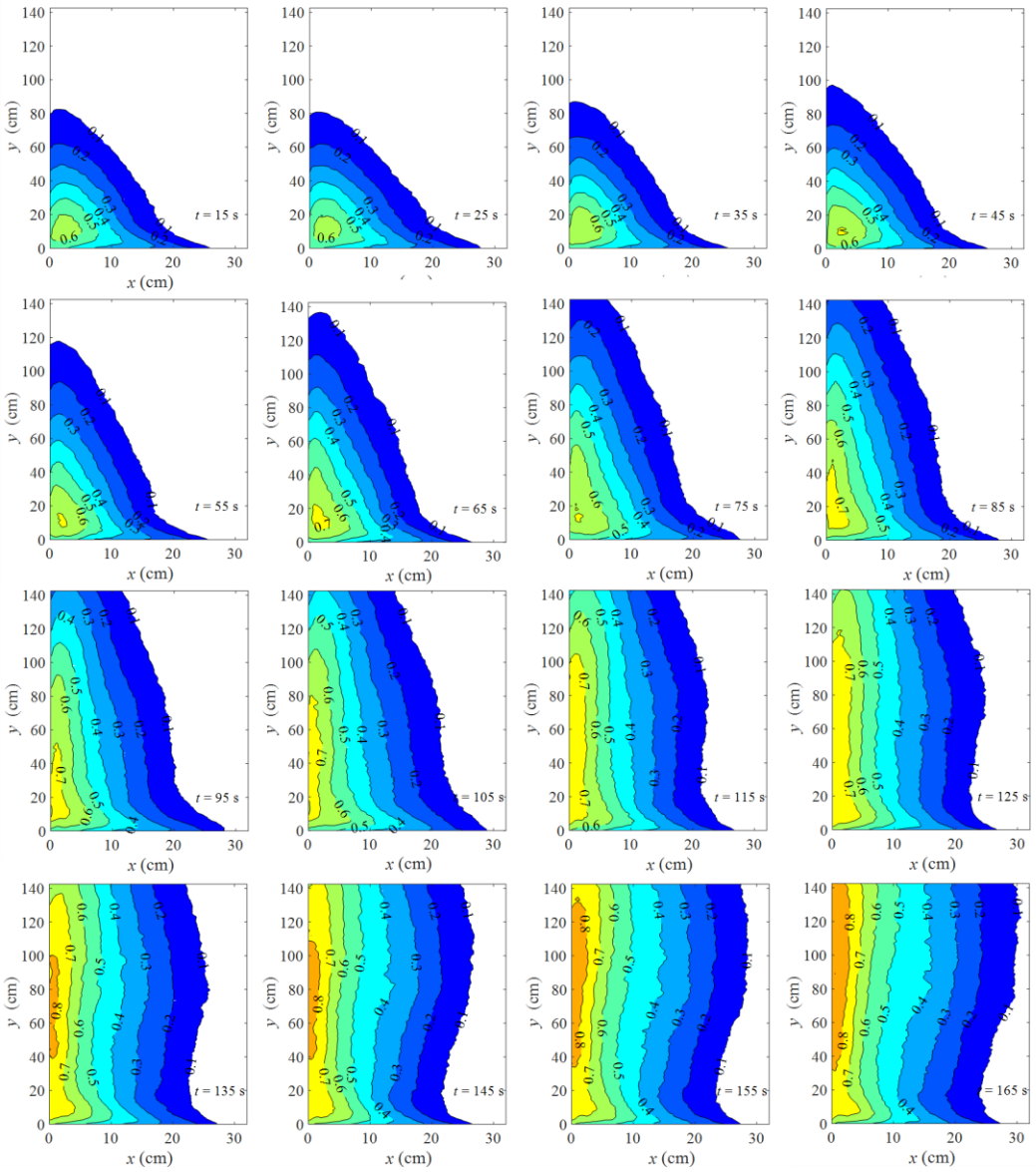

Figure 2-15. Relative intensities of 900 nm flame emissions projected onto a PMMA panel surface during key phases of flame spread on the corner wall

The radiation intensity contours grow in length and width with time similar to the flame heat flux contours shown in Figure 2-13. Assuming that the majority of the heat feedback to the PMMA panels is radiative in nature, which is a reasonable assumption for the flames of this size [66], and the majority of this radiation is emitted by soot, there

should be a discernable correlation between the flame heat flux and the projected radiation intensity. The presence of such a correlation was examined by plotting the radiation intensity data, which were spatially averaged around the gauge locations over 1.5 gauge diameter (1.43 cm) circles, against the corresponding total flame heat flux data. Figure 2-16 shows this data plotted for different *y* locations for all time intervals. At each *y* location, heat flux data at all *x* locations are included. All the data except for the data below 1% radiation intensity, which have negligible contribution to radiation, was fitted with a least-squares linear fit. The excluded data are shown in black on the figure. All linear fits were found to have a coefficient of determination above 0.7. An extrapolation of these lines to zero relative intensity provides a rough estimate of the convective contribution to the flame heat flux, which was 12 ± 4 kW m^{-2}, on average.

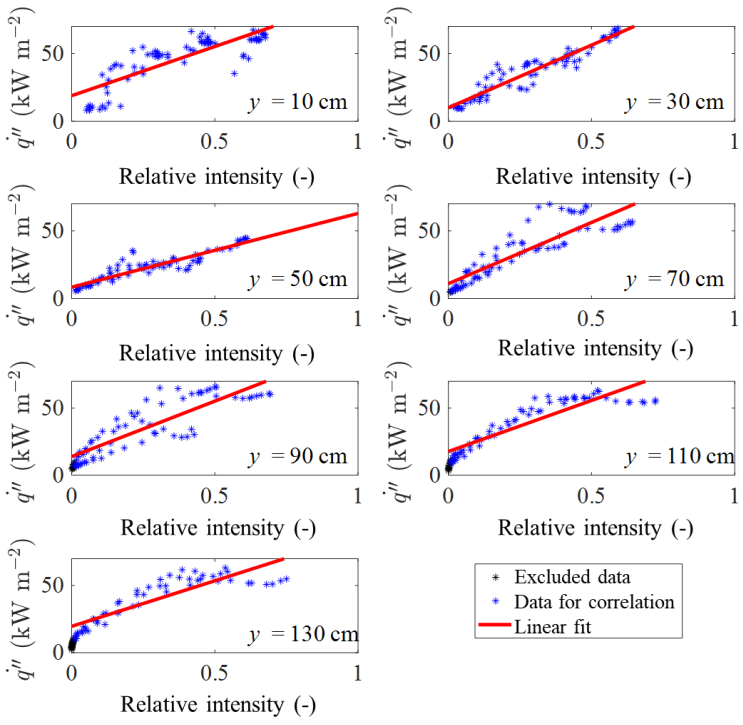

Figure 2-16. Average radiation intensity and heat flux correlation

The recorded video was further employed to characterize the overall shape of the spreading flame. This characterization was accomplished by defining a threshold greyscale intensity of 39 s^{-1} (50/(255×0.005 s)), which is normalized by the exposure time (5 ms), indicative of the presence of a flame in a certain location (x, y). The resulting binary images were subsequently binned in 10 s intervals and averaged to obtain flame probability contours shown in Figure 2-17. The isocontour corresponding to the probability of 0.5 is frequently used to define the shape of the flame [178] and is highlighted on the figure. This isocontour shows an apparent narrowing of the flame 10 to 50 cm above the edge of the burner at late stages of fire growth. As in the case of the flame heat flux data, this narrowing can be explained by intense lateral air entrainment in this region. The flame height of the steady propane burner is about 42 cm, which is lower than flame height of 87 cm reported for the same burner setting in a similar setup [115]. The reason for this discrepancy is unclear. The differences in the imaging techniques (monochromatic in this work versus filtered visible in [115]) and image post-processing may be partially responsible. The use of the narrower corner panels in the current work, which enhances air entrainment, may also explain the reduced flame height. The flame height is found to be slightly sensitive to the greyscale threshold – a 10% decrease in flame height corresponded to an increase in the greyscale threshold from 35 s^{-1} to 43 s^{-1}. A series of plots with the flame shape iso-contour (probability of 0.5) overlaid on the total flame heat flux contours are shown in Appendix B.

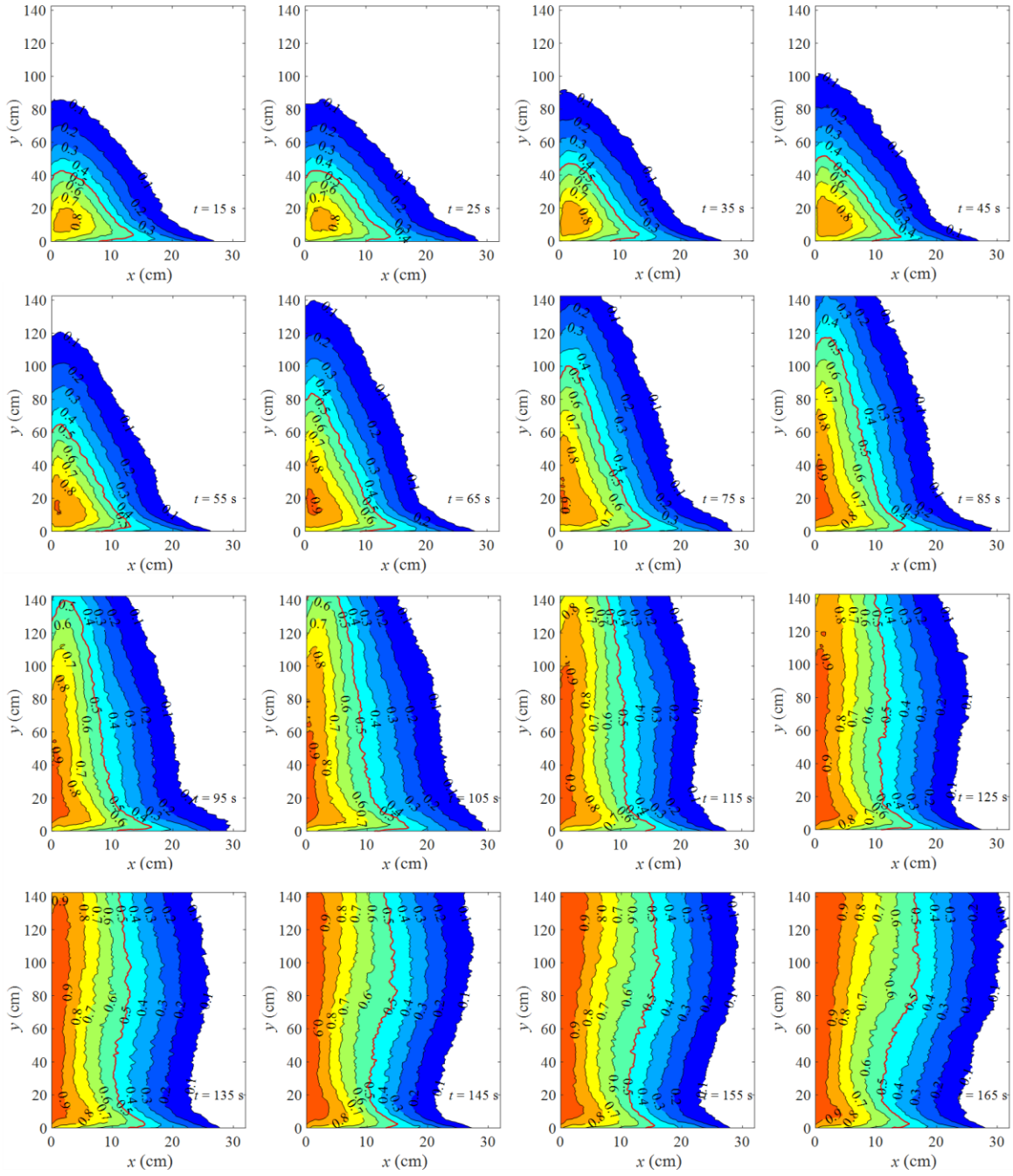

Figure 2-17. Flame presence probability maps obtained for key phases of flame spread on the corner wall (Solid red contour line correspond to probability of 0.5)

2.8. Flame Spread Modeling Framework

The availability of detailed flame heat feedback measurements and PMMA pyrolysis properties enabled detailed inputs of heating boundary conditions to numerical simulations of fire growth on the corner wall. In these simulations, each PMMA panel was divided into 28 areal elements, as shown in Figure 2-18. Each element contained a heat flux gauge at or close to its geometric center permitting the gauge measurements to be used to define thermal boundary conditions at the front surface of this element. The positions of the grid lines separating the elements were selected to maximize the accuracy with which each gauge represented the corresponding element.

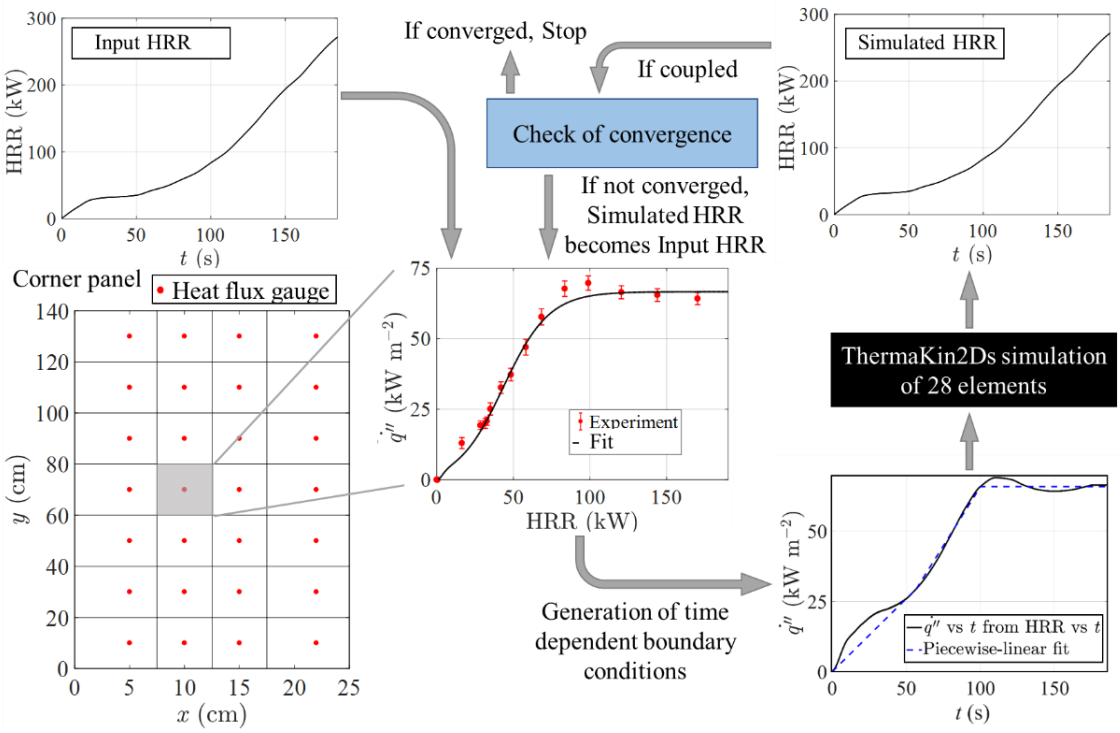

Figure 2-18. Overall workflow for the corner wall fire simulations

As illustrated in Figure 2-18, the simulations were carried out in either uncoupled or coupled mode. In the uncoupled mode, the mean HRR profile measured in the experiments was used as an input HRR to calculate the flame heat flux dependencies on time for each element using the fits shown in Figure 2-14. These time dependencies were subsequently fitted with a three-segment piecewise-linear expression, which facilitated implementation of these boundary conditions in a pyrolysis model. This heat feedback was represented either as convective or radiative. Details of this representation are discussed in the next section (Section 2.9). ThermaKin2Ds solver was used in a one-dimensional mode to model transient pyrolysis of PMMA and heat transfer through the Marinite I calcium silicate board (to which the PMMA panels were attached). 28 instances of this simulation were run, one for each element. The individual contributions of the elements were added to the heat release rate of the burner, HRR_b, to obtain the total simulated HRR:

$$\text{Simulated HRR} = HRR_b + 2\sum_{j=1}^{28} \dot{\dot{m}}_j'' A_j \Delta H_c \qquad (2\text{-}12)$$

In Eq. (2-12), $\dot{\dot{m}}_j''$ are the mass fluxes of gaseous PMMA pyrolyzate from individual panel elements; A_j are the surface areas of these elements and $\Delta H_c = 24.1$ kJ g^{-1} is the heat of combustion of the pyrolyzate measured during the validation of calorimetry for the large-scale setup. The burner heat release rate was represented by a piecewise-linear function including a linear rise during the first 10 s and a plateau of 30 kW after.

The purpose of the uncoupled simulations was to determine whether all key physical processes responsible for the flame spread are correctly accounted for in the presented model, which was accomplished through a comparison of the input (mean experimental) HRR with the resulting simulated HRR. The coupled simulations were

performed to examine predictive capabilities and limitations of the current model. In these simulations, the first input HRR profile was a guess taken as twice the heat release rate of the burner. A simulated HRR profile was subsequently generated using the same process as was used in the uncoupled simulations. A comparison between the resulting simulated and input HRR was carried out utilizing the following criterion:

$$\mathrm{CR} = \frac{1}{t_e}\int_0^{t_e} |\text{Input HRR} - \text{Simulated HRR}|dt \qquad (2\text{-}13)$$

If CR was found to be less than 5 kW for any t between 1 s after the burner ignition and the end of the simulation time, the simulated HRR profile was accepted as the final result. If CR did not satisfy this requirement, the simulated HRR was used as an input HRR for the next iteration. In the coupled simulations performed in this study, 4 to 6 iterations were required to obtain the final, converged HRR. The performance of these iterations was facilitated by development of a MATLAB script that was used to generate boundary condition parameters and post-process the results of individual ThermaKin2Ds simulations. Thermakin2Ds simulations were performed with a time step of $\Delta t = 1\times10^{-2}$ s and 5×10^{-5} m spatial discretization. Increasing or reducing the integration parameters by a factor of 2 did not produce significant changes in the simulations results. Each iteration required about 40 min on a single core of a modern PC.

For each simulation, quantitative comparison with experimental data was performed by calculating two parameters, average HRR error (HRR_{error}) and the Fire Growth Rate index (FIGRA). FIGRA is a measure of maximum rate of increase of HRR used to classify materials in an SBI test [7]. Although classification of flammable materials also requires quantification of smoke density, parameterized as Smoke Growth Rate index

(SMOGRA), the objective here was not to classify the material but to facilitate quantitative comparison of simulations. FIGRA was calculated according to Eq. (2-14), for HRR excluding the burner HRR contribution for the duration after the PMMA ignition (45 s). Eq. (2-15) was used to calculate average HRR error.

$$\text{FIGRA} = \max\left[\frac{\text{Simulated HRR} - HRR_b}{t}\right] \text{ for } t_{ig}^{PMMA} < t < t_e \qquad (2\text{-}14)$$

$$HRR_{error} = \frac{1}{t_e}\int_{t=0}^{t_e} \frac{(\text{Simulated HRR} - \text{Experimental HRR})}{\text{Experimental } HRR}\, dt \qquad (2\text{-}15)$$

2.9. Flame Spread Modeling Results

The flame heat flux time dependencies generated from the mean experimental *HRR* profile and fitted with three linear segments are shown in Figure 2-14. These segments were optimized to have least average error between the time dependent flame heat flux profile and the piecewise-linear fit. First, an intermediate point (end of Segment 1) was determined by assuming a final heat flux plateau as the maximum heat flux observed for each location at a location specific time. Then two linear segments were fit between the zero heat flux and the maximum heat flux with a variable intermediate point on the time dependent curve between these two end points. The final optimized intermediate point provided least average error between the fit and the time-dependent curve (Segment 1 and 2). The point corresponding to the plateau flame heat flux (end of segment 2) was determined by similar optimization procedure. In this case, two segments were fit between the optimized intermediate point and a plateau heat flux value at t = 185 s. The plateau point (an intermediate point for last two segments) was optimized within ±15% of the maximum heat flux point observed on the time dependent heat flux profile. The final

optimized plateau point provided least error between the time-dependent profile and all segments of the piecewise linear fit. Since these heat flux profiles represent the total (convective and radiative) heat flux to a water-cooled gauge, certain assumptions had to be made to convert these profiles to thermal boundary conditions to be used in the pyrolysis modeling. First, two limiting cases were considered:

In the first case, this heat flux was assumed to be purely radiative in nature. The piecewise-linear $\dot{q}''$, plus a small contribution from the background radiation (defined by the temperature of the cooling water circulating through the gauge, 291 K) was set to be incident onto the PMMA surface. The reflection of a small portion of this radiation and thermal radiative losses from the PMMA panels were accounted for by the model [129,132,148].

In the second case, the total flame heat flux was represented using a standard convection expression: $h(T_{flame} - T_{surf})$. The value of h was assumed to be a constant. It was computed to be 53.8 W m^{-2} K^{-1} from the maximum heat flux gauge reading obtained in this study, 65 kW m^{-2}, and the maximum temperature of a buoyant turbulent flame fueled by PMMA reported in the literature [179,180], T_{flame} = 1500 K. T_{surf} was defined in this calculation as the cooling water temperature. Using these values, the piecewise-linear $\dot{q}''$ (shown in Figure 2-19) was converted to a piecewise-linear T_{flame}, which was implemented in the pyrolysis simulations. During the simulations, T_{surf} was the temperature of PMMA surface. The model also accounted for the background radiation and thermal radiative losses from PMMA.

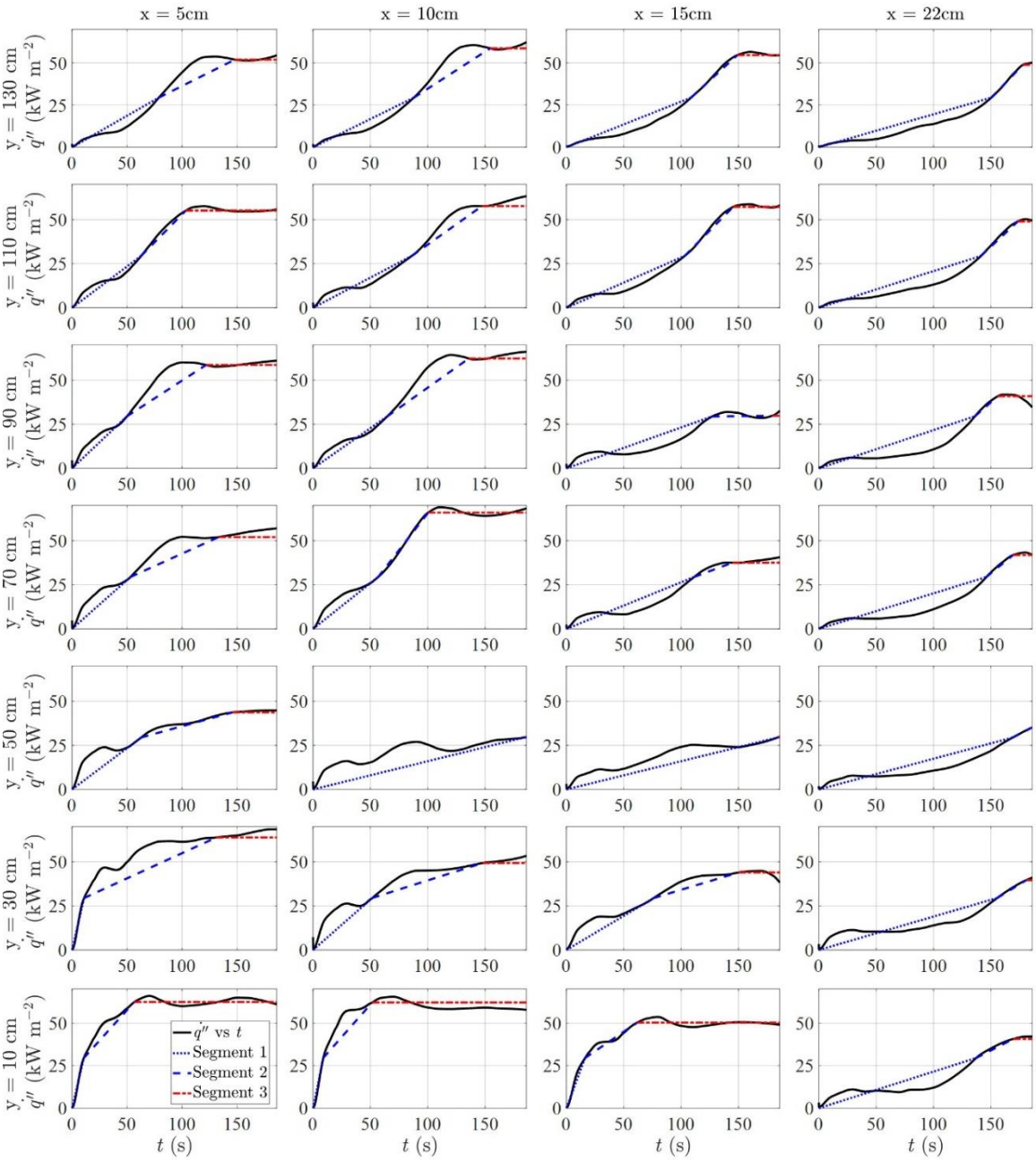

Figure 2-19. Total flame heat flux time dependencies generated using the mean experimental HRR and fitted with a piecewise-linear function

The results of these uncoupled simulations are compared with the mean experimental HRR in Figure 2-20. Two important conclusions can be made from this comparison. First, the modeled HRR profiles effectively bracket the experimental curve,

which means that the pyrolysis parameter set is generally consistent with the results of the current flame spread measurements. Second, representing the total heat flux as either convective or radiative has a substantial impact on the simulation results. For the early stages of fire growth, it is the convection expression that delivers an accurate prediction. For the late stages, the assumption that the flame heat flux is purely radiative produces a better agreement with experiments.

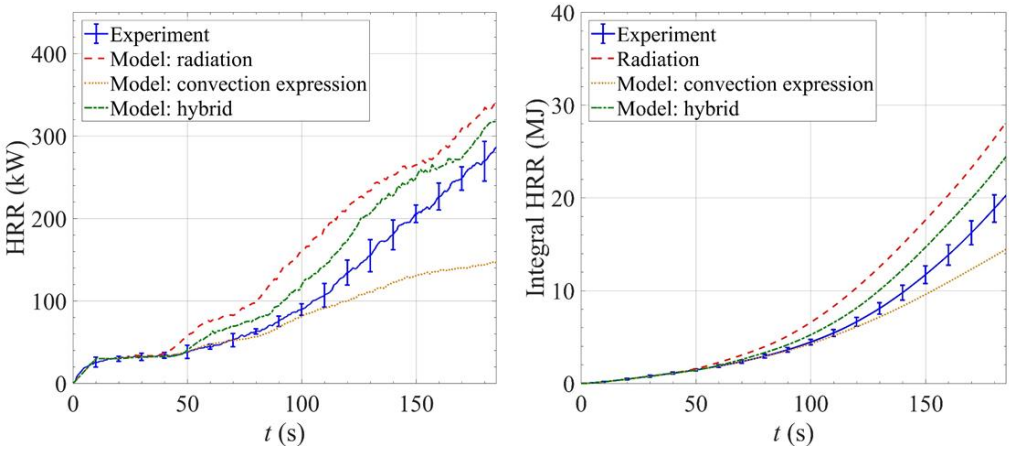

Figure 2-20. A comparison of the mean instantaneous and integral experimental HRR with results obtained from the uncoupled simulations

A natural extension of this exercise is to formulate a hybrid flame heat flux model. In this model, the first linear segment of $\dot{q}''$ (Segment 1 in Figure 2-19) was represented using the convection expression. Given an estimate of convective contribution reported in Section 2.7.3 (12 ± 4 kW m^{-2}), this segment, where $\dot{q}''$ is always below 30 kW m^{-2} (2.5 times convective contribution estimate), is expected to be dominated by convection. Segment 3 (the final plateau) was defined as radiative. Segment 2 was defined as a transition region, where the heat flux calculated using the convection expression was

linearly ramped down to zero, while the radiative flux was linearly ramped up from zero to the plateau value.

The results of the hybrid simulations are also shown in Figure 2-20. They do demonstrate a notably better overall agreement with experiments than either of the limiting cases. However, these results are still outside of the experimental uncertainties. It is clearly possible that this discrepancy is a consequence of a crude nature of the flame heat feedback model. The average HRR_{error} values and computed FIGRA values are reported in Table 2-4 for all the simulations on black PMMA. Predicted HRR for the uncoupled hybrid simulations agreed well within 17% of the experimental data. This was a significant improvement from 40 % overestimation for uncoupled simulation modeled with purely radiative heat flux model and 18 % underestimation for uncoupled simulation modeled with convection expression for heat flux.

It is also conceivable that the discrepancy in predictions is associated with uncertainties in the PMMA pyrolysis properties. During the analysis of PMMA pyrolysis performed in an earlier study [146], the heat capacity, C_p, of condensed-phase components was identified as the property whose variation had the most notable impact on the rate of pyrolyzate generation. This property value carries an uncertainty of about 10%. Increasing this heat capacity by 10% does not compromise the quality of the agreement between the model predictions and TGA-DSC and CAPA II experimental data, which were used in the model parameterization process. Time to mass loss was observed to be slightly affected at lower heat flux of 25 kW m^{-2} for CAPA II experiments, as seen in Figure 2-21.

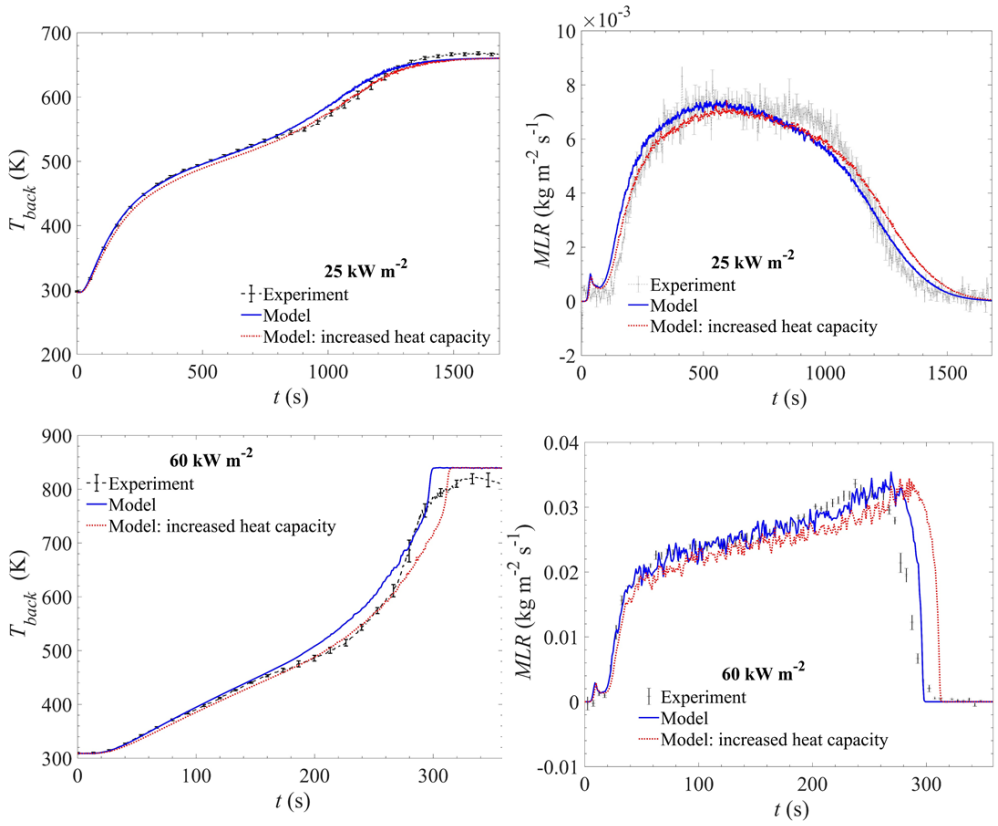

Figure 2-21. Comparison of CAPA II experimental results and CAPA II simulation results with original and increased heat capacity pyrolysis model

For the uncoupled simulation of large-scale fire, the delay in time to ignition resulting from the increase in heat capacity does produce a discernable improvement in the HRR prediction, as demonstrated in Figure 2-22. The average HRR_{error} reduced to 10% for uncoupled simulations with increased heat capacity. The sensitivity of the uncoupled simulations to other pyrolysis properties was also explored by systematically changing one parameter at a time in the pyrolysis model. Uncoupled simulations were conducted, in addition to the presented simulation with increased heat capacity, one at a time for each case – a) thermal conductivity increased by 10% (its uncertainty [166]), b) absorption coefficient increased by 30 % (its uncertainty [164,166]), c) Arrhenius reaction parameters

of the main decomposition curve changed to those of clear extruded PMMA (A_r = 1.5 × 10^{14} s^{-1}, E_r = 2.03 × 10^5 J mol^{-1}) [146], and d) emissivity increase to 0.98 (0.5-3% uncertainty [164]). Another uncoupled simulation was also performed with original pyrolysis parameters to understand the impact of the uncertainty of the heat flux measurements on the model predictions. This was done by decreasing the entire time-dependent heat flux profile by 10%, which corresponds to its average uncertainty (see Section 2.7.2). The uncoupled simulation with the heat flux decreased by 10% predict the HRR within the error bars of the experimental data, as also illustrated in Figure 2-22.

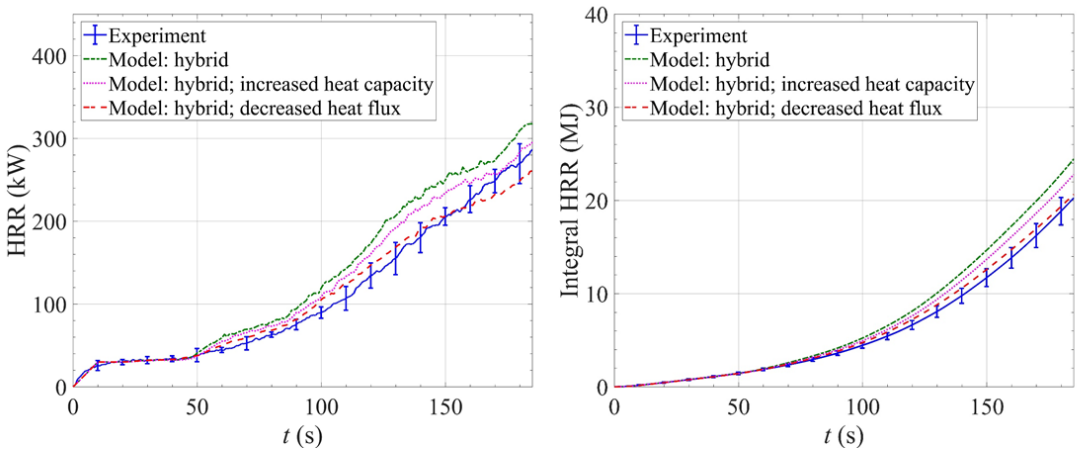

Figure 2-22. Sensitivity of the uncoupled simulations to the uncertainties in the heat flux and heat capacity of condensed-phase components of PMMA

The impact of change in each input parameter on the uncoupled simulation (solid green bars) is presented as a percentage change in average error of HRR from the corresponding uncoupled simulation with original hybrid model, in Figure 2-23. The percentage change in average error of HRR is calculated using the following equation,

$$\Delta HRR_{error} = \frac{HRR_{error}^{Input\ parameter\ change} - HRR_{error}^{Original\ model}}{HRR_{error}^{Original\ model}} \qquad (2\text{-}16)$$

The HRR_{error} of original uncoupled simulation using the hybrid heat flux model, calculated using Eq. (2-15), is 17%, so a negative value of ΔHRR_{error} in this figure represents improvement of overall HRR prediction. Thus, it can be inferred that increasing heat capacity and thermal conductivity parameters and decreasing the heat flux improves the HRR prediction (negative ΔHRR_{error}), while increasing emissivity makes the prediction worse (positive ΔHRR_{error}). Increasing absorption coefficient by 30% or using the alternative Arrhenius pair have negligible impact on uncoupled simulations. From this figure, it is evident that among the pyrolysis parameters, the uncertainty in the heat capacity has the most impact on the simulation, followed by thermal conductivity and emissivity. Considering all input parameters, the heat flux has the maximum impact on the HRR, with $\Delta HRR_{error} = -70\%$, corresponding to 10% reduction in the heat flux. This impact is also seen in Figure 2-22, where the uncoupled simulation using decreased heat flux predict the HRR within the experimental error bars. This is expected because decrease in the heat flux decreases the heat feedback on the material and consequently decreases the predicted mass loss rate.

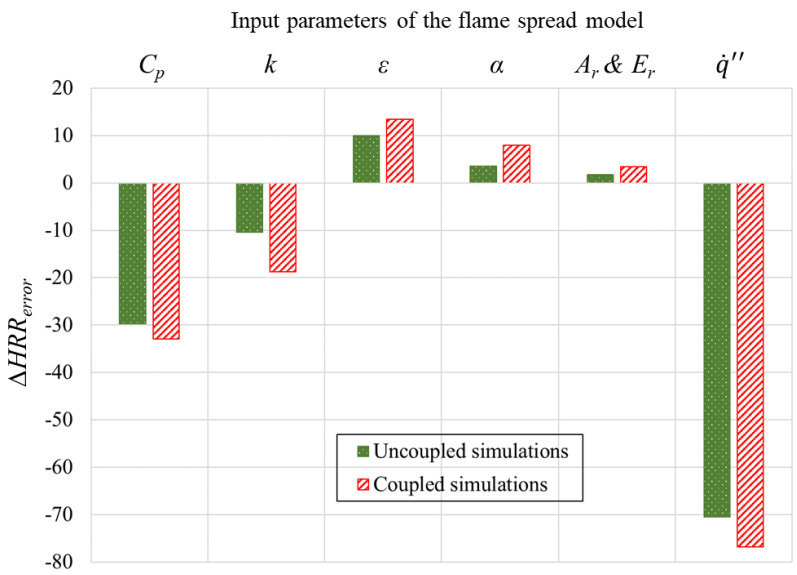

Figure 2-23. Percentage change in average error observed in the predicted HRR (ΔHRR_{error}) with a change in input parameters (pyrolysis parameters and heat flux) for coupled and uncoupled simulations conducted using hybrid heat flux model

The hybrid flame heat flux model and the pyrolysis models with the original and increased heat capacities were also used to perform the coupled simulations, the results of which are compared with the mean experimental HRR in Figure 2-24. Similarly, coupled simulations were also performed for the original pyrolysis model with the hybrid flame heat flux model with decreased heat flux. These combinations of the flame heat flux and pyrolysis models yielded the best agreement with experiments for the uncoupled simulations. The presented simulated HRR are fully converged (i.e., the input HRR and the output HRR are effectively identical). It was also established that the variation in the initial guess HRR had no impact on the final converged results.

The results of the coupled simulations with pyrolysis models with original and increased heat capacities demonstrate a large reduction in the quality of agreement with

experiments, with respect to the corresponding uncoupled simulations. The uncoupled simulation using the increased heat capacity produced HRR that was, on average, within 10% of the experimental data. For the corresponding coupled simulation, this difference increased to almost 45%. The difference in the HRR associated with the variation in heat capacity also increased significantly for the coupled simulations. Similarly, the difference in HRR, presented as ΔHRR_{error} (% change in HRR_{error} from original coupled simulation with hybrid model), associated with other pyrolysis properties shown in Figure 2-23 has increased significantly for the coupled simulations.

The coupled simulation using the decreased heat flux, however, are still within 15% of the average experimental data, which is a slight increase from the 8% average error of the uncoupled case using decreased heat flux. The decreased heat flux also impacts the coupled simulations the most among all the input parameters to the flame spread model ($\Delta HRR_{error} = -75\%$ from Figure 2-23). The FIGRA estimates for these simulations showed similar trends, the values for which, along with the HRR_{error} are shown below in Table 2-4.

Table 2-4. Relative HRR_{error} and FIGRA comparison for experiment and different simulation approaches.

		HRR_{error} (%)	**FIGRA (kW s^{-1})**
Experiment		0	1.4
Simulations	Radiation (uncoupled)	40	1.9
	Convection (uncoupled)	-18	0.9
	Hybrid (uncoupled)	20	1.7
	Hybrid (uncoupled; increased heat capacity)	10	1.6
	Hybrid (uncoupled; decreased heat flux)	8	1.3
	Hybrid (coupled)	65	2.3
	Hybrid (coupled; increased heat capacity)	45	2.0
	Hybrid (coupled; decreased heat flux)	15	1.4

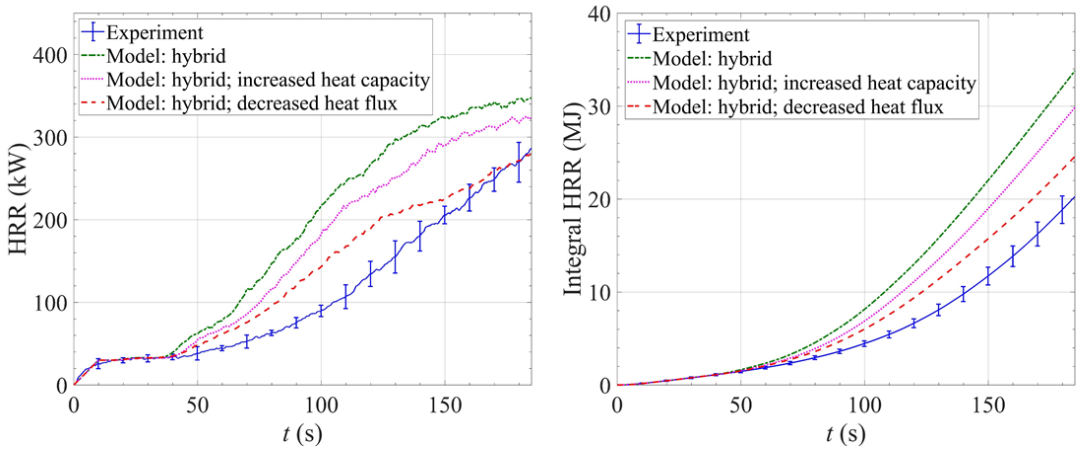

Figure 2-24. A comparison of the mean instantaneous and integral experimental HRR with heat release rates obtained from the coupled simulations

It is apparent that a strong feedback between the HRR and flame heat flux realized in these simulations leads to a significant amplification of errors introduced by relatively small uncertainties in the model parameters. A small initial over-prediction in the HRR causes an over-prediction in the flame heat flux which, in turn, leads to a larger over-prediction in HRR. This amplification of errors is rooted in the fundamental physics of this flame spread problem and, thus, is unavoidable.

2.10. Conclusion for Chapter 2

Flame spread over cast black PMMA was studied by performing hierarchical experiments and modeling starting from milligram-scale to large-scale flame spread tests. Milligram-scale thermogravimetric analysis (TGA), microscale combustion calorimeter (MCC) tests conducted on grounded PMMA samples and gram-scale Controlled Atmosphere Pyrolysis Apparatus (CAPA II) tests conducted on axisymmetric disc-like PMMA samples were used to collect data for pyrolysis model development. A detailed

pyrolysis model, which accounted for kinetics and thermodynamics of the thermal decomposition and transport of energy and mass in the condensed phase, was developed by inversely analyzing milligram and gram-scale experimental data. The inverse analysis technique for characterizing pyrolysis of cast black PMMA was automated using a hill-climbing optimization algorithm.

An experimental setup was then designed and built to study turbulent, buoyancy-driven flame spread on a vertical corner wall. Seven experiments were performed on cast black PMMA. Heat release rate, HRR, was measured using a fast response oxygen consumption calorimetry, which incorporated corrections for oxygen concentration change in the sensor flow induced by water vapor and carbon dioxide scrubber. The total flame heat flux was measured simultaneously at 28 locations distributed over the PMMA surface using water-cooled heat flux gauges. This heat flux was found to increase almost linearly with HRR until it reached a plateau for the regions closer to the corner. An empirical flame heat feedback model was formulated based on heat flux and HRR correlations.

A modified DSLR camera with increased spectral sensitivity was equipped with a 900 nm band pass filter to monitor emissions from soot during the flame spread experiments. The normalized radiation intensity projected onto the PMMA panel surface and flame presence probability were obtained for key stages of the fire growth. These radiation intensity data, which relate to soot volume fraction, can be used for validation of CFD simulations, provided that the spectrally resolved radiation from soot is computed. The relationship between the total flame heat flux and the projected radiation intensity was examined and found to have a notable degree of linear correlation. The contribution of

convection to the total flame heat flux was estimated using this correlation to be 12 ± 4 kW m^{-2}.

A numerical model of the corner wall flame spread process was developed by coupling the empirical flame heat feedback model and the comprehensive pyrolysis model. Using modeling, it was shown that the knowledge of the total flame heat flux by itself was insufficient to formulate thermal boundary conditions yielding accurate predictions. Relative contributions of convection and radiation need to be resolved. A hybrid model, combining a convective representation for the total flame heat flux below 30 kW m^{-2} and switching to radiative representation for the higher heat flux values, was formulated and yielded reasonable predictions. However, experimental measurements of radiation-convection split are necessary to improve accuracy.

A comparison between the uncoupled simulations, where the flame heat feedback was effectively prescribed to match the experimental measurements, with the coupled simulations, where the flame heat feedback was computed from the simulated HRR, revealed that the coupling significantly amplifies uncertainties in the model parameters. This amplification in not an attribute of a particular modeling approach developed in this study but rather a general feature of any model (including CFD) attempting to capture the essential physics of this type of flame spread. The results of this comparison indicate that the uncertainties in the key material pyrolysis properties and the flame heat feedback, which rarely fall below ±10%, would have to be reduced substantially to deliver fire growth predictions comparable in accuracy to measurements. The results also indicate that the model's ability to accurately compute convective and radiative portions of the flame heat feedback is critical for the quality of predictions.

Chapter 3: Experiments and Modeling of Pyrolysis and Flame Spread over Polyisocyanurate (PIR) Foam

The semi-empirical model developed in Section 2.8 predicted the HRR evolution for a flame spread scenario on PMMA, which degrades into its monomer without adding much complexity to the gas-phase combustion process. However, PMMA is not used as a wall-lining material due to its high flammability hazard and the application of the semi-empirical model methodology on a wall-lining material was deemed necessary. The complexity in the experimental behavior and model may increase for the wall-lining materials that have complex decomposition thermal decomposition mechanisms and form char that tends to inhibit flame spread.

A closed-cell Polyisocyanurate (PIR) foam core, by the trade name Tuff-R™ (supplied by DuPont Nemours Inc.) was selected as a representative example of such material. Tuff-R™ sheet is a PIR foam core sandwiched between foil facer which comprise of three-ply Kraft paper and aluminum foil. Tuff-R™ is a low density insulation that consists of around 80% Polyisocyanurate rigid cellular polymer, around 5% glass fiber, about 7% hydrocarbon blowing agent, and the remainder of foil facer composed of Kraft paper and aluminum foil [181].

3.1. Small-Scale Experiments

3.1.1. TGA-DSC Experiments

Cryogenically grounded samples of Tuff-R™ weighing between 5 and 5.5 mg were heated steadily at 5, 10, and 20 K min^{-1} in Netzsch F3 Jupiter Simultaneous Thermal

Analysis (STA) apparatus. All the samples were dried in the desiccator for at least 24 h before experimentation. STA was calibrated according to procedure described in Section 2.1.1 and [91].

A set of ten experiments were performed on Tuff-R™ in inert environment maintained by 50 ml min^{-1} N_2 flowrate for 10 K min^{-1} heating rate. Six additional tests were performed in similar anaerobic conditions for 5 K min^{-1} and 20 K min^{-1} heating rate. All tests were carried out in Pt-Rd crucible with lids to maximize thermal contact and heat flow sensitivity. Each lid had a small opening to allow uninhibited gas transport of gaseous decomposition products. The solid residue left behind at the end of these experiments was collected and five experiments were conducted at same conditions on the residue at a heating rate of 10 K min^{-1}. The experiments on the residue were primarily conducted to capture the heat flow (DSC) to facilitate analysis of heat capacity of the residue. In addition to these, three experiments were performed at 20 K min^{-1} in aerobic conditions of 21 % Oxygen and 79% Nitrogen, maintained by flowrate of 13 ml min^{-1} O_2 and 50 ml min^{-1} N_2. Aerobic conditions forced complete decomposition and oxidation of carbonaceous residue and thus provided insight into the inorganic constituent of the foam core polymer matrix, which was assumed to be the glass fibers.

3.1.2. MCC Experiments

Brief description of the MCC apparatus can be found in Section 2.1.2. Samples, desiccated for at least 24 h, with mass 4 mg to 6.6 mg were placed in a ceramic crucible that was inserted into the sealed MCC pyrolyzer. The combustor was maintained at 1223 K to ensure complete oxidation of all the emanating gases from the pyrolyzing section. A

constant heating rate of 10 K min^{-1} was maintained in the pyrolyzer section and the sample was heated from 348 K to 1023 K. The residue yield in the ceramic crucible was weighed after each experiment. The HRR was determined using the oxygen consumption calorimetry and recorded as a function of time and sample temperature. A total of five experiments were conducted to accumulate data and perform statistics.

3.1.3. CAPA II Experiments

CAPA II experimental setup is described briefly in Section 2.1.4. Samples of Tuff-R™ for these experiments were circular, axisymmetric disks with 7 cm diameter and 1.27 cm thickness. The front, flat surface of the sample was installed horizontally in the sample holder and was exposed to a specific heat flux imposed by a conical heater. The sample disks were cut from the same panels of Tuff-R™ which were used for large scale experiments. The aluminum foil facer on Tuff-R™ was completely removed from the back side and placed on the copper foil to maintain a good thermal contact. Experiments were conducted at external heat flux of 70 kW m^{-2} and 40 kW m^{-2}.

The test matrix and the condition of the aluminum foil facer on the front side are shown in Table 3-1 and the physical dimensions of a Tuff-R™ sample without the foil facer is given in Table 3-2. The presence of foil facer did not have a significant impact on the density of Tuff-R™. The impact of having the painted foil facer and high emissivity paint during thermal decomposition was investigated – the high emissivity paint used for two sample cases emulated the soot deposition in large scale fires. Three sample conditions were investigated – sample with no foil facer (I), sample with painted foil facer (II), and sample without a foil facer and half side painted black (III).

Table 3-1. Test matrix showing number of CAPA II experiments on Tuff-R™ samples with specific foil facer condition.

Heat flux	Foil facer condition		
	Sample (No foil) (I)	Painted foil (II)	Half painted sample (no foil) (III)
40 kW/m^2	2	-	-
70 kW/m^2	3	1	1

Table 3-2. Physical properties and dimension of Tuff-R™ sample with no foil facer (I).

	Tuff-R™ sample with no foil facer (I)
Initial diameter (m)	7×10^{-2}
Initial thickness (m)	1.28×10^{-2}
Mass (kg)	1.6×10^{-3}
Initial measured density (kg/m^3)	32

3.1.4. Cone Calorimeter Experiments

Cone calorimeter experiments were conducted on Tuff-R™ samples to calculate the heat release rate of the samples burning in air with a continuous flame over the sample surface. The presence of flaming combustion in an air environment in cone calorimeter imitates condition of a burning sample covered by the flame observed on a large scale. The cone calorimeter experiments were performed to investigate the potential impact of blowing agent on the burning rate. These samples, being thicker than the CAPA II samples and the milligram-scale samples (where the blowing agent was potentially lost due to cryogenic grinding), were better candidate to understand impact of the blowing agent trapped inside the polymer matrix.

Cone calorimeter tests followed the procedures suggested by ASTM 1354 [4] standard. Tuff-R™ samples having 2.54 cm thickness, without any foil facer coverings

were cut from the continuous panels to have a cross section area of 10 cm × 10 cm. Samples were measured to weigh 7.6 ± 0.6 g. The samples were placed in an aluminum foil holder which protruded about 0.2 cm above the sample surface to avoid any loss of sample during the test. The aluminum holder with the sample was placed onto a Kaowool PM ceramic fiber insulation board covering the mass balance platform. The sample holder was placed under a conical heater whose bottom surface was 2.54 cm above the sample surface, which is the same distance at which the external heat flux from the conical heater was measured before a test. Three tests exposed the sample surface to an external heat flux of 50 kW m^{-2} for about 250 s or until continuous flaming ceased for at least 30 s. After each test, the sample was weighed separately to determine the char yield.

The heat release rate was measured by oxygen consumption calorimetry, where a paramagnetic oxygen sensor was used to monitor the changes in oxygen concentration throughout the test duration. The sensor was calibrated against a reference of N_2 and air with 21.9 % O_2 on each test day. The C-factor for the cone calorimeter, a calibration constant used to quantify baseline correction for HRR measurements, was determined by using a controlled burner supplied with a known quantity of methane fuel.

3.2. Small-Scale Experiment Results

3.2.1. TGA-DSC Results

The mass loss rate, heat flow, mass fraction, and integral of heat flow, all normalized by initial mass, averaged over the set of ten experiments for the heating rate of 10 K min^{-1} are shown below in Figure 3-1. The error bars shown here represent two standard deviations of the mean obtained from ten experiments. The thermal

decomposition of the Tuff-R™ foam begins at around 410 K. The peak mass loss rate is seen around 600 K which corresponds to a large exothermic heat flow observed in the DSC curve. Multi-peak decomposition and an onset of exothermic reaction around 580 K is characteristic of a PIR foam [182]. Larger error bars are observed at higher temperatures in the case of heat flow due to higher uncertainty and fluctuations of the baseline data at higher temperatures in the STA apparatus. Residue yield after the experiments was about 32 ± 1 %.

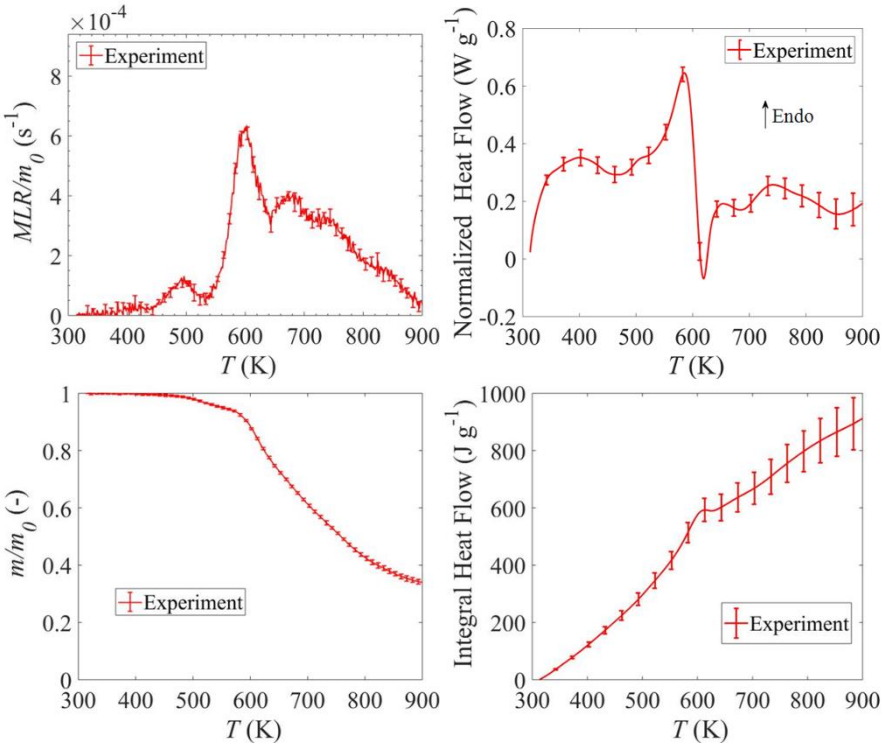

Figure 3-1. STA experiment data for Tuff-R™ heated at 10 K min^{-1}

The heat flow observed during the constant heating of the residue in inert environment is shown below in Figure 3-2. The near steady heat flow across the entire temperature range highlights the thermal stability of the residue structure. This heat flow data was used to determine the specific heat capacity of the residue for the development of

pyrolysis model. It is important to note here that the heating rate of STA takes time to reach a steady state, and the heat flow data for the residue reflects this behavior, thus, the initial peak at the beginning does not correspond to a degrading residue.

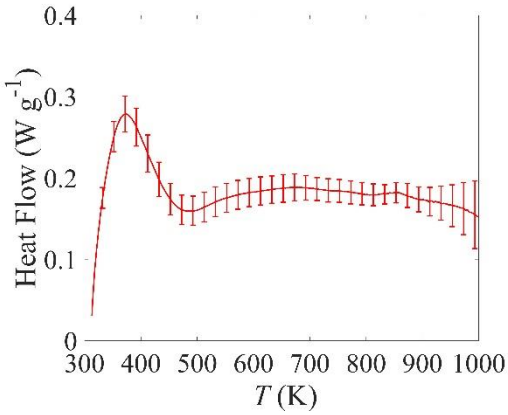

Figure 3-2. DSC Heat Flow of Tuff-R™ residue heated at 10 K min^{-1} in inert N_2 conditions

Mass fraction of Tuff-R™ pyrolyzed in an aerobic conditions at 20 K min^{-1} is shown in Figure 3-3. The glass fiber content, which was assumed to correspond to the unreacted residue left behind in these tests, was 4.1 ± 0.3 %.

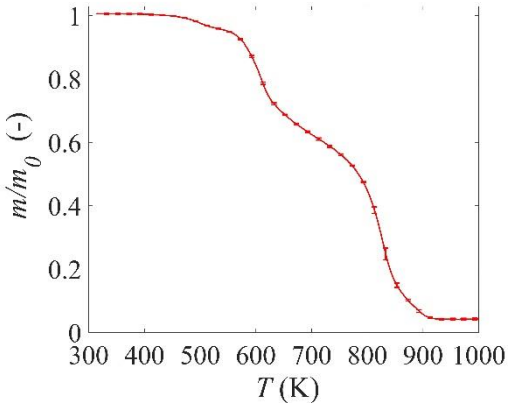

Figure 3-3. TGA mass fraction evolution of Tuff-R™ heated in air at 20 K min^{-1}

3.2.2. MCC Results

The heat release rate normalized by the initial mass versus temperature and integral HRR normalized by the initial mass vs time are shown in Figure 3-4 for Tuff-R™. The HRR data was corrected by constructing a linear baseline to account for baseline oxygen sensor drifts. The error bars shown here represent two standard deviations of the mean obtained from 5 repeatable experiments. The HRR shows multiple peaks throughout the decomposition process from 410 K to 1000 K.

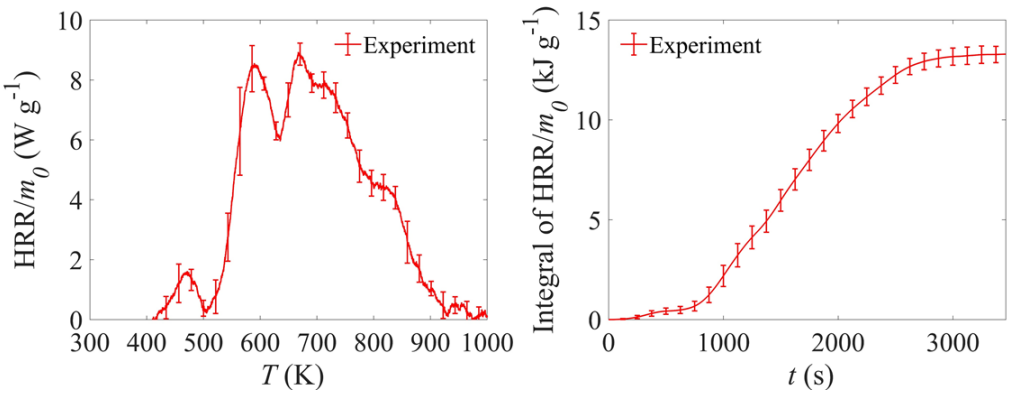

Figure 3-4. Normalized HRR and integral HRR for Tuff-R™ heated at 10 K min^{-1} in MCC

The heat of combustion normalized by the initial mass and normalized by the lost mass was calculated from the integral HRR curve and the measurement of residue yields. The relevant values are listed in Table 3-3. The residue yield in the MCC, 30.4 ± 0.4 %, was similar to the residue yields observed in the TGA experiments.

Table 3-3. Char yield, heat of complete combustion of Tuff-R™ from MCC experiments

	Residue yield from MCC (%)	**Heat of combustion normalized by initial mass (kJ g^{-1})**	**Heat of combustion normalized by lost mass (kJ g^{-1})**
Tuff-R™	30.4 ± 0.4	13.3 ± 0.4	19.1 ± 0.6

3.2.3. CAPA II Results

The photographs of the samples before and after the tests are shown in Figure 3-5 for a range of different conditions. The thermal decomposition of the sample is almost uniform across the front surface. The samples were observed to expand slightly towards the heater at the beginning of the experiments and then contract as the experiment proceeded. The sample underwent decomposition and formed carbonaceous char (inferred from the grey/black region after the test) as can be seen in Figure 3-5 (b). The cross section of the Tuff-R™ sample after a 40 kW m^{-2} test, seen in Figure 3-5 (c), indicate that the sample does not undergo complete decomposition across the entire depth at this set heat flux. The sample underwent complete decomposition for 70 kW m^{-2} set heat flux. The black paint applied on the sample with intact foil facer degraded with heat exposure and exposed the foil facer, as seen in Figure 3-5 (e). A slight apparent visual discrepancy for residue in Figure 3-5 (b) and Figure 3-5 (d) is solely due to lighting conditions when the photographs were taken.

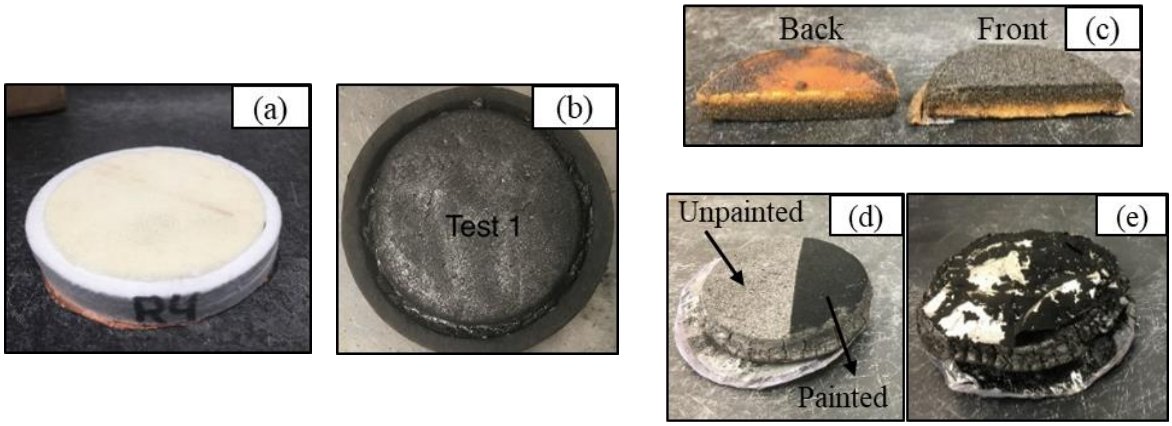

Figure 3-5. Tuff-R™ test sample (a) Before the test (Case I), (b) After the 70 kW m^{-2} test (Case I), (c) Front and back side of sample (Case I) after the 40 kW m^{-2} test, (d) Front face of half painted sample after the 70 kW m^{-2} test (Case III), (e) Front face of full painted sample with foil facer after the 70 kW m^{-2} test (Case II)

The mass loss rate (*MLR)* and back surface temperature (T_{back}) for a sample without any front foil facer (Case I) is shown in Figure 3-6.

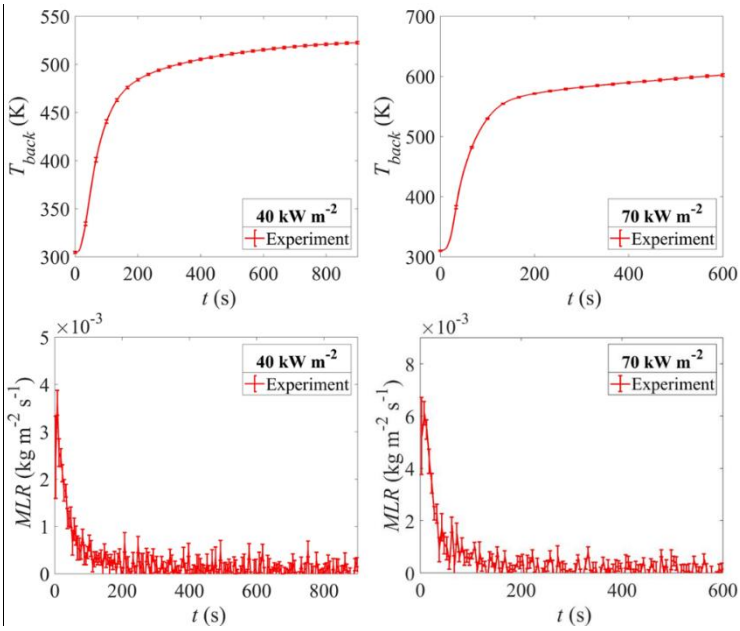

Figure 3-6. Back surface temperature and mass loss rate (MLR) and during CAPA II experiments on Tuff-R™ with no foil facer (Case I) at 40 kW m^{-2} and 70 kW m^{-2}

The back surface temperature increases at a faster rate at the start of the test and rises slowly after 200 s for both the heat fluxes and reaches a maximum temperature of around 520 K for 40 kW m^{-2} and 620 K for 70 kW m^{-2}. The mass loss rate for Tuff-R™ exposed to both the heat fluxes is highest right after exposure and peaks at 4×10^{-3} kg m^{-2} s^{-1} for 40 kW m^{-2} test and 7×10^{-3} kg m^{-2} s^{-1} for 70 kW m^{-2} test. Negligible mass loss is observed after 200 s after the onset of mass loss. Char density was determined to be 19.5 kg m^{-3}, obtained from measurements of dimensions and mass of a square cut-out of the residue from 70 kW m^{-2} test on Tuff-R™ sample with no foil facer (Case I).

Change in thickness for 70 kW m^{-2} test is quantified in Figure 3-7. The sample thickness was seen to change thickness uniformly across the radial direction. The sample first grew in thickness by about 25% and subsequently contracted by about 15% with respect to the original thickness.

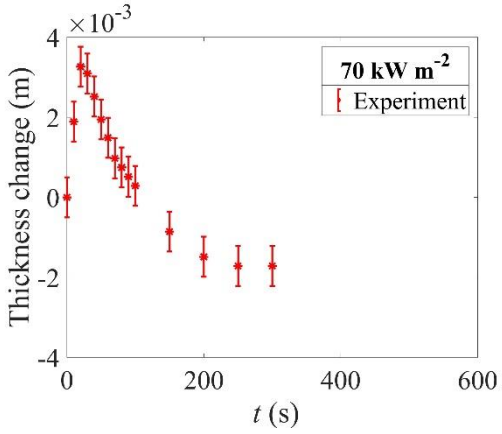

Figure 3-7. Thickness change quantified from side video camera for CAPA II test conducted at 70 kW m^{-2} on Tuff-R™

The back surface temperature for Tuff-R™ samples with painted foil facer (Case II) increase at a rate that is similar to the back surface temperature for sample with no foil

facer (Case I), as shown in Figure 3-8. The back surface temperature for painted foil facer are higher towards the end of the test than samples with no foil facer. Comparison of MLR is also shown in Figure 3-8, where a Savitsky-Golay filter was applied to smooth the noisy data and facilitate comparison. The peak MLR for sample with no foil facer (Case I) and the sample with painted foil facer (Case II) are quite similar. Although the MLR vs time curve for both are similar and within the uncertainty of measurement, the smoothened MLR for sample with painted foil facer (Case II) takes slightly longer to decrease than the smoothened MLR for sample with no foil facer (Case I). This indicates that when the foil facer is present, it may act as a mass barrier and will potentially have a larger impact on mass loss rate compared to sample without the foil facer.

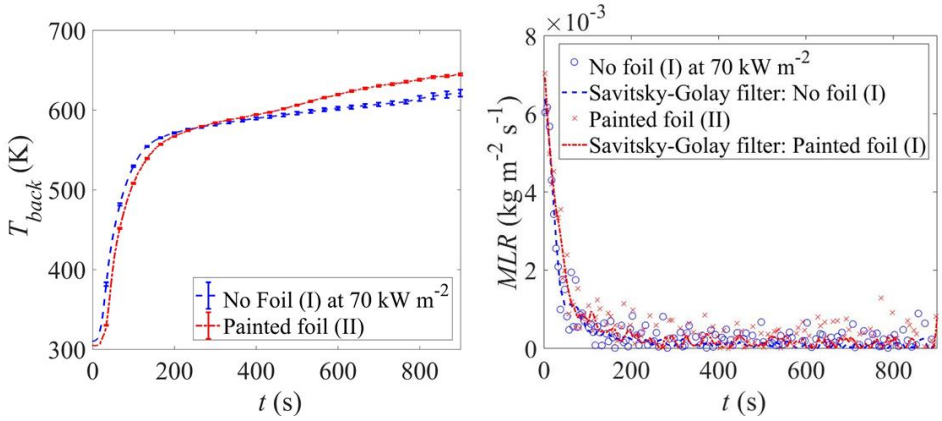

Figure 3-8. Back surface temperature and mass loss rate for CAPA II tests on Tuff-R™ with no foil facer (Case I) and painted foil facer (Case II) at 70 kW m^{-2}

The effect of painted and unpainted front face on back surface temperature for half-painted sample (Case III) is shown in Figure 3-9. Back surface temperature evolution during the first 200 s, where majority of mass loss is observed in all Tuff-R™ samples, was the same for the unpainted and painted halves, suggesting negligible impact of soot on

surface heat transfer and imply that the surface optical properties are similar to that of paint ($\varepsilon = 0.95$).

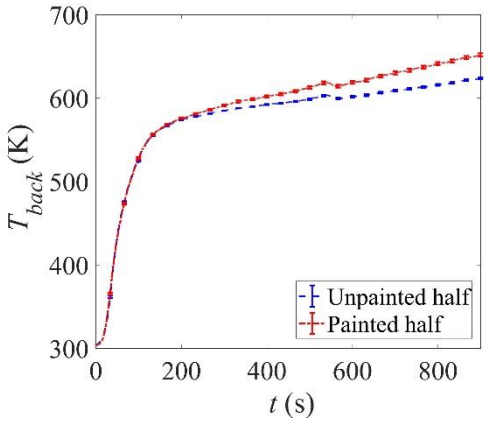

Figure 3-9. Back surface temperature for CAPA II tests on Tuff-R™ with no foil facer (Case III) with painted and unpainted front face

3.2.4. Cone Calorimeter Results

The Tuff-R™ sample ignited and sustained continuous flaming immediately after it was exposed to the 50 kW m^{-2} heat flux, as seen in Figure 3-10 (a). The visual transition is shown in Figure 3-10 for four instances through the duration of the test. After about 30 s after ignition, the sample began to expand slowly towards the conical heater, while the continuous flame started to transition to a fragmented flame above the sample, as shown in Figure 3-10 (b). About 70 s after ignition, the sample had warped and expanded to its maximum while the fragmentation of flame persisted, as seen in Figure 3-10 (c). After this point, intermittent flame was observed from the edges of the sample. After about 200 s, the flaming ceases completely accompanied by negligible mass loss and heat release. A non-combustible fractured structure, as seen in Figure 3-10 (d), with cracks across the visible surfaces is left behind.

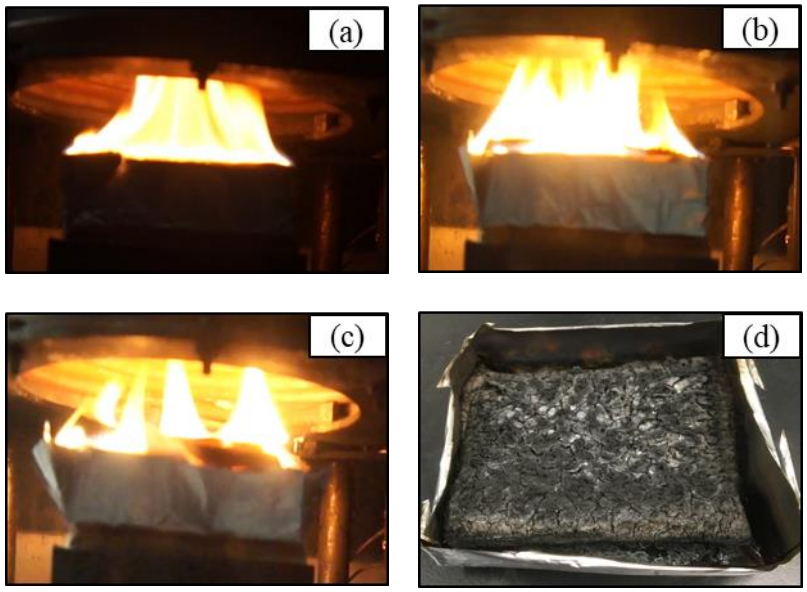

Figure 3-10. Tuff-R™ sample behavior during exposure to 50 kW m^{-2} external heat flux in the cone calorimeter. (a) Continuous flaming after ignition (~1 s), (b) Onset of sample warping/expanding and flame fragmentation (30 s), (c) Warped/expanded sample and continuous fragmented flame (70 s), (d) Residue remaining after the test

The residue yield was weighed and was found to be 18 ± 3 %, which is less than 32 ± 1 % observed in TGA and MCC experiments. As mentioned earlier, the cone samples were better candidate to understand the impact of blowing agent trapped inside the polymer matrix on the burning rate because the cone samples were thicker than CAPA II samples and the milligram-scale samples (where the blowing agent was lost due to cryogenic grinding). Therefore, the large variation in the residue yield can be attributed to the loss of blowing agent and possibly, to char oxidation and to uneven burning pattern due to expansion and warping of the sample during the test.

The mass loss rate (MLR), heat release rate (HRR), integral MLR, and integral HRR, all normalized by per unit area of the cross section of the sample, are shown in Figure 3-11.

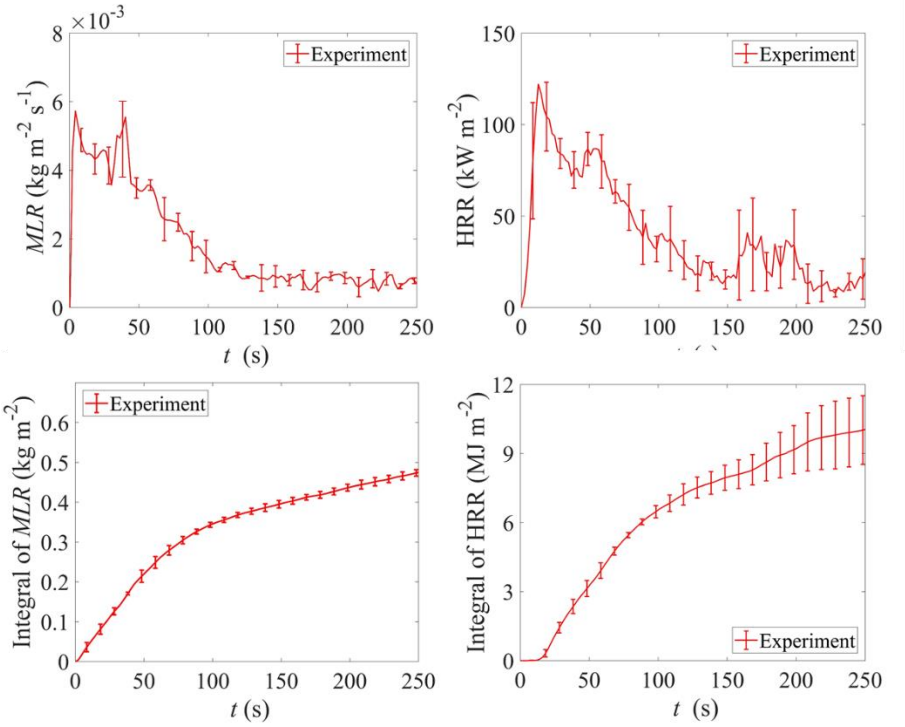

Figure 3-11. Mass loss rate (MLR), heat release rate (HRR), integral MLR, and integral HRR of cone calorimeter tests on Tuff-R™ exposed to external heat flux of 50 kW m^{-2}

The mass loss rate and the corresponding heat release rate increase immediately after the sample is exposed to the heat flux. A peak average MLR and HRR is observed immediately after ignition, with their values being 6×10^{-3} kg m^{-2} s^{-1} and 120 kW m^{-2} respectively. Errors shown in the figure were calculated as two standard deviation of the mean from three experiments. The average errors estimated for MLR and HRR are about 7 % and 9% of the respective maximum magnitudes. The integral HRR peaked at 10 ± 1.5 MJ m^{-2} at 250 s.

Heat of combustion (ΔH_c) was calculated by dividing the integral HRR at 250 s by initial mass or lost mass. The lost mass was obtained by integrating MLR for 250 s. This heat of combustion compared with corresponding values obtained from MCC are shown in Table 3-4. The ΔH_c values were calculated for the entire test duration of 250 s after ignition.

Table 3-4. Comparison of Tuff-R™ heat of combustion (ΔH_c) determined from Cone calorimeter and MCC

	Cone ΔH_c per unit lost mass (kJ g^{-1})	**MCC ΔH_c per unit lost mass (kJ g^{-1})**	**Cone ΔH_c per unit initial mass (kJ g^{-1})**	**MCC ΔH_c per unit initial mass (kJ g^{-1})**
Tuff-R™	21.3 ± 3	19.1 ± 0.6	13.9 ± 1	13.3 ± 0.4

The heat of combustion of Tuff-R™ obtained from cone calorimeter compares well with the ΔH_c from MCC. The average ΔH_c per unit initial mass is 13.9 ± 1 for cone calorimeter and 13.3 ± 0.4 from MCC. The average values for ΔH_c per unit lost mass is also within the error for cone calorimeter and MCC. This is in contrast to the expectation that the cone calorimeter ΔH_c values are less than that from MCC [5]. The similarity in ΔH_c values can be attributed to the fact that the residue yield in the cone calorimeter is less than MCC possibly due to the combustion of blowing agent in the cone calorimetry tests.

3.3. Tuff-R™ Pyrolysis Model

Pyrolysis model for Tuff-R™ was developed by following the framework used for PMMA, which was discussed in Section 2.3. Modeling parameters specific to Tuff-R™ are discussed wherever necessary.

3.3.1. Reaction Kinetics, Stoichiometry and Heats of Reaction.

First, TGA-DSC data were inversely analyzed to parameterize a global reaction scheme that could predict the mass loss rate and DSC heat flow of the thermal decomposition process at 10 K min^{-1}. The data for 5 K min^{-1} and 20 K min^{-1} served as the target for validating the developed pyrolysis model. The decomposition of Tuff-R™, as shown in Figure 3-1, was modeled using seven consecutive, first-order Arrhenius type reactions. During the modeling, the foam material was represented by a mixture of experimentally determined mixture of 95.9 wt. % reactive component TR and 4.1 wt. % non-reactive glass fiber component. Each reaction produced an intermediate component and a gas species. Intermediates were labeled as Tr_Int_1 through Tr_Int_7 and the evolving pyrolyzate gases were Gas_1 through Gas_7. Tr_Int_7 represents the final residue. The reaction mechanism, including the pre-exponential factors, A_r, activation energies, E_r, and mass-based stoichiometric coefficients, are shown below in Table 3-5.

Table 3-5. Decomposition reaction mass-based stoichiometry, kinetic parameters, and heat of reaction (positive heat values correspond to endothermic reactions) for Tuff-R™.

#	Reaction	A_r (s^{-1})	E_r (J mol^{-1})	ΔH_r (J kg^{-1})
1	TR → 0.992 Tr_Int_1 + 0.008 Gas_1	2.42×10^{8}	8.09×10^{4}	0
2	Tr_Int_1 → 0.96 Tr_Int_2 + 0.04 Gas_2	2.27×10^{7}	8.96×10^{4}	2.16×10^{4}
3	Tr_Int_2 → 0.80 Tr_Int_3 + 0.20 Gas_3	5.63×10^{8}	12.43×10^{4}	2.15×10^{5}
4	Tr_Int_3 → 0.92 Tr_Int_4 + 0.08 Gas_4	1.00×10^{8}	1.19×10^{5}	-1.60×10^{5}
5	Tr_Int_4 → 0.83 Tr_Int_5 + 0.17 Gas_5	2.84×10^{7}	1.24×10^{5}	9.37×10^{3}
6	Tr_Int_5 → 0.71 Tr_Int_6 + 0.29 Gas_6	6.85×10^{3}	8.85×10^{4}	1.06×10^{5}
7	Tr_Int_6 → 0.73 Tr_Int_7 + 0.27 Gas_7	5.47×10^{1}	6.89×10^{4}	2.06×10^{5}

Heat capacity of the initial reactive component (TR) was determined by dividing the heat flow by the instantaneous heating rate for the temperature range of 313 K to 420 K, before any decomposition. Heat capacity of the residue was also determined in a similar manner using the heat flow data (Figure 3-2) obtained for the residue. Heat capacity of TR and residue (Tr_Int_7) were expressed as linear temperature dependent functions, as shown in Table 3-6. The heat capacities of all the solid intermediates was fixed to be 1684 J kg^{-1} K^{-1}, which was the heat capacity of Tuff-R™ at 420 K. Heat capacity of glass fiber (GF), expressed as a linear temperature dependent function was obtained from the literature [167,183]. Heat capacities of the condensed-phase components are listed in Table 3-6. The heat capacities of the gas-phase decomposition products could not be obtained from the current measurements and were assumed to be equal to 2100 J kg^{-1} K^{-1}, which was the mean heat capacity of a collection of C1 to C8 hydrocarbons at a temperature of 600 K [132].

Heats of reactions were then subsequently computed by simulating a baseline sensible heat flow by forcing all heats of reaction to zero. Then the heats of reaction were estimated by subtracting the integral heat flow data from the baseline for the temperature range of the particular reaction. The final heats of reaction are shown in Table 3-5.

Table 3-6. Heat capacities of condensed-phase components of Tuff-R™

Component	**C_p (J kg^{-1} K^{-1})**
Glass fiber	$1.24 \times T + 442$
TR	$4.86 \times T - 357$
Tr_Int_1	1684
Tr _Int_2	1684
Tr _Int_3	1684
Tr _Int_4	1684

Tr _Int_5	1684
Tr _Int_6	1684
Tr _Int_7	$0.41 \times T - 883$

The model fit is compared with the experimental data in Figure 3-12. The residue yield of the model is within the uncertainties of the experimental data. The model is mostly in agreement with all the mean experimental data. The large exothermic heat flow observed in the DSC data is captured well with the exothermic reaction (Reaction 4).

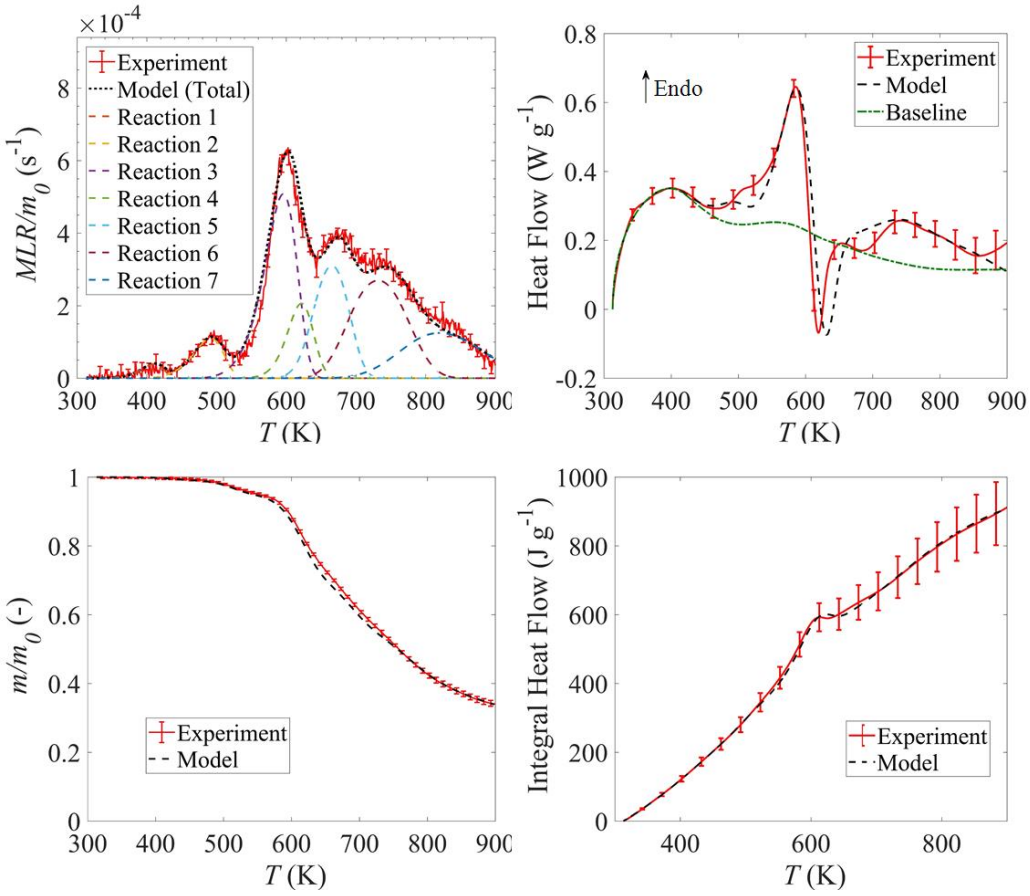

Figure 3-12. A comparison of Tuff-R™ model fit and experimental data for STA performed at 10 K min^{-1}

The reaction kinetics and associated thermodynamic parameters used in the model were then validated by predicting MLR and heat flow for 5 and 20 K min^{-1} TGA-DSC

tests. The comparison of predictions with the experimental data, shown in Figure 3-13, gives confidence on applicability of this model to predict pyrolyzate gas production rate at different heating rates than used for parameterization.

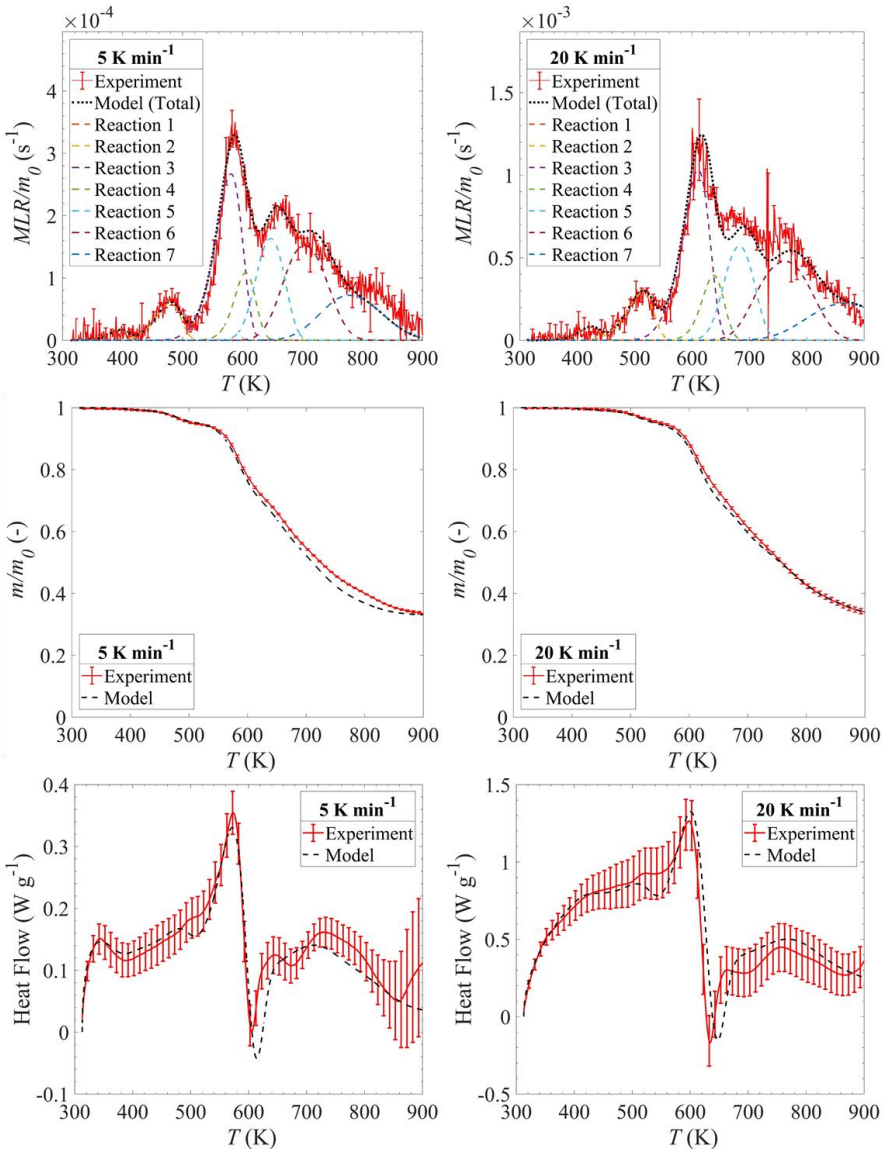

Figure 3-13. Pyrolysis model predictions of mass fraction, normalized MLR, and heat flow compared with experimental data for TGA-DSC performed on Tuff-R™ at 5 K min^{-1} (left column) and 20 K min^{-1} (right column)

3.3.2. Heat of Combustion of Pyrolyzate Gases

Heat of combustion, ΔH_c, values for the gaseous components, Gas_1 through Gas_7, of the reaction mechanism were determined by following the procedure discussed in Section 2.3.3 and are shown in Table 3-7. Pyrolysis in MCC was modeled in ThermaKin2Ds by expressing the heating boundary condition as per Eq. (2-1), and the heat release rate was determined only for temperature ranges with associated mass loss in STA. Contribution of Gas_1 to the heat release was determined to be zero. The modeled HRR versus experimental data is shown in Figure 3-14.

Table 3-7. Heat of complete combustion (ΔH_c) for pyrolyzate gases corresponding to apparent thermal decomposition mechanism for Tuff-R™.

Gaseous products	**ΔH_c (kJ g^{-1})**
Gas_1	0
Gas_2	15
Gas_3	15
Gas_4	8
Gas_5	24
Gas_6	20
Gas_7	33

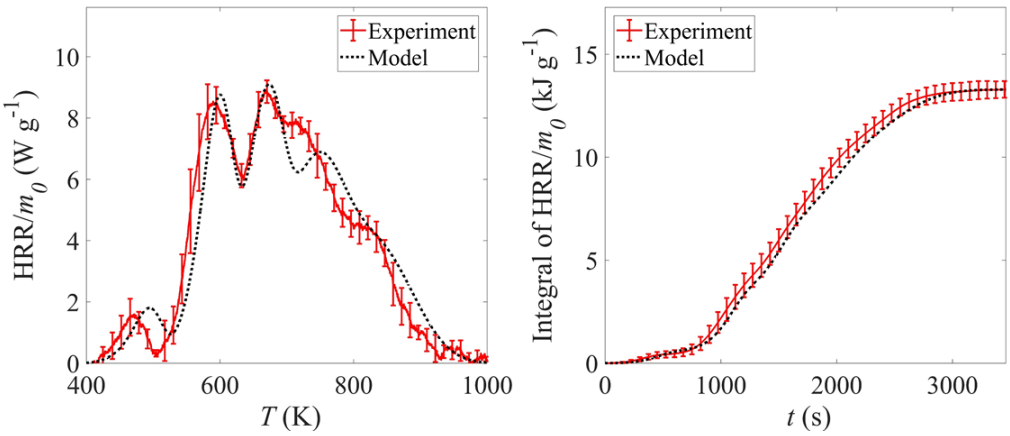

Figure 3-14. Model fit for HRR and integral HRR normalized by initial mass compared with MCC experimental data for Tuff-R™ at 10 K min^{-1}

3.3.3. Thermo-physical Properties

Thermal conductivities and densities of condensed phase components were optimized by inverse analysis of data obtained from CAPA II tests conducted at 70 kW m^{-2} heat flux. The hill-climbing optimization was implemented along with the goodness of fit criteria as discussed in Section 2.3.4. The experimental back surface temperature compared for each half (painted and unpainted), shown in Figure 3-9, indicated no significant difference in the first 200 s where majority of mass loss was observed. So, it was assumed that all the components had same emissivity of $\varepsilon = 0.95$. Due to the porous structure of the foam, absorption coefficient for all components was assumed to be $\kappa = 3200$ m^{-1} (or 100 m^2 kg^{-1}), which approximately represents the reciprocal of the depth of open pores located on the sample surface. Emissivity and absorption coefficient values for glass fiber were set to be 0.81 and 4160 m^{-1} respectively, as obtained from an online property database [183]. The gas transfer coefficient describing the transport of gases through the condensed phase

in response to a concentration and/or pressure gradient was prescribed as 2.0×10^{-5} m^2 s^{-1} in ThermaKin2Ds to simulate uninhibited transport.

The densities, ρ, were first optimized to fit thickness change dependency on time. After optimal density value was obtained after each hill-climbing optimization, the absorption coefficient was adjusted to maintain the constant absorption coefficient value of 3200 m^{-1} for all components. The thermal conductivities, *k*, were then optimized to fit experimental T_{back}. Since majority of the mass loss occurred before 200 s of the onset of mass loss at 70 kW m^{-2} and the increase of T_{back} after 200 s is negligible, the first 200 s of the T_{back} data were used as the optimization target. Initial constant thermal conductivity value of 0.1 W m^{-1} K^{-1} were assigned to the components and a lower limit of 0.04 W m^{-1} K^{-1} was assigned to have physically meaningful values. The results of the optimization exercise are shown in Figure 3-15, and Table 3-8 lists the final optimized thermo-physical parameter values for condensed-phase components.

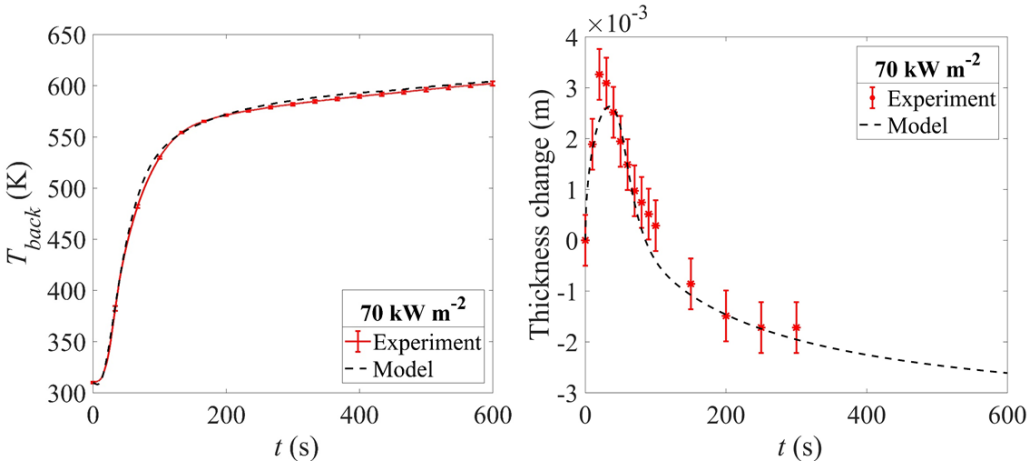

Figure 3-15. Back surface temperature and cross sectional profile expansion model fit compared with experimental data for Tuff-R™ at 70 kW m^{-2}

Table 3-8. Thermo-physical properties for condensed-phase components of Tuff-R™.

Reaction components	**Emissivity, ε (-)**	**Absorption coefficient, α [m^2 kg^{-1} (m^{-1})]**	**Thermal conductivity, k (W m^{-1} K^{-1})**	**Density, ρ (kg m^{-3})**
TR	0.95	102 (3200)	0.04	31.4
Tr_Int_1	0.95	215 (3200)	0.09	14.9
Tr_Int_2	0.95	108 (3200)	0.04	29.8
Tr_Int_3	0.95	173 (3200)	0.08	18.5
Tr_Int_4	0.95	185 (3200)	0.06	17.3
Tr_Int_5	0.95	195 (3200)	0.14	16.4
Tr_Int_6	0.95	231 (3200)	0.15	13.8
Tr_Int_7	0.95	238 (3200)	0.25	13.5
Glass Fiber	0.81	1.6 (4160)	0.36	2600

The experimental data of MLR and mass fraction for 70 kW m^{-2} and all data for 40 kW m^{-2} was used as a validation target for completely parameterized model. The model predictions agreed well with the experimental data, especially the peak MLR value for both the heat fluxes, as seen in Figure 3-16. The total mass at 70 kW m^{-2} was under predicted by the model. This under prediction was attributed to the inability of the model to account for the blowing agent lost during sample preparation for the milligram-scale tests, which were used to parameterize the thermal decomposition of Tuff-R™.

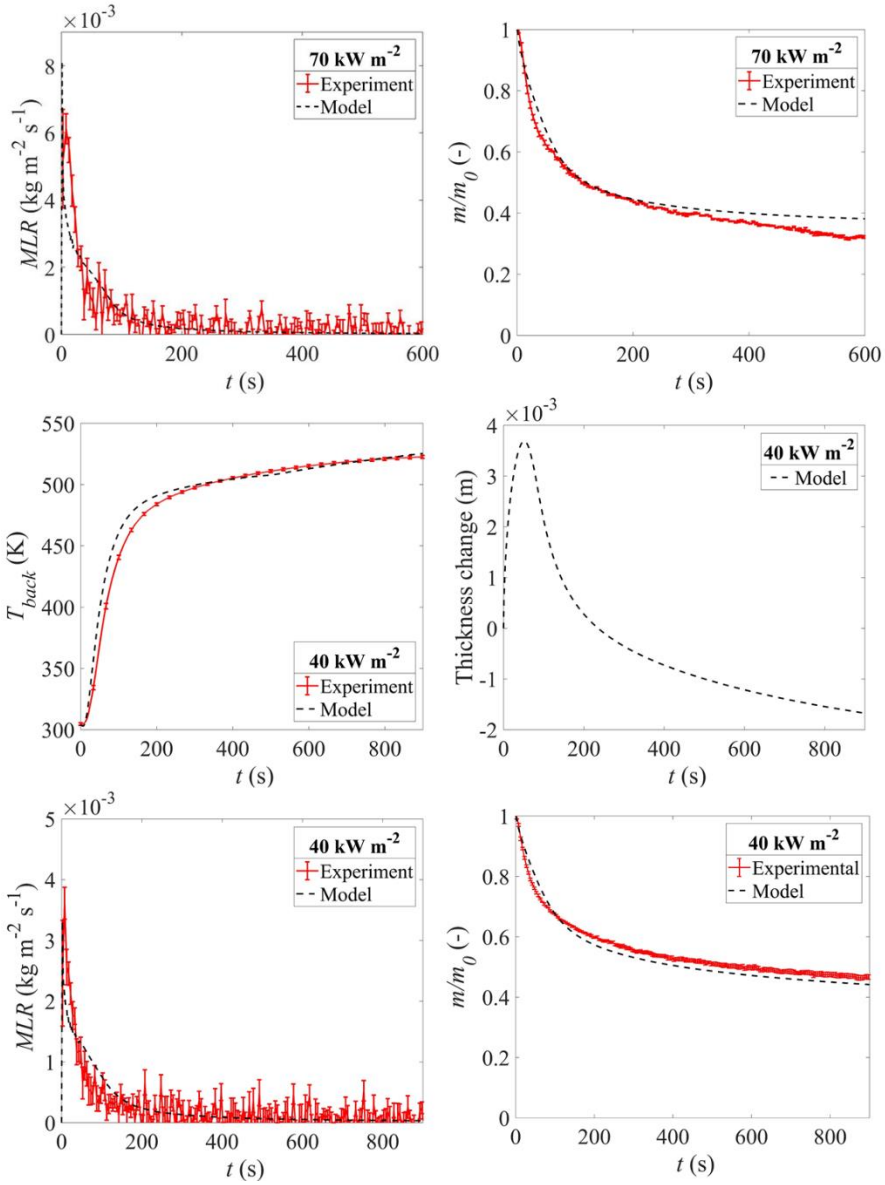

Figure 3-16. Validation of pyrolysis model predictions compared with the CAPA II data for Tuff-R™

3.3.4. Effect of Blowing Agent

As discussed earlier, the cone calorimeter test data, obtained on samples twice as thick as the CAPA II samples, were more likely to retain the blowing agent during sample preparation and conditioning process. Thus, modeling of cone calorimetry was speculated

to help better understand the influence of blowing agent on mass loss and consequently HRR.

Cone experiments were modelled using a one dimensional module of ThermaKin2Ds. Tuff-R™ sample of 2.54 cm thickness and 0.6 cm thick Kaowool backing insulation as used in the experiments were implemented in Thermakin2Ds with critical ignition mass flux calculated from virtual critical heat release rate. Virtual critical heat release rate, a product of critical mass flux and heat of combustion of a material, for variety of materials was found, theoretically [184] and confirmed later experimentally [185], to be 21 ± 6 kW m^{-2}. The critical ignition mass flux for prescribing flaming ignition criteria in TheraKin2Ds was thus determined by dividing this mean virtual critical heat release rate by the heat of complete combustion for respective gases, listed in Table 3-7.

The top boundary condition was defined as a radiative 50 kW m^{-2} heat flux with convective heat transfer coefficient of 9.5 W m^{-2} K^{-1} before flaming. When the mass flow crossed the critical ignition mass flux for a specific gas, the flaming was simulated by increasing the convective heat transfer coefficient to 15 kW m^{-2} K^{-1}, assuming a flame temperature of 2150 K, and a radiative heat flux feedback of 2.7 kW m^{-2}. These estimations of boundary conditions were obtained from previous studies based on experimental measurements and a detailed analysis of flame feedback [153]. The mass flow of pyrolyzate gases predicted by the cone simulations were multiplied by ΔH_c of respective gases listed in Table 3-7.

After cone simulation without the blowing agent component, a simulation was performed by including the blowing agent component in the Tuff-R™ pyrolysis model. It was observed during the experiments that about 0.1 cm layer at the surface had exposed

pores, indicating the escape of blowing agent from the surface layers. Therefore, a 7 % blowing agent, an approximate mass-based quantity based on the safety data sheet [181], was introduced in the interior region (0.0234 m) of the 0.0254 m sample. According to this datasheet, the blowing agent was iso-pentane. Thus, the heat capacity, thermal conductivity, and density of iso-pentane at 300 K were used for the blowing agent component. For the case of simulation with the blowing agent, the ΔH_c of the blowing agent was considered to be that of iso-pentane (ΔH_c = 49.5 kJ g^{-1}). The TR component was reset within the model to be impenetrable to gas flow (the gas transfer coefficient of 1.0 × 10^{-30} m^2 s^{-1}), which made sure that the blowing agent component was retained within the foam matrix until the TR component decomposed to TR_Int_1 through Reaction 1 (see Table 3-5).

Simulations were conducted for the experimental duration of 250 s with time step of 0.01 s and spatial discretization of 1×10^{-5} m. Increasing and decreasing the integration parameters by a factor of 2 did not change the simulation results, implying complete convergence of integration.

Mass loss rate and heat release rate predicted by the model with and without consideration of the blowing agent component are compared in Figure 3-17 with the experimental data. The MLR was predicted to be slightly different for the model with the blowing agent component than the model without. Total mass lost was estimated by integration of the MLR curve through the duration of the experiment. The model which included the blowing agent was better at predicting total mass lost. Associated heat release rate predicted from the model peaked at around 150 kW m^{-2} for both the models. Total heat released, obtained by integration of the HRR curve, was predicted to be closer and within

the uncertainties of the experimental data for the model with the blowing agent. Thus, the prediction of HRR for cone calorimeter scenario was significantly improved by the inclusion of the blowing agent, even though the MLR predictions were not significantly different.

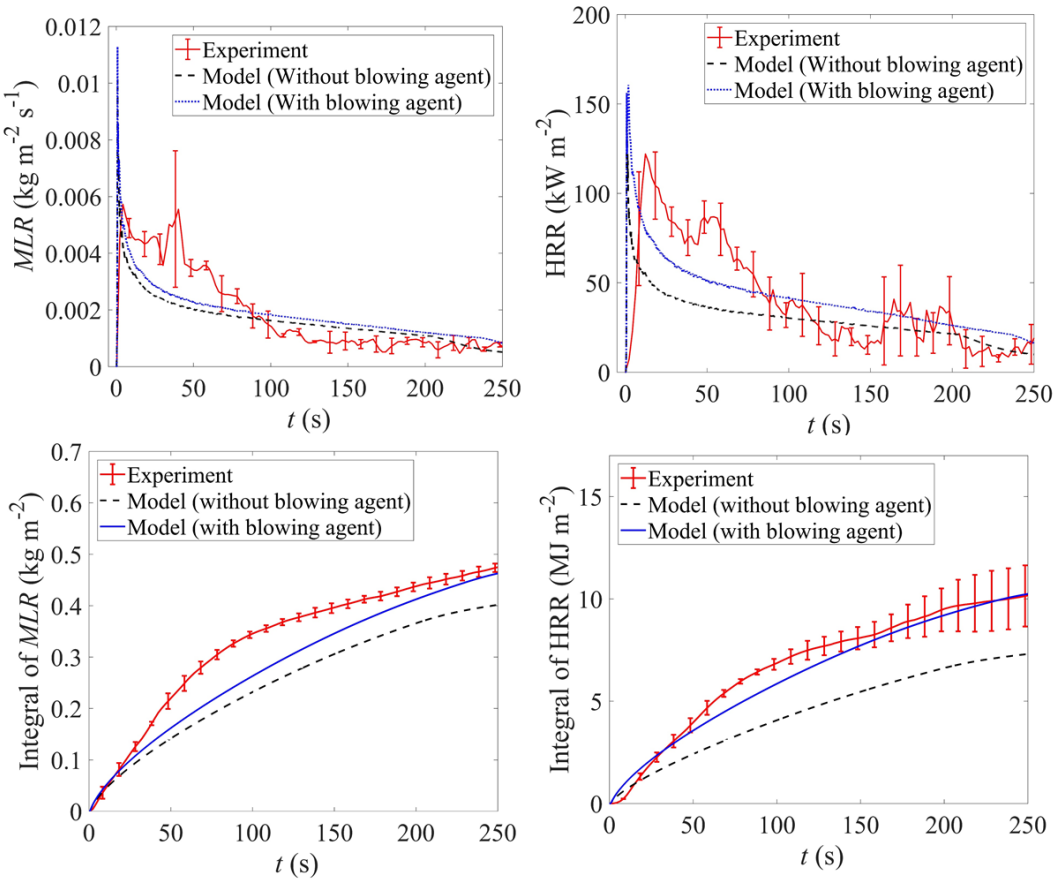

Figure 3-17. Comparison of cone calorimetry experimental data for Tuff-R™ and predictions of the models with and without the blowing agent component

3.4. Large Scale Experiments

Experiments were performed on Tuff-R™ in a large corner configuration, discussed in Section 2.5, with the purpose of obtaining measurements that quantified

crucial parameters during the flame spread on a wall lining PIR foam and investigate how these relate to the data obtained from large-scale experiments performed over PMMA.

3.4.1. Test setup

The test setup was maintained the same as shown in Figure 2-7. However, Tuff-R™ sheets used in these tests were 5.04 cm thick, 146 cm tall, and 60 cm wide. Being thicker than PMMA panels, it was decided to use wider panels to avoid any air entrainment flow disruptions introduced by the thicker samples which could create larger flow instabilities. Tuff-R™ sheets were mounted on Marinite I calcium silicate boards using a set of plastic washers which are recommended for commercial installations. Large-scale experiments were performed on two types of Tuff-R™ sample sheets – with or without the front aluminum foil facer. Two tests were performed on sheets without the foil facer on the front sides. One additional test was performed with the foil facer intact on the front side to understand its impact on the flame feedback. Aluminum foil facer was removed from the back side, the surface which was in contact with the Marinite I boards.

The entire assembly of the sample was placed at the same location under the hood such that the orientation of the corner matched with the previous setup. Calorimetry was performed with the same set of instrumentation as discussed in Section 2.5. The same DSLR camera having expanded spectral sensitivity equipped with a band-pass filter of 900 nm was placed at the same location to focus on flame progression over one Tuff-R™ panel.

The only difference in these tests were the limited number of locations at which the flame heat flux was measured. Eight water-cooled Schmidt-Boelter heat flux gauges were fixed flush with the front surface of the Tuff-R™ panels in each test at locations shown by

green (filled circles) in Figure 3-18. These locations were strategically selected to obtain a reasonable distribution of the heat flux along the vertical and horizontal direction so as to compare with the heat flux data from PMMA experiments.

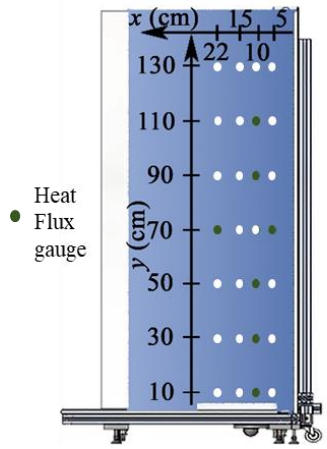

Figure 3-18. Location of heat flux gauges in flame spread tests over Tuff-R™ (White circles indicate additional heat flux gauge locations used in PMMA experiments)

The 30 kW propane sandbox burner was ignited by a remotely operated torch. Once the sample ignited, the samples were exposed to the propane flame for 600 s. This duration of exposure was decided based on preliminary testing which suggested negligible change in the heat release after 600 s.

3.5. Large Scale Experimental Results

In both cases (with or without the foil facer), the insulation panels ignited within 5–15 s after the burner was turned on. The ignition was followed by a formation of a single fire vortex that rolled from the bottom to the top of the corner. This vortex formation was attributed to a quick release of some of the blowing agent from the pyrolyzing foam. The flame was seen to spread over the top of the panels faster than it spread laterally. Significant

portion of the panel was still unburnt after the test, while majority of the thermal impact was evident near the corner where the propane flame directly impinged.

Image snapshots, obtained from the DSLR camera, of flame spread over Tuff-R™ samples with foil facer and without foil facer and are shown in Figure 3-19 and Figure 3-20 respectively for ten time stamps. The extents of each sub-image in both the figures represent the dimensions of the panel where the panel height (from the surface of the burner) of 142.5 cm correspond to the height of the sub-image and the width represents 30 cm of the panel width from the corner. In both the figures, $t = 0$ s correspond to the ignition of propane.

The flames are seen to spread across the entire panel in 10 s for Tuff-R™ without foil facer and it takes around 60 s for the height of Tuff-R™ sample with foil facer to be entirely engulfed in flames. When the flames covered the entire panel height for both type of samples, the relative width from the corner covered in flame was larger for sample with foil facer. The flame size remains the same after 160 s for both type of samples. This agrees well with visual observations where the flame after 160 s for both type of samples mostly comprised of the flickering turbulent propane burner flame. Comparing both the figures and flame spread progression, a slower increase in the flame size is observed in the case of Tuff-R™ with foil facer.

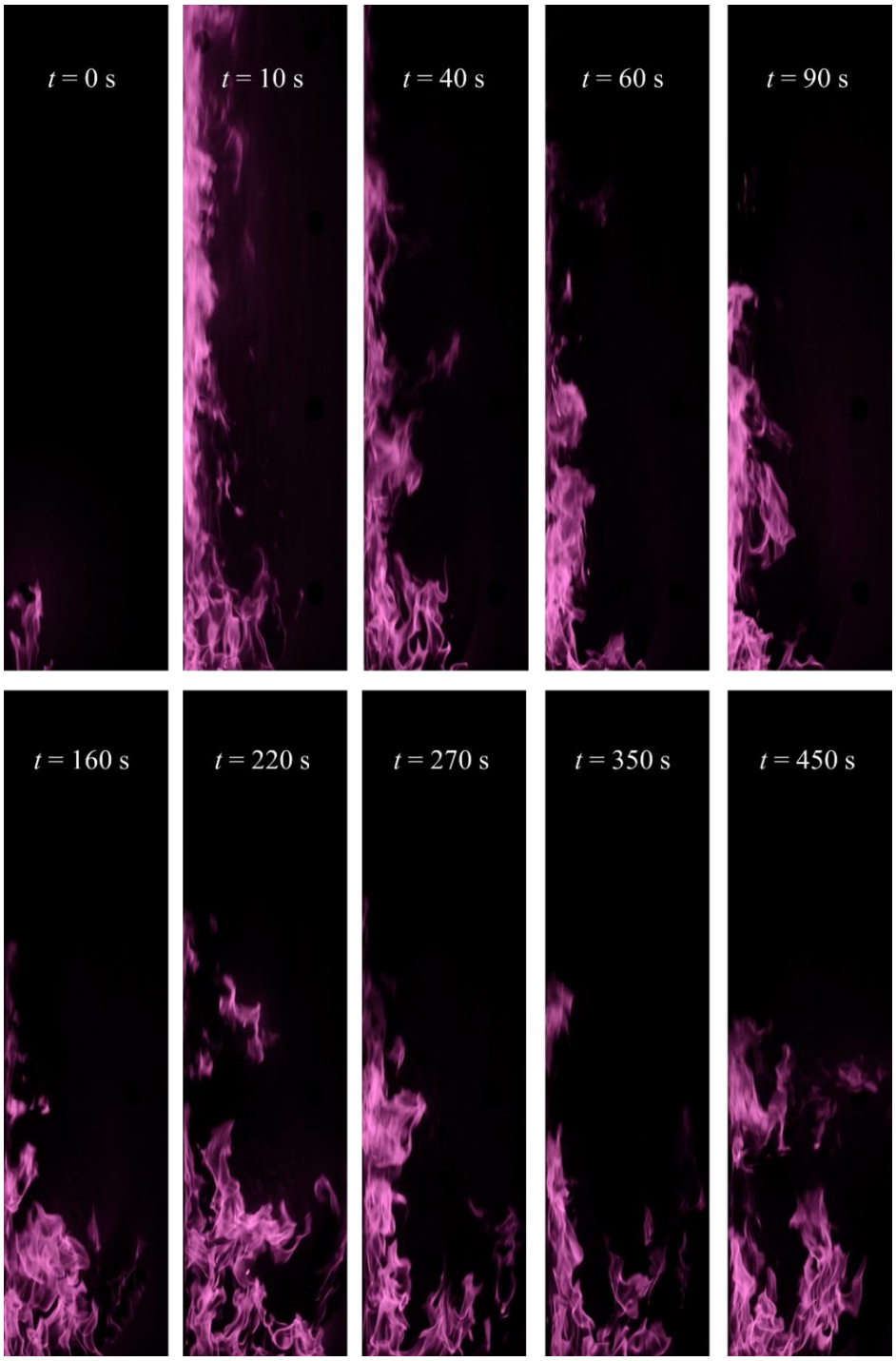

Figure 3-19 : Snapshots of flame spread over Tuff-R™ sample without foil facer (142.5 cm panel height corresponds to the height of each sub-image and the width of each sub-image represents 30 cm of panel width from the corner)

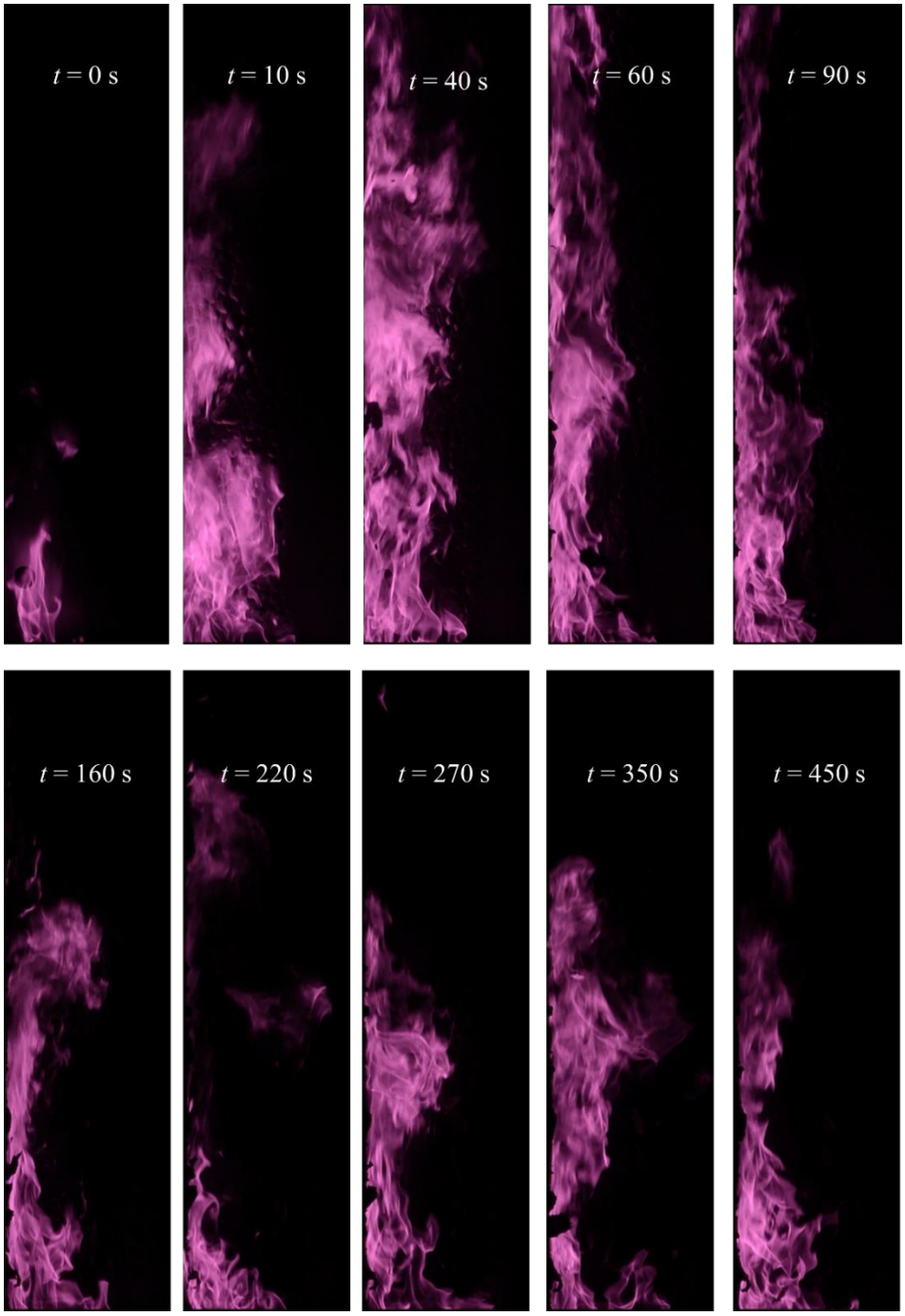

Figure 3-20 : Snapshots of flame spread over Tuff-R™ sample with foil facer (142.5 cm panel height corresponds to the height of each sub-image and the width of each sub-image represents 30 cm of panel width from the corner)

3.5.1. Heat Release Rate

The HRR of Tuff-R™ was calculated based on the same oxygen consumption calorimetry used for PMMA experiments. For the calorimetry expressions, an essential parameter is γ, which is the ratio of total moles of CO_2 and O_2 produced per mole of O_2 required for complete combustion of a fuel. This ratio was assumed to be γ = 1.4 for Tuff-R™ due to the lack of knowledge of the molecular formulae of the gaseous pyrolyzates. This value is the average of four fuels (see Appendix A: Calorimetry) representing a relatively wide complexity in molecular structure of pyrolyzate gases.

Figure 3-21 shows HRR (including contribution from the burner) vs time for Tuff-R™ with and without the foil facer for 600 s. Data for Tuff-R™ without foil facer represented here is an average of two tests. The error bars are calculated by assuming 10% uncertainty in the oxygen-consumption-based heat release measurements (Section 2.7.1).

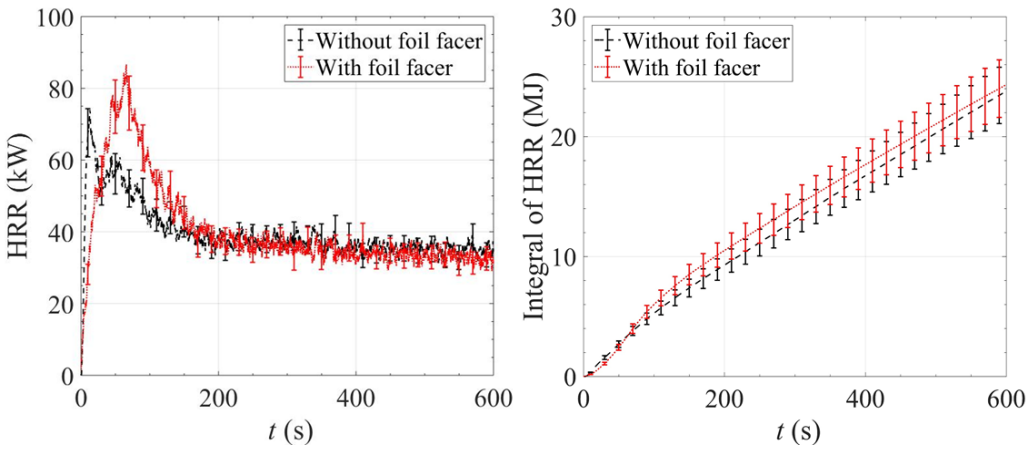

Figure 3-21. Mean HRR and integral HRR measured in the corner-wall flame spread experiments performed on Tuff-R™ with and without foil facer

All Tuff-R™ samples ignited right after propane ignition and the HRR increased to a peak HRR and then decreased somewhat linearly to a plateau value which was slightly more than propane HRR contribution. Rate of increase of HRR is, however, slower for Tuff-R™ with foil facer than Tuff-R™ without the foil facer. This is in agreement with the increase in the flame size for both type of samples, as observed from unprocessed flame spread images shown in Figure 3-19 and Figure 3-20. The HRR reaches its peak of 74 kW (from two tests) within the first 15 s of propane ignition for Tuff-R™ without the foil facer, and reaches the peak of about 86 kW within 65 s for Tuff-R™ with the foil facer. The foil facer on the front panel surfaces thus acted as a mass barrier and delayed the rise of HRR. Contribution of Tuff-R™ combustibles to the total heat release for samples with or without foil facer occurs primarily during the first 200 s after ignition. After the peak, the flame gradually subsides until t = 160 s, after which the propane contributes the most (31 ± 2 kW) to the HRR; the heat release rate is approximately 35 kW after 220 s.

3.5.2. Flame Heat Flux

Flame heat flux measured at the eight locations for Tuff-R™ samples with no foil facer were divided into 10 kW bins and then averaged for the two experiments. The data were binned according to HRR, unlike 10 s bins used for PMMA, due to non-monotonic nature of the HRR profile for Tuff-R™ and relatively larger steady HRR data after 220 s. The uncertainty calculation includes the contribution from the binning and averaging, and a contribution of 3% systematic uncertainty of calibration. Flame heat flux data for the single experiment on Tuff-R™ with the foil facer were also classified into similar 10 kW bins and uncertainty was determined from the data in these bins.

The flame heat flux from Tuff-R™ flame spread experiments were compared with the heat flux at corresponding locations from PMMA flame spread experiments. Flame heat flux obtained from experiments performed on Tuff-R™ with and without the foil facer are compared in Figure 3-22 with the PMMA data. The coordinates of the location (x, y) of the heat flux gauges (HFG) in cm, corresponding to location shown in Figure 3-18, are given for the respective plots.

The flame heat flux variation with HRR for Tuff-R™ with and without foil is similar at most locations. The insulation panel data exhibit a considerably larger scatter but, overall, follow the same trends as the data obtained for PMMA, which justifies the use of empirical correlation of heat flux and HRR developed using the PMMA data in the semi-empirical modeling of the panel experiments. The flame heat flux corresponding to somewhat steady HRR after 220 s is around the flame heat flux values observed for PMMA for similar HRR with the exception of (10, 10) location which shows a systematic discrepancy.

Incident heat flux at (10, 10) just after ignition from Tuff-R™ tests (both with and without foil) is found to be 50% or more lower than the corresponding heat flux in PMMA tests. As the foam sample is consumed, the sample first expanded and then was observed to reduce in thickness, especially near the base of the sample. This thickness change resulted in abstraction of the gauge surface and thereby was responsible for the systematic discrepancy observed for the heat flux at this location.

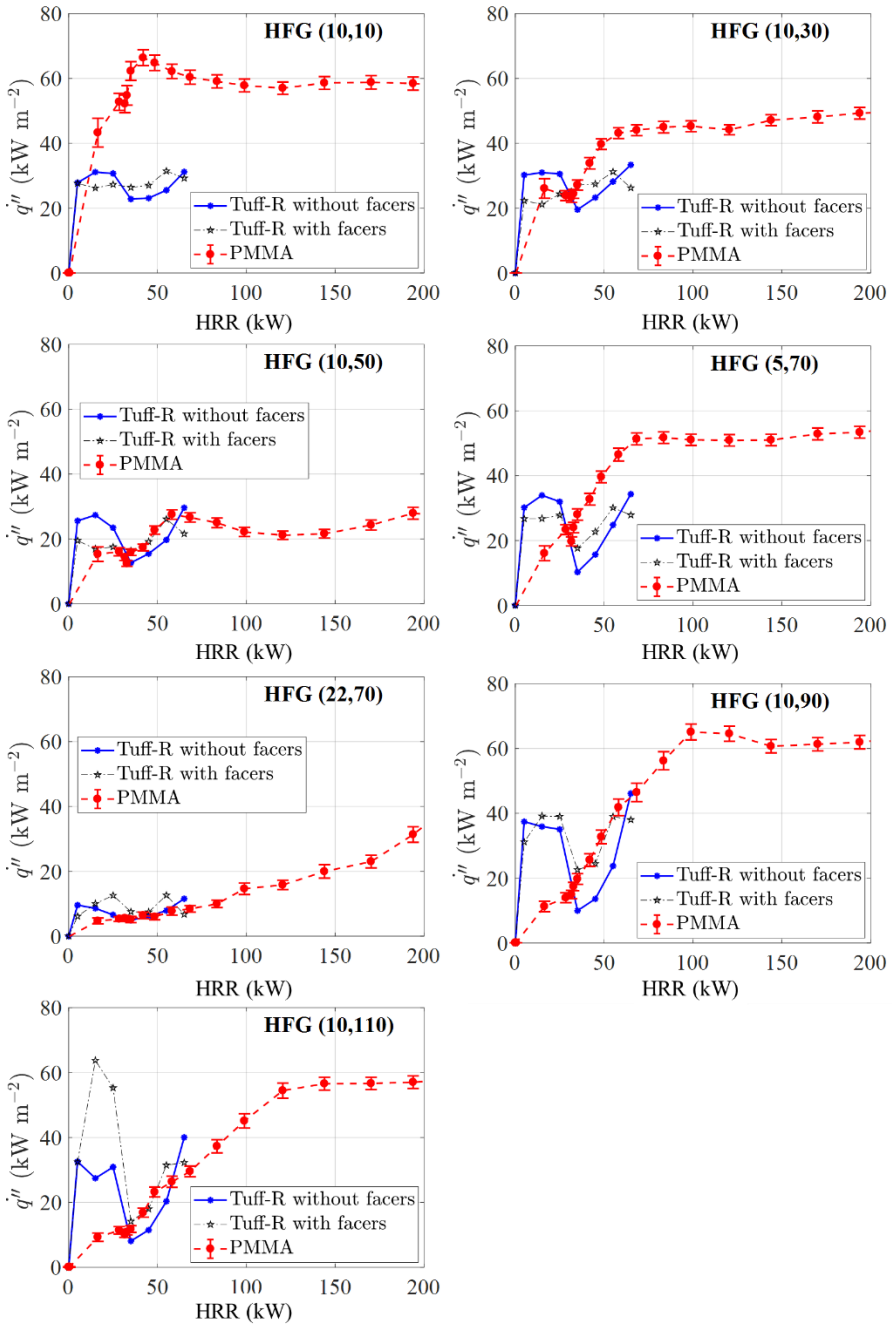

Figure 3-22. Comparison of flame heat flux vs HRR for Tuff-R™ and PMMA flame spread experiments

3.6. Flame Spread Modeling Framework

The relative similarity in flame heat flux measurement for Tuff-R™ and PMMA experiments, as seen in Figure 3-22, facilitates the application of the empirical flame heat feedback model developed using data obtained for PMMA for modeling flame spread on Tuff-R™. The experiments performed without foil facer were selected as the basis for comparing model predictions because the developed pyrolysis model did not include the mass transport inhibition effects induced by the presence of foil facer in the corner flame spread experiments.

The flame spread scenario was modeled in ThermaKin2Ds following the methodology discussed for PMMA in Section 2.8. However, an application of the hybrid model to the Tuff-R™ experiments was impractical due to highly non-monotonic behavior of the HRR with time and inability of the current modeling framework to define multiple transitions between convective and radiative heat feedback histories. Therefore, a decision was made to represent the heat feedback as purely radiative. Usage of purely radiative model in this case was further justified by higher sooting propensity of Tuff-R™ pyrolyzate compared to the PMMA pyrolyzate. Only coupled simulations were performed with radiative heating boundary conditions and using the comprehensive pyrolysis model discussed in Section 3.3.

Tuff-R™ panels were modeled in ThermKin2Ds by discretizing each panel in spatial 28 elements. Each of these elements was prescribed a heating boundary condition using an initial time-dependent input HRR and the empirical flame feedback model. The input HRR was assumed to be a time-dependent profile of 10 s linear rise to a steady value

of 60 kW. Simulations were conducted for 600 s for two types of pyrolysis models – one model with the blowing agent component, and one model without the blowing agent component to understand the impact of blowing agent on HRR predictions on the large-scale. Results of the pyrolysis simulations were used to compute Simulated HRR by adding up contributions from individual elements and the burner using the Eq. (3-1).

$$\text{Simulated HRR}(t) = \text{HRR}_\text{b}(t) + 2\sum_{j=1}^{28} A_j \left[\sum_{i=1}^{Ng} \dot{m}''_{ij}(t)\Delta H_c^i\right] \qquad (3\text{-}1)$$

The coupled simulations were performed by using the simulated HRR as the input HRR for next iteration until the convergence criteria for the simulations, calculated by Eq. (2-13), was satisfied. All simulations converged within 3 iterations. Thermakin2Ds simulations were performed with a time step of $\Delta t = 1\times10^{-2}$ s and 5×10^{-5} m spatial discretization. Increasing or reducing the integration parameters by a factor of 2 did not produce significant changes in the simulations results. Each iteration required about 80 min on a single core of a modern PC.

For quantitative comparison with experimental data and with no intention for material classification based on fire hazard, HRR_{error} and FIGRA values were computed using Eq. (2-14) and (2-15).

3.7. Flame Spread Modeling Results

Flame heat flux time dependencies generated from mean experimental HRR profile for Tuff-R™ and fitted with three linear segments are shown in Figure 3-23. Heat fluxes were set to be incident on Tuff-R™ by piecewise-linear $\dot{q}''$, including a small contribution

from background radiation, defined as black body radiation of water-cooled heat flux gauge surface (291 K).

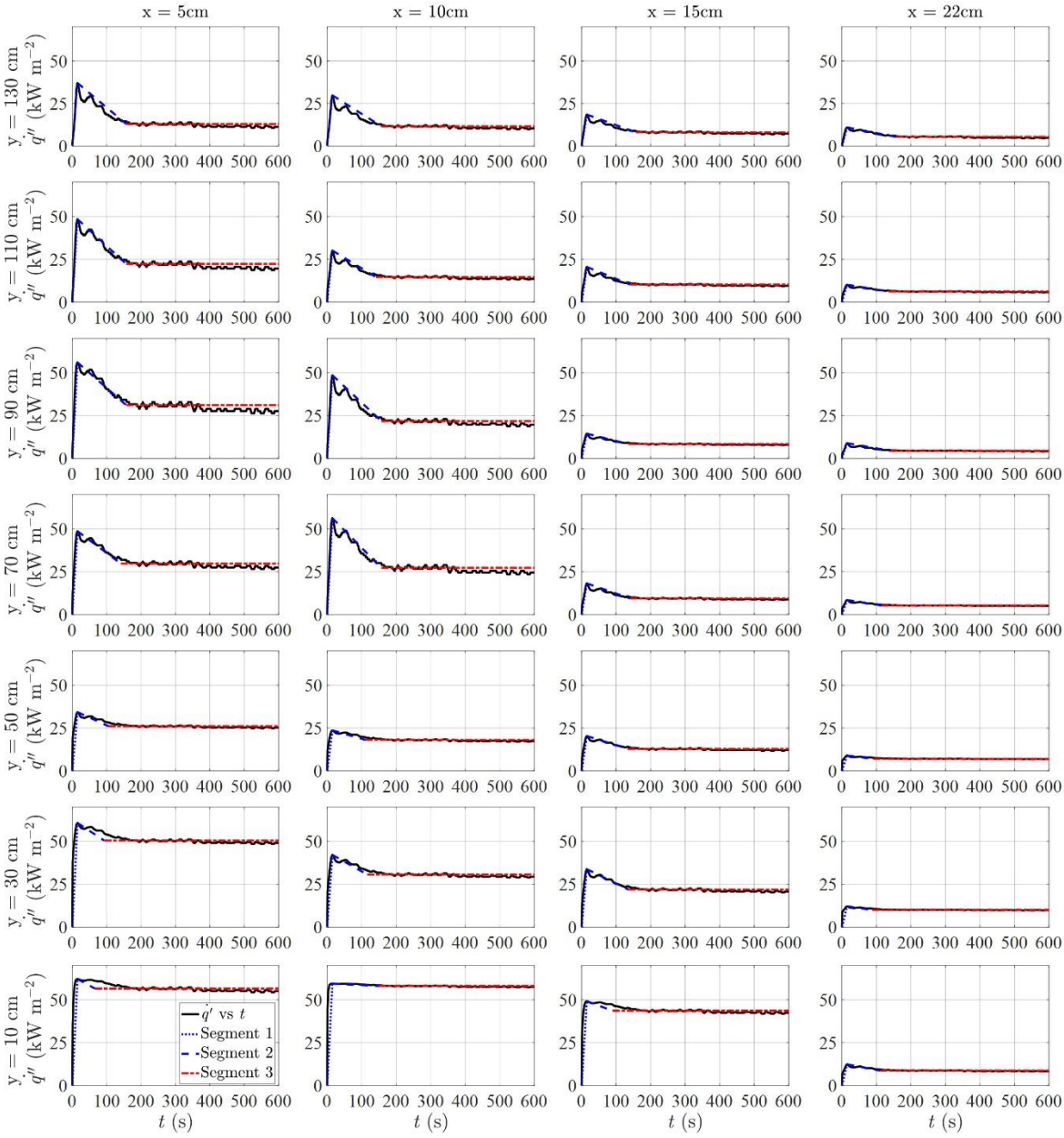

Figure 3-23. Total flame heat flux time dependencies for Tuff-R™ generated using the mean experimental HRR and fitted with a piecewise-linear function

The heat release rate predictions of fully-converged coupled simulations using models with and without the blowing agent component are shown in Figure 3-24 for Tuff-R™ compared with experimental data. The simulations for both the models qualitatively predict the trend of experimental HRR – an immediate rise in HRR, a peak HRR followed by a subsequent decline to a steady HRR value.

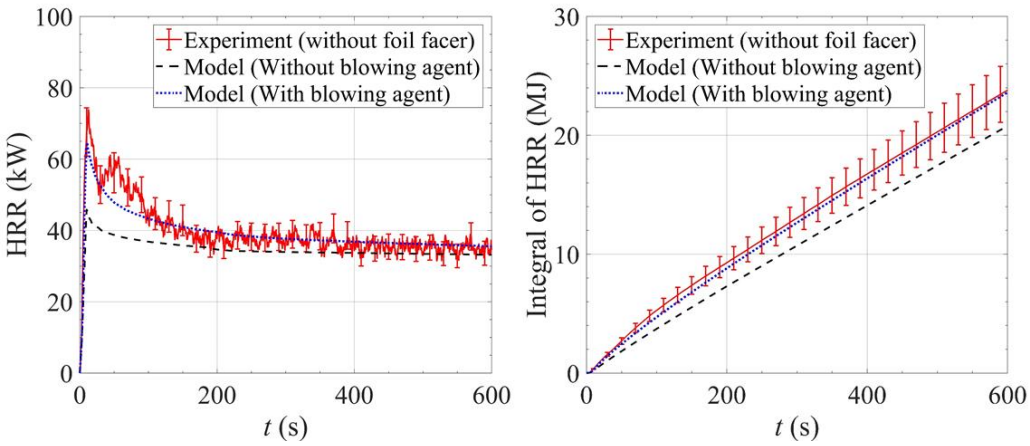

Figure 3-24. A comparison of the mean experimental HRR and integral HRR for flame spread on Tuff-R™ with heat release rates obtained from the coupled simulations using models with and without the blowing agent

The model predictions for simulations that included the blowing agent component were in better agreement with the experimental data than simulations without the blowing agent component. Average HRR_{error} was around -26% for simulations without the blowing agent component, while this error was reduced to -5% for the simulation with the blowing agent component. The peak HRR was also predicted within 12% of the experimental peak HRR value for the model with the blowing agent component. Table 3-9 compares HRR_{error} and predicted FIGRA values with experimental values.

Table 3-9. Comparison of HRR_{error} and FIGRA for *HRR* predictions during flame spread over Tuff-R™.

	HRR_{error} (%)	FIGRA (kW s^{-1})
Experiment	0	4.9
Model: radiation – without blowing agent	-26	4.0
Model: radiation – with blowing agent	-5	5.3

The FIGRA value of 4.9 kW s^{-1} for experiment was slightly over predicted by the simulation which considered the blowing agent component. It is important to note that FIGRA value is not a comprehensive indicator of fire hazard and although quantitatively the FIGRA value for PMMA (1.4 kW s^{-1}) is less than Tuff-R™, PMMA exhibits continuous flaming throughout the test and produces higher total heat.

The predictions further validate the approach to develop comprehensive pyrolysis model and the capability to predict large-scale fire scenario using the presented modeling approach. The ability of the model to predict close to experimental data validates the idea to generalize the flame spread model to complex material such as Tuff-R™. These model predictions are, however, considerably better than those obtained for PMMA, despite the fact that PMMA is considered a much simpler material to parameterize. The apparent inconsistency in model prediction can be explained by two factors. First, the purely radiative assumption for Tuff-R™ is more accurate because its gaseous pyrolyzates are likely to be better precursors for soot, which is the main radiating species. Second, the lack of significant flame spread on Tuff-R™ insulation panels substantially reduced the amplification of errors in the model parameters.

3.8. Conclusion for Chapter 3

The flammability of a Polyisocyanurate (PIR) foam product, Tuff-R™, manufactured by DuPont de Nemours Inc. was analyzed through experiments and modeling performed on a range of sample sizes having mass ranging from a milligram to a kilogram. A complete pyrolysis property set was parameterized using the hill-climbing optimization algorithm developed for inverse analysis of milligram-scale and gram-scale test data. TGA, DSC, and MCC were performed to understand the pyrolysis of cryogenically grounded Tuff-R™ in inert N_2 environment at heating rates between 5 to 20 K min^{-1}. Tuff-R™ pyrolyzed with multiple peaks, typical for a PIR foam, with the maximum peak mass loss rate observed at 600 K, which corresponds to a temperature when an exothermic heat flow was observed in the DSC data. Tuff-R™ degraded by leaving around 32 % residue in all the small-scale tests. A thermal decomposition mechanism comprising of seven first-order reactions in series was found necessary to accurately capture the thermal decomposition. MCC test data was used to determine heats of combustion of individual gaseous pyrolyzates corresponding to the reaction mechanism. Gram-scale tests were conducted using CAPA II apparatus at 40 kW m^{-2} and 70 kW m^{-2} set external radiative and this test data was used to optimize thermal conductivity and density of reaction intermediates and validate the pyrolysis model. Cone Calorimeter tests were performed at 50 kW m^{-2} set heat flux on 2.54 cm thick samples to better understand the effect of blowing agent on thicker samples than those used in CAPA II tests. It was determined from cone calorimetry data and simulations that the 7 wt. % gaseous blowing agent stored in the foam cells contributed significantly to the foam burning rate and had to be accounted for in fire simulations.

In large-scale experiments on Tuff-R™ with and without the foil facer, majority of heat released by both Tuff-R™ samples was during the initial 220 s after ignition. A general agreement was found between flame heat flux feedback variation with heat release rate for Tuff-R™ samples (with and without the foil facer) and data obtained from PMMA flame spread experiments. Therefore, the flame heat feedback model developed for PMMA (Section 2.7.2) was coupled with the validated Tuff-R™ pyrolysis model to predict large-scale fire dynamics during the flame spread over Tuff-R™.

Coupled simulations, where the simulated HRR was iterated until convergence, predicted the HRR for the large-scale tests on Tuff-R™ without foil facer. The fully-converged modeled HRR underpredicted the mean experimental data by as much as 26% when blowing agent component was not considered. The fully-converged modeled HRR predicted the experimental data within 5% when 7 wt. % blowing agent was included in the model. This modeling approach was thus found to perform well, indicating that it can potentially be extended to other materials, without modifications. Further, the application for this modeling framework was investigated for another wall-lining material, oriented strand board (OSB).

Chapter 4: Experiments and Modeling of Pyrolysis and Flame Spread over Oriented Strand Board

The hierarchical methodology developed until now was then extended further to another important building wall-lining material, Oriented Strand board (OSB). OSB sheets selected for this study was a PS2-10-compliant OSB manufactured by Georgia-Pacific Blue Ribbon. The exact same type of OSB was used by previous studies [186,187] to characterize the pyrolysis properties using the same approach as was used in this research study for PMMA and PIR foam. Sheets of dimensions 244 cm × 122 cm × 1.1 cm with a mean bulk density of 664 ± 56 kg m^{-3} purchased from a major U.S distributor, were used to cut corresponding samples for different scales of experimental setups.

4.1. Small-Scale Experiments

All the small-scale experiments necessary to develop the OSB pyrolysis model were performed by my colleagues in the research group. Only brief presentation of these results is provided here. Further details can be found in refs [186,187].

4.1.1. TGA-DSC Experiments

Finely grounded OSB samples with a particle size between 20 and 300 μm, desiccated in controlled environment (relative humidity about 25 %) for 48 hr, were used for conducting 10 anaerobic thermal decomposition tests in Pt-Rd crucibles with the lid at 10 K min^{-1}. Six tests were performed at 10 K min^{-1} in ceramic crucibles without the lid to understand the impact of the lid on thermal decomposition. Five tests were performed on the final residue collected from anaerobic tests to facilitate determination of specific heat

capacity of the final residue. Additional three tests were performed at 5 and 20 K min^{-1} each for validating the thermal decomposition model at heating rates different than those used for parameterization.

4.1.2. MCC Experiments

Three tests were performed on grounded OSB samples having mass between 4-6 mg. Samples were pyrolyzed in nitrogen and the gaseous pyrolyzates were mixed with excess oxygen and completely combusted in the combustor maintained at 1173 K. Instantaneous HRR was measured by oxygen consumption calorimetry.

4.1.3. CAPA II Experiments

CAPA II gasification tests were conducted on OSB following the procedure described in Section 2.1.4. Axisymmetric CAPA II samples cut from the OSB sheets were 7 cm in diameter and 1.1 cm thick. The samples were placed in a sample holder (Figure 2-2) surrounded by Kaowool insulation rings around it to maintain uniform heating primarily from the top. The sample was placed in good thermal contact on a copper foil, similar to how it was performed during experiments on PMMA and PIR foam. The back surface of the copper foil was painted with a black paint of known emissivity of 0.92. Back surface temperature of the sample was monitored by the IR camera which focused on the painted back surface of the copper foil. Simultaneously, mass loss data using a precision mass balance and front profile expansion using a video camera were monitored during the gasification tests. Anaerobic conditions (<1 vol. % O_2) during these gasification tests were maintained by a controlled nitrogen flow at 185 L min^{-1}.

The OSB sheets had a rough side and a smooth side, and thus, experiments were performed to understand the impact of OSB orientation, exposing a specific side to the heater. Six tests in total were conducted at set external radiant heat flux of 35 kW m^{-2} and 65 kW m^{-2} each to understand the impacts of the OSB orientation (smooth versus rough side) exposed to the radiant heater and/or of bulk density variation, and to accumulate data statistics for model parameterization.

4.2. Small-scale Experimental Results

Since the small-scale tests were conducted in another study, the experimental results are shown and briefly discussed along with the pyrolysis model description, in the following Section 4.3.

4.3. OSB Pyrolysis Model

The separate studies [186,187] which parameterized this model investigated the impact of non-uniform density on the pyrolysis model predictions of gasification tests. The pyrolysis model with non-uniform density did not impact the gasification MLR predictions a lot, and thus, the pyrolysis model used in this study was the model developed by assuming uniform bulk density of OSB of 664 kg m^{-3}. This model is briefly described here along with corresponding experimental data.

4.3.1. Reaction Kinetics, Stoichiometry, and Heats of Reaction

The experimental TGA-DSC data for 10 K min^{-1} test in the form of MLR, heat flow data, both normalized by initial mass, and mass fraction and integral of normalized heat flow are shown in Figure 4-1. The first peak in the MLR profile around 400 K could be

attributed to chemically-bound water, followed by the main decomposition curve and subsequent peaks observed at higher temperatures. From the mass-loss data, the chemically bound water was estimated to be about 1.9 %.

The MLR data for 10 K min^{-1} test was used for parameterizing apparent thermal decomposition reactions. The optimization algorithm, similar to the one developed using black PMMA (Section 2.3.1) and utilized for PIR foam (Section 3.3.1), was applied for parameterizing OSB thermal decomposition reaction kinetics using 10 K min^{-1} experimental data. Five first-order reactions in series were proposed for OSB thermal decomposition, given in Table 4-1. The first reaction captures the evaporation of chemically bound water, while reaction 2 through 4 are representative of MLR peaks at 540, 625, and 700 K respectively.

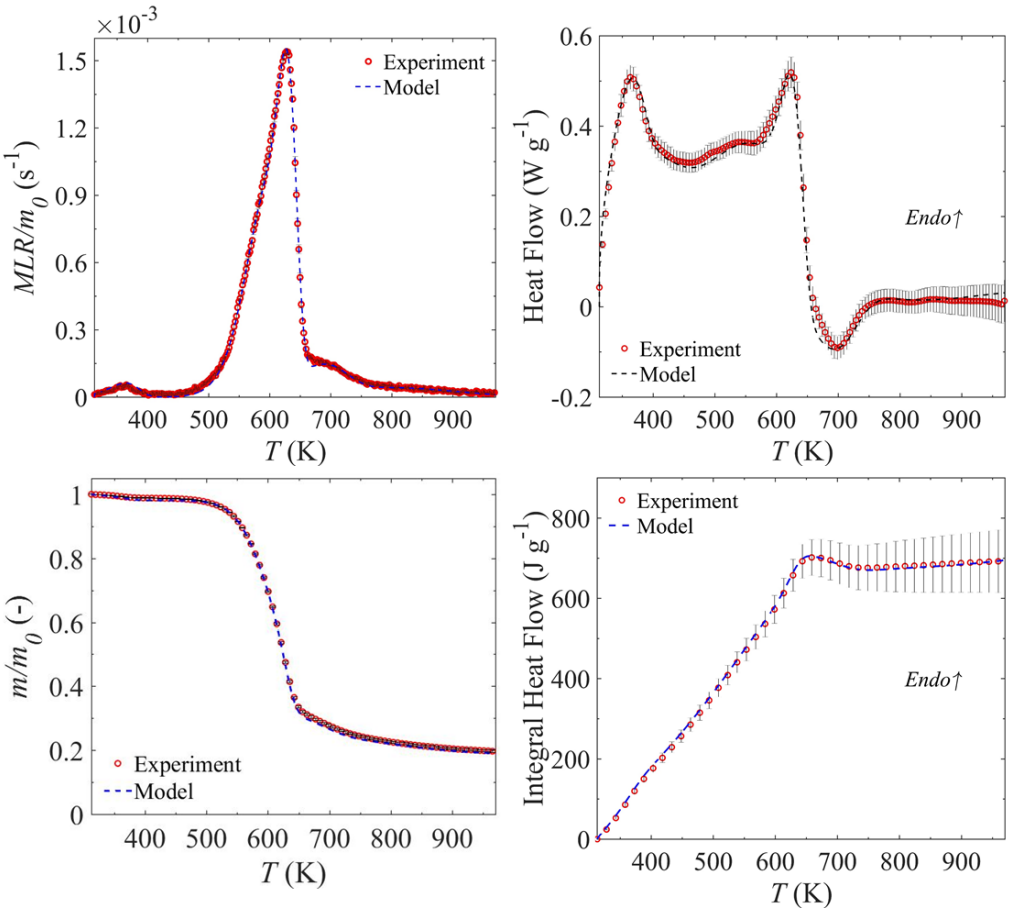

Figure 4-1. Experimental data for mass fraction, mass-loss rate, heat flow, and integral heat flow along with model fit for TGA-DSC tests performed at 10 K min^{-1}

Specific heat capacity of initial component (OSB) and the final residue (Char) was obtained from experimental data by dividing experimental heat flow data with instantaneous heating rate. A linear, temperature dependent heat capacity functions were estimated for both these components. Heat capacities for intermediate solid components were interpolated between heat capacity of OSB and Char in equal steps. The heat capacity of water was obtained from literature [165]. The heat capacity functions are given in Table 4-2. All gaseous components were assigned a heat capacity of 2100 J kg^{-1} K^{-1}, which is the mean heat capacity of C1 to C8 hydrocarbons at 600 K [132]. Heats of reaction was

estimated for each reaction by the difference of experimental data and a baseline sensible heat flow which was simulated by forcing all heats of reaction to zero. The estimated heats of reaction is also shown in Table 4-1.

Table 4-1. Decomposition reaction mass-based stoichiometry, kinetic parameters, and heat of reaction (positive heat values correspond to endothermic reactions) for OSB (1.9 wt. % Water and 98.1 wt. % OSB component).

Rxn #	**Reaction**	A_r **(s^{-1})**	E_r **(J mol^{-1})**	ΔH_r **(J kg^{-1})**
1	Water → Water_vapor	1.55×10^4	4.35×10^4	2.78×10^6
2	OSB→ 0.72 OSB_Int1 + 0.28 OSB_Gas1	1.56×10^7	1.04×10^5	6.82×10^3
3	OSB_Int1→ 0.45 OSB_Int2 + 0.55 OSB_Gas2	2.65×10^{12}	1.74×10^5	1.37×10^5
4	OSB_Int2→ 0.77 OSB_Int3 + 0.23 OSB_Gas3	8.93×10^3	8.37×10^4	-2.90×10^5
5	OSB_Int3→ 0.77 Char + 0.23 OSB_Gas4	4.40×10^{-1}	3.86×10^4	-2.32×10^5

Table 4-2. Heat capacity of all condensed phase components

Component	**Heat capacity (J kg^{-1} K^{-1})**
Water	$5200 - 6.7T + 0.011T^2$
OSB	$-159 + 4.53T$
OSB_Int1	$197 + 3.40T$
OSB_Int2	$553 + 2.27T$
OSB_Int3	$909 + 1.13T$
Char	1270

4.3.2. Heats of Combustion of Pyrolyzate gases

Heats of combustion, ΔH_c, of pyrolyzate gases, were estimated by simulating MCC tests and adjusting the ΔH_c values for each component until the experimental and simulated HRR were in agreement. Heat of combustion was assigned to only when for a corresponding HRR, there was an associated mass loss in TGA for the specific temperature. The ΔH_c values are listed below in Table 4-3. The effective total ΔH_c for OSB was estimated to be 13.1 kJ per gram of lost mass.

Table 4-3. Heats of combustion of pyrolyzates gases corresponding to OSB thermal decomposition reaction scheme.

Component	**ΔH_c (kJ g^{-1})**
Water_vapor	0
OSB_gas1	12.5
OSB_gas2	15.2
OSB_gas3	11.5
OSB_gas4	7.5

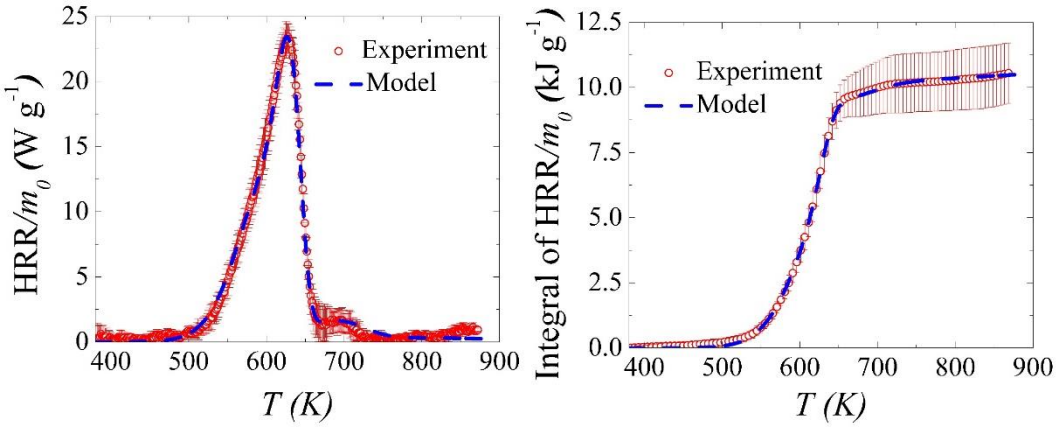

Figure 4-2. Comparison of MCC experimental instantaneous and integral HRR with model predictions

4.3.3. Thermo-physical properties

CAPA II experiments were simulated to optimize density and thermal conductivity of the intermediate solid components. Thermal decomposition reaction scheme shown in Table 4-1 was adopted and the CAPA II mean profile expansion data and mean back surface temperature data of the 65 kW m^{-2} tests were used for optimization of density and thermal conductivity respectively. This test was selected over the 35 kW m^{-2} test because the sample underwent complete decomposition only at 65 kW m^{-2}. The sample orientation (smooth or rough side exposed to the heater) of OSB did not impact the experimental data and thus only test data for the exposed rough side were used for inverse analysis. The experimental MLR data for CAPA II tests performed at 35 kW m^{-2} and 65 kW m^{-2} set radiant heat fluxes are shown in Figure 4-3

The profile expansion data indicated that the sample thickness increased uniformly by about 1.6 mm or 15 % of the original sample thickness. The intermediate solid component density was varied until the profile expansion predicted by the simulations agreed with the experimental data. Once the density of all components was optimized, the back surface temperature data was used as optimization target for thermal conductivity determination. The hill-climbing optimization algorithm described in Section 2.3 was used and the Eq. (2-3) served as the optimization function. The model fit of the back surface temperature, using these optimized density and thermal conductivity values, for the 65 kW m^{-2} CAPA II tests is shown in Figure 4-3.

The optimized density and thermal conductivity values are shown in Table 4-4. It is important to note than the density of OSB component is slightly below the mean bulk

density of the OSB sheet because the OSB also contains 1.9 wt. % of chemically bound water which contributes to its mass but not to the volume. This table also shows the emissivity values used for the solid components. The broadband emissivity value for the component OSB and Char was assigned to be 0.81 and 0.70 respectively, based on experimental data collected by Försth and Roos [188] for plywood, a similar engineered wood material. The emissivity values for other components were linearly interpolated. OSB was assumed to be optically opaque with no in-depth absorption by prescribing a high absorption coefficient ($\kappa = 1000\ m^2\ kg^{-1}$).

Table 4-4. Thermo-physical properties of solid components corresponding to thermal decomposition reaction scheme for OSB

Component	**Emissivity (-)**	**Thermal conductivity ($W\ m^{-1}\ K^{-1}$)**	**Density ($kg\ m^{-3}$)**
OSB	0.81	0.13	652
OSB_Int1	0.78	0.06	468
OSB_Int2	0.76	0.42	184
OSB_Int3	0.73	0.39	142
Char	0.70	0.53	108

Figure 4-3 also shown the model fit and model predictions compared with the reported experimental data. The MLR predictions and the back surface temperature prediction, also shown in Figure 4-3, serve as the validation for the pyrolysis properties. These figures indicate that the model predicts gasification tests with sufficient accuracy. The model, however severely under predicts the second MLR peak. This discrepancy was partially attributed to the shrinkage of OSB during the gasification test at later stages of the

tests, especially at the higher heat flux. The reduction in OSB sample created non-uniform heating conditions as the sample received additional heat from the exposed sides.

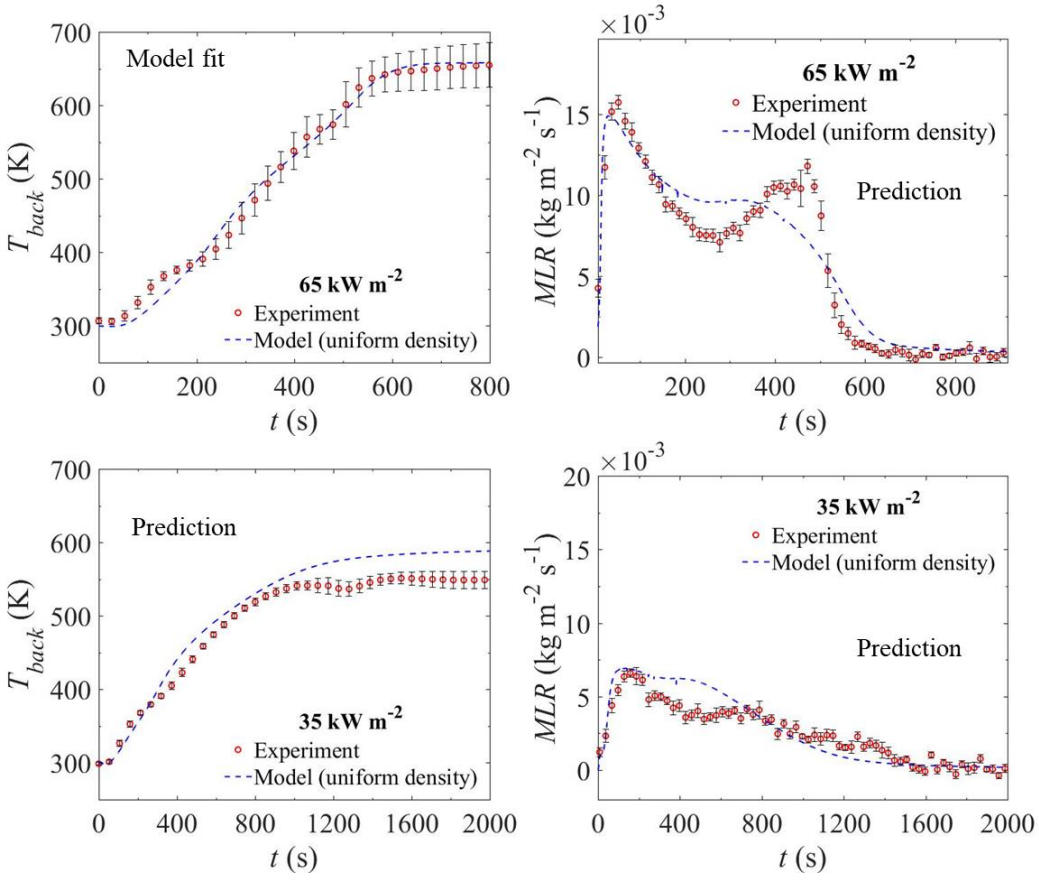

Figure 4-3. Experimental data for CAPA II tests conducted at 35 kW m^{-2} and 65 kW m^{-2} on OSB along with uniform density model fit and model predictions

4.4. Large-scale Experiments

The test setup described in Section 2.1 was used to perform experiments on two OSB panels having dimensions 146 cm × 50 cm × 1.1 cm mounted in the corner geometry on the Marinite I calcium silicate backing board. The OSB panels was mounted such that the rough side was exposed to the propane flame, similar to the CAPA II sample conditions which were used for thermo-physical property optimization. The conditions of the exhaust

flow and the propane burner were maintained exactly same as during the PMMA and PIR foam tests.

For the OSB test, the measurements during the experiments included measurements necessary for calorimetry, as discussed in Section 2.1. The same D800 DSLR camera with the modified sensor and a narrowband 900 nm filter was used to monitor emissions from the soot during the OSB flame spread. The camera was set at same conditions as used during the PMMA tests – ISO 320, F-9 aperture and exposure time of 5 ms.

The only difference in these tests was the use of heat flux gauges in 4 locations, as shown in Figure 4-4. These locations were selected to primarily compare total heat flux evolution with the data from experiments performed over PMMA.

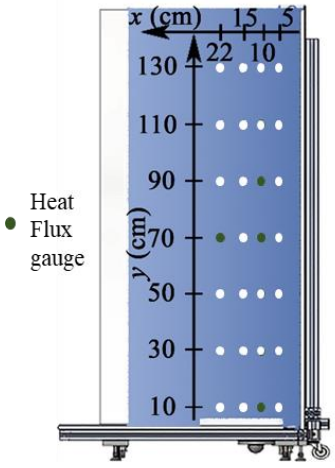

Figure 4-4. Locations (marked by green circles) of heat flux gauges for large-scale flame spread tests over OSB (Locations marked with white circles indicate additional locations used during PMMA experiments)

Three tests were performed to acquire sufficient data and determine statistics. Each test began with ignition of the 30 kW equivalent propane burner. The first test was

continued for about 600 s after the propane ignition and the remaining two tests were terminated at 300 s after propane ignition. The duration of the last two tests was reduced based on the observations from the first test, which are discussed in the next section. All tests were terminated by switching off the propane supply and the combustion was extinguished with a CO_2 extinguisher. The sample mass of OSB was measured before and after the last two tests to compute the effective total heat of combustion of OSB, and further validate the calorimetry.

4.5. Large-scale Experimental Results

In all the tests, the OSB supported flame spread. The first test which was conducted until 600 s after the propane ignition suggested that after 300 s the OSB begins to decouple and disintegrate from the Marinite I backing board. Since the purpose of the tests was to primarily study upward flame spread phenomenon, the remaining two tests were terminated at 300 s, before which the flames were seen to reach the top of the panels and then subside. After termination at 300 s, the OSB panels did not self-sustain flaming combustion and they were extinguished with a CO_2 extinguisher to avoid any mass loss due to smoldering combustion.

4.5.1. Heat Release Rate

Expressions for heat release rate described in Section 2.7.1 and derived in Appendix A: Calorimetry were used for calculating the HRR for OSB experiments. The parameter, γ, representing the ratio of total water and carbon dioxide produced per mole of oxygen consumed during complete combustion of OSB, was calculated by assuming OSB to be constituted of 40 wt. % cellulose, 32 wt. % hemicellulose, and 28 % lignin [189]. The

parameter, γ, was calculated by assuming complete combustion of the monomer of cellulose ($C_6H_{10}O_5$, γ = 1.83), hemicellulose ($C_5H_8O_4$, γ = 1.80), and lignin ($C_{81}H_{92}O_{28}$, γ = 1.41).

Mean experimental HRR evolution with time after propane ignition, *t*, until 300 s after propane ignition along with the integral HRR is shown below in Figure 4-5. This HRR includes the contribution from propane burner flame. The uncertainty of the HRR was obtained as two standard deviations of the mean from the three experiments for the 300 s duration shown here.

The HRR rises immediately above the propane flame contribution of 31 ± 3 kW within 20 s indicating ignition of OSB panels. The HRR increases somewhat linearly to a peak of about 120 ± 8 kW at *t* = 150 s. After the HRR reaches the peak, the HRR is somewhat steady around the peak value, with a slightly decreasing trend for the rest of the test until 300 s.

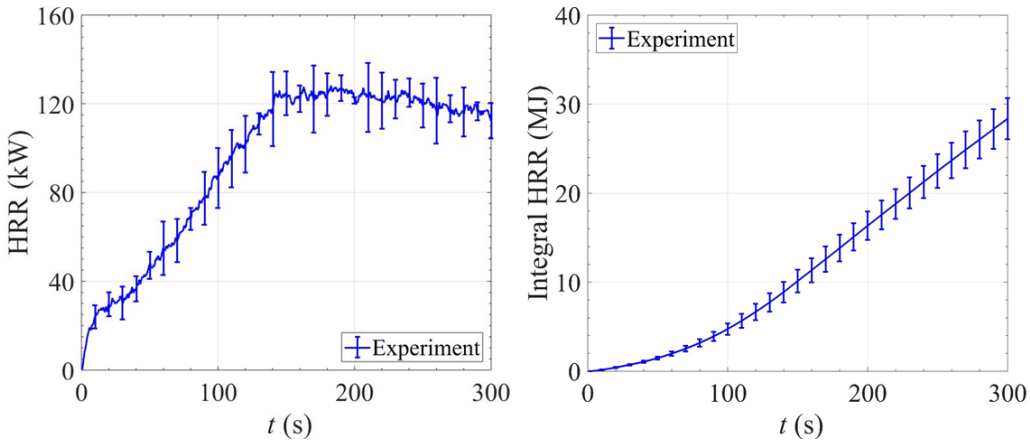

Figure 4-5. Mean HRR and integral HRR measured in the corner-wall flame spread experiments performed on OSB

Total heat released including the propane burner contribution at 300 s is 28.4 ± 2.3 MJ. However, for estimating total effective heat of combustion, the HRR data for the last two test until the HRR goes to zero (t = 400 s) were considered. The HRR was integrated until this time, to account for small HRR contribution from the mass loss from OSB after the propane burner was shut off. The total propane burner contribution at 400 s to the HRR was estimated to be about 11.8 MJ. HRR contribution of OSB was calculated by subtracting total propane burner contribution (11.8 MJ) from total HRR (about 31.4 MJ) at 400 s .The total effective heat of combustion of OSB was calculated by dividing the HRR contribution of OSB by the total lost mass (1635 g) measured as a difference between mass of OSB before and after the test. The total effective heat of combustion for OSB was then estimated to be 12.0 MJ per kg of lost mass. This value close to the effective heat of combustion value of 12.5 ± 0.8 MJ per kg of lost mass, determined from cone calorimetry experiments performed on the exact same OSB [187].

4.5.2. Flame Heat flux

Flame heat flux data was processed in the similar way as done for PMMA (Section 2.7.2), by first binning the data in the same 10 s intervals and then averaging the data within these bins and between the three experiments. The flame heat flux correlated with HRR for the 4 locations are shown in Figure 4-6. The flame heat flux for OSB tends to reach the same heat flux plateau as observed in the PMMA experiments, but the HRR at which the heat flux reaches the plateau is different for OSB than PMMA. For example, the rate of rise of heat flux with HRR is slower near the corner at x = 10 cm, y = 10 cm for OSB than for PMMA at the same location, while the rise rate is higher at x = 10 cm, y = 90 cm. Similarly, the rise rate at x = 22 cm, y = 70 cm is higher for OSB than for PMMA at the

same location, possibly indicating slightly different flame spread and/or structure of the flame supported by PMMA and OSB. The possibility of different flame structure was explored further in the following image analysis section.

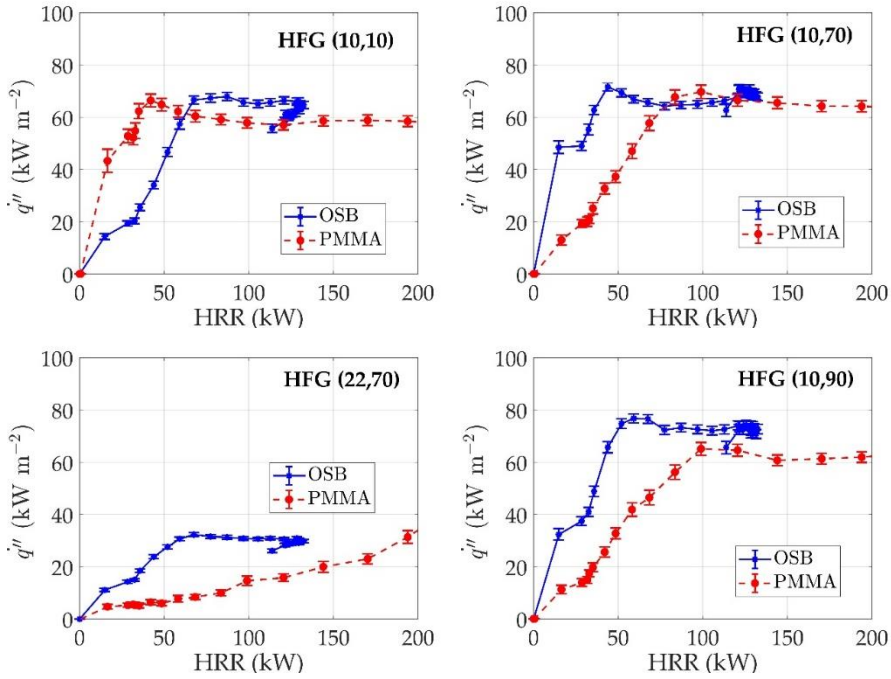

Figure 4-6. Comparison of flame heat flux vs HRR for OSB and PMMA flame spread experiments

4.5.3. Image Analysis

The images from DSLR camera for the OSB experiments for the narrowband of 900 nm wavelength were analyzed in exactly the same way as done for PMMA. First, the images were binned in 10 s bins, converted to greyscale by equal weighted mean of the R, G, and B channels, and then averaged within these bins and across the experiments. The average normalized intensity of greyscale images for PMMA and OSB are shown at three HRR in Figure 4-7. The absolute intensity is normalized here by the maximum intensity observed in PMMA for a particular HRR. Normalizing by the maximum PMMA intensity

can provide information about the percentage difference between intensities at a particular location for these materials, which can be correlated with observed heat fluxes.

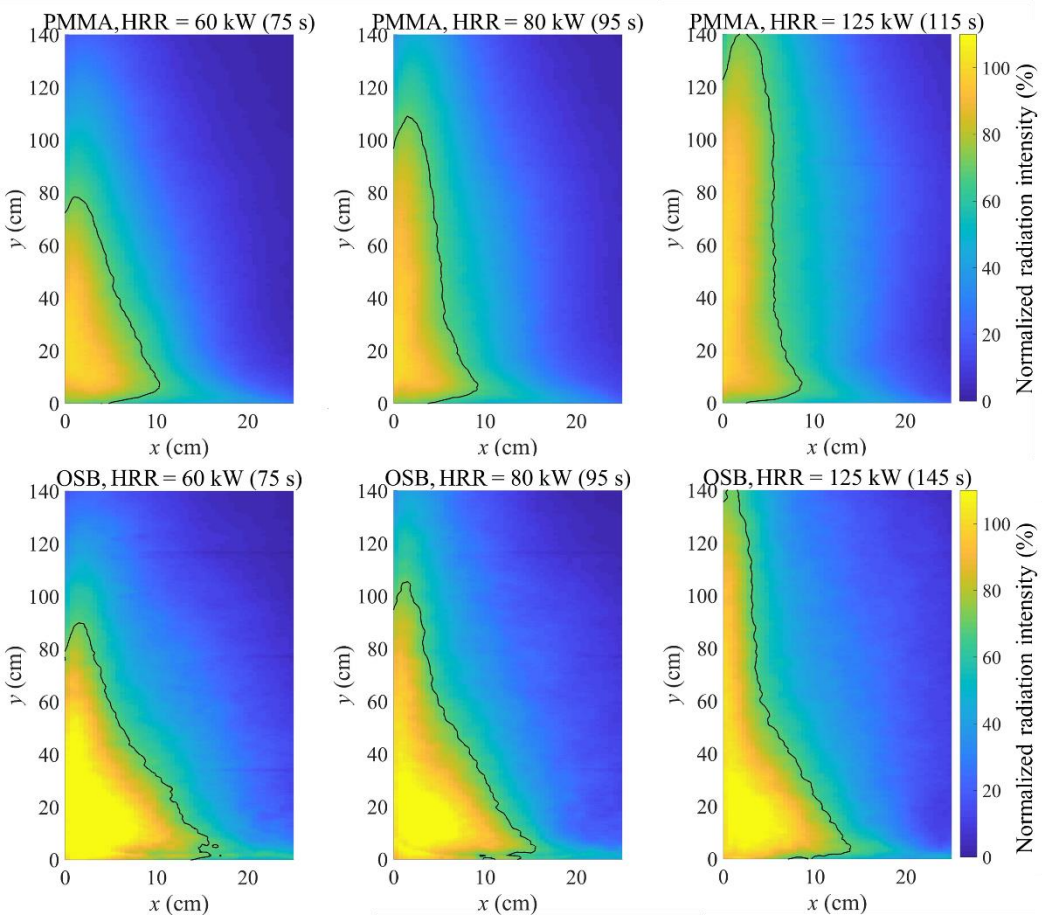

Figure 4-7. Comparison of normalized (by maximum intensity observed for PMMA at a given HRR value) radiation intensity for PMMA (top row) and OSB (bottom row) at 60, 80, and 125 kW. (The black solid line indicates a contour of 50% normalized radiation intensity)

At the same HRR, the radiation intensity for OSB is higher than PMMA in region approximately around the burner flame, indicated by greater than 100% normalized intensity for OSB in Figure 4-7. The normalized intensity for OSB, on the other hand, appears to be lesser or equal to PMMA at locations above 60 cm. The black contour line

representing 50% normalized radiation intensity also indicate qualitative differences in the radiation intensity contour for both materials at the same HRR.

The differences observed here in the normalized radiation intensities and the flame heat flux vs HRR trends may manifest in the form of errors in HRR predictions during the flame spread over OSB. This is further explored and discussed in Section 4.7.

4.6. Flame Spread Modeling Framework

Modeling framework developed in Section 2.8 was extended here to further test the robustness of the framework and the validity of assumptions for a complex wall-lining material such as OSB. Each of the 1.1 cm thick OSB panel was discretized into 28 elements. The pyrolysis model described in Section 4.3 was used to solve condensed-phase thermal decomposition coupled with mass and heat transfer. This pyrolysis model was coupled with the empirical flame heat feedback correlations developed using PMMA experimental data, discussed in Section 2.7.2. Both uncoupled and coupled simulations were performed for OSB, in order to investigate effects of differences in heat flux and HRR correlation observed for OSB compared to PMMA in Section 4.5.2.

The heating boundary conditions for the discretized elements were prescribed in similar way as done for PMMA. The heat flux profiles for the discretized elements for OSB panels were fitted with three piecewise-linear segments. The heating boundary condition for each element was described as these linear fits during the flame spread simulations. Each element was simulated as a 1D pyrolysis process exposed to the prescribed heating conditions in Thermakin2Ds. The HRR was the calculated using Eq. (3-1), which considered the contribution of the propane burner flame, production of individual

pyrolyzate gases predicted by ThermaKin2Ds their heats of combustion (Table 4-3), and the area of each element. For OSB, the heat flux profile fits were stipulated as purely radiation based or a hybrid of convection expression and radiation with a 30 kW m^{-2} threshold to switch from convection expression to radiation, similar to that used for PMMA. The heat flux represented by only convection expression was known to result in significant under-prediction of HRR predictions for PMMA, and thus was not considered here for OSB.

All simulations were performed in ThermaKin2Ds at a time step of 1×10^{-2} s and spatial resolution of 5×10^{-5} m. Changing these integration parameters by a factor of 2 did not change the predictions, indicating convergence.

4.7. Flame Spread Modeling Results

Flame heat flux dependencies with time for 28 locations using the experimental HRR as an input HRR is shown in Figure 4-8. This figure also shows three piece-wise linear fits for these locations. These heat flux values include a small correction for contribution from ambient radiation, estimated as black body radiation corresponding to temperature of 291 K representing temperature of cold water used for water-cooled gauges.

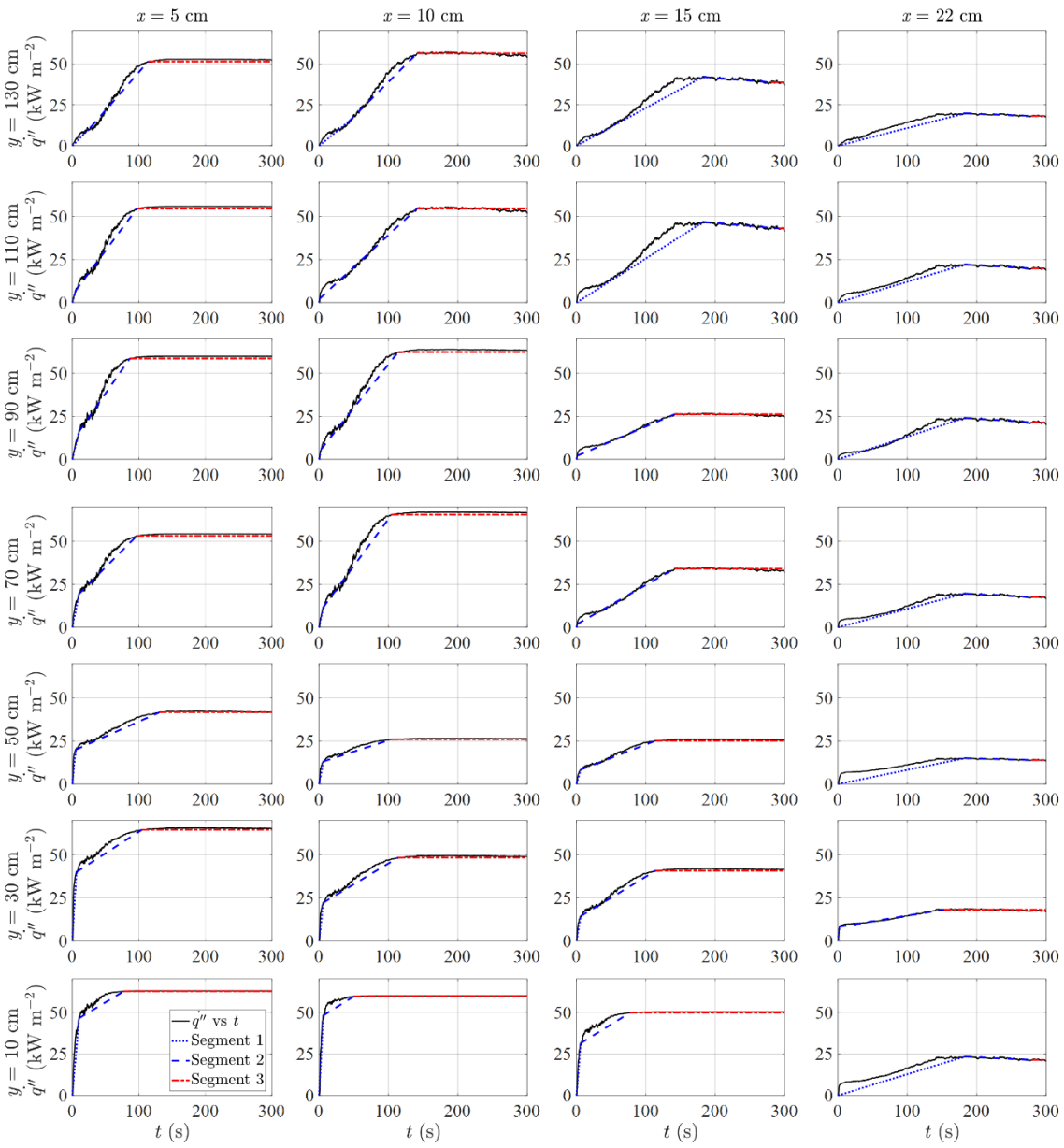

Figure 4-8. Total flame heat flux time dependencies for OSB generated using the mean experimental HRR and fitted with a piecewise-linear function

The results from uncoupled and coupled simulations for radiation or hybrid heat flux model are shown in Figure 4-9. The HRR predictions for all these cases agree very well with the experimental HRR during the initial rise when the flame begins to spread over the OSB panel. However, the peak HRR magnitude predicted by all the models is

about 20-25% below the experimental HRR peak of 125 kW. The time to peak is also predicted to be about 15-20% earlier than experimental time to peak HRR of 145 s. The HRR_{error} as calculated using Eq. (2-14) indicate that all the simulations underpredict the experimental HRR by around 15 %, on average. FIGRA value calculated using Eq. (2-15) is 0.7 kW s^{-1} for the experimental data, while the simulations on average predict a value of 0.65 kW s^{-1}.

Some aspect of under prediction of the peak could be associated with the fact that the OSB pyrolysis model under predicts the second peak observed in the cone calorimetry experiments [187]. The discrepancy in the HRR prediction was then investigated using uncoupled simulations with pure radiative heat flux assumption. Model using either radiation or hybrid heat flux predict similar HRR profiles and thus, pure radiative assumption of heat flux was used for the rest of the simulations.

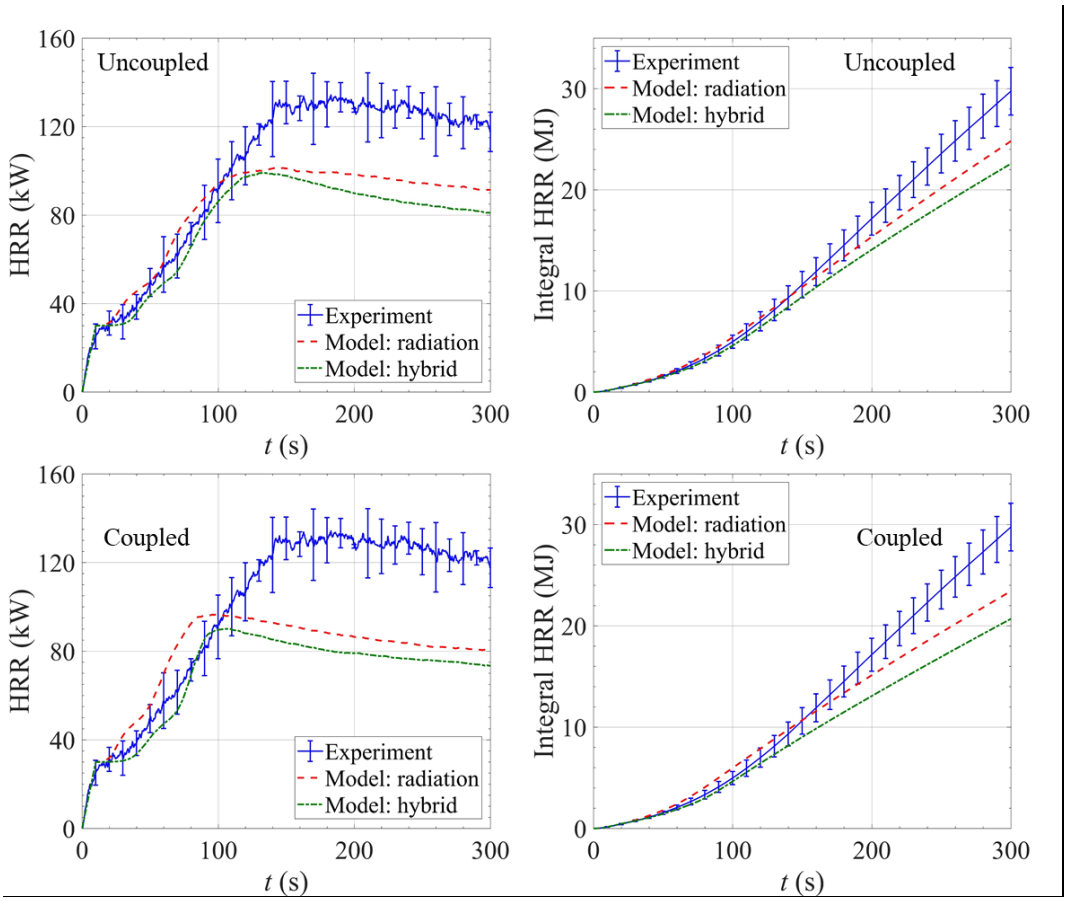

Figure 4-9. A comparison of the mean experimental HRR and integral HRR for flame spread on OSB with heat release rates obtained from uncoupled and coupled simulations

The discrepancy was first speculated to arise from the difference of wall re-radiation heat flux between OSB and PMMA. To explore this idea, the top surface temperature (T_{top}) and heat release rate per unit area (*HRRPUA*) time-dependent profile for each element were extracted from uncoupled simulation which used pure radiative heat flux representation. A critical ignition criteria based on HRRPUA for combustible solids is about 21 kW m^{-2} [184]. The elements were then flagged as 'burning' for the duration after which the HRRPUA exceeded 100 kW m^{-2}, a conservative value which is about 5 times the critical ignition criteria. Only these 'burning' elements were assumed to be

responsible for re-radiation contribution to the heat flux gauges on the adjacent wall. The T_{top} and HRRPUA distribution for a burning element centered around x = 10 cm, y = 10 cm for both PMMA and OSB is illustrated in Figure 4-10. Similar profiles were obtained for remaining 'burning' elements. The average top surface temperature for these 'burning' elements, taken as average of T_{top} after the element was flagged as 'burning', was estimated to be 810 K for OSB and 695 K for PMMA. The re-radiation from the burning surface to the adjacent walls was calculated by considering grey-body radiation from a surface at this average temperature to another surface at the temperature of water-cooled heat flux gauge (291 K) and also taking into account the view factor between the adjacent perpendicular surfaces.

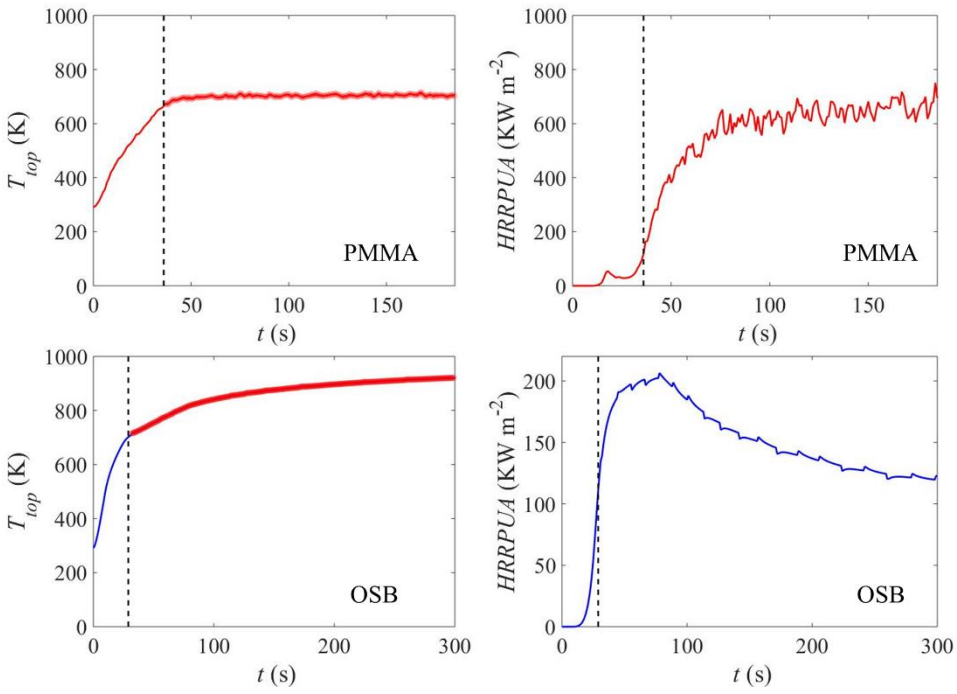

Figure 4-10. *HRRPUA* and T_{top} for element centered around x = 10 cm, y = 10 cm, for PMMA and OSB (The black dashed line represents the time when HRRPUA threshold is reached, and the shaded red data represents the data used for averaging T_{top})

The perpendicular surfaces for re-radiation calculation were simplified as two rectangles of dimensions 17.5 cm × 140 cm, perpendicular to each other along the larger dimension. These rectangles covered the extents of the burning elements and they are illustrated in Figure 4-11 (a). View factor between these two surfaces was calculated using Eq. (4-1) [190], for which the corresponding variables are illustrated in Figure 4-11 (b).

$$F_{1-2} = \frac{1}{(x_2 - x_1)(y_2 - y_1)} \sum_{l=1}^{2}\sum_{k=1}^{2}\sum_{j=1}^{2}\sum_{i=1}^{2}\left[(-1)^{(i+j+k+l)}\, G(x_i, y_j, \eta_k, \xi_l)\right]$$

$$G = \frac{1}{2\pi}\left\{(y-\eta)\left(x^2+\xi^2\right)^{1/2}\tan^{-1}(K) - \frac{1}{4}\left(x^2+\xi^2\right)(1-K^2)\ln\left[\left(x^2+\xi^2\right)(1+K^2)\right]\right\} \qquad (4\text{-}1)$$

where $K \equiv (y-\eta)/\left(x^2+\xi^2\right)^{1/2}$

In Eq. (4-1), parameters used for view factor calculation were $\xi_1 = x_1 = y_1 = \eta_1 = 10^{-6}$, $x_2 = \xi_2 = 17.5$, and $y_2 = n_2 = 140$. View factor for these two simplified rectangular plates was estimated to be $F_{1\text{-}2}$ = 0.28.

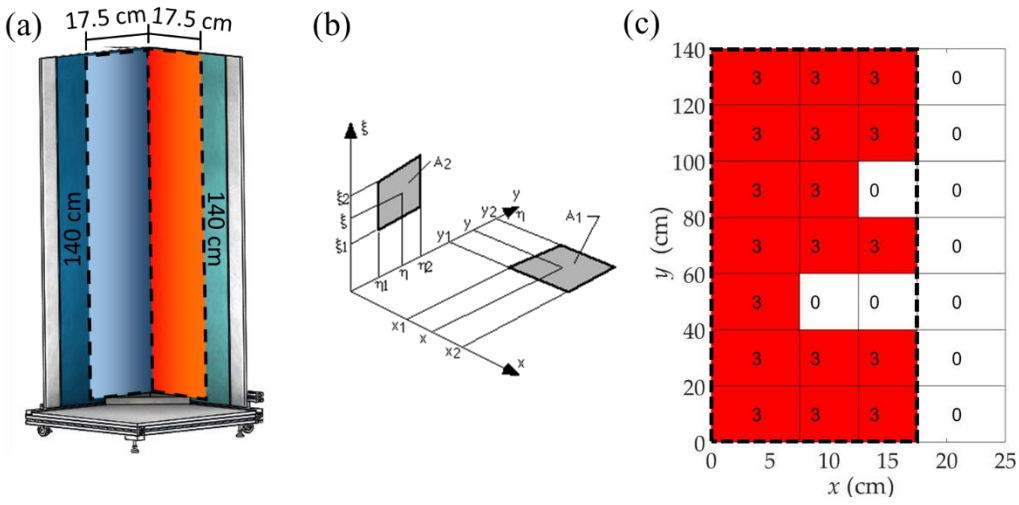

Figure 4-11. (a) Simplified representation of 'burning' elements as two rectangles (dashed black lines) perpendicular to each other along the length. (b) Schematic

corresponding to view factor calculation formula. (c) Schematic of 'burning' elements (in red) with net re-radiative correction (numbers in kW m^{-2} inside the elements)

The net re-radiative heat flux, from a rectangle at average T_{top} to a perpendicular rectangle representing water-cooled heat flux gauge at 291 K, for PMMA and OSB was then estimated using electrical analogy for the two-body problem [191], given by Eq. (4-2) through (4-5). In these equations, $\varepsilon_{1,OSB} = 0.7$, $\varepsilon_{1,PMMA} = 0.96, \varepsilon_2 = 1, \sigma = 5.67 \times 10^{-8}\ W\ m^{-2}K^{-4}, A_1 = A_2 = 2450\ cm^2$. The net radiative heat flux, calculated as a difference between re-radiative heat flux estimate for OSB and PMMA (Eq. (4-6)), was estimated to be + 3 kW m^{-2}. The additional heat flux of 3 kW m^{-2} was added to the plateau value of Segment 3 of the piece-wise linear fit for the respective burning element, as shown in Figure 4-11 (c). This decision was made because the heat flux for a particular element reached the steady peak value when the 'burning' criteria was satisfied.

$$q_{1\to2} = \frac{(E_1 - E_2)}{R_1 + R_2 + R_{12}} \times \frac{1}{A_1} \quad (4\text{-}2)$$

$$E_i = \sigma T_i^4 \quad (4\text{-}3)$$

$$R_i = \frac{1 - \varepsilon_i}{A_i \varepsilon_i}; \quad (4\text{-}4)$$

$$R_{1-2} = A_1 F_{1-2} \quad (4\text{-}5)$$

$$q_{net\ (additional)} = q_{1\to2\ (OSB)} - q_{1\to2\ (PMMA)} \quad (4\text{-}6)$$

Results of uncoupled simulations with the re-radiation correction to the heat flux for the specific elements is shown below in Figure 4-12 compared with the radiation uncoupled simulations. The re-radiation correction to the total heat flux has negligible impact on the HRR prediction. This could be partially attributed to lower average T_{top}

estimated for OSB because of the HRRPUA burning criteria. Another possible reason could be the change in emissivity of the OSB surface due to soot deposition. To explore this hypothesis, only the emissivity of char component was changed to 0.95, representing emissivity of soot particles in a candle flame [192]. However, changing the emissivity and including the re-radiation correction had negligible impact on the HRR predictions.

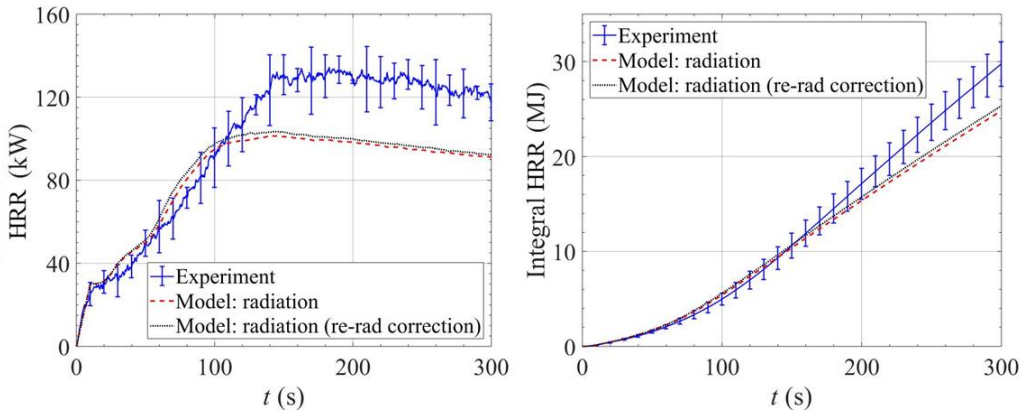

Figure 4-12. Mean experimental HRR and integral HRR predictions obtained from uncoupled simulations using either pure radiation heat flux or radiation heat flux with re-radiation correction, compared with experimental data for flame spread over OSB

After exploring multiple hypothesis, it was evident that the hypothesized correction factor of re-radiation and change in emissivity due to soot deposition were not the main reason for the observed underprediction of the peak HRR. Looking at the comparison of normalized radiation intensity of OSB and PMMA (Figure 4-7), it was further speculated that the error in the model predictions could be arising from the assumption that the flame heat flux versus HRR correlations developed using PMMA experimental data are valid for OSB. To examine this hypothesis, the normalized intensities of PMMA shown in Figure 4-7 were subtracted from the normalized OSB intensities to quantify the difference in

observed radiation intensity of the OSB and PMMA flame. This difference is shown in the Figure 4-13 below for three HRR along with the boundaries of 'burning' elements for OSB identified at the particular HRR. The number at the center of each element represent the % difference in the normalized intensity.

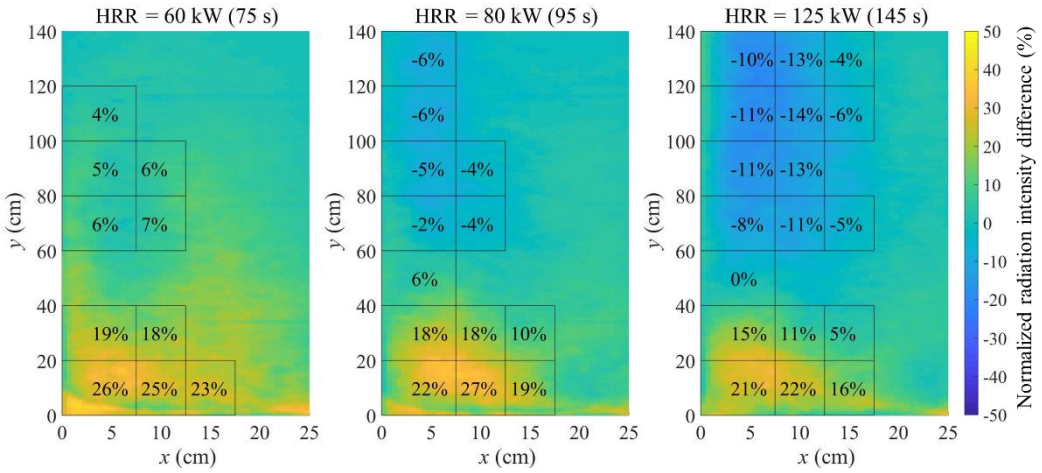

Figure 4-13. Difference in normalized radiation intensity between OSB and PMMA. The numbers inside the 'burning' elements at the particular HRR indicate the percent difference averaged within the extents of that element

The normalized intensity for OSB is clearly greater than PMMA by about 20% around the burner flame region, indicating a more radiative flame supported by OSB in the lower region of the panel. This figure and Figure 4-7 also indicate that the OSB flame structure is different than that observed for PMMA. The OSB panels could be supporting faster lateral flame spread than PMMA in the vicinity of the burner, also indicated by faster rise in heat flux with HRR at x = 22 cm, y = 70 cm for OSB than PMMA.

A wider flame with higher radiation intensity supported by OSB panels at the lower region than supported by PMMA could be either due to inherently more radiative flame or

due to larger portion of OSB burning near the bottom as a result of relatively faster lateral flame spread. The possibility of an inherently more radiatively intense flame over OSB could be due to smoldering combustion affecting the glow at 900 nm. However, during the 300 s of the large-scale tests, no visible traces of smoldering or glowing combustion were observed in the IR camera or the regular video camera (which was used for reference). Although smoldering combustion behind the flame is a possibility in a charring engineered wood, due to no direct observations, this possibility was rejected and thus, only the possibility of an inherently radiatively intense flame due to combustion was explored. Faster lateral flame spread could result from either larger radiation from the flame or heat transfer through the OSB panel in positive *x*-direction. To understand the dominating lateral spread mechanism, one additional large-scale test over the same dimension of the OSB panels was performed. However, in this test, at x = 12 cm, as shown in Figure 4-14, a 0.32 cm thick, 50 cm in length strip of OSB was cut out and replaced with a Kaowool insulation. The purpose of insulation was to inhibit any conductive heat transfer in lateral *x*-direction. Kaowool was selected because of its lower thermal conductivity (0.05 W m^{-1} K^{-1}) than that of Marinite I calcium silicate board (0.13 W m^{-1} K^{-1}). The insertion of an insulation piece at this location was decided based on normalized intensity plots for OSB in order to restrict any possibly conductive heat transfer in positive *x*-direction. This insulation was inserted on both the panels to maintain symmetry of the flame.

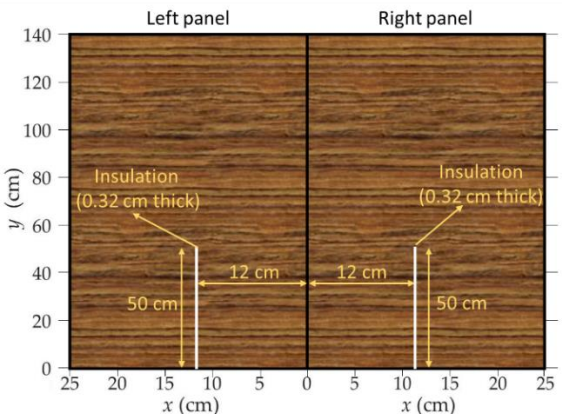

Figure 4-14. Schematic of additional experiment performed on OSB with symmetric insulation strip (0.32 cm thick)

The experiment was conducted in the same exact manner as described in Section 4.4, except for heat flux measurements. Calorimetry was performed and the comparison of the HRR profile for these tests with OSB having an insulation strip and for tests conducted over OSB without any modifications is shown below in Figure 4-15. The comparison indicates that the overall fire growth was not affected by the insulation strip.

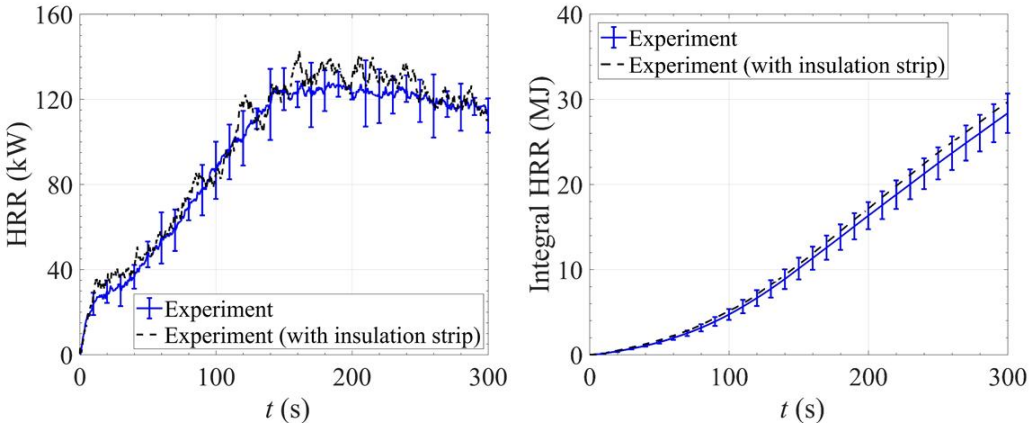

Figure 4-15. Comparison of HRR evolution for flame spread tests conducted over OSB with and without the insulation strip modification

The video from the DSLR camera was processed and the difference in normalized intensity plots for the same three HRR between OSB and PMMA are shown below in Figure 4-16 for these experiments. These experimental data indicate that the difference in the normalized intensity is higher or not significantly different (depending on the location on the panel) from that observed in Figure 4-13. This indicates that the thermal heat transport through OSB in positive *x*-direction (in lateral direction) does not play a major role in governing the structure of the flame supported by OSB. Thus, the flame appears to spread faster in lateral direction over OSB than that over PMMA primarily because of radiatively more intense flame than supported by PMMA. Thus, the primary reason for the discrepancy in the HRR prediction is attributed to the assumption that the same empirical heat feedback model developed over PMMA applies to OSB. This model provides a good prediction of the early stages of spread on OSB but it fails to predict lateral spread at late stages. This lateral flame spread appears to be driven by increased radiation from the bottom portion of the flame fueled by both propane and OSB pyrolyzates.

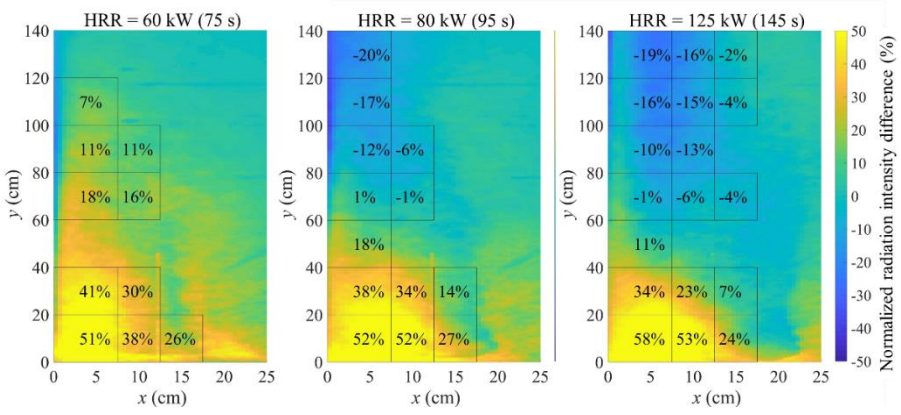

Figure 4-16. Difference in normalized radiation intensity (normalized by maximum intensity for PMMA at respective HRR) between large-scale experiments over PMMA and OSB (with insulation strip) for 60, 80, and 125 kW

4.8. Conclusion for Chapter 4

The hierarchical experiments and modeling followed previously for PMMA and PIR foam were performed for another widely used building product, oriented strand board (OSB). The small-scale experimental results and comprehensive pyrolysis model was developed for PS2-10-compliant 1.1 cm thick OSB in two separate previous studies conducted by Gong et. al [186,187]. The validated pyrolysis model was utilized in this study to further explore if it can be used to predict large-scale flame spread scenario.

Large-scale flame spread experiments conducted on OSB panels indicated that the OSB supported flame spread and the heat release rate (HRR) increased somewhat linearly to a peak HRR of about 125 kW. The flame spread over OSB was monitored using the modified DSLR camera equipped with a 900 nm narrowband filter. The radiation intensity obtained from processing the video was compared with radiation intensity for flame supported by PMMA. The radiation intensity distribution for OSB was found to be different from than for PMMA at the same HRR, with generally higher intensity near the region of the propane burner flame and somewhat lower intensity downstream of the burner. The differences in the radiation intensity indicate different flame structure for these two materials.

The flame spread modeling framework was applied to OSB by utilizing the same flame heat feedback model which was developed using experimental data obtained for PMMA. The validated pyrolysis model was coupled with this empirical flame feedback model and uncoupled and coupled simulations were conducted. For OSB, both these simulations provided excellent predictions during the early stages of fire compared with

experimental data. However, the peak HRR was predicted to be about 20% lower and the time to peak was predicted to be about 15% earlier than respective experimental values. Part of this discrepancy could be due to the limitations of the OSB pyrolysis model, which was shown in the developmental studies, to predict the second HRR peak of the cone calorimetry experiments. The other contributing factor to the discrepancy in the peak HRR prediction was investigated by exploring the potential differences in heat flux for OSB than that observed during PMMA experiments. However, neither the differences in re-radiative contribution to the heat flux for the burning OSB wall from the burning PMMA wall, nor the difference in higher emissivity of the OSB surface due to soot deposition affected the HRR predictions. It was concluded by observing the differences in the radiation intensity distribution for OSB and PMMA flames at same HRR that the OSB flame structure for the same HRR was different than the PMMA flame, thereby showing a limitation of the assumption of using the same flame heat feedback model for both these materials. So, contrary to successful HRR predictions on the PIR foam during the flame spread, the fuel-independent nature of the empirical flame heat feedback model is questionable and requires further investigation. Thus, although the model provided excellent predictions during the early development of the fire, the flame feedback correlations should be carefully investigated before its general applicability to other materials.

Chapter 5: Conclusion

5.1. Concluding Remarks

The dynamics of upward, buoyancy-driven, turbulent flame spread were investigated using a hierarchical experimentation and modeling approach. My primary contributions from the research work discussed in the dissertation are summarized below:

- The development of hill-climbing optimization algorithm (along with a former research colleague) that enabled the automation of the pyrolysis property parameterization process by inverse analysis of the small-scale experimental data.
- The designing and building of the large-scale experimental setup to perform flame spread experiments and diagnostics over three combustible solids in a corner scenario. Fast-response (13 s) calorimetry (whose development and validation is given in Appendix A), well-resolved heat flux (maximum ± 6 kW m^{-2} error), and spectrally resolved (900 ± 10 nm) radiation intensity data were the primary outcome of these experiments.
- The development, programming, and analysis of low-cost, numerical flame spread model using comprehensive pyrolysis solver, ThermaKin, which was operated as a sub-routine in a MATLAB script to simulate fire dynamics during the flame spread over three materials in the large-scale corner setup.

Hierarchical experiments and modeling across various scales of samples with masses ranging from milligrams to kilograms was conducted on three materials: poly (methyl methacrylate) (PMMA), Polyisocyanurate (PIR) foam, and oriented strand board

(OSB). Such an investigation across various scales was concluded to be essential for fundamental understanding of different controlling mechanisms of the flame spread problem, which involves complex interactions between gas-phase combustion, heat transfer to unburnt region, and condense-phase pyrolysis.

Pyrolysis of the three materials was comprehensively parameterized using inverse analysis of small-scale experimental data. The inverse analysis was automated using a hill-climbing optimization algorithm, coupled with a comprehensive pyrolysis solver, ThermaKin. Thermogravimetric analysis (TGA) and differential scanning calorimeter (DSC) were used to parameterize decomposition reaction kinetics and associated thermodynamics. Microscale combustion calorimetry (MCC) was used to determine heats of combustion of evolved pyrolyzate gases during thermal decomposition. Controlled Atmosphere Pyrolysis Apparatus II (CAPA II), a gasification test, was used to optimize thermo-physical properties, including density and thermal conductivity. Additional cone calorimetry tests were essential to account for components which were absent from the samples used for small-scale tests and pyrolysis model parameterization. This comprehensive pyrolysis model development exercise further extends and validates previously developed systematic methodology. It is also necessary to highlight the importance of characterizing the pyrolysis process of a material of interest due to complexity of material decomposition arising from different underlying chemical structures.

A large-scale experimental setup was built to study the dynamics of buoyancy-driven, turbulent, concurrent flame spread in a corner scenario over these three materials. A fully validated, fast-response calorimetry (13 s response time) was developed to achieve

heat release rate (HRR) data synchronization with other measurements collected during flame spread. Along with HRR, the flame heat flux, a primary parameter that governs the heat transfer to the unburnt surface during flame spread, was resolved spatially at 28 locations (every 20 cm in vertical direction and every 5 cm resolution away from the corner) over PMMA. A flame heat feedback model which correlated heat flux with the HRR, quantified the near linear increase of heat flux with HRR to a plateau. The flame heat flux was found to be primarily dependent on HRR and independent of the gaseous fuels from PIR foam. However, flame heat flux measured at limited locations for OSB showed different profile evolution with HRR than observed in the PMMA tests at the same locations. Along with these measurements, well-resolved soot radiation emission contours corresponding to a narrowband of 900 nm were estimated during the flame spread over PMMA using a modified DSLR camera, which provides valuable data for validating CFD studies which have spectrally resolved diagnostics. Radiation intensity measurements during flame spread over OSB were important to understand the differences in the intensities of the OSB and the PMMA flame, and thereby the flame heat flux.

Then, a low-cost, fast (requiring approximately 40 minutes for each simulation) numerical model was developed using ThermaKin to predict flame spread behavior over the materials. This model is realized by coupling the developed comprehensive pyrolysis models and empirical flame heat feedback model (obtained from large-scale experiments). This numerical model was able to predict HRR within 10% (best case) and 65% (worst case) of the average experimental data (depending on the input parameters) for flame spread in a corner scenario over PMMA. The model was sensitive to the uncertainty in the flame heat feedback (improving the average error in predicted HRR from 65% to 15%) and

also the treatment of flame heat feedback as convection, radiation, or hybrid (which estimated relative contributions of convection and radiation). The uncertainties in pyrolysis parameters also propagated into a maximum 35% change (or improvement for increased heat capacity value) in predicted average HRR error for the large-scale predictions. The amplification of errors of input parameters was not an attribute of a particular modeling approach developed in this study but rather a general feature of any model (including CFD) attempting to capture the essential physics of this type of flame spread. The results of this comparison indicate that the uncertainties in the key material pyrolysis properties and flame heat feedback, which rarely fall below ±10%, would have to be reduced substantially to deliver fire growth predictions comparable in accuracy to measurements. The flame heat feedback model was found to provide HRR predictions for the PIR foam within the experimental error bars, and within 15% of average experimental data for OSB. However, the peak HRR prediction for OSB was under predicted by about 15% in magnitude and time at which the peak steady HRR is reached. Although the model predicted HRR growth within the experimental uncertainty during the early stages of the fire for OSB, the discrepancy in the peak HRR value predicted for OSB was concluded to be primarily because of different flame structure and radiation intensity of the OSB flame than that of PMMA, suggesting the limitations of applying the fuel-independent empirical flame heat feedback model. Despite the discrepancy in the HRR predictions, the prediction capability and systematic approach of a developed flame spread modeling framework is very promising for creating a foundation to assist in screening of new materials before large scale production and standardized testing.

5.2. Future Work

The applicability of the flame spread modeling framework needs to be investigated further. Investigation of flame spread over OSB revealed that the time to ignition and general rate of increase in the HRR is predicted well by the model but also revealed the underprediction of the peak HRR value arising from the use of the same flame heat feedback empirical correlations as developed for PMMA. Future investigations should include more detailed understanding of the differences in flame heat flux during flame spread over different materials in a large-scale setup. Further insight into this could be possible by understanding the development of pyrolysis zone and its correlation with the flame heat flux during flame spread over non-charring (PMMA) and charring polymers (for PIR foam and OSB). Potential use of non-intrusive techniques and/or careful surface temperature measurements could provide well-resolved pyrolysis zone development profiles during the flame spread.

Additionally, examination is required to accurately identify flame heat feedback contributing mechanisms and to also understand if pyrolysis is affected on a large-scale scenario by flow field condition such as surface oxygen content. During the modeling process it was realized how complete knowledge of total flame heat flux was not sufficient to formulate heating boundary conditions in the numerical model and relative contributions of radiation and convection must also be defined. These contributions were estimated in this study but accurate measurements of such data are not widely available for turbulent wall fires in a corner geometry. Although surface oxygen content is known to be negligible over a surface covered by a diffusion flame [154,156], surface oxidation of solid panel in large scale setup is possible due to turbulent flow-field conditions. Surface oxidation is

known to affect the rate of pyrolyzate mass loss [153] and thus can potentially affect the heat released. Therefore, future work should also involve measurement of radiation-convection contribution to flame heat flux in corner wall-flame spread scenario and measurement of surface oxygen content.

For the modeling aspect, the presented semi-empirical modeling framework can be refined further by using information from future experiments proposed in the previous two paragraphs. The present experimental setup and tests should be modeled in a CFD software to further investigate the accuracy of CFD sub-models. Spectrally resolved emission data obtained by post-processing CFD results can be validated against the radiation intensity data reported in this study. This would be an important validation step for the sub-models used in the CFD models and thus help improve accuracy of the models.

Appendix A: Calorimetry

The calorimetry to estimate amount of energy generated due to the fire under the gas collection hood was developed based on the principle of oxygen consumption. The calculation of oxygen consumed was based on the same approach as used in the cone calorimetry standard [22]. However, equations used in the cone standard require system-specific calibration every-time before the experiment. Therefore, the objective here was to derive equations from first principles that circumvent the expense of calibrating the calorimetry before each experiment. Section A.1 elaborate the derivation process of the calorimetry equations used in this research to estimate heat release rate, Section A.2 discusses the procedure followed for processing the raw data: adjusting time delays and creating linear baselines. Section A.3 details the procedure followed for validation of calorimetry equations. In this section, experiments performed on known quantity of PMMA and Propane were used to estimate heat of combustion values for these fuels.

A.1. Derivation of Calorimetry Equations

The oxygen consumption principle is based on the observations of complete combustion of several organic fuels which suggests that, for every kiligram of oxygen consumed, 13.1×10^6 J of energy is released. The instantaneous heat release rate, HRR, can be estimated by knowing the mass of oxygen consumed, $\Delta \dot{m}_{O_2}$(kg s^{-1}) using equation (A - 1).

$$\boldsymbol{HRR} = \mathbf{E}.\,\Delta \dot{\mathbf{m}}_{\mathbf{O_2}} \qquad (\text{A - 1})$$

Where E is 13.1 × 10^6 J per kg O_2 consumed. Accuracy in quantifying $\Delta \dot{m}_{O_2}$ depends on the degree of detail in quantifying chemical changes that occur during the combustion process and its consequential impact on the flow field surrounding the fire. Care was taken to correct for changes in the oxygen concentration associated with the removal of H_2O and CO_2 from the oxygen sensor flow. Both environmental moisture, and H_2O and CO_2 generated in combustion were also taken into account. Figure A-1 shows a schematic of the control volume that was used to derive equations to calculate $\Delta \dot{m}_{O_2}$.

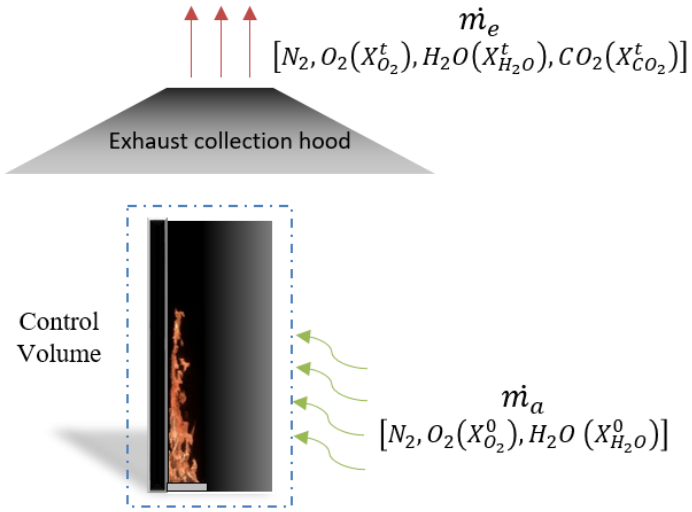

Figure A-1. Schematic of calorimetry

Major assumptions of the flow field condition that impact the calculations are as following.

I. Reactants, or inlet air constitute only of major constituents that are present in considerable quantities. The chemical species considered here are nitrogen, oxygen and water vapor.

II. Combustion is assumed to be a complete reaction of available reactants producing carbon-di-oxide and water vapor.

III. Mass flow rate of inlet air is non-variant across the control volume, i.e. $\dot{m}_a = \dot{m}_e$.

IV. Air is an ideal gas and molecular weight of air is unaffected by the combustion process.

Mass flow of air into the control volume is $\dot{m}_a$ *(kg s^{-1})* and mass flow of combustion products out of the control volume is $\dot{m}_e$ *(kg s^{-1})*. If the $Y_{O_2}^0$ is ambient oxygen mass fraction in $\dot{m}_a$ and $Y_{O_2}^t$ is oxygen mass fraction $\dot{m}_e$ at a time, *t (s)*, respectively, mass of oxygen consumed can be quantified by Eq. (A - 2), and applying assumption *III*.

$$\Delta \dot{\mathbf{m}}_{\mathbf{O_2}} = \dot{\boldsymbol{m}}_{\boldsymbol{a}} \boldsymbol{Y}_{\boldsymbol{O_2}}^{\boldsymbol{0}} - \dot{\boldsymbol{m}}_{\boldsymbol{e}} \boldsymbol{Y}_{\boldsymbol{O_2}}^{\boldsymbol{t}} = \dot{\boldsymbol{m}}_{\boldsymbol{e}} \left(\boldsymbol{Y}_{\boldsymbol{O_2}}^{\boldsymbol{0}} - \boldsymbol{Y}_{\boldsymbol{O_2}}^{\boldsymbol{t}} \right) \qquad \text{(A - 2)}$$

Eq. (A - 3), derived from Bernoulli's equation [193] and ideal gas assumption IV, can be used to compute mass flow, $\dot{m}_e$ *(kg s^{-1})*, and volumetric flow rate, V*(m^3 s^{-1})*, of the exhaust gases.

$$\dot{\boldsymbol{m}}_{\boldsymbol{e}} = \mathbf{V} \boldsymbol{\rho}_{\boldsymbol{e}} = \boldsymbol{C}_{\boldsymbol{f}}^{\boldsymbol{e}} \boldsymbol{A} \sqrt{\frac{2 \Delta \boldsymbol{P}}{\boldsymbol{T}_{\boldsymbol{e}}} \left(\frac{\boldsymbol{P}_{\boldsymbol{a}} \boldsymbol{M}_{\boldsymbol{e}}}{\boldsymbol{R}} \right)} \qquad \text{(A - 3)}$$

Where, C_f^e is the flow coefficient of the averaging pitot tube, ΔP is the differential pressure in Pa, A is the area of cross section of the duct in m^2, P_a is the ambient pressure in Pa. R is the universal gas constant 8.314 J mol^{-1} K^{-1}, and the density of exhaust gases is ρ_e in kg m^{-3}.

If Y_{O_2} and X_{O_2} denote mass fraction and mole fraction respectively of oxygen, the change of mass fraction of oxygen can be expressed, as shown in Eq. (A - 4), as mole fraction by definition and assuming constant molecular weight of exhaust gases, assumption IV. Here, and in following discussion, the superscript '*0*' represents value at

initial condition and '*t*' represents respective variable value at time, *t*. Subscripts of molecular formula of gas components are used to represent respective quantities for those gases.

$$\left(\boldsymbol{Y}_{\boldsymbol{O_2}}^{\boldsymbol{0}} - \boldsymbol{Y}_{\boldsymbol{O_2}}^{\boldsymbol{t}}\right) = \frac{\boldsymbol{M_{O_2}}}{\boldsymbol{M_e}}\left(\boldsymbol{X}_{\boldsymbol{O_2}}^{\boldsymbol{0}} - \boldsymbol{X}_{\boldsymbol{O_2}}^{\boldsymbol{t}}\right) \qquad (A - 4)$$

Employing assumption *I,* the initial mole fraction of oxygen in inlet air can be simplified by definition, as shown in Eq. (A - 5) and (A - 6), where '*n*' denote the number of moles of a particular gas.

$$X_{O_2}^0 = \frac{n_{O_2}^0}{n_{O_2}^0 + n_{H_2O}^0 + n_{N_2}^0} \qquad (A - 5)$$

$$\frac{1}{X_{O_2}^0} = \underbrace{\frac{n_{O_2}^0 + n_{N_2}^0}{n_{O_2}^0}}_{I} + \underbrace{\frac{n_{H_2O}^0}{n_{O_2}^0}}_{II} \qquad (A - 6)$$

Initial ambient measured mole fraction of oxygen, $X_{O_2}^{m,0}$ is the inverse of term *I* in equation (A - 6). Correcting for the ambient relative humidity (%) can be done by computing Absolute Humidity (or mole fraction) of Water vapor in the ambient air as follows.

$$X_{H_2O}^0 = \frac{n_{H_2O}^0}{n_{O_2}^0 + n_{H_2O}^0 + n_{N_2}^0} \qquad (A - 7)$$

$$\frac{1}{X_{H_2O}^0} = 1 + \frac{n_{O_2}^0}{n_{H_2O}^0} + \frac{n_{N_2}^0}{n_{O_2}^0}\frac{n_{O_2}^0}{n_{H_2O}^0} \qquad (A - 8)$$

$$\frac{1}{X_{H_2O}^0} - 1 = \frac{n_{O_2}^0}{n_{H_2O}^0}\left(1 + \frac{n_{N_2}^0}{n_{O_2}^0}\right) \qquad (A - 9)$$

$$\frac{n_{H_2O}^0}{n_{O_2}^0} = r_{H_2O}^0 = \left(\frac{1}{X_{H_2O}^0} - 1\right)^{-1} \frac{1}{X_{O_2}^{m,0}} \qquad (A - 10)$$

Term *II* in equation (A - 6) which represents the ratio of initial moles of water vapor to oxygen ($r_{H_2O}^0$) computed using equation (A - 10) can be used to simplify the ambient oxygen mole fraction in the inlet air,

$$\boldsymbol{X_{O_2}^0 = X_{O_2}^{m,0}\left(1 - X_{H_2O}^0\right)} \qquad (A - 11)$$

Calculation of initial water mole fraction, were performed using Eq., (A - 12) by accounting for ambient conditions. The saturation pressure of Water vapor, $P_{H_2O}^v$ *(Pa)*, at the ambient temperature, T_a *(K)* can be calculated using Tetens equation, Eq. (A - 13) with A = 0.61078 *Pa*, B = 17.27, C = 4714.71 *K* and D = -35.7 *K* for the ambient temperature above 273 K [194]. This equation estimated vapor pressure of saturated Water vapor from 270 K to 320 K within 1% of the vapor pressure values given by NIST Webbook [174].

$$\boldsymbol{X_{H_2O}^0 = \frac{(RH^0)/100 \times P_{H_2O}^v}{P_a}} \qquad (A - 12)$$

$$P_{H_2O}^v = \mathrm{A}.\exp^{\left(\frac{BT_a - C}{T_a + D}\right)} \times 10^3\ Pa \qquad (A - 13)$$

Nitrogen mole fraction in the inlet air was the balance of mole fractions obtained from equations (A - 11) and (A - 13). The molecular weight of the air can thus be computed by definition, using equation (A - 14). Here, M_{O_2} is 32×10^{-3} kg mol^{-1}, M_{H_2O} is 18×10^{-3} kg mol^{-1} and M_{N_2} is 28×10^{-3} kg mol^{-1}.

$$\boldsymbol{M_e = M_{O_2}X_{O_2}^0 + M_{H_2O}X_{H_2O}^0 + \left(1 - X_{O_2} - X_{H_2O}\right)M_{N_2}} \qquad (A - 14)$$

The values of ambient pressure, temperature, relative humidity data and initial oxygen mole fraction were termed as baseline quantities. Small drifts in the baseline quantities due to the fire were accounted for by linear baseline, discussed later in Section A.2.2. Before the baseline correction, data were synchronized by accounting for time delays in the fluid flow to various instrumentation, discussed later in Section A.2.1.

After complete combustion in the control volume, CO_2 and H_2O produced during combustion add to the effluent stream composition. At certain time, *t*, the oxygen mole fraction in the exhaust gases can be written as given in Eq. (A - 15) through Eq. (A - 17),

$$X_{O_2}^t = \frac{n_{O_2}^t}{n_{O_2}^t + n_{N_2}^t + n_{H_2O}^t + n_{CO_2}^t} \qquad (A - 15)$$

$$n_{H_2O}^t = n_{H_2O}^0 + n_{H_2O}^c \qquad (A - 16)$$

$$\frac{1}{X_{O_2}^t} = \underbrace{\frac{n_{O_2}^t + n_{N_2}^t}{n_{O_2}^t}}_{III} + \underbrace{\frac{n_{H_2O}^0}{n_{O_2}^t}}_{IV} + \underbrace{\frac{n_{H_2O}^{c,t} + n_{CO_2}^{c,t}}{n_{O_2}^t}}_{V} \qquad (A - 17)$$

Water vapor and CO_2 produced from combustion are denoted by superscript '*c*' and are shown as $n_{H_2O}^{c,t}$ and $n_{CO_2}^{c,t}$ respectively. Term *III* in Eq. (A - 17) is the inverse of mole fraction of oxygen, $X_{O_2}^m$, measured by the oxygen sensor at time, *t*, after combustion begins. Term *IV* in Eq. (A - 17) was assumed to be equivalent to $r_{H_2O}^0$ in Eq. (A - 10) since the number of moles of oxygen are abundant due to the nature of experiments. The error introduced in *HRR* due to this assumption is about 2%. This sensitivity was studied by changing $r_{H_2O}^0$ by a factor of 0.95 to 1.1 of the original ratio for estimating *HRR* from a test on black PMMA with known mass. The ratio range considers a wide range of observable

oxygen depletion in a fire scenario under the hood. Term *V* in Eq. (A - 17) can be simplified algebraically, as shown in Eq. (A - 18) through Eq. (A - 20), to account for the amount of H_2O and CO_2 produced due to the combustion process. Here, $\Delta n_{O_2}^t$, is the difference of moles of oxygen before and after the combustion.

$$\frac{n_{H_2O}^{c,t} + n_{CO_2}^{c,t}}{n_{O_2}^t} = \frac{\frac{n_{H_2O}^{c,t}}{\Delta n_{O_2}^t} + \frac{n_{CO_2}^{c,t}}{\Delta n_{O_2}^t}}{\frac{n_{O_2}^t}{\Delta n_{O_2}^t}} \quad \text{(A - 18)}$$

$$\frac{n_{O_2}^t}{\Delta n_{O_2}^t} = \frac{\frac{n_{O_2}^t}{n_{O_2}^t + n_{N_2}^t}}{\frac{\Delta n_{O_2}^t}{n_{O_2}^t + n_{N_2}^t}} = \frac{X_{O_2}^m}{\frac{\Delta n_{O_2}^t}{n_{O_2}^t + n_{N_2}^t}} \quad \text{(A - 19)}$$

$$\frac{\Delta n_{O_2}^t}{n_{O_2}^t + n_{N_2}^t} = \frac{n_{O_2}^0}{n_{O_2}^t + n_{N_2}^t} - X_{O_2}^m = \frac{X_{O_2}^{m,0}}{\frac{n_{O_2}^t + n_{N_2}^t}{n_{O_2}^0 + n_{N_2}^0}} - X_{O_2}^m \quad \text{(A - 20)}$$

$$\gamma = \frac{n_{H_2O}^{c,t} + n_{CO_2}^{c,t}}{\Delta n_{O_2}^t} \quad \text{(A - 21)}$$

By assuming inert nature of Nitrogen in the fire, the moles of N_2 can be assumed to be conserved. Further assuming that the total number of moles of nitrogen and oxygen are conserved, Eq. (A - 20) can be simplified further as shown in Eq. (A - 22) and Eq. (A - 23). Due to the abundance of total moles of oxygen and nitrogen available, the maximum error in *HRR* calculation due to this assumption is about 2.5 %, found by performing sensitivity analysis for this ratio, shown as term *VI* in Eq. (A - 22). This ratio was varied by a factor of 0.98 to 1.02 of the estimated theoretical mole ratios for propane combustion

corresponding to a 200 kW fire size, with inlet air flow assumed equivalent to air flow used for this test setup (0.56 $m^3\ s^{-1}$).

$$\frac{\Delta n_{O_2}^t}{n_{O_2}^t + n_{N_2}^t} = \frac{X_{O_2}^{m,0}}{\left(1 - X_{O_2}^{m,0}\right) + \underbrace{X_{O_2}^m}_{VI}} - X_{O_2}^m \qquad (A - 22)$$

$$\frac{n_{O_2}^t}{\Delta n_{O_2}^t} = \frac{X_{O_2}^m}{\frac{X_{O_2}^{m,0}}{\left(1 - X_{O_2}^{m,0}\right) + X_{O_2}^m} - X_{O_2}^m} \qquad (A - 23)$$

The numerator of Eq. (A - 18) indicating total amount of combustion products produced per mole of O_2 consumed is denoted by γ, given by Eq. (A - 21). The values of γ for complete combustion of few hydrocarbon fuels which represents a range of fuels and plastics is explored here. This analysis can be extended further to any fuel used, provided the chemical formula is known. Assumptions *I* and *II*, allow us to write a complete molar stoichiometric combustion reaction in oxygen for an unsaturated fuel like Ethylene *(C_2H_4)*, Propane *(C_3H_8)* and a monomer of Poly (methyl methacrylate) *($C_5H_8O_2$)* and Poly(ethyl terephthalate) *($C_{10}H_8O_4$)* as given below in Eq. (A - 24) through Eq. (A - 27) respectively. For each of these fuels, the value of Eq. (A - 21), or γ, is shown below in Table A-1.

$$C_2H_4 + 3O_2 \rightarrow 2CO_2 + 2H_2O \qquad (A - 24)$$

$$C_3H_8 + 5O_2 \rightarrow 3CO_2 + 4H_2O \qquad (A - 25)$$

$$C_5H_8O_2 + 6O_2 \rightarrow 5CO_2 + 4H_2O \qquad (A - 26)$$

$$C_{10}H_8O_4 + 10O_2 \rightarrow 10CO_2 + 4H_2O \qquad (A - 27)$$

Table A-1. Moles of products per mole oxygen consumed for complete combustion of fuels

Fuel	$\boldsymbol{\gamma}$
$\mathbf{C_2H_4}$	1.33
$\mathbf{C_3H_8}$	1.4
$\mathbf{C_5H_8O_2}$	1.5
$\boldsymbol{C_{10}H_8O_4}$	1.4

The γ values listed are for typical fuels ranging from unsaturated to saturated hydrocarbons and partly oxygenated fuels. The average of γ value showed in Table A-1 is 1.4 and vary from 1.33 for Ethylene to 1.5 for PMMA. For the purpose of black PMMA flame spread experiments data analysis, a value of 1.5 was used for γ. The error introduced in maximum *HRR* by changing this ratio from 1.3 to 1.8 for a black PMMA validation test was less than 6 %. Combining Eq. (A - 23) and introducing γ, Eq. (A - 18) can be simplified as,

$$\frac{n_{H_2O}^{c,t} + n_{CO_2}^{c,t}}{n_{O_2}^{t}} = \gamma \left(\frac{\dfrac{X_{O_2}^{m,0}}{\left(1 - X_{O_2}^{m,0}\right) + X_{O_2}^{m}} - X_{O_2}^{m}}{X_{O_2}^{m}} \right) \qquad \text{(A - 28)}$$

$$\frac{1}{X_{O_2}^{t}} = \frac{1}{X_{O_2}^{m}} + r_{H_2O}^{0} + \gamma \left(\frac{\dfrac{X_{O_2}^{m,0}}{\left(1 - X_{O_2}^{m,0}\right) + X_{O_2}^{m}} - X_{O_2}^{m}}{X_{O_2}^{m}} \right) \qquad \text{(A - 29)}$$

$$\boldsymbol{X_{O_2}^{t} = \frac{X_{O_2}^{m}}{1 + \gamma \left(\frac{X_{O_2}^{m,0}}{\left(1 - X_{O_2}^{m,0}\right) + X_{O_2}^{m}} - X_{O_2}^{m} \right) + r_{H_2O}^{0} X_{O_2}^{m}}} \qquad \text{(A - 30)}$$

Equations (A - 1), (A - 2), (A - 3), (A - 4), (A - 11), (A - 12), (A - 14), and (A - 30) can be combined into Eq. (A - 31) to predict the instantaneous heat released by a fuel burning under the hood.

$$HRR_{corner} = EC_f^e A \left(\frac{2\Delta P}{T_e}\left(\frac{P_a M_e}{R}\right)\right)^{0.5} \frac{M_{O_2}}{M_e}\left(X_{O_2}^0 - X_{O_2}^t\right) \qquad (A - 31)$$

This *HRR* derived from these equations is referred to as HRR_{corner} for comparison with *HRR* estimated from the traditional approach discussed in Section A.3.

A.2. Data Processing for calculating HRR

For each test, the PTH sensor was switched on first to collect ambient data for 60 seconds. This was followed by 60 seconds of data collection of initial conditions of pertinent instrumentation. Data collection for each test was terminated about two minutes after the combustion ceased or after all the sensors reached a steady final value after sufficient time had elapsed. All the data obtained from the DAQ were first synchronized in time from the time of propane ignition.

A.2.1 Adjusting for Time Delays

The delays are the time required for the exhaust gas to reach respective sensor. Delay times reported here were repeatable when the exhaust flow rate was maintained at 0.56 $m^3\ s^{-1}$. The time of ignition was referred from a K-type thermocouple placed about 5 $\times\ 10^{-3}$ m above the burner. Time of ignition was determined as the time when the thermocouple temperature was 10 % higher than the ambient temperature. The time constant of this thermocouple to reach a 63.2% of a step change is less than 1 second and thus provide a reliable basis for the time of ignition. The inherent response times,

corresponding to 63.2 % of total change, of all the sensors to a thermal or chemical change were also less than the flow delay times and thus corrections for response times were unnecessary.

The time delay for the flow to reach the exhaust thermocouples, gauged from response to a thermal change underneath the hood was determined to be 3 seconds. The same temporal shift was applied to differential pressure signal. Corrections were done for the time-delay of 10 s associated with the transport of gases through the gas sampling system. The response time of the gas sampling system was determined to be 3 s.

A.2.2 Baseline Correction

The baseline quantities such as initial oxygen mole fraction, $(X_{O_2}^0)$ often slightly drifted due to the fire. This was accounted by formulating a linear change between initial and final quantities to form a baseline for heat release calculations. Figure A-2 shows an example of baseline correction for the measured oxygen mole fraction, $X_{O_2}^m$, after adjusting for the time delay of the oxygen sensor. Important changes and regions in time which are used for baseline correction are marked on the figure.

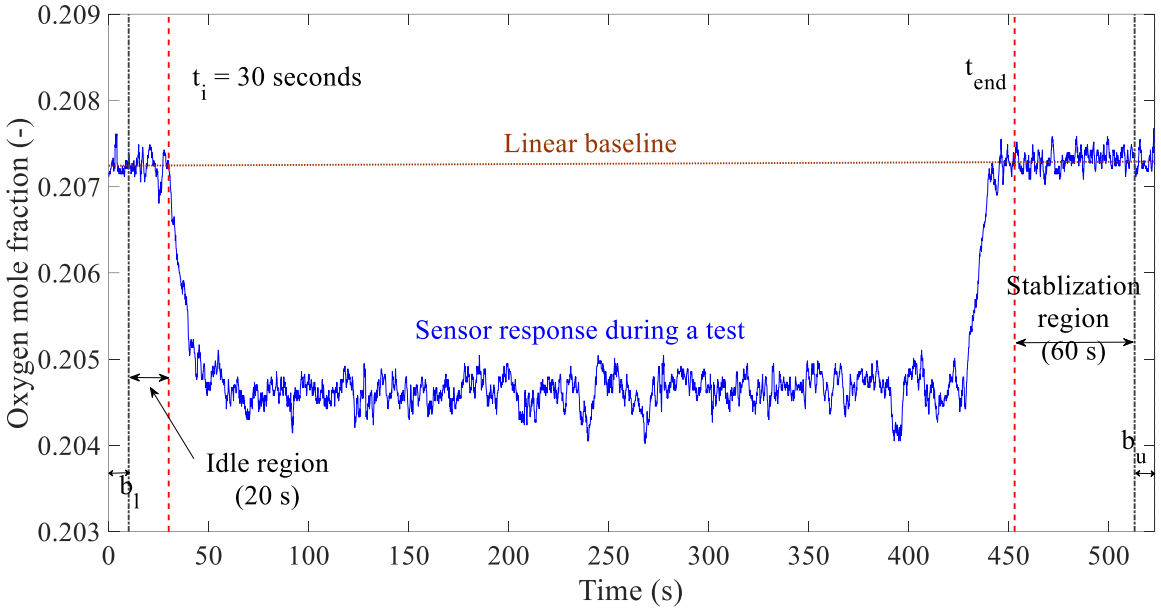

Figure A-2. Example of a baseline correction

Time of ignition is denoted as $t_i\ (s)$ is 30 seconds in Figure A-2. Average of first 10 seconds of data in the region b_l were considered as the initial conditions. End of combustion, denoted as $t_{end}(s)$ in Figure A-2, was determined similar to the time of ignition, from the thermocouple above the burner. This time corresponds to the time when the thermocouple temperature dropped within 20 % of the ambient temperature. A stabilization time of about 60 s was considered to allow all sensors to settle to final steady values. Average of 10 seconds of data in the region b_u, after the stabilization region, was considered as final baseline quantities. A linear fit between the regions b_l and b_u for oxygen mole fraction measurement then formed the baseline for *HRR* calculation.

Similar baseline linear interpolations were obtained for ambient pressure, (P_a), initial water vapor mole fraction, $(X^0_{H_2O})$, ambient temperature (T_a), resulting molecular weight (M_e) and the actual initial molar fraction of oxygen corrected for water vapor $(X^0_{O_2})$.

A.2.3 Data Representation

All the calculations were done on raw data obtained from the DAQ. However, a moving 10-point average, or one second in time, was used to represent all the data in plots to reduce the noise.

A.3. Calorimetry Validation

A.3.1 Validation Experiment Setup and Data Analysis Procedure

The calorimetry equations derived in Section A.1 was applied to two scenarios for validation. These scenarios were chosen to represent wide range of fire intensities that would be studied under the hood.

I. Pool fire over a 5.8 mm thick black Poly (methyl methacrylate) sheet of surface area 50×50 cm^2 weighing 1.752 kg.

Black cast PMMA sheet, the same as used in corner flame spread tests, was placed in an insulation tray with Aluminum tape protruding above the PMMA sheet on all sides. This prevented any potential melting or dripping of the polymer outside the enclosure and ensured combustion of the entire sheet. Figure A-3 (a) shows the pool fire above the PMMA sheet. Negligible char was observed to be left behind and the entire mass of PMMA was assumed to be completely burnt at the end of the test.

II. Propane fired burner with constant flow rate of 6.47×10^{-4} kg s^{-1} for 414 seconds.

The sandbox ensured a uniform gas flow out of the burner. Alicat flow controller with 50 SLPM (1.53×10^{-3} kg s^{-1} of propane) range was used to maintain the flow at 21.23 SLPM (6.47×10^{-4} kg s^{-1}) of propane for 414 seconds. Figure A-3 (b) shows the fire above

the propane sandbox burner. Total propane burnt was obtained by monitoring flow of propane during the test.

(a) (b)

Figure A-3. (a) Burning of PMMA sheet (b) Propane sandbox burner

To compare the capability of equations derived in Section A.1 to predict *HRR*, it was compared with oxygen consumption calorimetry procedure suggested by ASTM 1354 [4], referred as cone type calorimetry hereafter. ASTM 1354 suggests use of following equation for calculating the heat release rate, $HRR_{\text{Cone}}(W)$,

$$HRR_{Cone} = E.(1.10)C\sqrt{\frac{\Delta P}{T_e}}\frac{X_{O_2}^{m,0} - X_{O_2}^{m}}{\left(1.105 - 1.5X_{O_2}\right)} \qquad (A - 32)$$

Here, 1.105 is the ratio of molecular weights of oxygen to air, $X_{O_2}^{m,0}$ is the baseline linear fit of oxygen mole fraction, and $X_{O_2}^{m}$ is the oxygen mole fraction at time, *t*, as measured by the sensor without any corrections after adjusting for the time delays. The factor C, which otherwise is obtained by calibrations under the cone calorimeter, is estimated after comparing earlier equations, (A - 3) and (A - 31),

$$C = C_f^e A \sqrt{\frac{2P_a M_e}{R}} \qquad \text{(A - 33)}$$

Where, the quantities P_a and M_e are linear, time varying baseline obtained as explained in Section A.2.2.

A.3.2 Validation Test Results

Standard exhaust flow, exhaust temperatures and oxygen mole fraction responding to the combustion in both validation tests is shown below in Figure A-4. All the data shown here are synchronized to the 30 *s* prior to ignition. The temperature of the exhaust gases reaches a maximum of about 480 K for the PMMA sheet test. The quasi-steady nature of the propane burner test can be confirmed by stable temperatures around 330 K after about 180 seconds for the propane burner test in Figure A-4 (d). The oxygen mole fraction for the PMMA test shown in Figure A-4 (e) drops to the least value of about 19 % while fluctuates around a steady value of 20.15 % for the propane burner test as shown in Figure A-4 (f).

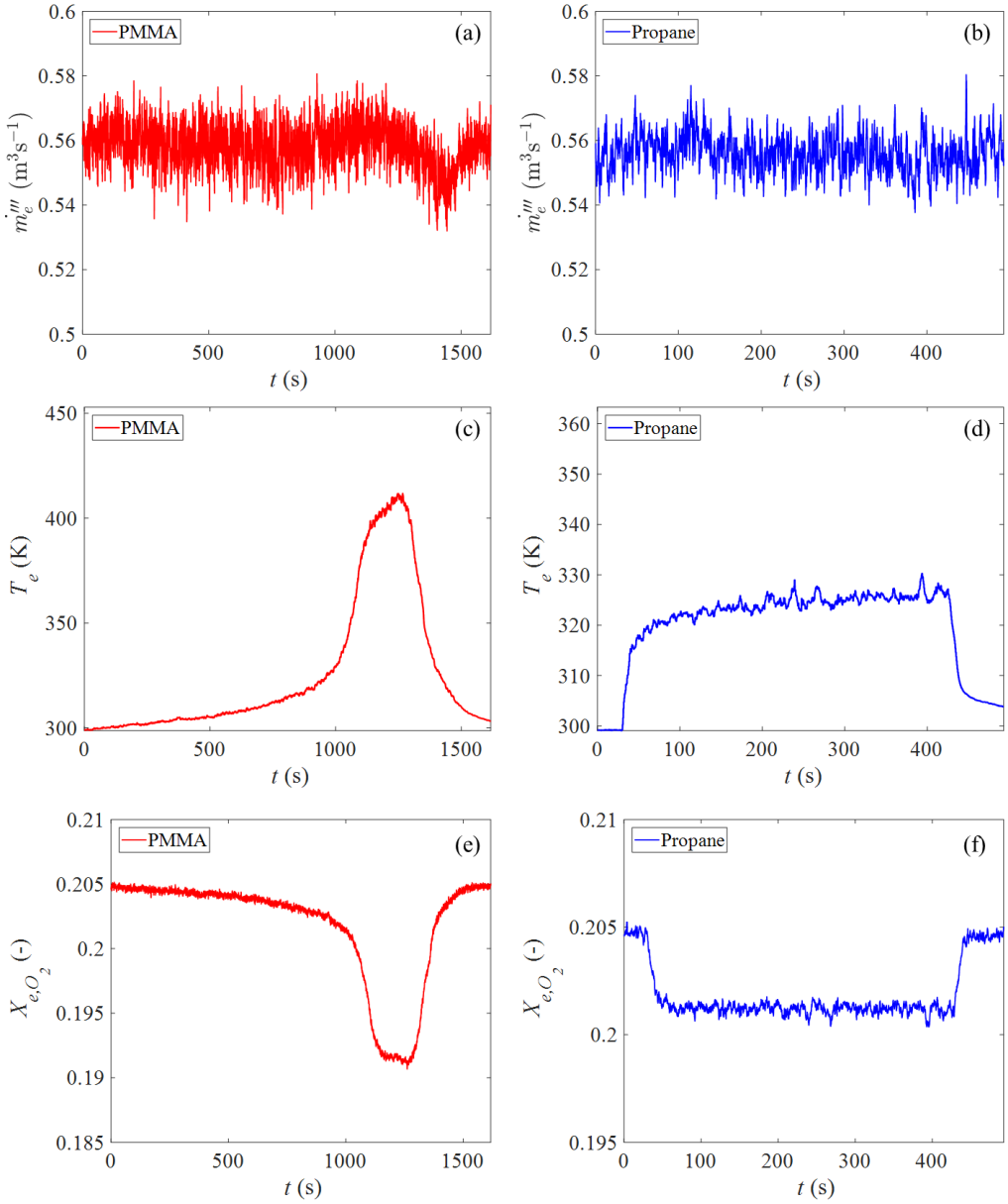

Figure A-4. Standard exhaust flow, exhaust temperature and oxygen mole fraction for validation test. (a, c, e) Black PMMA sheet (b, d, f) Propane burner

The heat release rate (HRR) and integral heat released calculated for both these tests using both corner calorimetry and cone-type calorimetry is shown in Figure A-5. For these calculations, the value of γ were fuel specific values, as given in Table A-1. The heat release rate estimated using both calorimetry methods qualitatively look similar. Maximum

heat release rate for PMMA sheet is about 110 kW and about a steady 31 kW for the Propane burner test.

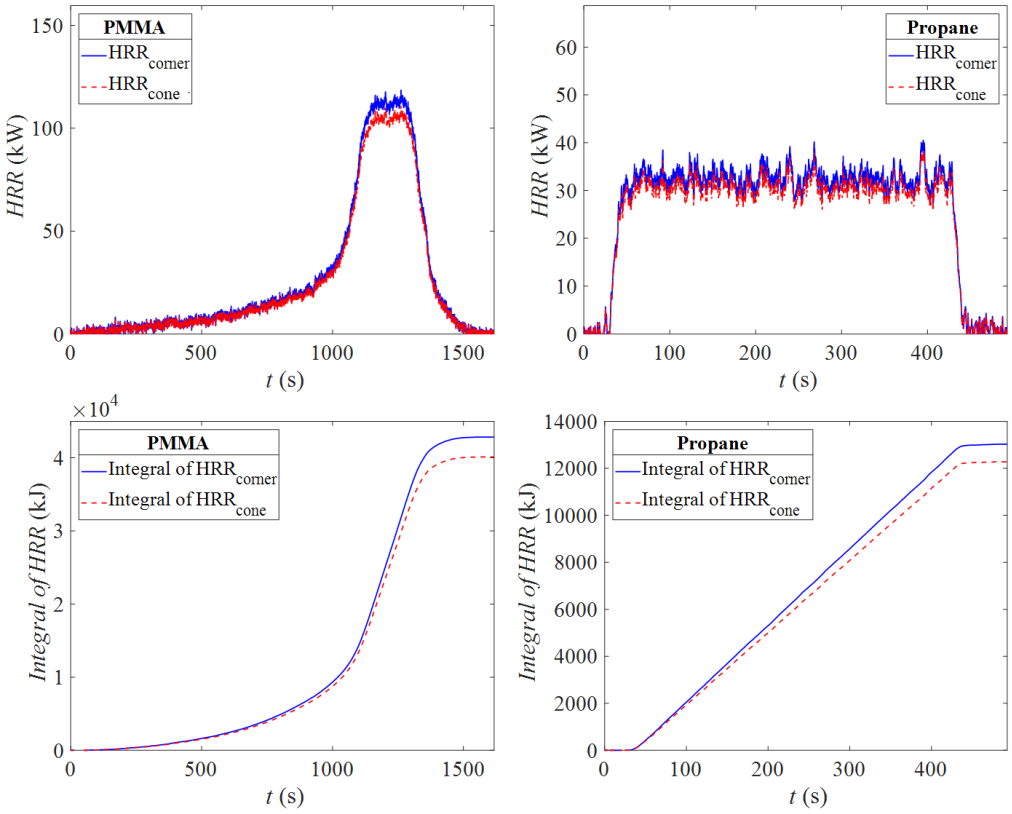

Figure A-5. Heat release rate and integral heat release for black PMMA sheet (left) and Propane burner (right)

The value of integral of the transient HRR curve, shown in Figure A-5 (c) and (d), at the end of the test gives an estimate of total heat released during the combustion process. The heat of combustion is found by dividing the total heat released by the total mass burned. Total mass estimated to be burned for propane is about 0.27 kg. The heat of combustion values, per kg of lost mass, estimated for both these tests is given below in Table A-2.

Table A-2. Heat of combustion values for PMMA and Propane calculated from two types of calorimetry equations.

Material	Corner calorimetry (J kg^{-1})	Cone type calorimetry (J kg^{-1})
PMMA	24.1×10^6 (− 1%)	22.9×10^6 (− 9%)
Propane	47.1×10^6 (− 1%)	44.5×10^6 (− 6%)

The heat of complete combustion for PMMA is reported to be $(24.5\pm0.5)\times10^6$ J kg^{-1} of lost mass, obtained from cone calorimetry experiments [175] and can be estimated theoretically to be 25.1×10^6 J kg^{-1} by assuming complete combustion (Eq. (A - 26)) and using oxygen consumption principle. Similarly, complete combustion reaction of Propane (C_3H_8) (Eq. (A - 25)) imply that, theoretically, 3.63 kg O_2 is consumed for every kg of Propane burned. Heat of combustion of Propane estimated using oxygen consumption principle is determined to be 47.5×10^6 J kg^{-1} of Propane. The percentage error shown in Table A-2 are relative to the theoretical heat of combustion values for both the fuels.

The corner calorimetry equations are thus able to capture the transient heat release rate for the range of fires tested. These predictions qualitatively agree with the predictions from well-established cone-type calorimetry principle and are quantitatively better. The fast response, synchronized, and validated calorimetry equations to predict HRR gives confidence in applying it to a large experiment of flame spread on PMMA.

Appendix B: Miscellaneous Plots

B.1. Radiative heat flux measurements

Two experiments were conducted to measure radiative portion of the heat flux away from the flame, at locations shown in Figure B. 1. Total eight 9.53 mm diameter Schmidt-Boelter heat flux gauges were used, of which two were radiometers equipped with a ZnSe window having a 150° view angle. The remaining six were total heat flux gauges spaced 25 cm from each other in the vertical *y* direction above the surface of the burner, starting from *y* = 10 cm. The two radiometers were placed alongside the total heat flux gauges at two locations, *y* = 35 cm and *y* = 85 cm (shown in red), to compare what fraction of the total heat flux received by the gauges is radiative in nature. All gauges were located at *x* = 70 cm, *z* = 70 cm from the corner, as shown in the figure below.

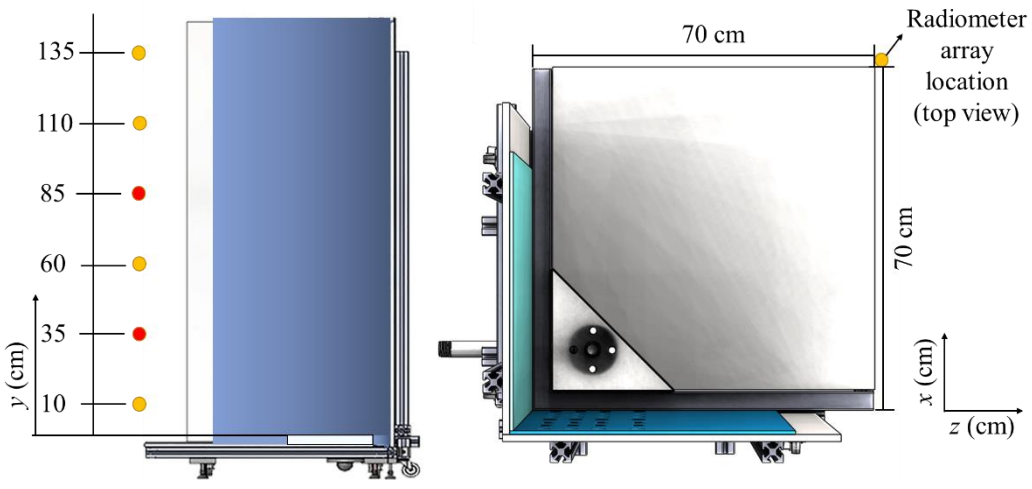

Figure B. 1. Schematic of experimental setup where radiative heat fluxes during the flame spread over PMMA were measured by total heat flux gauges (yellow circles). The red circles indicate locations which also had a radiometer along with the total heat flux gauges.

First, the heat flux measurements from the radiometer (uncorrected for the 150° view angle) and the total heat flux gauge at the same location were compared in Figure B. 2. This figure indicates that the total heat flux observed corresponds to the radiative portion of the heat flux. A deviation of about 0.5 kW m^{-2} is observed between the radiometer and the total heat flux reading at y = 35 cm, while these two measurements have excellent agreement at y = 85 cm.

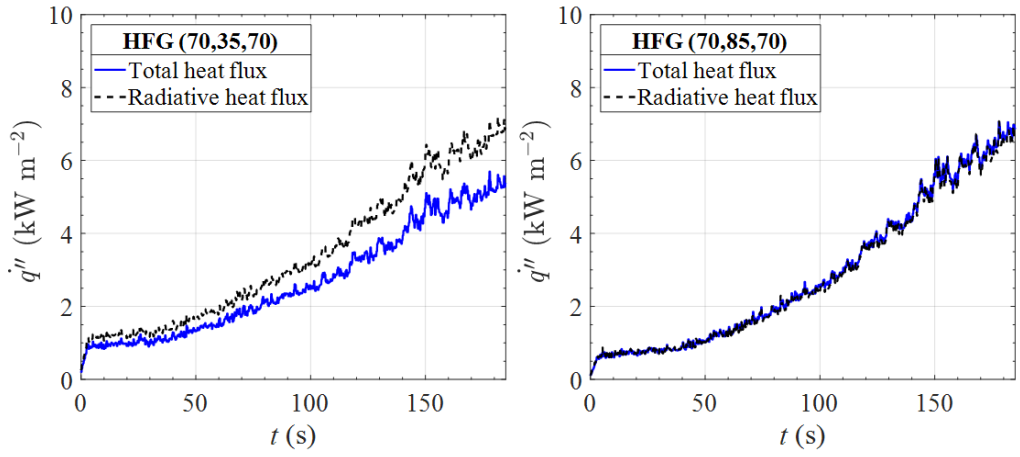

Figure B. 2. Comparison of heat flux measured by total heat flux gauge and the radiometer at two locations.

So, assuming that the total heat flux measurements represent the radiative portion of the heat flux received from the flame at the measured locations, the total heat flux measurements for the two tests are provided below in Figure B. 3.

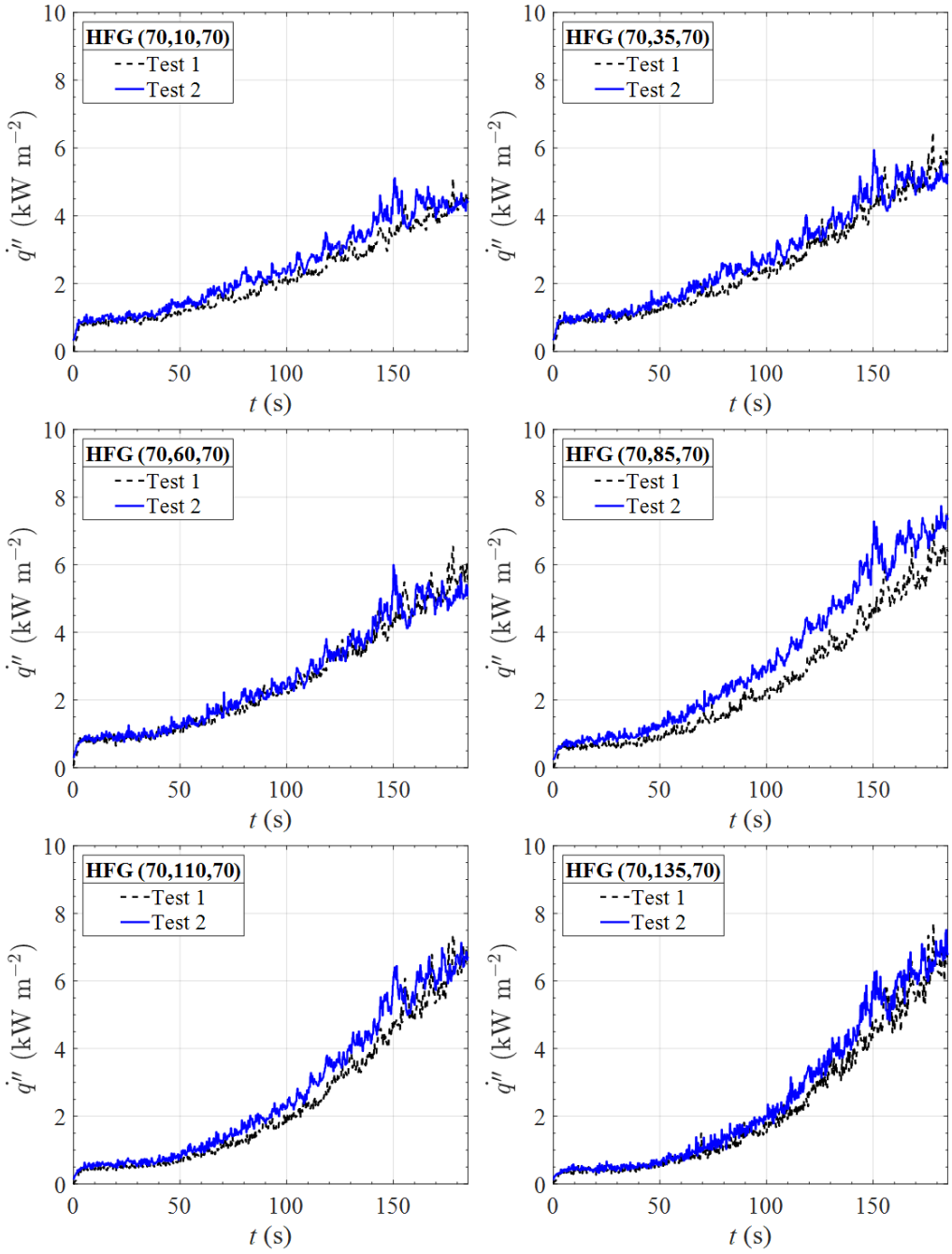

Figure B. 3. Total heat fluxes representative of the radiative portion of the heat flux measured during the flame spread tests over PMMA.

B.2. Flame heat flux contour overlaid with flame shape contour

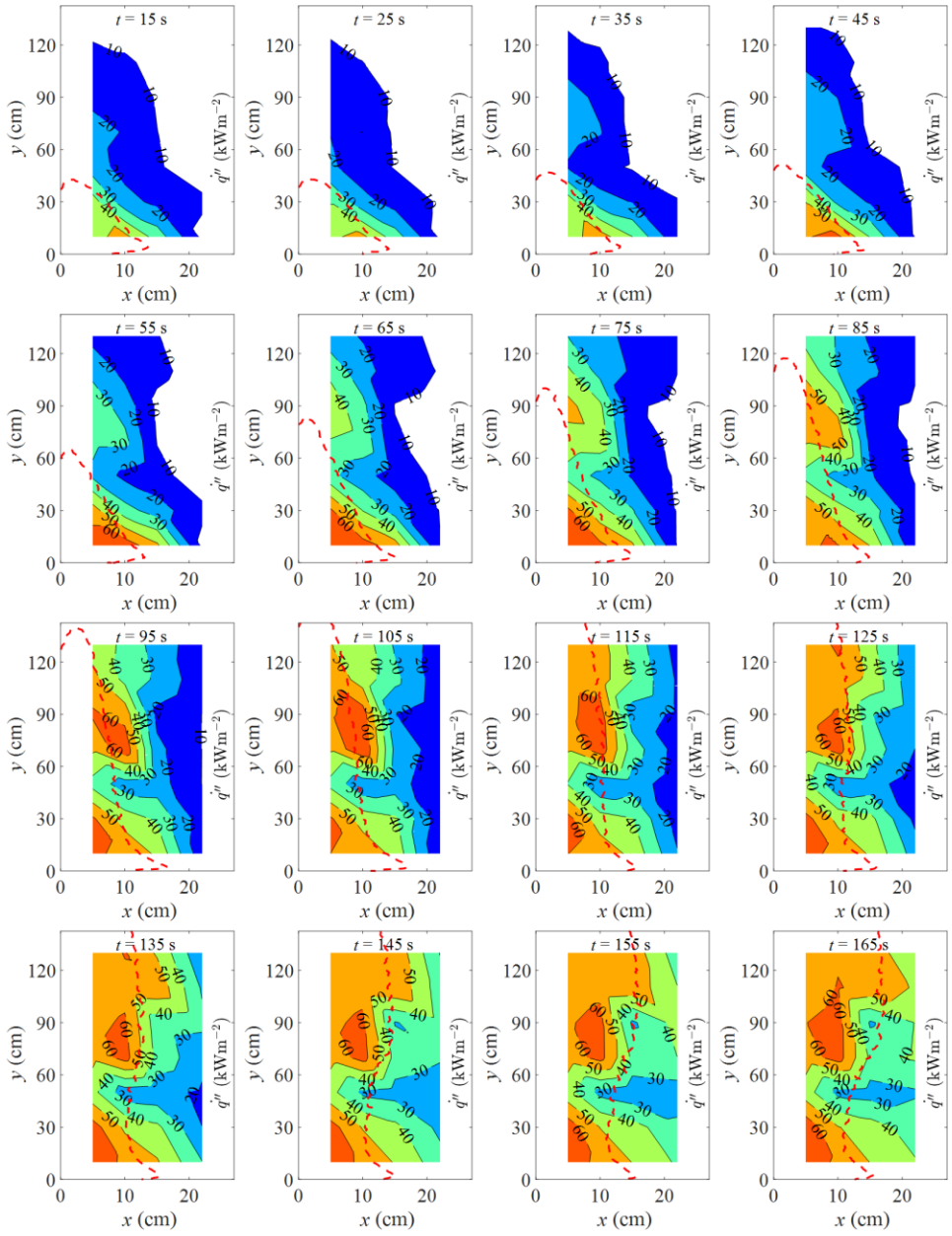

Figure B. 4. Mean interpolated flame heat flux contour for flame spread experiments conducted over PMMA overlaid with flame shape contour (dashed red line) defined as flame probability of 0.5

References

[1] Richtie H., Plastic Pollution, Our World Data. **2018**. https://ourworldindata.org/plastic-pollution.

[2] Geyer R., Jambeck J.R., Law K.L., Production, use, and fate of all plastics ever made, Sci. Adv. 3 **2017** e1700782. https://doi.org/10.1126/sciadv.1700782.

[3] Evarts B., Fire Loss in the United States During 2018, Natl. Fire Prot. Assoc. **2019**. https://www.nfpa.org/News-and-Research/Data-research-and-tools/US-Fire-Problem/Fire-loss-in-the-United-States.

[4] ASTM 1354 - Standard Test Method for Heat and Visible Smoke Release Rates for Materials and Products Using an Oxygen Consumption Calorimeter, **2017**. https://doi.org/10.1520/E1354-15A.1.8.

[5] Lyon R.E., Walters R.N., Stoliarov S.I., Safronava N., Principles and Practice of Microscale Combustion Calorimetry, Fed. Aviat. Adm. **2013**.

[6] ISO-9705 - Reaction to fire tests — Room corner test for wall and ceiling lining products, **2016**.

[7] EN-13823 - Reaction to fire tests for building products - Building products excluding floorings exposed to the thermal attack by a single burning item, **2004**.

[8] Apte V.B., Flammability testing of materials used in construction, transport and mining, 1st ed., Woodhead Publishing, **2006**.

[9] Schartel B., Hull T.R., Development of fire-retarded materials — Interpretation of cone calorimeter data, Fire Mater. 31 **2007** 327–354. https://doi.org/10.1002/fam.

[10] Yan Z., Holmstedt G., CFD and experimental studies of room fire growth on wall lining materials, Fire Saf. J. 27 **1996** 201–238. https://doi.org/10.1016/S0379-7112(96)00044-6.

[11] Quintiere J.G., The Application of Flame Spread Theory to Predict Material Performance, J. Res. Natl. Bur. Stand. (1934). 93 **1988** 61. https://doi.org/10.6028/jres.093.007.

[12] Karlsson B., North G., Gojkovic D., Using Results from Performance-Based Test Methods for Material Flammability in Fire Safety Engineering Design, J. Fire Prot. Eng. 12 **2002** 93–108. https://doi.org/10.1177/1042391502012002313.

[13] Bill R.G., Croce P.A., The International FORUM of Fire Research Directors: A position paper on small-scale measurements for next generation standards, Fire Saf. J. 41 **2006** 536–538. https://doi.org/10.1016/j.firesaf.2006.05.005.

[14] Emmons H.W., Fundamental problems of the free burning fire, Symp. Combust. 10 **1965** 951–964. https://doi.org/10.1016/S0082-0784(65)80238-7.

[15] Williams F.A., Mechanisms of fire spread, Symp. Combust. 16 **1977** 1281–1294. https://doi.org/10.1016/S0082-0784(77)80415-3.

[16] Tsai K.C., Turnbull J., Will G., Drysdale D., Upward flame spread: Heat transfer to the unburned surface, Fire Saf. Sci. 7 **2003** 117–128. https://doi.org/10.3801/IAFSS.FSS.7-117.

[17] Jiang L., He J.J., Sun J.H., Sample width and thickness effects on upward flame spread over PMMA surface, J. Hazard. Mater. 342 **2018** 114–120. https://doi.org/10.1016/j.jhazmat.2017.08.022.

[18] Hasemi Y., Thermal modeling of Upward Flame Spread, Fire Saf. Sci. 1 **1986** 87–

96. https://doi.org/10.3801/iafss.fss.1-87.
[19] Grant G., Drysdale D., Numerical modelling of early flame spread in warehouse fires, Fire Saf. J. 24 **1995** 247–278. https://doi.org/10.1016/0379-7112(95)00022-L.
[20] Brehob E.G., Kim C.I., Kulkarni A.K., Numerical model of upward flame spread on practical wall materials, Fire Saf. J. 36 **2001** 225–240. https://doi.org/10.1016/S0379-7112(00)00054-0.
[21] Rangwala A.S., Buckley S.G., Torero J.L., Upward flame spread on a vertically oriented fuel surface: The effect of finite width, Proc. Combust. Inst. 31 **2007** 2607–2615. https://doi.org/10.1016/j.proci.2006.07.235.
[22] Fernandez-Pello A.C., Hirano T., Controlling Mechanisms of Flame Spread, Fire Sci. Technol. 2 **1982** 17–54. https://doi.org/10.3210/fst.2.17.
[23] Turns S.R., An Introduction to Combustion: Concepts and Applications, 2nd ed., McGraw-Hill series in mechanical engineering, **2000**.
[24] Babrauskas V., Peacock R.D., Heat release rate: Single most important variable in fire hazard, Fire Saf. J. 18 **1992** 255–278.
[25] Cleary T.G., Flammability Characterization with the LIFT Apparatus and the Cone Calorimeter, Fire Retard. Chem. Assoc. **1992** 99–115. https://tsapps.nist.gov/publication/get_pdf.cfm?pub_id=912214%0A.
[26] Tewarson A., Flammability Parameters of Materials: Ignition, Combustion, and Fire Propagation, J. Fire Sci. 12 **1994** 329–356. https://doi.org/10.1177/073490419401200401.
[27] Biteau H., Steinhaus T., Schemel C., Simeoni A., Marlair G., Bal N., Torero J.L., Calculation Methods for the Heat Release Rate of Materials of Unknown Composition, Fire Saf. Sci. 9 **2008** 1165–1176. https://doi.org/10.3801/IAFSS.FSS.9-1165.
[28] Marlair G., Cwiklinski C., Tewarson A., An analysis of some practical methods for estimating heats of combustion in fire safety studies, in: Interflam, Edinburgh, U.K, **1999**. https://hal-ineris.archives-ouvertes.fr/ineris-00972167 (accessed August 28, 2020).
[29] Walters R.N., Hackett S.M., Lyon R.E., Heats of combustion of high temperature polymers, Fire Mater. 24 **2000** 245–252. https://doi.org/10.1002/1099-1018(200009/10)24:5<245::AID-FAM744>3.0.CO;2-7.
[30] Cardozo R.L., Prediction of the enthalpy of combustion of organic compounds, AIChE J. 32 **1986** 844–848. https://doi.org/10.1002/aic.690320514.
[31] Van Krevelen D.W., Te Nijenhuis K., Properties of polymers: their correlation with chemical structure; their numerical estimation and prediction from additive group contributions, 4th ed., Elsevier, **2009**.
[32] Schartel B., Kebelmann K., Fire Testing for the Development of Flame Retardant Polymeric Materials, in: Flame Retard. Polym. Mater., CRC Press, **2019**: pp. 35–55. https://doi.org/10.1201/b22345-3.
[33] Thornton W.M., XV. The relation of oxygen to the heat of combustion of organic compounds, London, Edinburgh, Dublin Philos. Mag. J. Sci. 33 **1917** 196–203. https://doi.org/10.1080/14786440208635627.
[34] Huggett C., Estimation of rate of heat release by means of oxygen consumption measurements, Fire Mater. 4 **1980** 61–65. https://doi.org/10.1002/fam.810040202.
[35] Tewarson A., Generation of heat and chemical compounds in fires, in: SFPE Handb.

Fire Prot. Eng., 3rd ed., **2002**: pp. 3 (82-161).
[36] Janssens M.L., Measuring rate of heat release by oxygen consumption, Fire Technol. 27 **1991** 234–249. https://doi.org/10.1007/BF01038449.
[37] Janssens M.L., Calorimetry, in: SFPE Handb. Fire Prot. Eng., 5th ed., **2016**: pp. 905–951. https://doi.org/10.1007/978-1-4939-2565-0.
[38] Chow W.K., Han S.S., Heat release rate calculation in oxygen consumption calorimetry, Appl. Therm. Eng. 31 **2011** 304–310. https://doi.org/10.1016/j.applthermaleng.2010.09.010.
[39] White J.P., Link E.D., Trouvé A., Sunderland P.B., Marshall A.W., A general calorimetry framework for measurement of combustion efficiency in a suppressed turbulent line fire, Fire Saf. J. 92 **2017** 164–176. https://doi.org/10.1016/j.firesaf.2017.06.009.
[40] Swann J.D., Ding Y., McKinnon M.B., Stoliarov S.I., Controlled atmosphere pyrolysis apparatus II (CAPA II): A new tool for analysis of pyrolysis of charring and intumescent polymers, Fire Saf. J. 91 **2017** 130–139. https://doi.org/10.1016/j.firesaf.2017.03.038.
[41] Brohez S., Uncertainty analysis of heat release rate measurement from oxygen consumption calorimetry, Fire Mater. 29 **2005** 383–394. https://doi.org/10.1002/fam.895.
[42] Brohez S., Delvosalle C., Marlair G., Tewarson A., The Measurement of Heat Release from Oxygen Consumption in Sooty Fires, J. Fire Sci. 18 **2000** 327–353. https://doi.org/10.1177/073490410001800501.
[43] Sette B.J.G., Critical considerations on the use of a bi-directional probe in heat release measurements, Fire Mater. 29 **2005** 335–349. https://doi.org/10.1002/fam.886.
[44] Sette B.J.G., Theuns E., Merci B., Vandevelde P., Temperature effects on themass flow rate in SBI and similar heat-release rate test equipment, Fire Mater. 31 **2007** 53–66. https://doi.org/10.1002/fam.925.
[45] Janssens M.L., Variability in oxygen consumption calorimetry tests, in: ASTM Spec. Tech. Publ., **2002**: pp. 147–162. https://doi.org/10.1520/stp10953s.
[46] Smith E.E., Heat release rate calorimetry, Fire Technol. 32 **1996** 333–347. https://doi.org/10.1007/BF01037743.
[47] Ito A., Kashiwagi T., Characterization of flame spread over PMMA using holographic interferometry sample orientation effects, Combust. Flame. 71 **1988** 189–204. https://doi.org/10.1016/0010-2180(88)90007-7.
[48] Markstein G.H., de Ris J., Upward fire spread over textiles, in: Symp. Combust., **1973**: pp. 1085–1097. https://doi.org/10.1016/S0082-0784(73)80098-0.
[49] Tewarson A., Ogden S.D., Fire behavior of polymethylmethacrylate, Combust. Flame. 89 **1992** 237–259. https://doi.org/10.1016/0010-2180(92)90013-F.
[50] Fernandez-Pello A., Williams F.A., Laminar flame spread over PMMA surfaces, Symp. Combust. 15 **1975** 217–231. https://doi.org/10.1016/S0082-0784(75)80299-2.
[51] Frey A.E., T'ien J.S., A theory of flame spread over a solid fuel including finite-rate chemical kinetics, Combust. Flame. 36 **1979** 263–289. https://doi.org/10.1016/0010-2180(79)90064-6.
[52] Leventon I.T., Stoliarov S.I., Evolution of flame to surface heat flux during upward

flame spread on poly(methyl methacrylate), Proc. Combust. Inst. 34 **2013** 2523–2530. https://doi.org/10.1016/j.proci.2012.06.051.
[53] Leventon I.T., Korver K.T., Stoliarov S.I., A generalized model of flame to surface heat feedback for laminar wall flames, Combust. Flame. 179 **2017** 338–353. https://doi.org/10.1016/j.combustflame.2017.02.007.
[54] Saito K., Quintiere J.G., Williams F.A., Upward Turbulent Flame Spread, Fire Saf. Sci. 1 **1986** 75–86. https://doi.org/10.3801/iafss.fss.1-75.
[55] Pizzo Y., Consalvi J.L., Querre P., Coutin M., Audouin L., Porterie B., Torero J.L., Experimental observations on the steady-state burning rate of a vertically oriented PMMA slab, Combust. Flame. 152 **2008** 451–460. https://doi.org/10.1016/J.COMBUSTFLAME.2007.06.020.
[56] Honda L.K., Ronney P.D., Mechanisms of concurrent-flow flame spread over solid fuel beds, Proc. Combust. Inst. 28 **2000** 2793–2801. https://doi.org/10.1016/s0082-0784(00)80701-8.
[57] Pizzo Y., Consalvi J.L., Querre P., Coutin M., Porterie B., Width effects on the early stage of upward flame spread over PMMA slabs: Experimental observations, Fire Saf. J. 44 **2009** 407–414. https://doi.org/10.1016/j.firesaf.2008.09.003.
[58] Ahmad T., Faeth G.M., Turbulent wall fires, in: Symp. Combust., **1979**: pp. 1149–1160. https://doi.org/10.1016/S0082-0784(79)80109-5.
[59] Hasemi Y., Tokunaga T., Some Experimental Aspects of Turbulent Diffusion Flames and Buoyant Plumes from Fire Sources Against a Wall and in a Corner of Walls, Combust. Sci. Technol. 40 **1984** 1–18. https://doi.org/10.1080/00102208408923795.
[60] Quintiere J., Harkleroad M., Hasemi Y., Wall Flames and Implications for Upward Flame Spread, Federal Aviation Administration, **1985**.
[61] Back G., Beyler C., Dinenno P., Tatem P., Wall Incident Heat Flux Distributions Resulting From An Adjacent Fire, Fire Saf. Sci. 4 **1994** 241–252. https://doi.org/10.3801/iafss.fss.4-241.
[62] Lattimer B.Y., Heat transfer from Fires to Surfaces, in: SFPE Handb. Fire Prot. Eng., 5th ed., **2016**: pp. 745–798. https://doi.org/10.1007/978-1-4939-2565-0.
[63] Delichatsios M.M., Mathews M.K., Delichatsios M.A., An upward Fire Spread and Growth Simulation, Fire Saf. Sci. 3 **1991** 207–216. https://doi.org/3801/IAFSS.FSS.3-207.
[64] Qian C., Saito K., An Empirical Model For Upward Flame Spread Over Vertical Flat And Corner Walls, Fire Saf. Sci. 5 **1997** 285–296. https://doi.org/10.3801/iafss.fss.5-285.
[65] Kokkala M., Baroudi D., Parker W., Upward Flame Spread On Wooden Surface Products: Experiments And Numerical Modelling, Fire Saf. Sci. 5 **1997** 309–320. https://doi.org/10.3801/iafss.fss.5-309.
[66] Orloff L., De Ris J., Markstein G.H., Upward turbulent fire spread and burning of fuel surface, Symp. Combust. 15 **1975** 183–192. https://doi.org/10.1016/S0082-0784(75)80296-7.
[67] Fernandez-Pello A.C., A theoretical model for the upward laminar spread of flames over vertical fuel surfaces, Combust. Flame. 31 **1978** 135–148. https://doi.org/10.1016/0010-2180(78)90124-4.
[68] Tsai K.C., Drysdale D., Flame height correlation and upward flame spread

modelling, Fire Mater. 26 **2002** 279–287. https://doi.org/10.1002/fam.809.
[69] Markstein G.H., De Ris J., Wall-fire radiant emission-Part 2: Radiation and heat transfer from porous-metal wall burner flames, Symp. Combust. 24 **1992** 1747–1752. https://doi.org/10.1016/S0082-0784(06)80204-3.
[70] Mowrer F.W., Williamson R.B., Estimating Room Temperatures from Fires along Walls and in Corners, Fire Technol. 23 **1987** 133–145.
[71] Takahashi W., Tanaka H., Sugawa O., Ohtake M., Flame and Plume Behavior in and near a Corner of Walls, Fire Saf. Sci. 5 **1997** 261–271.
[72] Poreh M., Garrad G., A study of wall and corner fire plumes, Fire Saf. J. 34 **2000** 81–98. https://doi.org/10.1016/S0379-7112(99)00040-5.
[73] Alpert R.L., Evaluation of the Hazard of Fire Resistant Materials Using Measurements from Laboratory and Parallel Panel Tests, Fire Saf. Sci. 7 **2003** 41–57.
[74] Di Blasi C., The Burning of Plastics, in: Plast. Flammabl. Handb., 3rd ed., Hanser, **2004**: pp. 47–132. https://doi.org/10.3139/9783446436695.004.
[75] Staggs J.E.J., Modelling thermal degradation of polymers using single-step first-order kinetics, Fire Saf. J. 32 **1999** 17–34. https://doi.org/10.1016/S0379-7112(98)00026-5.
[76] Quintiere J.G., Fundamentals of fire phenomena, John Wiley & Sons, **2006**.
[77] De Ris J.N., Spread of a laminar diffusion flame, in: Symp. Combust., **1969**: pp. 241–252. https://doi.org/10.1016/S0082-0784(69)80407-8.
[78] Lyon R.E., Jansses M.L., Polymer Flammability, Department of Transportation, **2005**.
[79] Fernandez-Pello A.C., Flame Spread Modeling, Combust. Sci. Technol. 39 **1984** 119–134. https://doi.org/10.1080/00102208408923786.
[80] Di Blasi C., Modeling of solid- and gas-phase processes during thermal degradation of composite materials, Polym. Degrad. Stab. 54 **1996** 241–248. https://doi.org/10.1016/s0141-3910(96)00049-3.
[81] Di Blasi C., Influences of sample thickness on the early transient stages of concurrent flame spread and solid burning, Fire Saf. J. 25 **1995** 287–304. https://doi.org/10.1016/0379-7112(96)00010-0.
[82] Kashiwagi T., Polymer combustion and flammability-Role of the condensed phase, Symp. Combust. 25 **1994** 1423–1437. https://doi.org/10.1016/S0082-0784(06)80786-1.
[83] Kashiwagi T., Inabi A., Hamins A., Behavior of primary radicals during thermal degradation of poly(methyl methacrylate), Polym. Degrad. Stab. 26 **1989** 161–184. https://doi.org/10.1016/0141-3910(89)90007-4.
[84] Marongiu A., Faravelli T., Bozzano G., Dente M., Ranzi E., Thermal degradation of poly(vinyl chloride), J. Anal. Appl. Pyrolysis. 70 **2003** 519–553. https://doi.org/10.1016/S0165-2370(03)00024-X.
[85] Nyden M.R., Coley T.R., Mumby S., Application of Molecular Dynamics to the Study of Thermal Degradation in Aromatic Polymers. I: Polystyrene, Polym. Eng. Sci. 37 **1997**.
[86] Stoliarov S.I., Westmoreland P.R., Nyden M.R., Forney G.P., A reactive molecular dynamics model of thermal decomposition in polymers: I. Poly(methyl methacrylate), Polymer. 44 **2002** 883–894. https://doi.org/10.1016/S0032-

3861(02)00761-9.
[87] Batiot B., Rogaume T., Collin A., Richard F., Luche J., Sensitivity and uncertainty analysis of Arrhenius parameters in order to describe the kinetic of solid thermal degradation during fire phenomena, Fire Saf. J. 82 **2016** 76–90. https://doi.org/10.1016/j.firesaf.2016.03.007.
[88] Rogaume T., Thermal decomposition and pyrolysis of solid fuels: Objectives, challenges and modelling, Fire Saf. J. 106 **2019** 177–188. https://doi.org/10.1016/j.firesaf.2019.04.016.
[89] Lautenberger C., Rein G., Fernandez-Pello C., The application of a genetic algorithm to estimate material properties for fire modeling from bench-scale fire test data, Fire Saf. J. 41 **2006** 204–214. https://doi.org/10.1016/j.firesaf.2005.12.004.
[90] Rogaume T., Valencia L.B., Guillaume E., Richard F., Luche J., Rein G., Torero J.L., Development of the thermal decomposition mechanism of polyether polyurethane foam using both condensed and gas-phase release data, Combust. Sci. Technol. 183 **2011** 627–644. https://doi.org/10.1080/00102202.2010.535574.
[91] Li J., Stoliarov S.I., Measurement of kinetics and thermodynamics of the thermal degradation for non-charring polymers, Combust. Flame. 160 **2013** 1287–1297. https://doi.org/http://dx.doi.org/10.1016/j.combustflame.2013.02.012.
[92] Aboulkas A., El K., Bouadili A. El, Thermal degradation behaviors of polyethylene and polypropylene. Part I : Pyrolysis kinetics and mechanisms, Energy Convers. Manag. 51 **2010** 1363–1369. https://doi.org/10.1016/j.enconman.2009.12.017.
[93] Matala A., Hostikka S., Mangs J., Estimation of pyrolysis model parameters for solid materials using thermogravimetric data, Fire Saf. Sci. 9 **2008** 1213–1223. https://doi.org/10.3801/IAFSS.FSS.9-1213.
[94] Stoliarov S.I., Crowley S., Lyon R.E., Linteris G.T., Prediction of the burning rates of non-charring polymers, Combust. Flame. 156 **2009** 1068–1083. https://doi.org/10.1016/J.COMBUSTFLAME.2008.11.010.
[95] Stoliarov S.I., Crowley S., Walters R.N., Lyon R.E., Prediction of the burning rates of charring polymers, Combust. Flame. 157 **2010** 2024–2034. https://doi.org/10.1016/j.combustflame.2010.03.011.
[96] Bal N., Rein G., On the effect of inverse modelling and compensation effects in computational pyrolysis for fire scenarios, Fire Saf. J. 72 **2015** 68–76. https://doi.org/10.1016/j.firesaf.2015.02.012.
[97] Lautenberger C., Fernandez-Pello A., Optimization Algorithms for Material Pyrolysis Property Estimation, Fire Saf. Sci. 10 **2011** 751–764. https://doi.org/10.3801/IAFSS.FSS.10-751.
[98] Torero J.L., Scaling-Up fire, Proc. Combust. Inst. 34 **2013** 99–124. https://doi.org/10.1016/j.proci.2012.09.007.
[99] Marcos C., Khan M.M., Krishnamoorthy N., Chatterjee P., Yi W., Dorofeev S.B., Experiments and Modeling of Single- and Triple-Wall Corrugated Cardboard: Effective Material Properties and Fire Behavior, Fire Mater. **2011** 625–636.
[100] Guillaume E., Camillo A., Rogaume T., Application and Limitations of a Method Based on Pyrolysis Models to Simulate Railway Rolling Stock Fire Scenarios, Fire Technol. 50 **2014** 317–348. https://doi.org/10.1007/s10694-013-0379-9.
[101] Zeinali D., Gupta A., Maragkos G., Agarwal G., Beji T., Chaos M., Wang Y., Degroote J., Merci B., Study of the importance of non-uniform mass density in

numerical simulations of fire spread over MDF panels in a corner configuration, Combust. Flame. 200 **2019** 303–315. https://doi.org/10.1016/j.combustflame.2018.11.020.
[102] Brown A., Bruns M., Gollner M., Hewson J., Maragkos G., Marshall A., Mcdermott R., Merci B., Rogaume T., Stoliarov S., Torero J., Trouvé A., Wang Y., Weckman E., Proceedings of the first workshop organized by the IAFSS Working Group on Measurement and Computation of Fire Phenomena (MaCFP), Fire Saf. J. 101 **2018** 1–17. https://doi.org/10.1016/j.firesaf.2018.08.009.
[103] Williamson R.B., Revenaugh A., Mowrer F.W., Ignition Sources in Room Fire Tests and Some Implications for Flame Spread Evaluation, Fire Saf. Sci. 3 **1991** 657–666. https://doi.org/10.3801/IAFSS.FSS.3-657.
[104] Qian C., Saito K., Turbulent Flame Spread on Vertical Corner Walls, in: Combust. Institute/Eastern States Sect. Meet., Princeton, NJ, **1993**: pp. 338–341.
[105] Ohlemiller T., Cleary T., Shields J., Effect of ignition conditions on upward flame spread on a composite material in a corner configuration, Fire Saf. J. 31 **1998** 331–344. https://doi.org/10.1016/S0379-7112(98)00019-8.
[106] Ohlemiller T.J., Estimating Fire Growth on Composite Materials in a Corner Configuration, in: 45th Int. SAMPE Symp., California, U.S.A, **2000**: pp. 1229–1243.
[107] Zeinali D., Verstockt S., Beji T., Maragkos G., Degroote J., Merci B., Experimental study of corner fires — Part II : Flame spread over MDF panels, Combust. Flame. 189 **2018** 491–505. https://doi.org/10.1016/j.combustflame.2017.10.023.
[108] Lattimer B.Y., Sorathia U., Thermal characteristics of fires in a combustible corner, 38 **2003** 747–770. https://doi.org/10.1016/S0379-7112(03)00066-3.
[109] Lattimer B.Y., Sorathia U., Thermal characteristics of fires in a noncombustible corner, Fire Saf. J. 38 **2003** 709–745. https://doi.org/10.1016/S0379-7112(03)00065-1.
[110] Lannon C.M., Stoliarov S.I., Lord J.M., Leventon I.T., A methodology for predicting and comparing the full-scale fire performance of similar materials based on small-scale testing, Fire Mater. 42 **2018** 710–724. https://doi.org/10.1002/fam.2524.
[111] Dillon S., Analysis of ISO 9705 room corner test: Simulations, Correlations and Heat flux measurements, Master of Science thesis, University of Maryland, College Park, **1998**.
[112] Kokkala M., Characteristics of a Flame in an Open Corner of Walls, in: Proc. from Interflam Conf., Canterbury, UK, **1993**: pp. 13–24.
[113] Tanaka T., Nakaya I., Yoshida M., Full Scale Experiments for Determining the Burning Conditions To Be Applied To Toxicity Tests., Fire Saf. Sci. 1 **1986** 129–138. https://doi.org/10.3801/iafss.fss.1-129.
[114] Lattimer B.Y., Hunt S.P., Wright M., Modeling fire growth in a combustible corner, 38 **2003** 771–796. https://doi.org/10.1016/S0379-7112(03)00067-5.
[115] Zeinali D., Verstockt S., Beji T., Maragkos G., Degroote J., Merci B., Experimental study of corner fires — Part I : Inert panel tests, Combust. Flame. 189 **2018** 472–490. https://doi.org/10.1016/j.combustflame.2017.09.034.
[116] Hietaniemi J., Hostikka S., Vaari J., FDS simulation of fire spread – comparison of model results with experimental data, VTT Build. Transp. **2004** 51.

[117] Zhang J., Delichatsios M., Colobert M., Assessment of Fire Dynamics Simulator for Heat Flux and Flame Heights Predictions from Fires in SBI Tests, Fire Technol. 46 **2010** 291–306. https://doi.org/10.1007/s10694-008-0072-6.
[118] Hakkarainen T., Kokkala M.A., Application of a one-dimensional thermal flame spread model on predicting the rate of heat release in the SBI test, Fire Mater. 25 **2001** 61–70. https://doi.org/10.1002/fam.760.
[119] Hjohlman M., Andersson P., van Hees P., Flame Spread Modelling of Complex Textile Materials, Fire Technol. 47 **2011** 85–106. https://doi.org/10.1007/s10694-009-0128-2.
[120] Van Mierlo R., Sette B., The Single Burning Item (SBI) test method - A decade of development and plans for the near future, Heron. 50 **2005** 191–207.
[121] Quintiere J.G., A Simulation Model for Fire Growth on Materials Subject to a Room - Corner Test, Fire Saf. J. 20 **1993** 313–339.
[122] Wade C., Barnett J., A room-corner Fire Model Including fire growth on Linings and Enclosure Smoke-Filling, J. Fire Prot. Eng. 8 **1997** 183–193.
[123] Hees P. Van, Hertzberg T., Hansen A.S., Development of a Screening Method for the SBI and Room Corner using the Cone Calorimeter, SP Rep. **2002**.
[124] van Hees P., Andersson P., Hjohlman M., Wenne N., Hassan M.A., Use of Cone Calorimeter and ConeTools software for development of innovative intumescing graphite systems, Fire Mater. 34 **2010** 367–384. https://doi.org/10.1002/fam.1032.
[125] Leventon I.T., Li J., Stoliarov S.I., A flame spread simulation based on a comprehensive solid pyrolysis model coupled with a detailed empirical flame structure representation, Combust. Flame. 162 **2015** 3884–3895. https://doi.org/10.1016/j.combustflame.2015.07.025.
[126] Hostikka S., Mcgrattan K.B., Large Eddy Simulation of Wood combustion, in: Int. Interflam Conf., Edinburgh, U.K, **2001**: pp. 755–762.
[127] Lundström V.F., van Hees P., Guillaume É., A review on prediction models for full-scale fire behaviour of building products, Fire Mater. 41 **2017** 225–244. https://doi.org/10.1002/fam.2380.
[128] Zhang J., Dembele S., Karwatzki J., Wen J.X., Effect of radiation models on CFD simulations of upward flame spread, Fire Saf. Sci. 8 **2005** 421–432. https://doi.org/10.3801/IAFSS.FSS.8-421.
[129] Stoliarov S.I., Lyon R.E., Thermo-kinetic model of burning for pyrolyzing materials, Fire Saf. Sci. 9 **2008** 1141–1152. https://doi.org/10.3801/IAFSS.FSS.9-1141.
[130] Li J., Stoliarov S.I., Measurement of kinetics and thermodynamics of the thermal degradation for charring polymers, Polym. Degrad. Stab. 106 **2014** 2–15. https://doi.org/10.1016/j.polymdegradstab.2013.09.022.
[131] Chaos M., Khan M.M., Krishnamoorthy N., De Ris J.L., Dorofeev S.B., Evaluation of optimization schemes and determination of solid fuel properties for CFD fire models using bench-scale pyrolysis tests, Proc. Combust. Inst. 33 **2011** 2599–2606. https://doi.org/10.1016/j.proci.2010.07.018.
[132] Swann J.D., Ding Y., Stoliarov S.I., Characterization of pyrolysis and combustion of rigid poly(vinyl chloride) using two-dimensional modeling, Int. J. Heat Mass Transf. 132 **2019** 347–361. https://doi.org/10.1016/j.ijheatmasstransfer.2018.12.011.

[133] Matala A., Hostikka S., Pyrolysis modelling of PVC cable materials, Fire Saf. Sci. 10 **2011** 917–930. https://doi.org/10.3801/IAFSS.FSS.10-917.
[134] Di Blasi C., Modeling chemical and physical processes of wood and biomass pyrolysis, Prog. Energy Combust. Sci. 34 **2008** 47–90. https://doi.org/10.1016/j.pecs.2006.12.001.
[135] Lautenberger C., Fernandez-Pello C., Generalized pyrolysis model for combustible solids, Fire Saf. J. 44 **2009** 819–839. https://doi.org/10.1016/j.firesaf.2009.03.011.
[136] Lautenberger C., Gpyro – A Generalized Pyrolysis Model for Combustible Solids: Technical Reference, **2014**.
[137] Stoliarov S.I., Technical Reference for Numerical Pyrolysis Model ThermaKin2Ds, **2017**.
[138] Mcgrattan K., Hostikka S., Mcdermott R., Floyd J., Vanella M., Weinschenk C., Overholt K., Fire Dynamics Simulator User's Guide, Natl. Inst. Stand. Technol. **2017**.
[139] ASTM E2058 - Standard Test Methods for Measurement of Material Flammability Using a Fire Propagation Apparatus (FPA), **2017**. https://doi.org/10.1520/E2058-13A.2.
[140] Coats A.W., Redfern J.P., Thermogravimetric analysis. A review, Analyst. 88 **1963** 906–924. https://doi.org/10.1039/AN9638800906.
[141] Vovelle C., Delfau J.L., Reuillon M., Bransier J., Laraqui N., Experimental and Numerical Study of the Thermal Degradation of PMMA, Combust. Sci. Technol. 53 **1987** 187–201. https://doi.org/10.1080/00102208708947026.
[142] Marquis D.M., Batiot B., Guillaume E., Rogaume T., Influence of reaction mechanism accuracy on the chemical reactivity prediction of complex charring material in fire condition, J. Anal. Appl. Pyrolysis. 118 **2016** 231–248. https://doi.org/10.1016/j.jaap.2016.02.007.
[143] Lyon R.E., Heat release kinetics, Fire Mater. 24 **2000** 179–186. https://doi.org/10.1002/1099-1018(200007/08)24:4<179::AID-FAM736>3.0.CO;2-V.
[144] Rein G., Lautenberger C., Fernandez-Pello A.C., Torero J.L., Urban D.L., Application of genetic algorithms and thermogravimetry to determine the kinetics of polyurethane foam in smoldering combustion, Combust. Flame. 146 **2006** 95–108. https://doi.org/10.1016/j.combustflame.2006.04.013.
[145] Fateh T., Richard F., Rogaume T., Joseph P., Experimental and modelling studies on the kinetics and mechanisms of thermal degradation of polymethyl methacrylate in nitrogen and air, J. Anal. Appl. Pyrolysis. 120 **2016** 423–433. https://doi.org/10.1016/J.JAAP.2016.06.014.
[146] Fiola G.J., Chaudhari D.M., Stoliarov S.I., Comparison of Pyrolysis Properties of Extruded and Cast Poly(methyl methacrylate), Fire Saf. J. **2020**. https://doi.org/10.1016/j.firesaf.2020.103083.
[147] McKinnon M.B., Stoliarov S.I., Pyrolysis model development for a multilayer floor covering, Materials (Basel). 8 **2015** 6117–6153. https://doi.org/10.3390/ma8095295.
[148] Stoliarov S.I., Leventon I.T., Lyon R.E., Two-dimensional model of burning for pyrolyzable solids, Fire Mater. 38 **2014** 391–408. https://doi.org/10.1002/fam.2187.
[149] McKenna S.T., Jones N., Peck G., Dickens K., Pawelec W., Oradei S., Harris S.,

Stec A.A., Hull T.R., Fire behaviour of modern façade materials – Understanding the Grenfell Tower fire, J. Hazard. Mater. 368 **2019** 115–123. https://doi.org/10.1016/j.jhazmat.2018.12.077.
[150] Guillaume E., Dréan V., Girardin B., Benameur F., Fateh T., Reconstruction of Grenfell Tower fire. Part 1: Lessons from observations and determination of work hypotheses, Fire Mater. 44 **2020** 3–14. https://doi.org/10.1002/fam.2766.
[151] Madorsky S.L., Thermal Degradation of Organic Polymers, Intersci. Publ. **1964**.
[152] Rhodes B.T., Quintiere J.G., Burning rate and flame heat flux for PMMA in a cone calorimeter, Fire Saf. J. 26 **1996** 221–240. https://doi.org/10.1016/S0379-7112(96)00025-2.
[153] Mccoy C.G., Tilles J.L., Stoliarov S.I., Empirical Model of flame heat feedback for simulation of cone calorimetry, Fire Saf. J. 103 **2019** 38–48. https://doi.org/10.1016/j.firesaf.2018.11.006.
[154] Korobeinichev O., Gonchikzhapov M., Tereshchenko A., Gerasimov I., Shmakov A., Paletsky A., Karpov A., An experimental study of horizontal flame spread over PMMA surface in still air, Combust. Flame. 188 **2018** 388–398. https://doi.org/10.1016/j.combustflame.2017.10.008.
[155] Zhang J., Shields T.J., Silcock G.W.H., Effect of melting behaviour on upward flame spread of thermoplastics, Fire Mater. 21 **1997** 1–6. https://doi.org/10.1002/(sici)1099-1018(199701)21:1<1::aid-fam583>3.3.co;2-g.
[156] Korobeinichev O.P., Karpov A.I., Bolkisev A.A., Shaklein A.A., Gonchikzhapov M.B., Paletsky A.A., Tereshchenko A.G., An experimental and numerical study of thermal and chemical structure of downward flame spread over PMMA surface in still air, Proc. Combust. Inst. 000 **2018** 1–8. https://doi.org/10.1016/j.proci.2018.06.005.
[157] Staggs J.E.J., Population balance models for the thermal degradation of PMMA, Polymer. 48 **2007** 3868–3876. https://doi.org/10.1016/j.polymer.2007.04.075.
[158] Comuce M., Rogaume T., Richard F., Fateh T., Luche J., Rousseaux P., Kinetics and Mechanisms of the Thermal Degradation of Polymethyl Methacrylate by TGA/FTIR Analysis, Sixth Int. Semin. Fire Explos. Hazards. **2016**.
[159] Annual Energy Outlook 2019, U.S. Energy Inf. Adm. **2019**. https://www.eia.gov/outlooks/aeo/.
[160] Biswas K., Shrestha S.S., Bhandari M.S., Desjarlais A.O., Insulation materials for commercial buildings in North America: An assessment of lifetime energy and environmental impacts, Energy Build. 112 **2016** 256–269. https://doi.org/10.1016/j.enbuild.2015.12.013.
[161] Marotte B., Toronto's Norbord riding the rising wave of OSB sales, Globe Mail. **2016**. https://www.theglobeandmail.com/report-on-business/forest-products-firm-norbord-riding-the-rising-wave-of-osb-sales/article30985989/ (accessed May 5, 2021).
[162] Kashiwagi T., Inaba A., Brown J.E., Differences in Pmma Degradation Characteristics and Their Effects on Its Fire Properties., Fire Saf. Sci. 1 **1986** 483–493. https://doi.org/10.3801/IAFSS.FSS.1-483.
[163] Lyon R.E., Safronava N., Senese J., Stoliarov S.I., Thermokinetic model of sample response in nonisothermal analysis, Thermochim. Acta. 545 **2012** 82–89. https://doi.org/10.1016/j.tca.2012.06.034.

[164] Linteris G., Zammarano M., Wilthan B., Hanssen L., Absorption and reflection of infrared radiation by polymers in fire-like environments, Fire Mater. 36 **2012** 537–553. https://doi.org/10.1002/fam.1113.
[165] McKinnon M.B., Stoliarov S.I., Witkowski A., Development of a pyrolysis model for corrugated cardboard, Combust. Flame. 160 **2013** 2595–2607. https://doi.org/10.1016/j.combustflame.2013.06.001.
[166] Li J., Gong J., Stoliarov S.I., Gasification experiments for pyrolysis model parameterization and validation, Int. J. Heat Mass Transf. 77 **2014** 738–744. https://doi.org/10.1016/j.ijheatmasstransfer.2014.06.003.
[167] Ding Y., Swann J.D., Sun Q., Stoliarov S.I., Kraemer R.H., Development of a pyrolysis model for glass fiber reinforced polyamide 66 blended with red phosphorus: Relationship between flammability behavior and material composition, Compos. Part B Eng. 176 **2019** 107263. https://doi.org/10.1016/j.compositesb.2019.107263.
[168] Fiola G.J., Improving Inverse Analysis of Pyrolysis Model Parameterization Using Hill Climbing Algorithms, University of Maryland, **2019**.
[169] Ding Y., McKinnon M.B., Stoliarov S.I., Fontaine G., Bourbigot S., Determination of kinetics and thermodynamics of thermal decomposition for polymers containing reactive flame retardants: Application to poly(lactic acid) blended with melamine and ammonium polyphosphate, Polym. Degrad. Stab. 129 **2016** 347–362. https://doi.org/10.1016/j.polymdegradstab.2016.05.014.
[170] Incropera F.P., DeWitt D.P., Bergman T.L., Lavine A.S., Fundamentals of Heat and Mass Transfer, 6th ed., **2007**.
[171] Cengel Y.A., Introduction to thermodynamics and heat transfer, McGraw-Hill New York, **1997**.
[172] Siegel R., Howell J.R., Thermal radiation heat transfer, 4th ed., Taylor & Francis, **2002**.
[173] Frances C.E., A non-intrusive method for temperature measurements in flames produced by milligram-sized solid samples, Masters of science thesis, University of Maryland, College Park, **2014**.
[174] NIST Chemistry WebBook, n.d. https://webbook.nist.gov/chemistry/ (accessed November 15, 2019).
[175] Luche J., Rogaume T., Richard F., Guillaume E., Characterization of thermal properties and analysis of combustion behavior of PMMA in a cone calorimeter, Fire Saf. J. 46 **2011** 451–461. https://doi.org/10.1016/j.firesaf.2011.07.005.
[176] Zhang J., Delichatsios M., Colobert M., Hereid J., Hagen M., Bakirtzis D., Experimental and numerical investigations of heat impact and flame heights from fires in SBI tests, Fire Saf. Sci. 9 **2008** 205–216. https://doi.org/10.3801/IAFSS.FSS.9-205.
[177] Eric R., Alain G., Guillaume E., Sainrat A., Blanc C., Yardin C., Guillaume E., Molinier C., Sainrat A., Lievre M., EGOLF SBI Thermal Attack Measurements Round Robin 2, **2005**.
[178] Zukoski E.E., Cetegen B.M., Kubota T., Visible structure of buoyant diffusion flames, in: Twent. Symp. Combust., Michigan, U.S.A, **1984**: pp. 361–366.
[179] McCaffrey B.J., Purely Buoyant Diffusion Flames : Some Experimental Results, Center for Fire Research, **1979**.

[180] Audouin L., Kolb G., Torero J.L., Most J.M., Average centreline temperatures of a buoyant pool fire obtained by image processing of video recordings, Fire Saf. J. 24 **1995** 167–187. https://doi.org/10.1016/0379-7112(95)00021-K.
[181] Safety data sheet-The Dow Chemical Company, TUFF-R^{TM} C 2.00 Inch Commer. Insul. Sheathing. **2015**.
[182] Vitkauskiene I., Makuška R., Stirna U., Cabulis U., Thermal properties of polyurethane-polyisocyanurate foams based on poly(ethylene terephthalate) waste, Mater. Sci. 17 **2011** 249–253. https://doi.org/10.5755/j01.ms.17.3.588.
[183] MatWeb-Material Property Data, n.d. http://www.matweb.com/search/datasheet.aspx?MatGUID=d9c18047c49147a2a7c0b0bb1743e812 (accessed November 8, 2019).
[184] Lyon R.E., Quintiere J.G., Criteria for piloted ignition of combustible solids, Combust. Flame. 151 **2007** 551–559. https://doi.org/10.1016/j.combustflame.2007.07.020.
[185] Lundström F.V., Sunderland P.B., Quintiere J.G., van Hees P., de Ris J.L., Study of ignition and extinction of small-scale fires in experiments with an emulating gas burner, Fire Saf. J. 87 **2017** 18–24. https://doi.org/10.1016/j.firesaf.2016.11.003.
[186] Gong J., Zhu H., Zhou H., Stoliarov S.I., Development of a pyrolysis model for oriented strand board. Part I: Kinetics and thermodynamics of the thermal decomposition, Orig. Artic. J. Fire Sci. 39 **2021** 190–204. https://doi.org/10.1177/0734904120982887.
[187] Gong J., Zhou H., Zhu H., McCoy C.G., Stoliarov S.I., Development of a pyrolysis model for oriented strand board. Part II: thermal transport parameterization and bench-scale validation, J. Fire Sci. **2021**.
[188] Försth M., Roos A., Absorptivity and its dependence on heat source temperature and degree of thermal breakdown, Fire Mater. 35 **2011** 285–301. https://doi.org/10.1002/fam.1053.
[189] Sjostrom E., Wood chemistry: fundamentals and applications, Gulf professional publishing, **1993**.
[190] Howell J.R., A catalog of radiation configuration factors, 3rd ed., Web, n.d. http://www.thermalradiation.net/sectionc/C-15.html (accessed May 5, 2021).
[191] Brewster M.Q., Thermal radiative transfer and properties, John Wiley & Sons, **1992**.
[192] Emissivity of Common Materials (Candle Soot), n.d. https://www.omega.co.uk/literature/transactions/volume1/emissivitya.html#c (accessed June 3, 2021).
[193] Gad-el-Hak M., Basic instruments, Handb. Fluid Dyn. CRC Press. Part. 33 **1998** 1–22.
[194] Monteith J., Unsworth M., Principles of environmental physics: plants, animals, and the atmosphere, Academic Press, **2013**.